On the Nature of Dynamic Cavity Collapse Using X-ray Phase Contrast Imaging



Emilio Millar Escauriza

St Edmund Hall

University of Oxford

Supervised by

Dr Daniel Eakins

A thesis submitted for the degree of

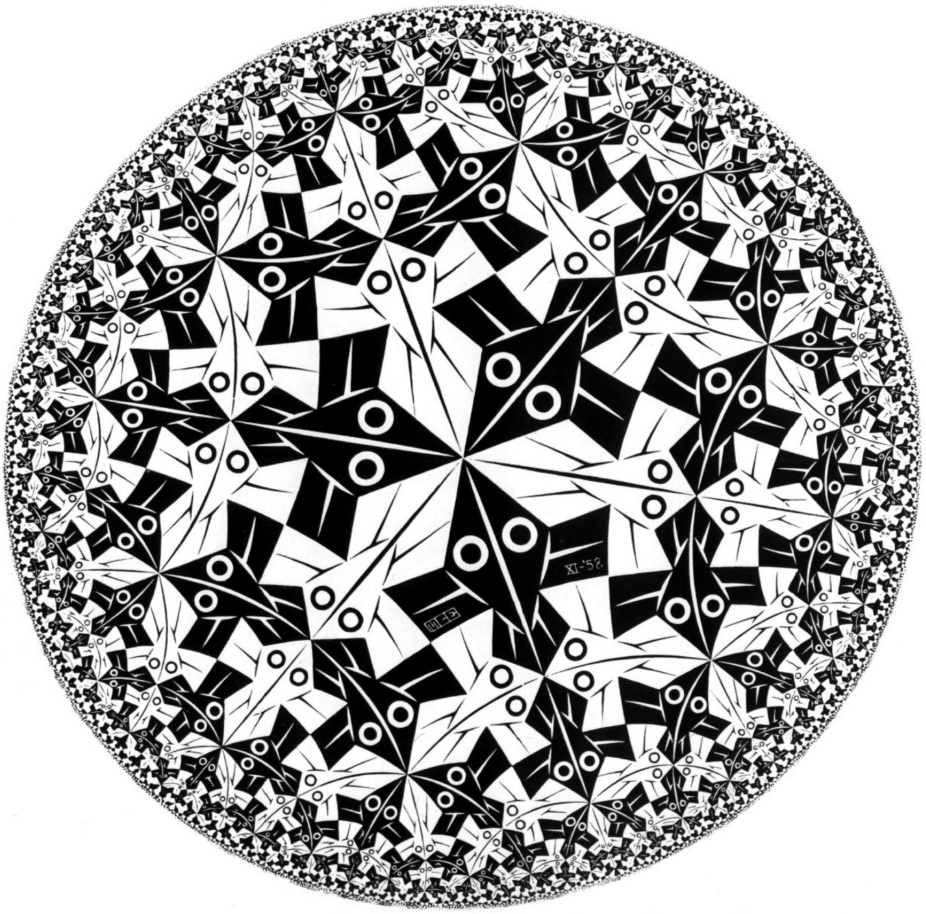
Doctor of Philosophy

Hilary 2021

For Mum, Dad, and Evan.

I do my best to make things happen, I create disorder
to order, as it were.

— Fyodor Dostoevsky, *The Brothers Karamazov*



— M C Escher, *Circle Limit I*

Abstract

The presence of cavities in materials under dynamic load significantly affects the way in which energy is distributed, by causing localised extrema of pressure and temperature when they collapse. There is interest in 'cavity collapse', as the phenomena has come to be known, from a wide range of fields, with the intention of either mitigating or harnessing the extraordinary conditions created. Most notably, there are applications in the medical sciences, in the development of energetic materials, and from research into nuclear fusion. A key aspect of understanding the phenomenon is to observe it directly, which allows comparison to numerical simulations of the process. This has been successfully achieved for cavities in fluids through established high-speed optical imaging techniques. However, capturing cavity collapse in solid media has remained elusive, due to the difficulties that even transparent solids pose in using visible light illumination. In this work cavities in the solid polymer poly[methyl methacrylate] (PMMA) – collapsed under shock loading – are captured with high-speed synchrotron X-ray imaging. The brilliant and hard X-rays delivered by beamline ID19's undulator source, combined with the beam's high level of spatial coherence, result in phase contrast enhanced radiographs that reveal details of the collapse process in new and exquisite detail. For this purpose, two separate gas gun systems are transported to the European Synchrotron Radiation Facility (ESRF), over multiple experimental campaigns, generating a wide range of pressure states. To image the experiments, a custom-made, multi-camera indirect X-ray imaging system is developed, capable of capturing 100 ps time resolved frames from individual X-ray pulses for 10s of μs at frame rates up to 5.68 Mfps.

The radiographic results show the impacted cavities exhibiting a wide range of behaviours as the shock loading pressure is increased. Strength-dominated collapse is observed at the lower pressures, with features like cracking and fragmentation cause by damage, and perturbations that form along the cavity interface, which indicate the presence of shear banding. The spacing between the bands is shown to decrease as the shock pressure increases, which indicates the increased proportion of melt within the PMMA medium. Above a threshold shock pressure, bulk melting is mostly complete and hydrodynamic modes of cavity collapse are seen, with jet formation, and, at the very highest pressures, the formation of a hot plasma inside toroidal vortices. A head-to-head comparison is performed between the experimental results and 2D/3D simulations run in the code SCIMITAR3D, with broad and close agreement with the experiments. This gives confidence in details from the simulations not available from the experi-

ments, such as the local evolution of density, pressure, and most notably temperature during collapse. In the strength regime a network of high-temperature shear bands form, emanating from perturbations along the cavity interface, as are seen in the experimental radiographs. A re-shock generated by the collapse further heats the region, resulting in large temperature rises. At the highest shock pressures there is heating from the shock, followed by further heating during collapse and the mixing of material in toroidal vortices, resulting in a highly intense hot spot. Analysis of the collapse time vs. loading pressure, with additional simulations on aluminium, copper and stainless steel, reveal what appears to be a general scaling law for collapse time based solely on loading pressure, geometry and material stiffness.

This work represents a significant experimental advancement in research into cavity collapse, providing new insight into the transition between strength and hydrodynamic states during intense shock loading. As well as being relevant to the fields interested in the specific phenomenon, the results are relevant to areas beyond, such as shear banding, damage and crack formation, and jet instability formation. The results also showcase the capabilities of the high-speed imaging system used in the experiments, and the quality of radiographic imaging that can be obtained through synchrotron radiography, as well as the techniques necessary to analyse the results. This work lays the foundation for future work into cavity collapse, with many avenues left to explore, such as multiple interacting cavities collapsing in a solid, and further investigation into the precise role that strength plays in the collapse dynamics.

Declaration

The content presented in this thesis is the product of my own work. Due to the collaborative nature of this project, the experimental and computational aspects were performed with many researchers both internal and external to the Dynamic Behaviour Materials group. Where included, author contributions are acknowledged or referenced accordingly.

Publications

During my project I published two first author papers and one co-first authored paper, which are the basis of Chapters 3-5, and I am listed as an author on an experiment our group facilitated, in collaboration with a group from Lawrence Livermore National Laboratory (LLNL). I had opportunity to present my project at the Shock Compression of Condensed Matter (SCCM) 2019 conference, for which the proceeding was peer reviewed. I am also listed as an author on a proceeding with collaborators from Fraunhofer EMI, and a talk at the 3rd Studies of Dynamically Compressed Matter with X-rays (DYCOMAX) workshop given by Dr David J Chapman, a senior researcher in our group. Furthermore, I am a listed author on a paper submitted to the 2021 Mechanical and Physical Behaviour of Materials Under Dynamic Loading (DYMAT) conference, for work in collaboration with researchers at Université Grenoble Alpes. Full details of these publications are listed as follows.

Papers

- **E M Escauriza**, M P Olbinado, M E Rutherford, D J Chapman, J C Jonsson, A Rack and D E Eakins, *Ultra-high-speed indirect X-ray imaging system with versatile spatio-temporal sampling capabilities*, **Applied Optics** 57, 8 (2018). https://doi.org/10.1364/AO.57.005004

- **E M Escauriza**, J P Duarte, D J Chapman, M E Rutherford, L Farbaniec, J

C Jonsson, L C Smith, M P Olbinado, J Skidmore, P Foster, T Ringrose, A Rack and D E Eakins, *Collapse dynamics of spherical cavities in a solid under shock loading*, **Scientific Reports** 10, 8455 (2020).
https://doi.org/10.1038/s41598-020-64669-y

- N K Rai, **E M Escauriza**, D E Eakins and H S Udaykumar, *Mechanics of shock induced cavity collapse in poly(methyl methacrylate) (PMMA): Comparison of simulations and experiments*, **Journal of the Mechanic and Physics of Solids** 143, 104075 (2020).
https://doi.org/10.1016/j.jmps.2020.104075

- D J Miller, R S Crum, M A Homel, D E Eakins, D J Chapman, J C Jonsson, M E Rutherford, **E M Escauriza**, L C Smith, E B Herbold, J Lind, M C Akin, *Hugoniot measurements utilizing in situ synchrotron X-ray radiation*, **Journal of Dynamic Behavior of Materials** 5 (2019).
https://doi.org/10.1007/s40870-019-00187-x

Proceedings

- **E M Escauriza**, D J Chapman, J P Duarte, J C Johnsson, L Farbaniec, M E Rutherford, L C Smith, M P Olbinado, A Rack, D E Eakins, *Ultra-high-speed X-ray imaging of shock-induced cavity collapse in a solid medium*, SCCM Conference 2019, **AIP Conference Proceedings** 2272, 110003 (2020).
https://doi.org/10.1063/12.0000933

- M Jäcklein, K Kappe, A Pfaff, M Bierdel, K Hoschke, M Wickert, W Riedel, J Forster, D E Eakins, **E M Escauriza**, L C Smith, A Rack, *Dynamic compression of 3D printed metallic mesostructures with in-situ X-ray imaging*, **International Symposium on Impact Engineering** (2019).

- D J Chapman, L Farbaniec, M E Rutherford, L C Smith, J C Jonsson, **E M Es-**

cauriza, A Rack, D E Eakins, *Application of XPCI to the incipient stages of material failure on ID19*, **3rd Workshop on Studies of Dynamically Compressed Matter with X-rays (DYCOMAX)** (2021).

- B Lukić, B Blasone, Y Duplan, P Forquin, **E M Escauriza**, M E Rutherford, D J Chapman, M P Olbinado, A Rack, *Ultra-high speed X-ray imaging of dynamic fracturing in cementitious materials under impact*, **DYMAT** (2021).

In addition to my SCCM2019 conference talk, I was also fortunate to be able to present my work on the following occasions.

Oral presentations

- *Ultra high-speed X-ray imaging of dynamic cavity collapse*, Annual ESRF Structure of Materials meeting, (19/03/2018, France).
- *A case study in ultra-high-speed X-ray imaging: shock-cavity interactions in a solid medium*, Solid Mechanics, Materials and Engineering Group (SMMEG) Junior Researcher Seminar, (11/06/2020, UK).

Poster presentations

- *X-ray phase contrast imaging of dynamic cavity collapse*, HERCULES European School, (27/2-30/3/2017, France).
- *Single-bunch X-ray phase contrast imaging of dynamic cavity collapse at beamline ID19* ESRF Student Days, (13-15/10/2017, France).

Acknowledgements

First and foremost, I owe a great deal to my DPhil supervisor Dr Daniel Eakins, for giving me the opportunity to embark on this journey. His trust, wisdom and good humour were a guiding light throughout.

I am also particularly grateful for my time working in the lab with many inspirational researchers. Dr David Chapman, who taught me the true meaning of dotting the i's and crossing the t's. Dr João-Pedro Duarte, whose positivity was infectious and energy often hard to keep up with. The jazz music and calm demeanour of Dr Lukasz Farbaniec brought a sense of style to the lab.

I was very lucky to have been introduced to my collaborator Dr Nirmal Rai and his supervisor at the University of Iowa, Prof H S Udaykumar. In my meetings with Nirmal I learned to see the funny side of research, and I'm glad I was able to share a beer him at a conference in Portland.

I am grateful for the time I spent at First Light Fusion, thanks to the vision of Dr Nick Hawker. During my visits, Jon's encouragement and guidance always came at just the right time. Shout out to Peta and Tim for bringing the fun on one of our campaigns in France.

I want to give special thanks to my fellow DPhil students, for our time spent at Imperial College and Oxford. I could talk endlessly about body mechanics with Liam. John taught all about Kendo basics and brought the chill vibes. Michael's

stories were entertaining and he always had good advice. From Tom I learned about grown up things like how to resurface a driveway. I will always have fond memories of our week-long stints at the ESRF in France, where many a long night spent at beamline ID19 descended into delirium. We persevered through thick and thin, and spirits remained high.

It was a pleasure getting to know the additions to our group while at Oxford. I had many an entertaining discussion with Elie, Chanel and Maureen. Our lively debates were a welcome distraction from a hard day in the lab.

I had a great year working at the ESRF, in the lab and on the ski slopes. Thanks to Dr Alexander Rack, I was able to meet the eclectic bunch of characters, Margie, Camille, Vincent, Dennis, Maxime, Pierre-Jean, Yin and David.

I also want to thank the people in our lab who keep the wheels from falling off. Karen, for always being two steps ahead and her patience with my badly written emails. Stuart, Jeff and the other technicians at Oxford, for their help during my experiments and humouring my silly questions.

I am forever grateful to my Mum, Dad and brother Evan, to whom this thesis is dedicated. They have been my ever present rock during these years.

Finally, I want to wish the best of luck to the new additions to our group. Sharing my work with Mila during her fourth year was a great experience, and I enjoyed showing Ed the often frustrating ins and outs of the coating machine. Dave needs to properly explain his project to me on our next surf trip.

Oxford, April 2021 E M E

Funding

This research was funded by a joint ESRF and First Light Fusion Ltd studentship.

Contents

Abstract i

Declaration iii

Publications iv

Acknowledgements vii

Contents xiii

List of Figures xiv

List of Tables xviii

1 Introduction 1

1.1 Motivation 1

1.1.1 Medical applications 4

1.1.2 Energetic materials 6

1.1.3 Nuclear fusion 8

1.2 Literature review 10

1.2.1 Early research into cavity collapse 10

1.2.2 Experimental developments 12

1.2.3 Shock-cavity interactions 15

1.2.4 Computational studies on shock-cavity interactions 20

1.2.5 Cavity collapse in solids 21

1.2.6 Energy localisation and shear banding 25
1.2.7 X-ray imaging of impact studies 29
1.3 Summary 34
1.4 References 37

2 Methods **49**
2.1 Gas gun systems 49
2.1.1 Single-stage gas gun 50
2.1.2 Two-stage gas gun 53
2.1.3 Flyer and target design 55
2.2 Synchrotron imaging 63
2.2.1 Indirect X-ray imaging 63
2.2.2 The ESFRF synchrotron 65
2.2.3 The imaging system 70
2.2.4 Synchronisation 74
2.3 Analytical methods 79
2.3.1 Image processing and data extraction 79
2.4 Computational methods 84
2.4.1 Governing equations 85
2.4.2 Hytrac 87
2.4.3 SCIMITAR3D 88
2.5 References 88

3 Radiographic imaging system **93**
3.1 Introduction 94
3.2 Instrumentation 98
3.3 Ultra high-speed radiography 101
3.4 Conclusions 109
3.5 References 110

4 Cavity collapse experimental results **113**

4.1 Introduction . . . 114
4.2 Methods . . . 117
4.2.1 Extracting parameters . . . 117
4.2.2 Shear banding analysis . . . 123
4.2.3 Hydrodynamic simulations . . . 129
4.3 Results . . . 131
4.3.1 Shock state calculations . . . 131
4.3.2 Experimental data . . . 135
4.3.3 The strength regime . . . 135
4.3.4 The hydrodynamic regime . . . 136
4.3.5 Cavity collapse time evolution . . . 140
4.3.6 Cavity interface dynamics . . . 146
4.3.7 Fourier analysis of interface perturbations . . . 149
4.4 Discussion . . . 153
4.5 Summary . . . 156
4.6 References . . . 157

5 Comparison of simulations and experiments 163

5.1 Introduction . . . 165
5.2 Methods . . . 168
5.2.1 Computational methods . . . 168
5.2.2 Experimental methods . . . 173
5.2.3 Image processing and parameter extraction . . . 175
5.2.4 Creating overlay images . . . 177
5.3 Results and discussion . . . 179
5.3.1 Cavity collapse under 1.25 GPa shock strength . . . 180
5.3.2 Cavity collapse under 1.84 GPa shock strength . . . 186
5.3.3 Cavity collapse under higher shock strengths, 4.10 GPa and 16.60 GPa . . . 190
5.3.4 Parameter variation with loading pressure . . . 197

5.3.5 Collapse time study on different materials 202
5.4 Conclusions 214
5.5 References 217

6 Conclusions and research outlook **221**
6.1 Conclusions 221
6.2 Research outlook 227

List of Figures

1.1 Versluis et al. snapping shrimp images 2
1.2 Cavitation damage to propeller 3
1.3 Browning et al. targetted drug delivery diagram 5
1.4 Roy et al. cavity collapse array simulations 7
1.5 Betney et al. shock-cavity array simulation plots 9
1.6 O. Reynolds apparatus diagram 11
1.7 Rayleigh collapse diagram 12
1.8 Kornfeld & Suvorov's collapse shapes 13
1.9 Damage to aluminium from a collapsing cavity 14
1.10 Experiment vs. simulations cavity collapse interface 15
1.11 Dear & Field shock-cavity interaction images 17
1.12 Swantek & Austin cavity array under shock loading 18
1.13 Hawker & Ventikos 3D simulation images 20
1.14 Rai et al. 3D simulations 22
1.15 Rai et al. simulation of HMX SEM scan 23
1.16 Austin et al. shear localisation simulation 24
1.17 Armstrong et al. cavity collapse radiographs 26
1.18 Shear banding cylinder experiment 28
1.19 Lovinger et al. shear band simulations 30
1.20 Rack et al. phase contrast example 31
1.21 Willey et al. exploding flyer PCI 32
1.22 Jensen et al. PCI example 33

1.23 Rutherford et al. powder impact study 34

2.1 Single-stage gas gun 51
2.2 Two-stage gas gun 53
2.3 Flyer and target parameters 55
2.4 Impedance matching Hugoniot plots 57
2.5 Single-stage targets. 60
2.6 Single-stage targets. 62
2.7 X-ray sources brilliance plot 66
2.8 Phase contrast enhancement diagram 69
2.9 Imaging system 71
2.10 Camera phase difference diagram 73
2.11 Experimental timeline 75
2.12 Schematic diagram of wiring 76
2.13 Photograph of synchronisation system 78
2.14 Flat field correction figure 80
2.15 Image flipping transform 81
2.16 Image registration transform 83
2.17 Canny edge detection 84

3.1 UHS radiographic imaging camera configurations 97
3.2 UHS radiographic imaging timing diagram 100
3.3 Simulated photon flux of LYSO:Ce and GAGG:Ce scintillators . . . 102
3.4 Annotated UHS radiograph images 103
3.5 Comparison of radiographs from the two different cameras 107

4.1 Shock front measurement 118
4.2 Decreasing area example 119
4.3 Cavity interface displacement 120
4.4 Lineout method figure 124
4.5 Fourier analysis figure 127

4.6 Peak and valley locations 128
4.7 Hytrac grid convergence study 130
4.8 Example cavity collapse radiographs 134
4.9 Low-impact velocity cavity collapse radiographs 137
4.10 Medium-impact velocity cavity collapse radiographs 138
4.11 High-impact velocity cavity collapse radiographs 139
4.12 Cavity collapse experiments area vs. time plots 140
4.13 Cavity collapse experiments times vs. pressure plots 141
4.14 Cavity collapse acceleration vs. pressure 146
4.15 Cavity collapse simulations jet displacement vs. time 147
4.16 Cavity collapse experiments jet displacement vs. time 147
4.17 Selected frames of 4 mm cavity results 150
4.18 Selected frames of 6 mm cavity results 151
4.19 Mean peak spacing vs. time 152

5.1 Domain diagram for simulations in SCIMITAR3D 168
5.2 Grid convergence for SCIMITAR3D cavity collapse simulations . . 169
5.3 Experimental overview diagrams 174
5.4 Overlay plots diagrams 178
5.5 $p = 1.25\,\mathrm{GPa}$ comparison figure 181
5.6 2D 1.25 GPa shock temperature plot 183
5.7 3D 1.25 GPa shock iso-surface temperature plots 185
5.8 $p = 1.84\,\mathrm{GPa}$ comparison figure 188
5.9 2D 1.84 GPa shock temperature plot 189
5.10 $p = 4.10\,\mathrm{GPa}$ comparison figure 191
5.11 2D 4.10 GPa shock temperature plot 192
5.12 $p = 16.60\,\mathrm{GPa}$ comparison figure in 2D and 3D 194
5.13 16.60 GPa shock temperature 2D and 3D plots 196
5.14 Collapse time vs. loading pressure 198
5.15 Jet and release velocities vs. particle velocity 200

5.16 Interface acceleration vs. loading pressure 202
5.17 All experiments and simulations t'_{col} vs. p/p_0 205
5.18 All experiments and simulations α vs. $C_L\sqrt{\rho/p_s}$ 209
5.19 All experiments and simulations β vs. C_L/C_s 210

List of Tables

4.1 Material U_s-u_p Hugoniot relations 131
4.2 Cavity collapse experiments results table 133

5.1 Material parameters for SCIMITAR simulations 171
5.2 Selected experiment parameters table 174
5.3 Parameters for SCIMITAR collapse time material study 203
5.4 Results of simulations on aluminium, copper and stainless steel . 204

Chapter 1

Introduction

In this Chapter the research motivations are first outlined, followed by a survey of relevant works in the literature review. This is followed by summary and an outline of the aims of this work.

1.1 Motivation

A cavity can be considered an unoccupied space in an otherwise continuous material medium. Depending on the field of research, cavities are also referred to as 'bubbles' [1–3], 'voids' [4–6], 'pores' [7–9] and 'inhomogeneities' [10–12]. Cavities can exist mechanically inert within a medium, such as static bubbles in fluid or as fluid-filled gaps in solids. For these cavities the forces supporting the walls of the cavity are in equilibrium, and thus remain stationary. In the present work we are instead interested with the type that collapses under pressure in the surrounding medium. In our examples of cavities in a fluid or solid, collapse may occur because of an increase in pressure that disturbs the equilibrium of the supporting forces along the cavity structures. Due to a large pressure field in a hydrostatic medium, or from an impulse on the medium, the supporting forces are overwhelmed and the cavities collapse. Alternatively, a sudden drop in pressure

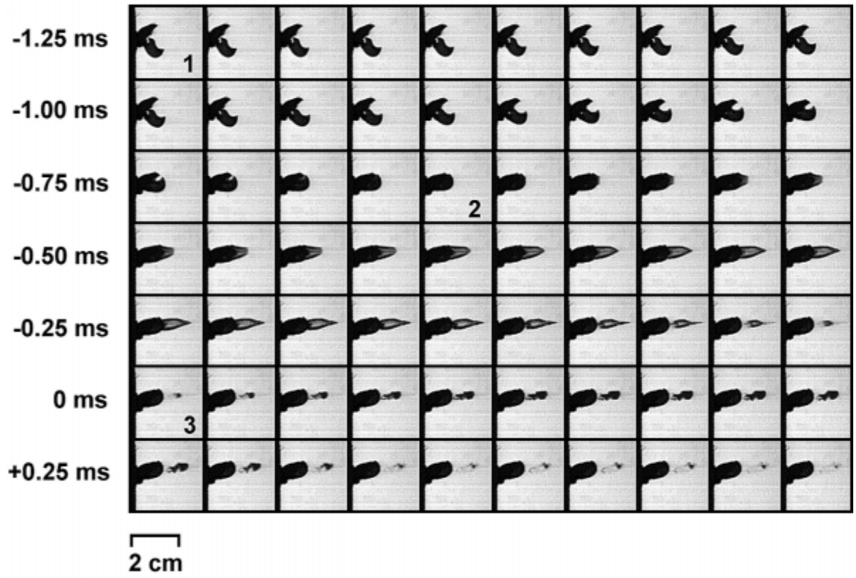


Figure 1.1: High-speed images of the snapper claw of the alpheid shrimp closing, from Versluis et al. [13]. The peak of the measured sound intensity is at 0 ms, in the frame labelled 3.

in a fluid may lead to the formation of cavities, which then collapse when the pressure increases to its initial level.

A well-known example of this occurs in nature, when the large claw of the alpheid shrimp (also known as the 'snapping' or 'pistol' shrimp) rapidly closes. It uses the energy produced by the collapsing cavity to kill prey and communicate [13, 14]. High-speed imaging of the shrimp's claw in action can be seen in Fig. 1.1, which shows high-speed images from a study by Versluis et al. [13]. The peak of the pressure wave is generated after the claw has closed, and is caused by a cavity that forms in the low pressure region generated by the closing claw, which subsequently collapses. In engineering, 'cavitation damage' has been studied since the late 19^{th} century – the phenomenon was investigated because of damage to a new generation of fast moving ship propellers [15]. Figure 1.2 shows the extent of this type damage, which is still a problem today, even to the propellers of modern small boats. Both of these examples demonstrate why there has been much interest in collapsing cavities in a wide range of research fields: extraordinary states of pressure and temperature can be generated locally during the collapse of a cavity. For this reason, much of this research revolves around trying

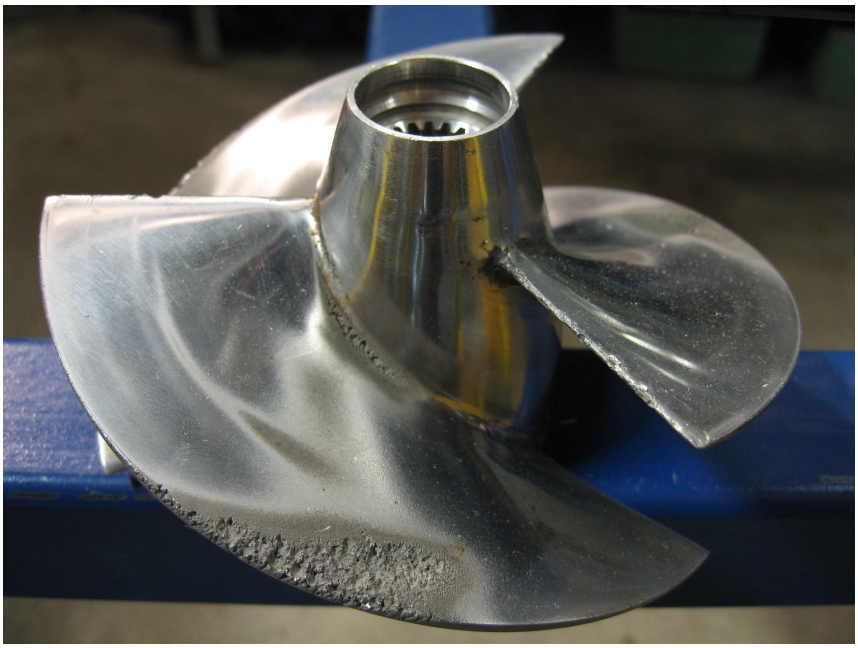


Figure 1.2: Cavitation damage to the propeller of a small boat. Damage is most severe on the portions of the blades that move fastest. From Erik Axdahl under the Creative Commons Attribution-Share Alike 2.5 Generic license.

to harness or mitigate the local energy spikes caused by collapsing cavities.

While the collapse of cavities in fluids has been studied extensively, for reasons that will be discussed, cavity collapse in solids is less well understood. This dearth of knowledge is the motivation for this work, which focuses on the collapse of cavities in a solid medium. The more general case of such cavities would be a random distribution of various sizes and shapes of cavity, with some coalesced to form networks. Such a material could be described as a foam. There are many examples in which such cavities are present: in the setting of concrete, cavities form during the drying process [16], and during laser powder bed additive manufacturing [17, 18]. If either of these materials are subjected to impulsive load, the presence of collapsing cavities will influence the mechanisms by which energy is dissipated. Furthermore, understanding the collapse of underground cavities during mining explosions is critical for safety [19]. To model the problem of a cavity collapsing in a solid, a stripped-back model is studied: the experiments and simulations look at the collapse of a single spherical cavity, collapsing under intense shock loading. As we will see in the following Chapters, despite this

simplification there are a great many experimental and numerical challenges to capture the behaviour of even a single cavity collapsing in a solid. The aim of this work is to develop cutting-edge experimental techniques to capture this phenomenon and extract quantitative information through novel analysis, in order to test numerical predictions of the process through modelling. The results will improve our understanding of the behaviour of cavities in a solid under shock loading, advancing the field and paving the way for future research.

1.1.1 Medical applications

As in engineering, cavity collapse can also be a destructive problem in the medical sciences: similar to ship propellers, cavitation, i.e. the action of large clouds of collapsing cavities, can cause damage to mechanical heart valves [20]. Therefore, understanding how to mitigate this damage is vital for the development of long-lasting valve materials. Additionally, cavitation damage is thought to play a role in head injuries and impact wounds, such as from bullet penetration [21]. However, there are also many constructive medical uses of the energy localisation from cavity collapse. Through 'shockwave lithotripsy' [22–25], and more recently 'focused ultrasound lithotripsy' [26], cavitation is utilised to disintegrate problematic gall and kidney stones, allowing the patient to pass the stones more easily [21]. Furthermore, the action of oscillating cavities [27] and collapsing cavities [28–30] have been utilised to clean surfaces and wounds without the need of potentially harmful chemicals. However, in the case of cavitation (collapse), for both lithotripsy and cleaning, collateral damage to biological tissues in the patient is a significant risk [21]. Consequently, there has been interest in experimentally measuring [30] and modelling [31] the phenomenon to try and mitigate potential damage.

A significant example of current techniques being developed to harness cavity collapse in the medical context is targetted drug delivery, whereby the efficacy of

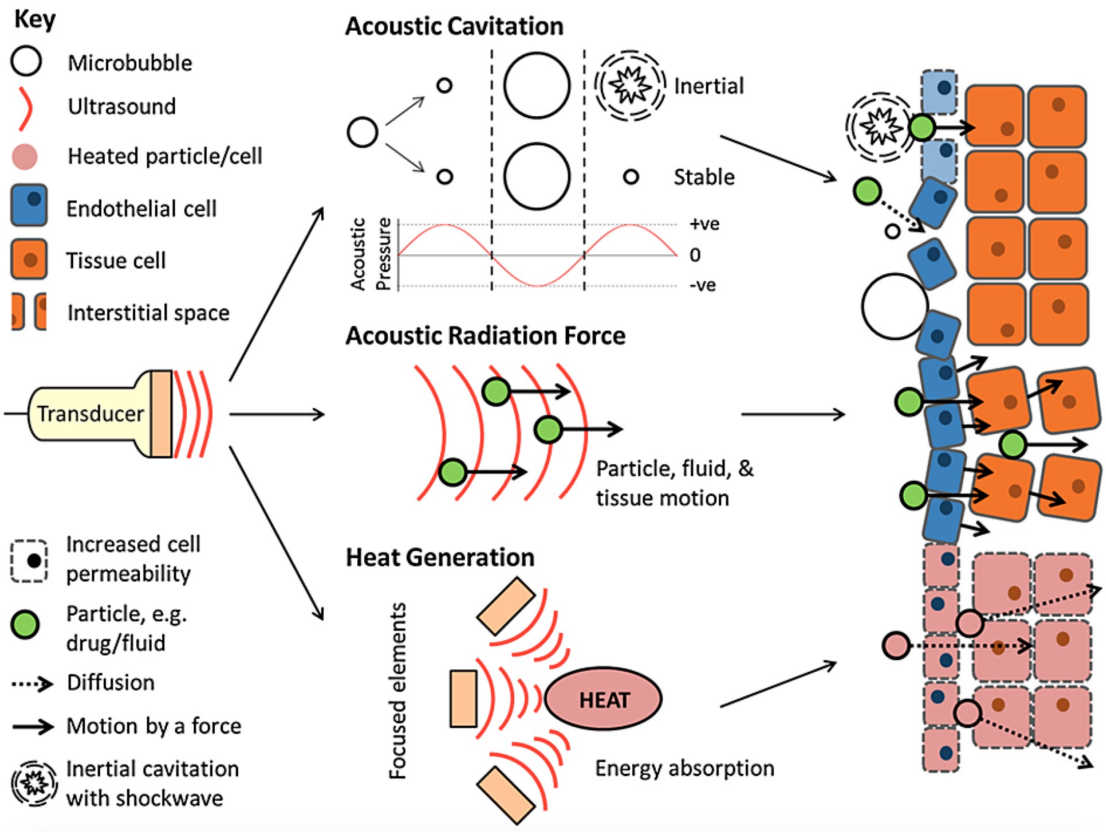


Figure 1.3: Diagram of the mechanisms of targetted drug delivery, from Browning et al. [32].

therapeutic compounds can be increased through the action of clouds of cavities induced in the tissue [33–35]. Development of this technique is motivated by the difficulty in 'targetting' drugs at tumours, due to the poor vasculature that can result during its growth. Consequently, patients are given large doses of drugs, and are burdened with severe side effects [21, 35]. The process of the targetting is demonstrated in the diagram of Browning & Stride [35] (originally appearing in Browning et al. [32]), in Fig. 1.3: an ultrasonic transducer acts through three simultaneous mechanisms: (i) acoustic cavitation causes oscillation and collapse, which forces drug particles into the target tissue; (ii) acoustic radiation creates a fluid flow in the direction of the target tissues; and (iii) heat energises the tissues, also increasing the rate of drug absorption. Efforts are being made to understand these mechanisms to increase the effectiveness of this promising therapy [34, 36], in which cavity collapse plays a key role. For more details on cavity collapse in the medical context, see Brennen's 2015 review [21].

1.1.2 Energetic materials

Historically there has been keen interest in cavity collapse for the research of ignition mechanisms of energetic materials [37–39], and this continues to be a diverse area of study. By energetic materials, we mean materials that have a large amount of stored chemical energy that can be released in a short amount of time, such as explosives, propellants and fuels. Initiation of energy release can occur through, among other mechanisms, heating, shock loading, or an electrical spark [40]. It has long been known that the reaction rate of such materials strongly depends on temperature [38], meaning the formation of localised 'hot spots' can increase the rate and lower the initiation threshold significantly [41].

Through experimental [37, 38, 42–44] and numerical [7, 39, 45] studies, it is also clear that the presence of 'inhomogeneous' regions in explosives, i.e. cavities, in-

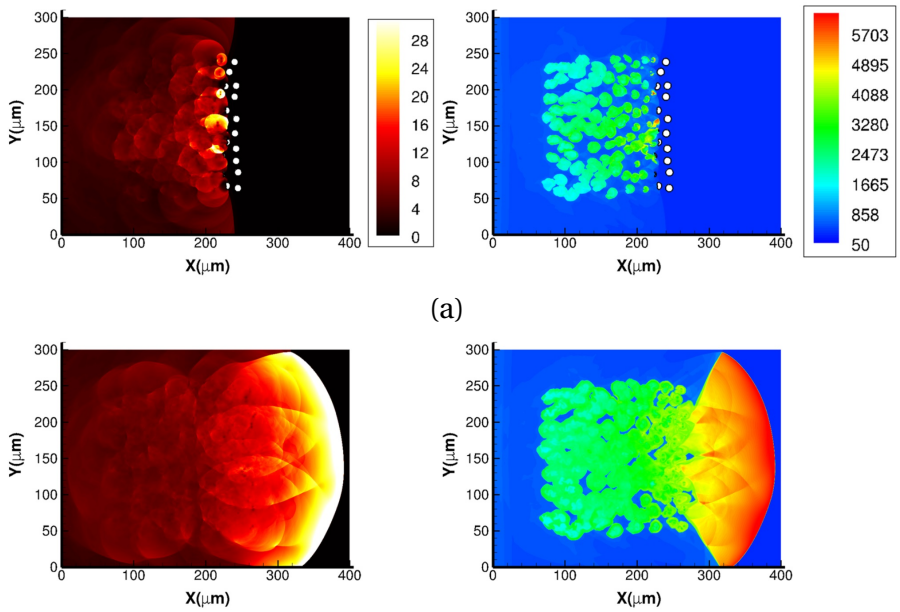


Figure 1.4: Reactive simulation images from a Roy et al. [46] study on shock-loaded HMX containing 10 μm diameter cylindrical cavities impacted with a 9.5 GPa shock, at two time instances of (a) 49.7 ns and (b) 68.2 ns. The left- and right-hand plots show pressure [GPa] and temperature [K], respectively.

creases the occurrence of hot spots, and therefore lowers the initiation threshold. A striking visual representation of this process can be seen in the 2D simulation work of Roy et al. [46], in Fig. 1.4, where an array of randomly assorted 10 μm diameter voids (making up 20% of the domain volume) is impacted from the left with a 9.5 GPa shock. The collapsing cavities greatly increases local pressure and temperature, which leads to detonation of the medium, visible as the high pressure and temperature shock front in Fig. 1.4b. This example of high-level simulation study demonstrates the need for direct experimental validation, for which there is currently a limited number of studies [42, 47, 48].

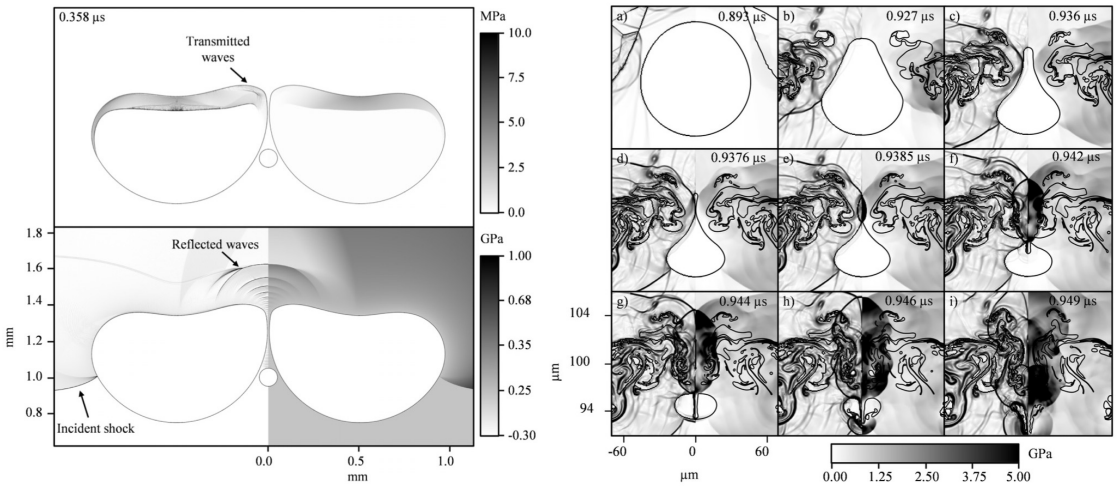
More specifically, there is a clear challenge in observing cavity collapse in solid energetic media, due to the optical opacity of many materials and, even in the case of transparent materials, refractive effects [49]. There is clear motivation then to use X-rays, because of their penetrative nature, which makes them well suited for studying sub-surface behaviour in solids [50]. Flash X-rays have been used to record impact studies [51, 52], and more recently phase contrast en-

hanced radiography has been developed at synchrotrons [53, 54]. The short pulse duration, high-energy and spatial coherence of synchrotron X-rays makes them ideal for studying dynamic experiments in solids [55, 56]. For this reason, in the present work X-rays are chosen to record shock-cavity interactions in a solid medium, in order to reveal new details of the collapse process over a wide range of pressure states.

1.1.3 Nuclear fusion

Scientists have investigated sonoluminescence, a process in which oscillating cavities (rapidly dilating and contracting) are produced in a fluid using standing sonic waves, as a way of producing highly localised spikes in pressure and temperature. Upon each cycle of collapse, a flash of light ('luminescence') is produced, which is known to originate from a plasma that forms in the final stages of collapse [57, 58]. In an effort to quantify these intense conditions, light-scattering experiments have been performed by Barber et al. [59], who found that small changes in cavity radii resulted in a 200-fold increase in the emitted light intensity, thus demonstrating the potential for sonoluminescence to produce events with very high pressures and temperatures. Following this study, simulations by Moss et al. [60] suggested that "table-top micro-thermonuclear fusion", commonly called sonofusion, could be possible if the luminescence duration could be reduced to picoseconds. Despite the theoretical models and controversial claims that fusion had been achieved using sonoluminescence apparatus [61], as it stands there is still no good experimental evidence that sonofusion is possible [62, 63]. Nonetheless, the investigation into viable techniques continues [64–66].

Cavity collapse through shock loading may yet also provide a viable method to generate nuclear fusion [67–69]. In their high-resolution numerical simulation study, Hawker & Ventikos [70] speculate that, compared to sonoluminescent cav-



(a) (b)

Figure 1.5: Simulation plots from the Betney et al. [3] study on shock-loaded cavity arrays in a liquid. (a) Two large cavities and a smaller cavity during the early stages of collapse after impact with a 1 GPa shock. Left side is a schlieren representation of density and the right grey scale indicates pressure. (b) A zoom view of the smaller cavity during the later stages of the interaction, revealing complex jetting. The grey scale shading indicates pressure.

ity collapse, "the intense conditions created by shock-driven [cavity] collapse could well prove to have the same potential for exploitation." From the same group, a more recent study by Betney et al. [3] conducted an investigation into multiple neighbouring cavities under shock loading, to determine the optimum relative cavity sizes and orientations that would increase the peak pressures generated by collapse. The largest amplification of pressure relative to the initial shock was produced by arranging a small cavity below the centre point of two larger upstream cavities side-by-side, as can be seen in Fig. 1.5. The geometry of the simulation can be seen in Fig. 1.5a, where the third cavity is many times smaller than the two larger cavities. The 'pinching' effect generated by the collapse of these two cavities generates an intense jet in the smaller cavity, and a large spike in pressure, as shown in Fig. 1.5b. The result was that the maximum pressure of the small cavity collapse was 40 times larger than the input shock pressure [3].

These studies show the potential of shock-cavity interactions, and thus motivate the study of the phenomena experimentally. However, capturing cavity collapse

directly is challenging, especially using optical imaging, because of refraction by the spherical cavity interface. For this reason, in the current work short-duration synchrotron X-ray pulses are used as the illumination source, due to the low refraction of X-ray by matter. Furthermore, X-rays offer the opportunity to study larger cavities cast in solid media, thus allowing cavity collapse in both solids and liquids (at very high shock pressures) using the same experimental setup.

1.2 Literature review

There is a rich history of cavity collapse research, starting with two of the giants of British physics, Osborne Reynolds and Lord Rayleigh, whose consideration of the problem was a small part of their extensive research into the physical world. Just like many of today's researchers in the various fields looking at cavity collapse, their interest in the phenomenon lay in the great power of what, at first glance, may seem like an innocuous occurrence. Here are detailed the key findings of this research, and the experimental and computational techniques used to capture them.

1.2.1 Early research into cavity collapse

Although cavities form frequently in nature, it was first presented experimentally by Osbourne Reynolds in an 1895 paper for the Royal Society [71]. Reynolds demonstrated that when water is boiled inside an inclined tube with a kink near the end, it makes a distinct rumbling sound, similar to the sound a kettle makes coming to boil. Cavities (vapour bubbles) formed in the low-pressure region after the kink collapse when they enter the high-pressure region further up the tube, producing an audible sound. He observed a similar phenomenon in fast-flowing water inside a horizontal 'Venturi' tube, which has a constriction in the middle. In this case, the sound can be explained by Bernoulli's law: cavities form in the region immediately after the constriction, due to the sudden drop in pres-

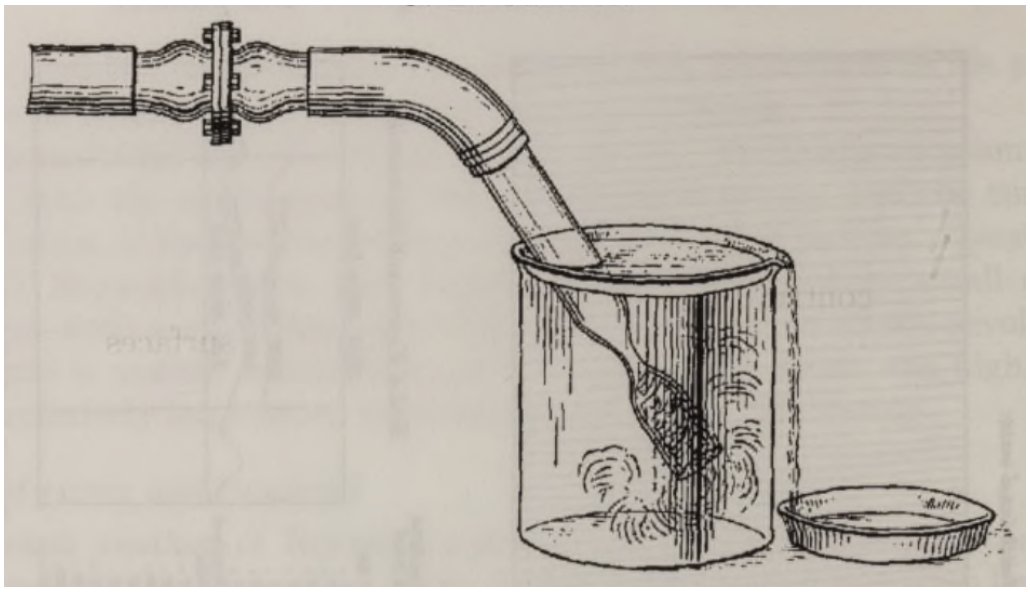


Figure 1.6: Diagram showing apparatus similar to that used by O. Reynolds to demonstrate water 'boiling at room temperature' [72]

sure in the fluid that occurs when its velocity increase, and subsequently collapse as the tube widens and the pressure increases. A diagram showing such an experimental setup can be seen in Fig. 1.6 [72].

Early attempts to model the phenomenon primarily came from the effort to solve the issue of damage to ship propellers and other vibrating machinery submerged in water, which came to be known as 'cavitation damage'. Initial modelling of the problem was developed by Besant in the 1850s [73], and then by Reynolds, but it was Lord Rayleigh who provided the first complete analytic model of a cavity in water collapsing under hydrostatic compression, in his seminal correspondence, *"On the Pressure Developed in a Liquid During the Collapse of a Spherical Cavity"*, published in Philosophical Magazine in 1917 [74]. A diagram showing the geometry of the model, and variables used in the analysis, is presented in Fig. 1.7. The expression Rayleigh derived provides an equation of motion for the bubble surface in terms of the difference between the pressure inside the cavity and the pressure in the fluid far from the cavity [75] (when surface tension and viscosity effects are included, it is known as the Rayleigh-Plesset equation [75, 76]).

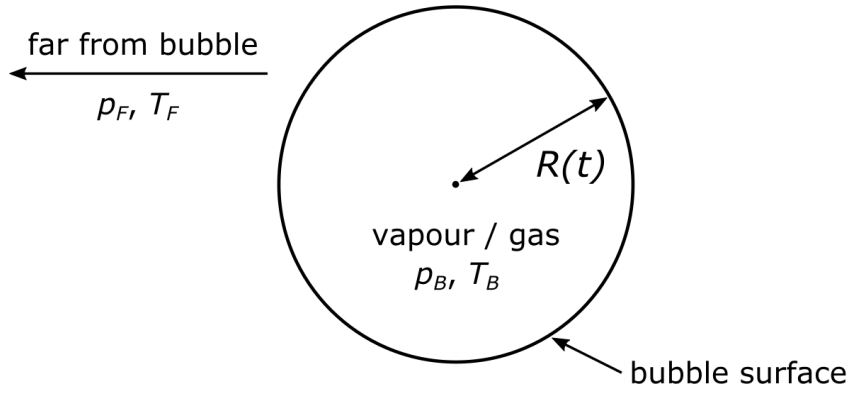


Figure 1.7: Diagram of the spherical cavity geometry used by Rayleigh to derive his cavity collapse equation of motion. The key variables in the final expression are the cavity radius at radius, vapour pressure inside the cavity, and the pressure and density in the liquid far from the cavity. Adapted from a figure of Brennen [75].

Rayleigh's analysis predicted that the pressure field generated in the region of the cavity at the later stages of collapse was indeed large enough to cause significant damage to solid surfaces. However, theorist and engineer S. S. Cook, who also worked with Rayleigh, had theorised that damage during cavitation could also be caused by direct blows from the inner liquid surface of the collapsing cavity against the solid boundary of the metal propeller, in the case that a cavity forms on or close to the boundary [15]. Although his model was incomplete, as we will see below, it was later found that cavity impact is the likely cause of damage.

1.2.2 Experimental developments

The early experimental work of Parsons & Cook [15] in the early 1900s revealed only the large-scale action of numerous cavities on large objects, such as when a propeller moves rapidly through water, or when a metal rod is placed in fast-flowing water. Similarly, Gaines [77] and others observed that a metal rod vibrating at a high frequency would deteriorate if submerged in water, again explained by the formation and collapse of cavities on the rod's surface. The indirect structural analysis of Mousson [78] revealed that the collapse pressures of water cavities near solid metal surfaces were indeed high enough to account

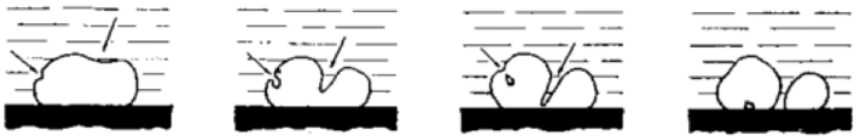


Figure 1.8: Diagrams of Kornfeld & Suvorov showing the collapse shapes of a cavity collapsing on a solid boundary, observed during their experimental work [80]. The arrows indicate the direction in which the liquid jets move.

for the damage. However, contrary to this finding, the *in-situ* measurement of collapse pressures by Haller found pressure values much less than Rayleigh's estimate [79].

Kornfeld & Suvorov's 1944 high-speed imaging study was the first to capture the formation and collapse of individual cavities [80]. The images challenged the assumption of Rayleigh's model that collapse is spherically symmetric (a model that had not been further developed for almost 30 years), revealing the surface shape of a cavity collapsing away from a solid boundary is very unstable. Nonetheless, they concluded that the central ideas of the theories of Cook and Rayleigh were still valid, but noted the pressure of a spherical collapse is the limiting case, meaning the vast majority of free, hydrostatic collapses will not have pressures high enough to cause significant damage. They proposed the damage is in fact best explained when Cook's impact theory is applied to an unstable cavity collapsing on the surface of a solid boundary, as"the pressure conditioned by these blows may reach up to several thousand atmospheres [$\sim$100 MPa]" [80]. Though they do not use the term, this is the first mention of a phenomenon in which the of the far side of a cavity involutes and forms a liquid 'jet' that strikes the far side of the cavity (which, in this case, is also the solid boundary). The principle is demonstrated with a diagram in the Kornfeld and Suvorov paper, which can be see in Fig. 1.8, of various collapse shapes that can occur when a cavity collapses against a solid boundary.

The next significant development in the theory of cavity collapse dynamics was

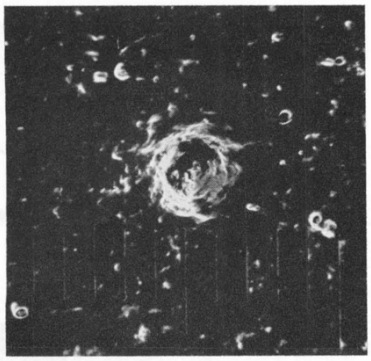


Figure 1.9: Damage sustained to an aluminium sheet by a collapsing hemispherical cavity, from an experimental study by Naudé & Ellis [82]. The scale of the notches is 0.1 mm per division.

the analytic work of Plesset & Milton [81], who looked at instability growth on the surface of a spherical cavity in a liquid medium. They found that small perturbations on the cavity surface could grow significantly, as observed in the Kornfeld & Suvorov [80] experiment. Naudé & Ellis [82], and later Benjamin & Ellis [83], extended the analytic treatment to look at the instability of a hemispherical cavity on a solid boundary in a liquid medium, and tested the theory against high-speed imaging experiments. The results confirmed the prediction that a growing hemisphere on a solid boundary will collapse by involuting, and produce a jet toward the boundary. Despite measuring a lower impact pressure than expected from theory, the damage caused by collapsing cavities on the aluminium boundary was significant, confirming the damage potential of direct blows against solid surfaces from liquid jets. Figure 1.9 shows the pitting on aluminium caused by a collapsing hemispherical cavity in contact with the surface, obtained by Naudé & Ellis [82].

Analysis of jetting during asymmetrical cavity collapse was further advanced by Plesset & Chapman, in their 1971 numerical study to provide an account of a cavity collapsing in a low-pressure liquid near a solid boundary [84]. Due to the inadequacies of perturbation-based analytic theories in dealing with large initial deformations of the cavity surface, they developed a numerical method to simulate the problem. The results confirmed the formation of a jet opposite of

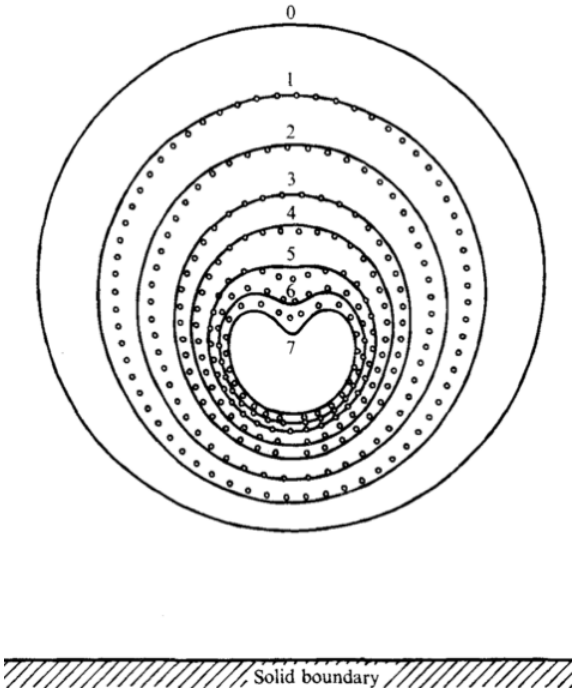


Figure 1.10: Diagram from Lauterborn & Bolle [85] showing experimental results (dotted lines) and theoretical predictions [82] (solid lines) of the cavity interface over time when collapsing near a solid boundary. The maximum cavity radius was 2.6 mm and the distance of the cavity centre to the solid boundary was 3.9 mm.

the boundary, and moving toward the boundary. The study looked at two cases: (i) when the cavity was close to the boundary, and (ii) when just touching the boundary. Both simulations predicted that a jet will form and moved toward the boundary. The predictions, including the collapse shapes and jet tip velocities, were confirmed by the experiment of Lauterborn & Bolle [85] – using a technique developed by Felix & Ellis [82], they focused a laser to a point in water near a solid boundary to produce a cavity. A comparison between the cavity interface time evolution extracted from experiments and the numerical prediction can be seen in Fig. 1.10, in which there is good agreement.

1.2.3 Shock-cavity interactions

Further advancements in cavity collapse research came with the development of techniques for studying stable cavities subjected to dynamic loading through the action of a planar shockwave in the cavity medium. This allows the initial

size of the cavity to be finely controlled, and enables the study of a shock interacting with an array of multiple cavities. Interest in shock-cavity interactions began with experiments on explosives containing inhomogeneous inclusions by Campbell et al. [37, 38]. The results indicated that the shock interacts with the inhomogeneities (which can be thought of as cavities) and produce 'hotspots' – small, localised regions within the material with very high pressure and temperature. The hotspots liberate energy and strengthen the shock, thus producing a chain of collapsing cavities that raises the temperature of the explosive, eventually leading to detonation, at a lower shock strength compared to a homogeneous medium. A numerical study by Mader subsequently found that, as the shockwave interacts with the cavity, a single jet will form on the upstream side of the cavity (relative to the direction of the planar shock) and move toward the opposite side of the cavity. Although the shape of the collapse is very similar to the hydrostatic collapse near a solid boundary, shock-loaded collapse differs in that the upstream side of the cavity is not at first 'aware' of the collapse process [49], whereas a cavity near a solid boundary experiences an asymmetrical pressure gradient across its entire outer surface before the collapse begins [83]. Mader confirmed that a hot-spot is formed upon collapse, which leads to a detonation front that propagates through the explosive medium [39].

Individual and multiple shock-cavity interactions were later captured by Dear & Field et al. [48, 49], and later by Bourne & Field [86, 87], who performed experiments with 2D cylindrical cavity geometry (as opposed to 3D spherical) by impacting cylindrical voids in gelatine blocks with a plane-surface projectile fired from a gas gun. The shocks generated were of sufficient intensity to overwhelm the low strength of the gelatine, thus producing hydrodynamic behaviour. The technique enabled control of the initial cavity shape and size, as well as the number of cavities, and the use of a gas gun meant the shockwave strength could be accurately tuned by varying the impact velocity of the projectile. High-speed schlieren photography was used to capture the collapse events, and an image

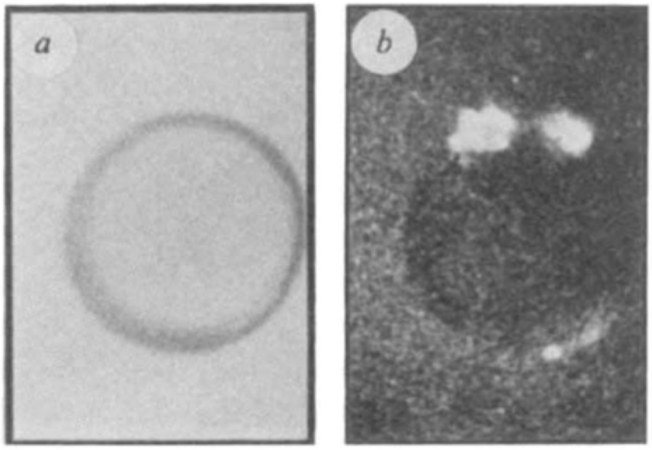


Figure 1.11: Images from the experimental study of Dear & Field [48]. (a) A 3 mm diameter cavity before impact. (b) A silhouette of the cavity after an impact upwards with a shock of strength 0.26 GPa, with two bright spots of luminescence generated by the collapse.

intensifier allowed the position of hotspots to be recorded. The jet shapes and velocities closely matched the numerical predictions of Mader's study [39], and the luminescence data confirmed the presence of hotspots in the two 'lobes' of the collapsing cavities, as is shown in Fig. 1.11 [48].

The theoretical work of Hansson & Mørch looked at the dynamics of collapsing clusters of cavities, and found that the collapsing array can focus the energy and produce a final collapse pressure an order of magnitude larger than the initial shock [88]. This finding corroborated the claim of the Mader study that collapsing inhomogeneities amplify the pressure throughout an impacted explosive [39]. Dear & Field [49] applied their hydrogel techniques to impact multiple cavities. The results showed that the collapse of one layer will occur after the previous layer, because of shielding from the pressure waves, and that certain cluster geometries could lead to pressure amplification. It was also found that the jet velocities from single- and multiple-cavity interactions were significantly higher than the jet velocities measured in the Plesset & Chapman [84] experiment that looked at a cavity near a solid boundary. This, they concluded, went some way to explaining the extensive damage caused by the action of many cavitation bubbles forming on the surface of machinery. More recently, Swantek & Austin [89]

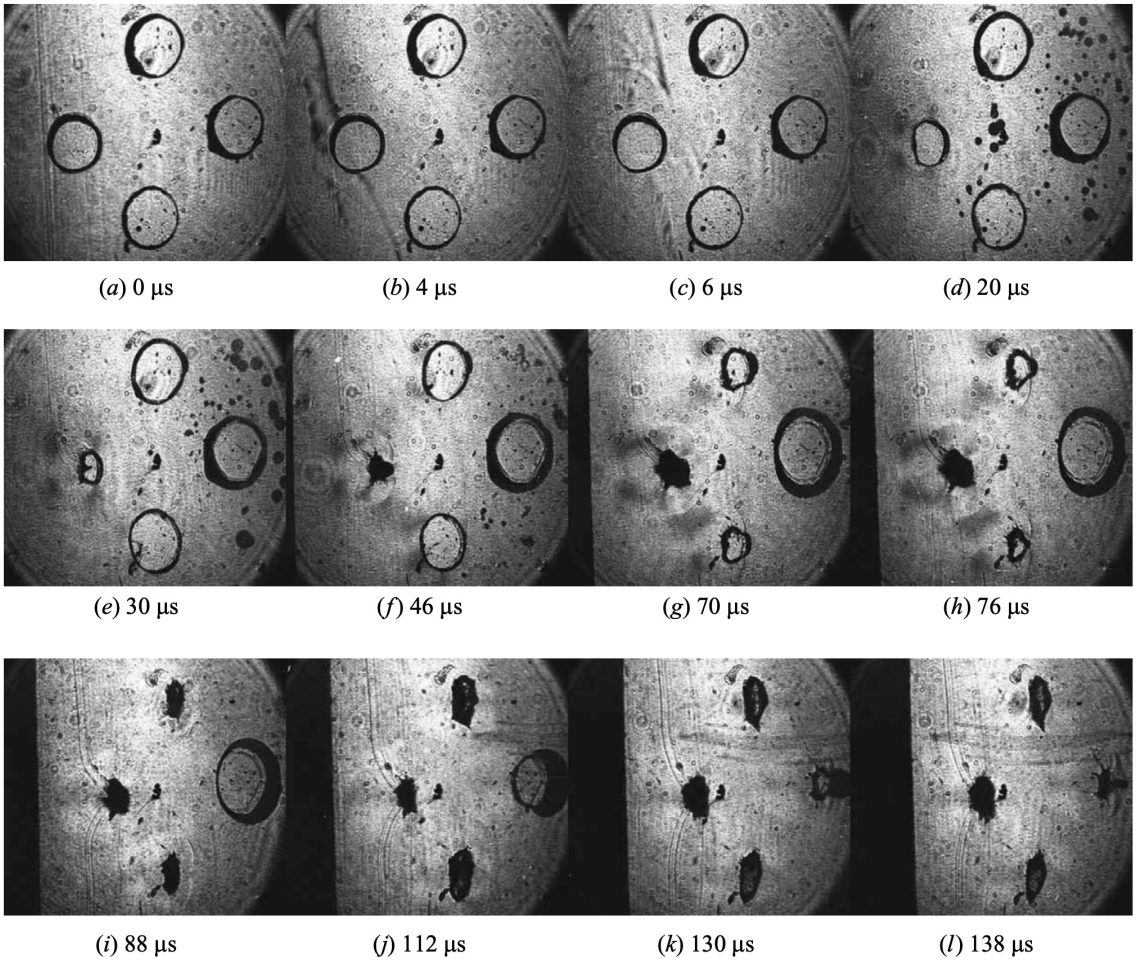
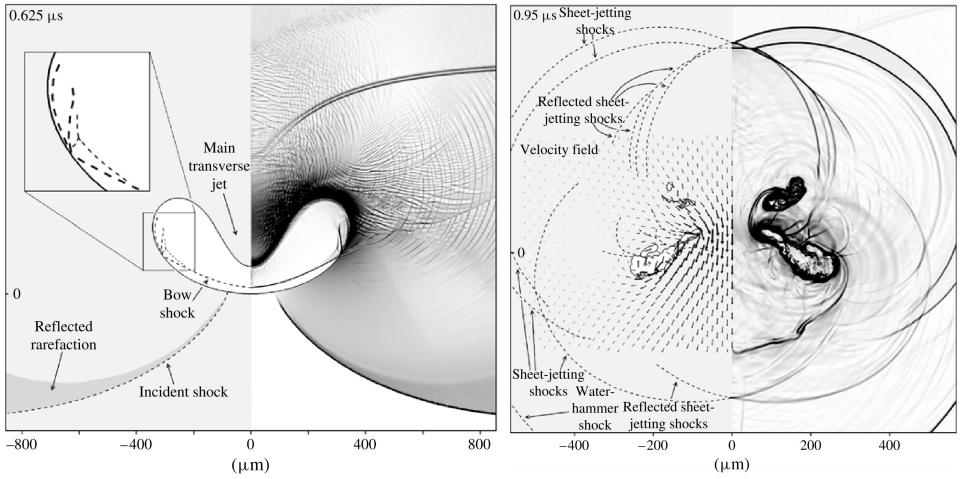


Figure 1.12: Images from the Swantek & Austin study into arrays of cavities under shock loading. Four cavities with an initial 3 mm diameter are impacted from the left with a 40 MPa shock. (a)-(l) The collapse processes of the cavities at different times.

also studied multiple cavities, again using gelatine blocks to examine arrays of cylindrical cavities, comparing their work to the Dear and Field study. For single cavity collapse, they found good agreement in the relationship between the time taken for the cavity to fully collapse and the pressure generated by the shock. An image sequence from their study is shown in Fig. 1.12, in which four equispaced 3 mm diameter cavities are impacted from the left.

Although the gelatine blocks provide a highly-controlled method for imaging cavity collapse experiments, the technique is limited in that the gelatinous solid must be transparent for visualisation of the shockwave. Furthermore, when using higher density media such as solids, refraction effects from damage distorts the images, increasing the difficulty of analysis. It should also be noted that, up until the late 1980s, the main *in-situ* diagnostic tools available to scientists in cavitation research were high-speed visible photography, piezoelectric pressure probes [90], and velocimetry methods [91]. The high-speed imaging of liquids presented the challenge that the liquid must be transparent, and produced refraction that distorted the images. Haas & Sturtevant tackled these issues by combining shadowgraphy with high-speed photography, which allowed them to produce flow visualisations of mixing of two gases [10]. They achieved this by containing a spherical gas cavity in a microfilm membrane inside an outer gaseous medium, thus allowing a stable 3D geometry cavity to be impacted with a shock through the gas, which mixed the gas inside the cavity upon impact. Such a technique would of course be much more difficult to achieve in a liquid medium, given the propensity of hydrostatic compression to collapse any cavity contained within the medium. However, for solids, in which a stationary cavity can be supported, such a scenario is easily achievable, as will be seen in this thesis. This builds upon the techniques of the gelatin technique of Dear & Field, with the added advantage of being able to explore spherical geometries. However, the challenge then is visualising the collapse process, given the distortions to solids that occur under dynamic compression, which renders optical imaging



(a) (b)

Figure 1.13: Rendered images from the 3D simulations of Hawker & Ventikos [70], where a 1 mm cavity is impacted from above with a 1 GPa shock. (a) A jet forms in the direction of the shock. (b) A toroidal vortex is formed after collapse.

unviable. For this reason, as we will see in the following section, research into cavity collapse in solid media has primarily been limited to numerical simulations. However, with the advent of high-speed synchrotron X-ray imaging, visualising the sub-surface dynamics of cavity collapse *in-situ* is now possible. Advancements of these radiography techniques over the past decade is presented in the final section of this literature review.

1.2.4 Computational studies on shock-cavity interactions

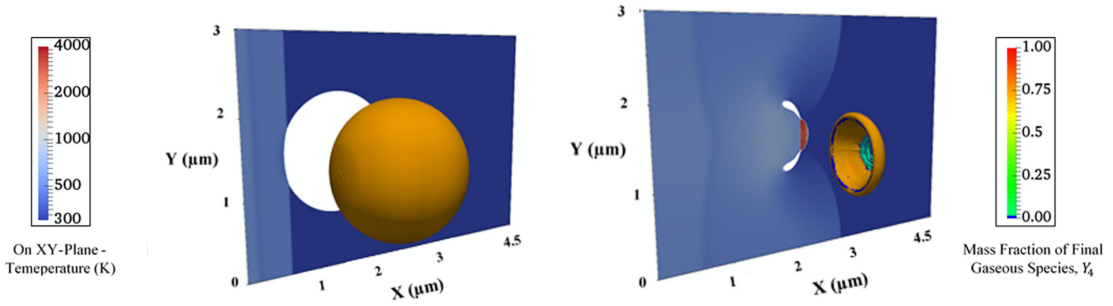
Because of the technical difficulty of studying the phenomenon experimentally, and the fact that limited number measurements that can be obtained, there are extensive computational studies on shock-induced cavity collapse in fluids [92–96]. A notable work is the 2012 high-resolution numerical simulation study of Hawker & Ventikos [70], who produced a comprehensive qualitative analysis of every stage of a single cavity shock-loaded in a liquid medium, looking at 2D and 3D geometries, and comparing results from a wide range of loading shock strengths. Images from a simulation of a 1 GPa shock on a 1 mm cavity can be seen in Fig. 1.13. In the early stages of collapse, shown in Fig. 1.13a, a 'jet' forms and propagates in the direction of the incident shock. After collapse, rotational

forces deposited during collapse create a toroidal vortex, a snapshot of which is shown in Fig. 1.13b. The results of the study showed that the peak pressure upon jet impact for a spherical cavity is ∼40% higher than a cylindrical cavity under the same loading conditions.

1.2.5 Cavity collapse in solids

As detailed above, applying optical imaging techniques to cavity collapse in solid materials poses an unrealistic challenge. Experiments have been performed at moderate strain rates to analyse the stress and temperature response of cylindrical PMMA cavities under weak laser shock compression [8] and under compression from a split Hopkinson bar [97]. However, the cavities in these works were subjected to low strains, meaning the solid medium did not accumulate a large amount of damage, and as a result the cavities remained close to their initial diameter, i.e. they did not collapse. However, in the 1970s Chaudhri & Field captured the silhouette of a 1 mm cylindrical cavity in plasticine, plate-impacted with an explosive, thus giving a projected measure of the cavity closure through time [42]. To the knowledge of the present author, no such experiment has been repeated since. Consequently, until much more recently experimental research into the complete collapse of cavities in solids has been restricted to observations through indirect diagnostics. For example, Campbell et al. [38] investigated the effect of pore and grain size in a shock-impacted explosive by measuring the free-surface velocity and *in-situ* internal resistivity during initiation.

Because of these difficulties, research into cavity collapse in solids has primarily come in the form of computational studies looking at shocks propagating through a solid medium containing cavities. Simulations of single-cavities in a solid medium subjected to strong shocks has primarily been modelled for a medium of cyclotetramethylene-tetranitramine (HMX) [4, 7, 9, 98, 99]. For these higher shock strengths, hydrodynamic behaviour is observed. In such cases, the



(a) (b)

Figure 1.14: Rendered images from the 3D simulations of Rai et al. [100]. A 1.55 µm cavity in HMX is impacted from the left with a 9.5 GPa shock. Frames shown at times after impact of (a) $t = 0.12\,\mathrm{ns}$ and (b) $t = 0.61\,\mathrm{ns}$. The colours in the projected 2D plane (left colour bar) show temperature [K] and the 3D colouring (right colour bar) shows the mass fraction of the final gaseous species, Y_4.

shape of collapse is the same as for collapse in a fluid medium, with the formation of a jet followed by jet impact. Rai et al. simulated a spherical cavity in HMX in 3D, as well as three other cavity shapes, interacting with a strong shock [100]. Compared to 2D simulations, the additional spatial dimension creates increased mixing through highly intense vortices [101], which means that, "the reacted HMX mass and hot-spot intensity is significantly higher than in the 2D predictions". Figure 1.14 shows images rendered from the 3D simulations – in the second image the jet has impacted the far cavity interface and is beginning to form a toroidal vortex.

Multiple cavities in HMX under shock loading have also been simulated, to explore the interactions between collapsing cavities [4, 46, 98, 102]. Although the simulation demand is greater, multiple cavities more closely represents a real physical system, such as manufactured pressed HMX, in which many cracks and cavities will be distributed. A study by Rai et al. [103] studied the effect of void elongation and orientation relative to the shock direction, to investigate the sensitivity of HMX reaction to these changes. It was found that elongated voids generate a more intense hotspot upon collapse [103]. The findings were applied to a micron-scale SEM scan of a real HMX sample to create a simulation of an arbitrary sample, by identifying dark regions in the image and labelling as cavi-

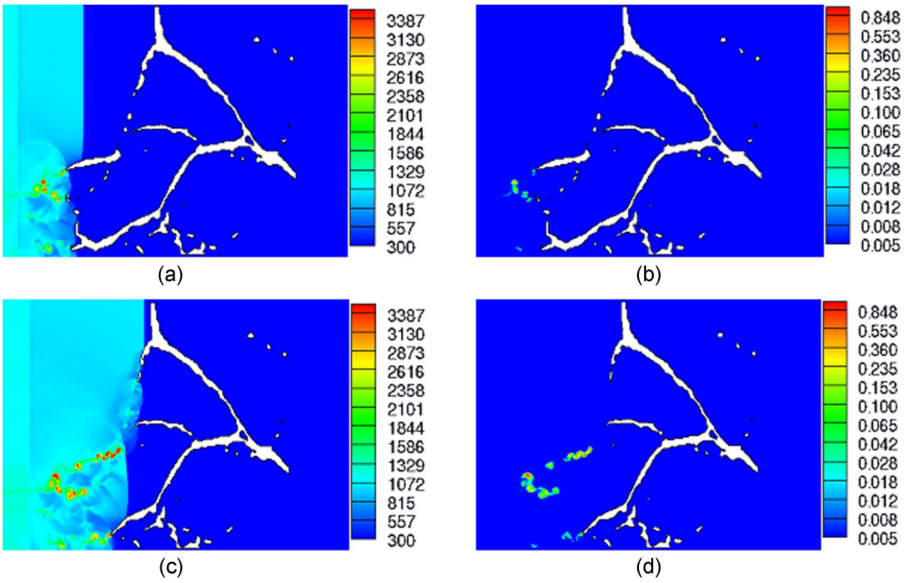


Figure 1.15: Simulation of SEM scanned HMX crystal loaded, with a 1000 m/s particle velocity. (a) & (c) Temperature [K] at $t = 0.48\,\mathrm{ns}$ and $t = 0.86\,\mathrm{ns}$. (b) & (d) mass fraction of reacted material at the same respective times.

ties for the simulation. Images from the simulation are shown in Fig. 1.15, with the temperature and reacted mass fraction represented by the colour bar. Compared to the collapse of a single spherical cavity, the process is far more complex [103].

For the case of weaker shocks in solids, fully hydrodynamic behaviour is not observed, as the shock strength is not large enough to fully overwhelm the shear forces in the cavity medium [104]. Computational studies of lower shock strength impacts on cavities predict localised melting and energy localisation in the form of shear bands in HMX [9, 102, 105, 106], triaminotrinitrobenzene (TATB) [107] and hexanitrostilbene (HNS) [108] explosives. This localisation has been proposed as another mechanism through which ignition may be activated in explosives like HMX [5]. Images from a simulation in this regime, by Austin et al., are shown in Fig. 1.16. The network of shear localisation, known as 'shear bands', are clearly visible in the temperature plot. These bands generate heat far from the cavity, where the initial hot spot is formed. Thus, the activation threshold is lower than predicted by a model in which there is no cavity [9].

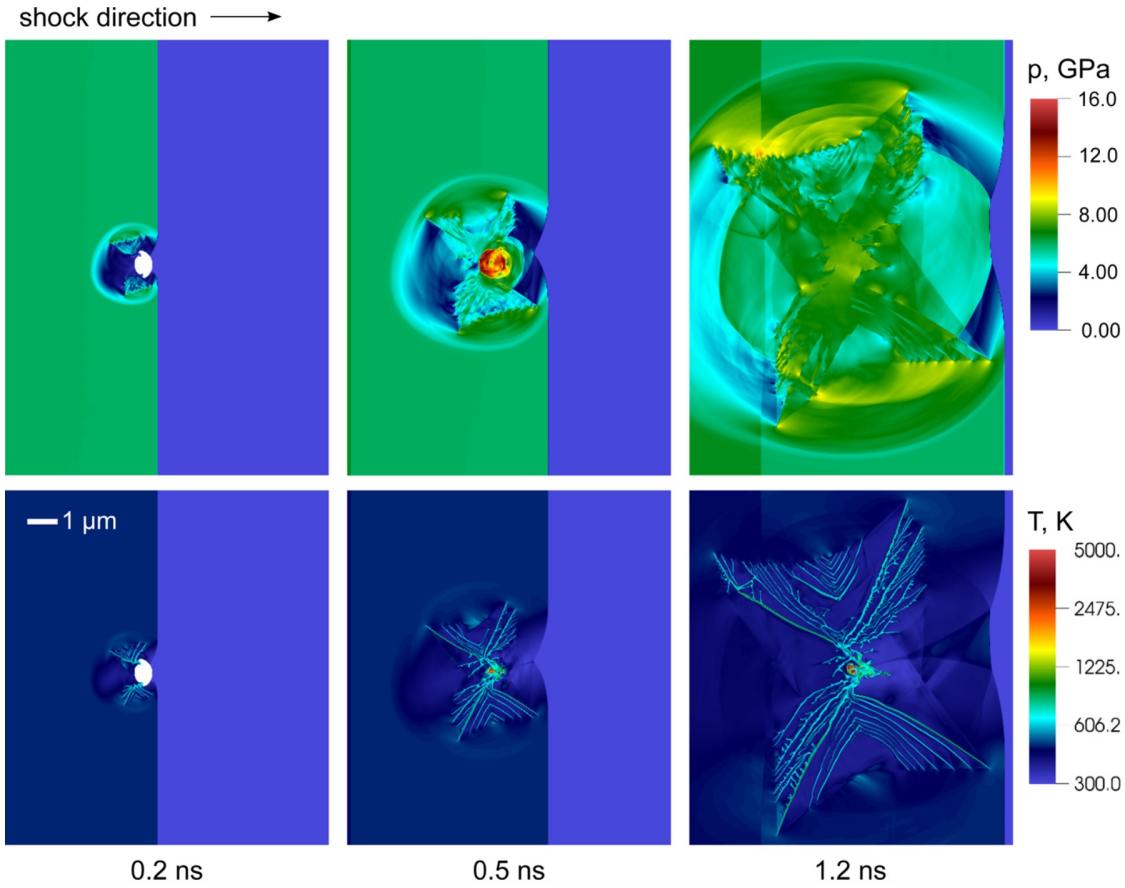


Figure 1.16: Simulation images from Austin et al. [106], where a 1 µm diameter cavity in HMX is loaded from the left with a shock. The top and bottom rows have colouring representing the pressure [GPa] and temperature [K], respectively.

Despite the difficulty of capturing hot spot formation experimentally, in the early 90s Field was able to impact a sample of HMX place on heat-sensitive film [44]. The discoloured regions of the recovered film showed roughly parallel regions of increased temperature, cause by shear bands. These band formations were predicted by the later simulations on cavity collapse in HMX [9, 106]. In recent years Armstrong et al. were able to experimentally capture cavity collapse in solids in real time. By utilising high-speed synchrotron radiography at the Advanced Photon Source (APS) synchrotron, they studied shock-cavity interactions by embedding hollow glass microspheres in both a polydimethylsiloxane-based polymer and trinitrotoluene (TNT) [109, 110]. Annotated radiographs from the experiment, and a comparison to an earlier simulation work [106], can be seen in Fig. 1.17. The sub-mm sized voids are visible in the TNT (the 'pedestal' is part of the manufacturing process) before and after impact. The close-up image in the bottom-right radiograph contains low-density white spots in approximately the same location as where the simulations by Austin et al. [106] predict high-temperature vortices to occur. These images demonstrate a further difficulty of capturing cavity collapse, even when using X-rays, which avoids the refraction issues of optical imaging: it is not possible to capture more than one frame of collapse per cavity, since the time between X-ray illuminations is 153.4 ns and the shock speed is $\sim$6 km/s, meaning the wave propagates $\sim$1 mm per frame. This distance is many times greater than the $\sim$0.2 mm cavity diameter. As will be seen in the present work, the solution for this problem, i.e. to increase the amount of data captured per event, is to either, (a) increase the cavity size, or (b) decrease the time between frames. Both are viable solutions, but each pose further technical problems and theoretical considerations.

1.2.6 Energy localisation and shear banding

As we saw from the cavity collapse studies detailed above, there are a variety of mechanisms that can lead to energy localisation. In fluids, it is primarily the

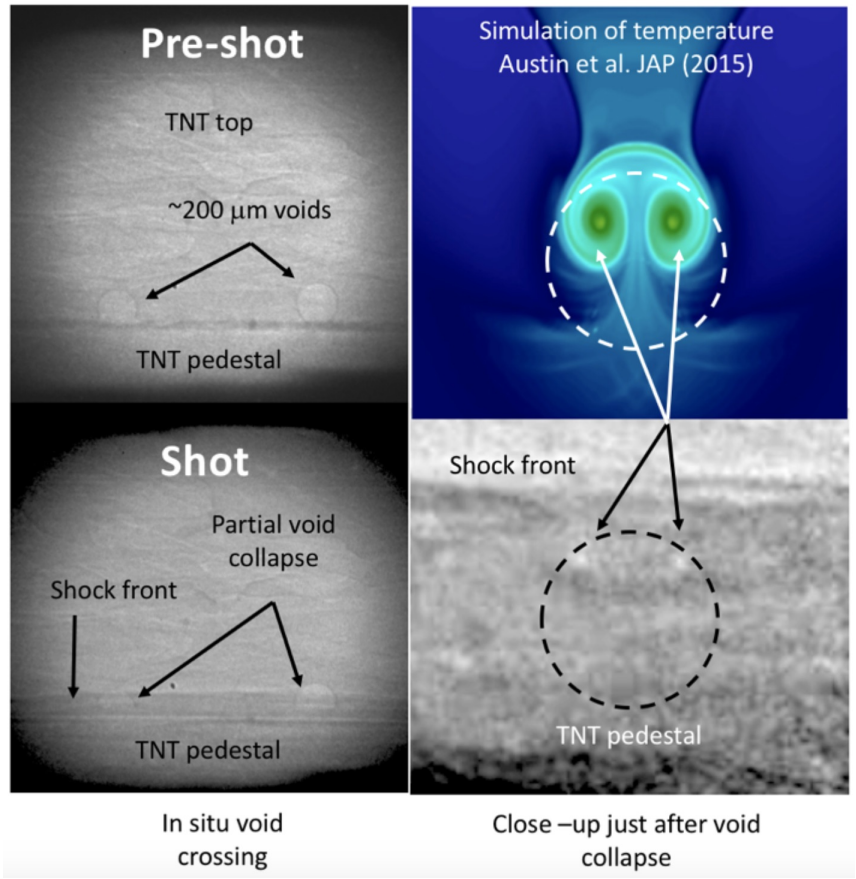


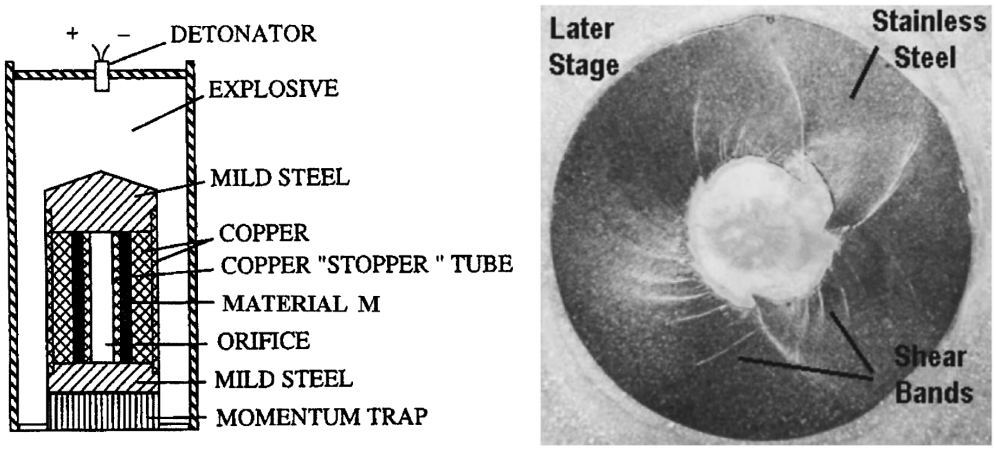
Figure 1.17: Images from the Armstrong et al. [110] radiographic imaging study on shock-loaded glass microspheres in TNT. On the left is shown the cavities before and after loading from below with a 20 GPa shock. On the right, a close up of the radiograph reveals a lower density region, in the same approximate location as high-temperature vortices predicted by simulations [106].

presence of cavities that cause this localisation, when cavities collapse either under hydrostatic compression [74, 76, 80] or under shock loading [10, 101, 111, 112]. In these cases the two competing mechanisms are heating through compression of gases inside the cavity [58, 87, 96], and mixing [10, 113] and dissipation [7] of that heat within the cavity medium during and after collapse [111] – this is of particular interest for the development of inertial confinement fusion targets, where the mixing of 'hot' and 'cold' fuel decreases the energy yield of the fusion reaction [114].

In impacted solids, the complexity of energy localisation increases significantly, and there is much interest in the mechanisms because of its relevance to the ignition of explosives [38, 42, 47, 115]. Along with the adiabatic heating, jet impact and material mixing that occurs in liquids, Field [44] identified many additional mechanisms that may lead to ignition: friction between sliding surfaces; the formation of adiabatic shear bands; heating at crack tips; and heating at dislocation pileups, among others. Field notes that, "[these] processes all involve the conversion of mechanical or electrical energy to thermal energy" [44].

Of particular interest in the present work, in which cavity collapse is observed in a solid medium *in-situ* using high-speed radiography, is the formation of adiabatic shear bands, for the simple reason that, as predicted by simulations of low-strength shocks on HMX [5, 9, 106], these bands lead to perturbations and damage in the solid cavity medium that are visible in the images. Experimental measurement of other variables, such as temperature and electrical measurements, is not the focus of this study, and, when considered, must be inferred from the dynamics of collapse and through simulations.

Shear bands, also known as shear localisation, are regions of a material that have undergone highly concentrated plastic deformation during sheared loading [118]. These localised regions form in approximately parallel sheets, giving the appearance of banded layers of deformation in recovered samples [119], which may



(a) (b)

Figure 1.18: Experiment to dynamically produce shear bands in a thick-walled cylinder. (a) Cylindrical section diagram of the experiment, from Meyers et al. [116]: the cylindrical material sample 'M' is loaded radially inward with an explosive. Copper and steel linings shape and contain the shock before it comes in contact with the sample. (b) From the results of Xue et al. [117]: the shear bands of a loaded 304L stainless steel cylinder. The bands are said to be at the 'later stage' because of the fully developed bands that traverse the entire cylinder.

present as cracks if failure occurs along the bands, or simply as bands of large localised strain [118]. For a shear band to occur, the thermal softening from plastic deformation must overcome the opposing strain and strain rate hardening effects [118, 119]. However, as Walley notes in his 2007 review article, "because inertia is involved, the phenomenon cannot be understood simply as a materials property: geometry and structure must play a role." [119].

Under shock loading, shear bands will form in a material in the shock pressure region between the onset of plastic failure – above the yield stress of the material – and hydrodynamic deformation at very high pressures (the lower and upper threshold pressures are highly material dependent) [118]. The geometry of these bands, i.e. the individual widths of the bands, the final band lengths, and the spacing between bands, have been studied [117, 120–124]. Experimental work on explosively loaded thick-walled cylinders can be seen in Fig. 1.18, which shows the experimental setup [116] ans the results of a test on 314L stainless steel [117]. The bands are visible in Fig. 1.18b as pale lines that emanate from

the inner surface of the cylinder at an angle to the normal, in the direction of the outer surface. Despite these important works, visualising band formation in real time experimentally is difficult. Developments in synchrotron radiography has now allowed shear band formation, even before damage onset, to be captured [125].

Of particular relevance to the present work is the spacing between bands, since, as will be seen the cavity collapse radiographs in Chapter 4 and the simulations in Chapter 5, perturbations form along the cavity interface at sites where the shear bands form during shock loading. As shown above in the simulations of Austin et al. [106] in Fig. 1.16, these bands form networks inside the material away from the cavity interface. Simulations of the shear banding experiment in Fig. 1.18 have also been conducted, and the results of one of the simulations on 304L stainless steel is show in Fig. 1.19, which is coloured according to the value of effective plastic strain, ϵ_{pl}. At early times the shear bands start to form (top right zoom view), which organise into larger bands that emanate outwards at later times. At 6 µs the large-scale perturbations along the inner surface of the cylinder correspond to the base of the fully developed shear bands. This is directly analogous to the shear bands that form during shock-loaded cavity collapse [5, 9, 106], and which will capture experimentally for the first time in this work.

1.2.7 X-ray imaging of impact studies

Imaging using a synchrotron X-ray source offers a powerful diagnostic tool for dynamic experiments, due to the continuous stream of pulses that are generated by the electrons accelerated around a synchrotron's 'storage ring'. In the last decade, scientists first at the Advanced Photon Source (APS) and then the European Synchrotron Radiation Facility (ESRF) have utilised the high level of spatial coherence of the X-rays produced at certain synchrotron beamlines to enhance

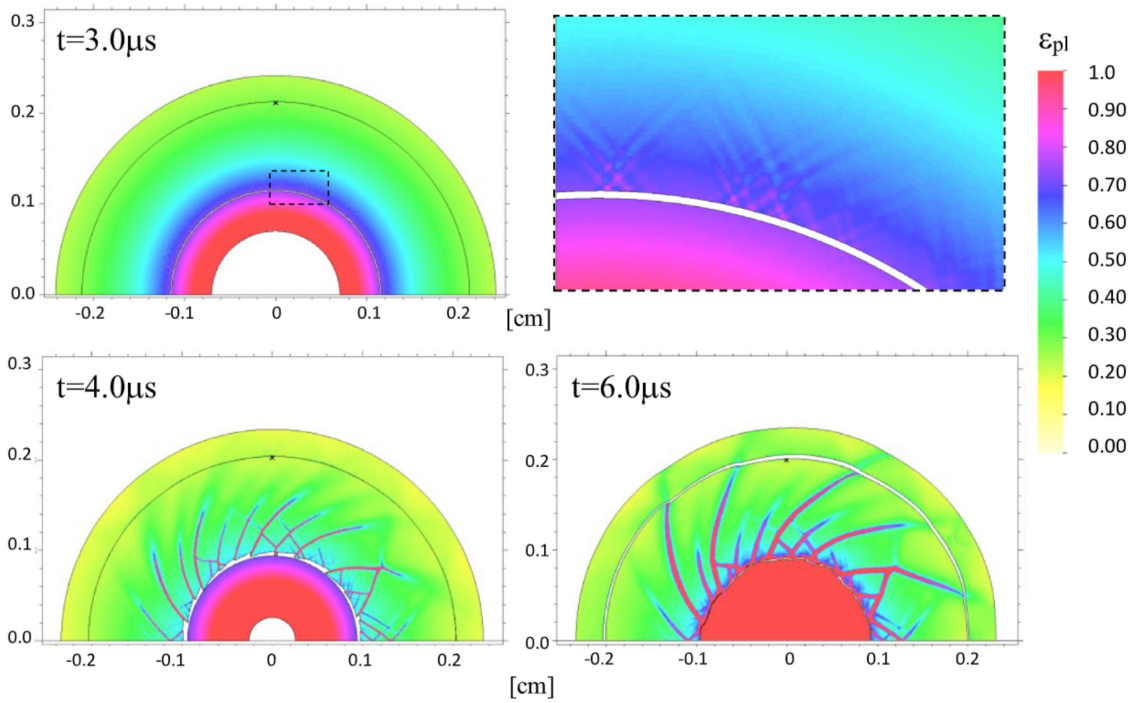


Figure 1.19: Simulations of Lovinger et al. [126] showing the effective plastic strain, ϵ_{pl} at different times for a 304L stainless steel thick-walled cylinder, loaded radially inward.

material edges and interfaces, using a technique know as 'phase-contrast imaging' (PCI) [127, 128] – more details of this are given in Chapter 2. An example of phase contrast enhancement can be seen in Fig. 1.20, which shows radiographs of a human hair taken at increasing sample-to-detector distances. Contrast at the edges of the crossing hairs is clearly enhanced by bright interference fringes. Too close and the recorded image only displays the attenuation due to the magnitude of the material-dependent mass attenuation properties [129] (far left image) and too far the interference fringes become too spread out, which distorts the object (not shown in the figure). The optimal distance, where the edges are enhanced as bright or dark fringes (far right image), is determined from the X-ray spectrum and detector resolution, the effects of which can be simulated before performing an experiment [129, 130]. The detector records the X-rays 'indirectly' by using a scintillator to absorb the photons and re-emit in the visible spectrum, which can then be recorded with a commercial optical camera. All of the studies discussed in this section use indirect detector systems, because of the low cost

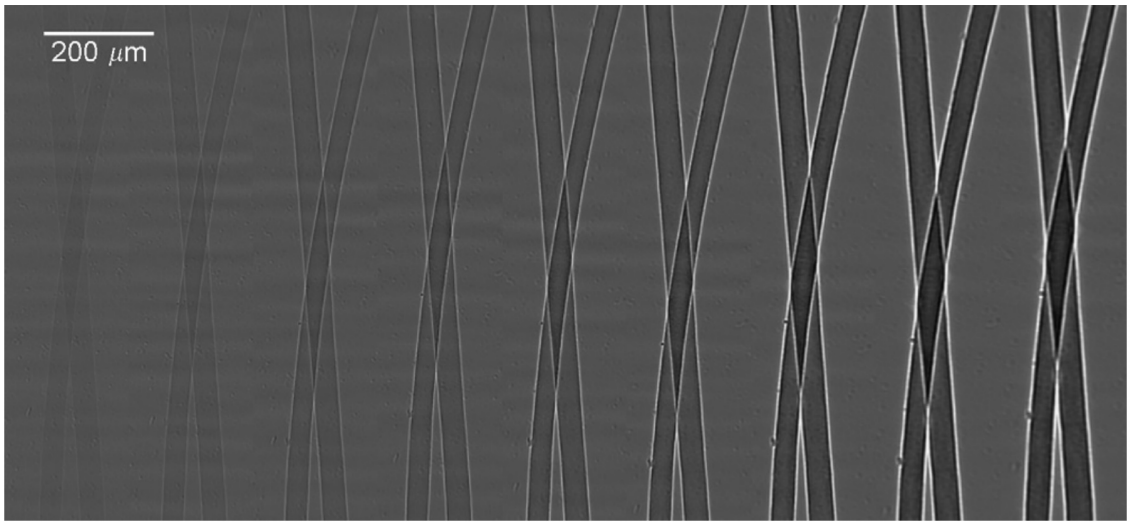
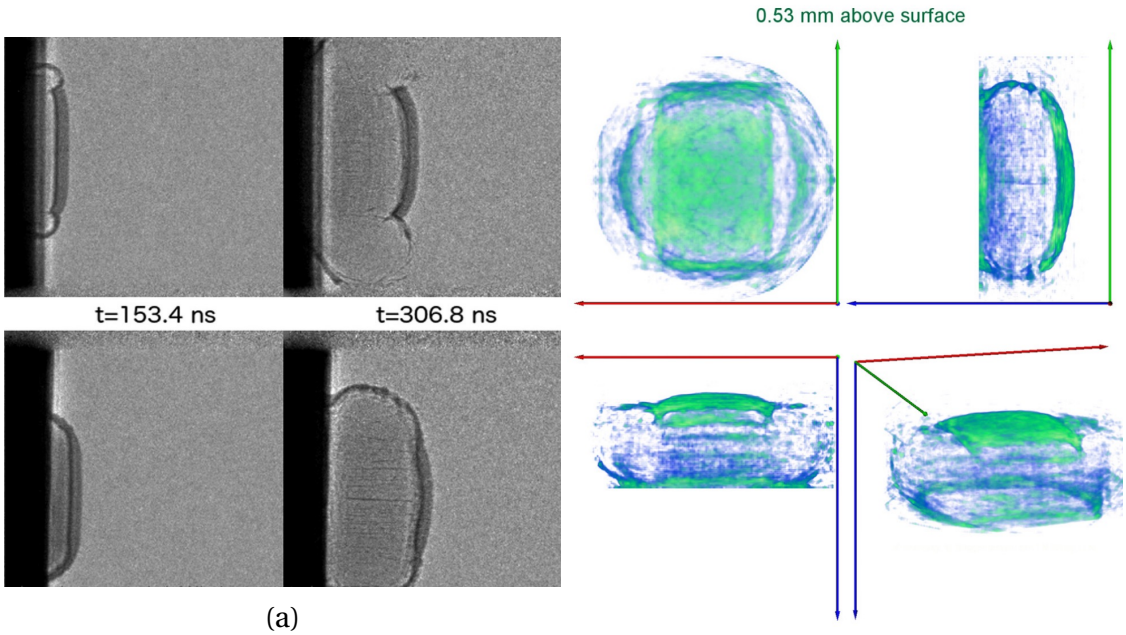


Figure 1.20: Radiograph images of a human hair by Rack et al. [131], taken from left to right at sample-to-detector distances from 20 to 1,140 mm

and high frame rates achievable compared to direct detectors. Further comparison between the two detector types is presented in Chapter 3, where the author's paper on the imaging system used in the experiments is presented.

At the APS synchrotron beamline 32-ID, PCI has been used to image fast processes involving liquids, such as water droplet coalescence [132], dense jet flow [133], and bubble bursting [134]. Furthermore, at the same synchrotron, PCI of solid materials has been performed, to capture PMMA spheres [135] and HMX crystals [136] dynamically compressed with a Kolsky bar. A powerful example of the potential of PCI came from Willey et al., who imaged along two orthogonal directions (in separate experiments) to construct a 3D rendering of an exploding foil flyer [137]. This of course assumed that the repeatability of the exploding flyer is very high. Two images from the study are shown in Fig. 1.21, with Fig. 1.21a showing the two sets of radiographs at two time instances and the 3D rendering in Fig. 1.21b. As the images were illuminated by a single X-ray pulse, the time resolution is $\sim$100 ps, and the time between frames is 153.4 ns, the time between sequential X-ray pulses in '24 bunch mode' at the APS synchrotron. Further explanation of bunch structure is also given in Chapter 3.

Of particular relevance to the present study is the work on gas gun impact per-



(a) (b)

Figure 1.21: X-ray PCI imaging of an exploding foil flyer by Willey et al. [137]. (a) The flyer at two time instances, from two mutually orthogonal directions, normal to the direction of flyer motion. (b) A 3D rendering of the flyer, from 4 different viewpoints. Orientation indicated by the coloured axes.

formed at APS. Using the 'IMPULSE' gas gun system at beamline 32 ID-B [53, 138, 139], PCI has, among other applications, been used to record the compression of lattice materials [140–142], an additively manufactured energetic material simulant [143] and jet formation in cerium samples with cut grooves [144, 145]. By impacting a steel cylinder into vitreous carbon, Jensen et al. [138] were able to capture crack formation in the carbon sample using PCI, as can be seen in Fig. 1.22. This early study in high-speed, single-bunch PCI demonstrated the potential of this technique for revealing details completely unavailable using more conventional impact study diagnostics. Although more than one camera is used simultaneously with the IMPULSE imaging system, a drawback is the limited number of frames that can be obtained, since each of the PI-MAX cameras used can record a maximum of two frames per event [53]. As will be demonstrated in Chapter 3, using a camera with a higher frame capacity greatly increases the amount of data acquired in each experiment.

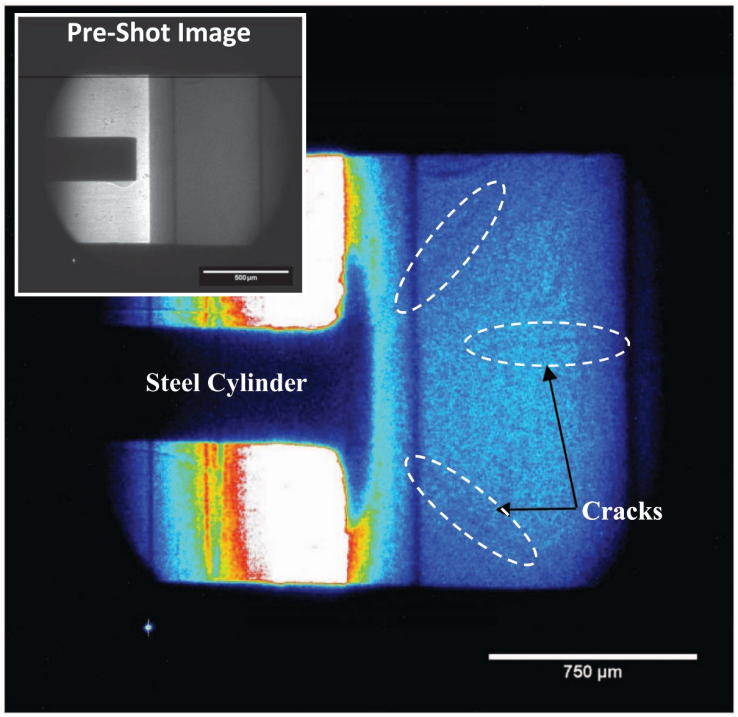


Figure 1.22: Steel cylinder impact on vitreous carbon, captured using PCI at the APS synchrotron, from Jensen et al. [138]. Colouring in the larger image indicates greyscale value.

High-speed synchrotron PCI has also been performed at the ESRF synchrotron's beamline ID19. The bright hard X-ray source, large beam size and high level of spatial coherence of the beamline make it ideally suited for dynamic radiography studies [146]. Rack et al. established the beamline as a centre for such studies, imaging crack propagation in glass [147], and with collaborators studying laser shock compressed polymer foam [148] and pulsed-power driven wire explosions in water [149]. After Eakins & Chapman developed an impact system at the Diamond Light Source (DLS) synchrotron in the UK [54], their system was used at the ESRF to capture the gas gun impact of polymers [150] and 3D printed metallic lattices [151]. The imaging system was also used to capture split Hopkinson compression of shear titanium alloy specimens [125] and fracture and fragmentation of chondrite specimens [152]. In the same group, led by Eakins, Rutherford et al. also evaluated the performance of scintillators for high-speed radiography, which are a key component in indirect imaging systems [153]. Using these findings, powder samples under gas gun impact were investigated through PCI

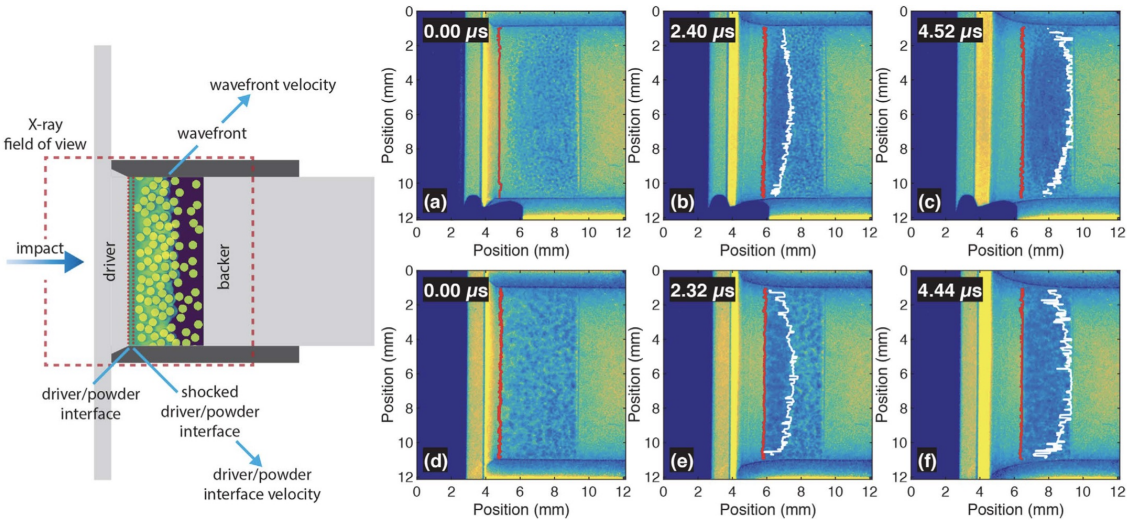


Figure 1.23: High-speed radiography study on powder samples by Rutherford et al. [154]. (Left) Diagram of the setup. (Right, a-c) Radiographs of the powder with small chondrules. (Right, d-e) Radiographs of the powder with large chondrules.

[154, 155]. Radiographs from this study can be seen in Fig. 1.23, from which the shock front position in the powder was extracted through image analysis. Similar techniques will be presented in the current work, in the study of shock-cavity interactions in Chapters 4&5, where edge detection is used to extract interface locations from the radiographs. The methods for these techniques, and the subsequent analytical methods, are given in the following Chapter.

1.3 Summary

The works above highlight the wide ranging fields of research interested in the cavity collapse phenomenon. We have seen the early interest because of cavitation damage, which continues to be a problem when designing mechanical systems in fluids, and in the medical context in mechanical heart valve design. Then later experimental developments, particularly high speed imaging to capture phenomenon, revealed the importance of asymmetrical collapse on the effect a cavity can have on a surface. Of importance in the research of energetic materials, and in some medical applications like shockwave lithotripsy, understanding the interaction between shocks and cavities is of vital importance. To

this end there have been numerous numerical simulation studies, and a limited amount of groundbreaking experimental work.

We also saw how observing the phenomenon in fluid media has proven particularly challenging, with most of our understanding gained through indirect means or with simulations. This work is closely related to the more general understanding of energy localisation that occurs in impacted solids – shear bands forming in impacted cylinders mimics the type of loading we see in shock-cavity interactions in solids. Ultra high-speed X-ray imaging developed at the APS and ESRF synchrotrons provides, for the first time, a cutting-edge technique for observing such phenomena in real time. Research at these institutions has already revealed new details of sub-surface behaviour in solids that is obscured with optical imaging.

Motivated by the need to understand cavity collapse in the medical, nuclear fusion and energetic material contexts, this work focuses on capturing shock-induced cavity collapse in a solid with synchrotron radiography. Building on newly developed experimental techniques, a new imaging system is developed and applied to the cavity collapse in a solid. The system records new detail for extended periods of time, from the onset of shock interaction to full cavity closure, over a wide range of shock loading conditions. In a further aspect of this work, the radiographic results are directly compared to simulations performed in the simulation code SCIMITAR3D, and confirm the capabilities of our models to accurately capture finer details of the collapse process. The simulation results also suggest the need of further investigation, as they point to the possibility of general scaling laws for cavity collapse in various material media.

Based on my survey of the literature and my motivations, the objectives for this work are as follows.

- Further advance an imaging system capable of capturing images with se-

quential synchrotron X-ray pulses, for use in dynamic impact experiments at the ESRF.

- Assess the performance of the imaging system and plan for future modifications to improve the system.
- Capture shock-induced cavity collapse in the solid medium PMMA through gas gun impact, over a range of loading pressures, to generate collapse from the strength to hydrodynamic regimes.
- Process and analyse the radiographic data to investigate the collapse process and obtain meaningful metrics.
- Perform simulations of the experiments to assess the validity of existing models, reveal details not available experimentally, and explore cavity collapse in a range of materials.

It is fortunate the Chapter structure of this Thesis naturally follows the chronologically order of my three published papers. In Chapter 3.2, my first paper, on the imaging system used at the ESRF, highlights the challenges associated with capturing sequential synchrotron X-ray pulses. The Applied Optics journal paper [156] also outlines how future advances in synchrotron and imaging technology will greatly expand the scope of dynamic synchrotron imaging studies. Then, in Chapter 4, which is largely based on my second paper published in Scientific Reports [157], the radiographic results are presented in detail, showcasing the unprecedented quality of the images. It is the first time shock-induced cavity collapse in a solid is captured over such a wide range of shock states, and over such extended time periods. Metrics for quantifying cavity collapse are also explored, and it is discovered that a qualitative transition from strength-like behaviour to hydrodynamic behaviour is borne out in the analysis. Chapter 5 is expanded upon in a third paper, published in the Journal of the Mechanic and Physics of Solids [158] and written in collaboration with Dr Nirmal K Rai of Los Alamos Na-

tional Laboratory (LANL) (previously at the University of Iowa). The experimental results are compared to simulations in a head-to-head fashion, and demonstrate the capability of the models to capture the key features of shock-cavity interactions over the whole range of loading conditions studied. This work highlights many avenues of future investigation, which will be discussed in the conclusions and outlook in Chapter 6.

1.4 References

[1] A Shima, K Takayama, Y Tomita, and N Ohsawa, "Mechanism of Impact Pressure Generation from Spark-Generated Bubble Collapse Near a Wall," *AIAA J.*, vol. 21, no. 1, pp. 55–59, 1983.

[2] S W Ohl, E Klaseboer, and B C Khoo, "Bubbles with shock waves and ultrasound: a review," *Interface Focus*, vol. 5, 2015.

[3] M R Betney, B Tully, N A Hawker, and Y Ventikos, "Computational modelling of the interaction of shock waves with multiple gas-filled bubbles in a liquid," *Phys. Fluids*, vol. 27, no. 3, 2015.

[4] A Kapahi and H S Udaykumar, "Dynamics of void collapse in shocked energetic materials: Physics of void-void interactions," *Shock Waves*, vol. 23, no. 6, pp. 537–558, 2013.

[5] N K Rai and H S Udaykumar, "Void collapse generated meso-scale energy localization in shocked energetic materials: Non-dimensional parameters, regimes, and criticality of hotspots," *Phys. Fluids*, vol. 31, no. 016103, 2019.

[6] M Subramani, C Czarnota, S Mercier, *et al.*, "Dynamic response of ductile materials containing cylindrical voids," *Int. J. Fract.*, vol. 222, pp. 197–218, 2020.

[7] R Menikoff, "Pore Collapse and Hot Spots in HMX," in *Shock Compression Condens. Matter*, 2003.

[8] X Ma, X Li, X Zheng, *et al.*, "Weak shock loadings induce potential hot spots formation around an intergranular pore," *J. Appl. Phys.*, vol. 121, no. 115102, 2017.

[9] H K Springer, S Bastea, A L Nichols, *et al.*, "Modeling The Effects of Shock Pressure and Pore Morphology on Hot Spot Mechanisms in HMX," *Propellants, Explos. Pyrotech.*, vol. 43, no. 8, pp. 805–817, 2018.

[10] J F Haas and B Sturtevant, "Interaction of weak shock waves with cylindri-

cal and spherical gas inhomogeneities," *J. Fluid Mech.*, vol. 181, pp. 41–76, 1987.

[11] G Layes, G Jourdan, and L Houas, "Experimental investigation of the shock wave interaction with a spherical gas inhomogeneity," *Phys. Fluids*, vol. 17, no. 2, pp. 1–4, 2005.

[12] G Layes, G Jourdan, and L Houas, "Experimental study on a plane shock wave accelerating a gas bubble," *Phys. Fluids*, vol. 21, no. 7, 2009.

[13] M Versluis, B Schmitz, A von der Heydt, and D Lohse, "How Snapping Shrimp Snap : Through Cavitating Bubbles," *Science (80-.).*, vol. 289, 2000.

[14] D Lohse, B Schmitz, and M Versluis, "Snapping shrimp make flashing bubbles," *Nature*, vol. 413, 2001.

[15] C A Parsons and S S Cook, "Investigation into the causes of corrosion or erosion of propellers," *Engineering*, p. 107, 1919.

[16] Z L Zhang and B J Wachenfeldt, "Numerical study on the heat storing capacity of concrete walls with air cavities," *Energy Build.*, vol. 41, no. 7, pp. 769–773, 2009.

[17] C Zhao, K Fezzaa, R W Cunningham, *et al.*, "Real-time monitoring of laser powder bed fusion process using high-speed X-ray imaging and diffraction," *Sci. Rep.*, vol. 7, no. 3602, 2017.

[18] C Lun, A Leung, S Marussi, *et al.*, "In situ X-ray imaging of defect and molten pool dynamics in laser additive manufacturing," *Nat. Commun.*, vol. 9, no. 1355, 2018.

[19] S Wang, X Li, and D Wang, "Void fraction distribution in overburden disturbed by longwall mining of coal," *Environ. Earth Sci.*, vol. 75, no. 2, pp. 1–17, 2016.

[20] E Rambod, M Beizaie, M Shusser, *et al.*, "A Physical Model Describing the Mechanism for Formation of Gas Microbubbles in Patients with Mitral Mechanical Heart Valves," *Ann. Biomed. Eng.*, vol. 27, no. 6, pp. 774–792, 1999.

[21] C E Brennen, "Cavitation in medicine," *Interface Focus*, vol. 5, no. 5, pp. 1–12, 2015.

[22] J E Field, "The physics of liquid impact, shock wave interactions with cavities, and the implications to shock wave lithotripsy," *Phys. Med. Biol.*, vol. 36, no. 11, pp. 1475–1484, 1991.

[23] W Sass, M Braünlich, H P Dreyer, *et al.*, "The mechanisms of stone disintegration by shock waves," *Ultrasound Med. Biol.*, vol. 17, no. 3, 1991.

[24] T Kodama and K Takayama, "Dynamic Behaviour of Bubbles During Extra-

corporeal Shock-Wave Lithotripsy," *Ultrasound Med. Biol.*, vol. 24, no. 5, pp. 723–738, 1998.

[25] M Bailey, L Crum, J A Mcateer, and O A Sapozhnikov, "Cavitation in shock wave lithotripsy," in *Fifth Int. Symp. Cavitation*, (Osaka), 2003.

[26] D L Sokolov, M R Bailey, and L A Crum, "Use of a dual-pulse lithotripter to generate a localized and intensified cavitation field," *J. Acoust. Soc. Am.*, vol. 110, no. 1685, 2001.

[27] P R Birkin, D G Offin, C J B Vian, and T G Leighton, "Electrochemical 'bubble swarm' enhancement of ultrasonic surface cleaning," *Phys. Chem. Chem. Phys.*, vol. 17, no. 21709, 2015.

[28] C D Ohl, M Arora, R Dijkink, *et al.*, "Surface cleaning from laser-induced cavitation bubbles," *Appl. Phys. Lett.*, vol. 89, no. 074102, 2006.

[29] G L Chahine, A Kapahi, J K Choi, and C T Hsiao, "Modeling of surface cleaning by cavitation bubble dynamics and collapse," *Ultrason. Sonochem.*, vol. 29, pp. 528–549, 2016.

[30] B Verhaagen and D F Rivas, "Measuring cavitation and its cleaning effect," *Ultrason. Sonochem.*, vol. 29, pp. 619–628, 2016.

[31] E Johnsen and T Colonius, "Shock-induced collapse of a gas bubble in shockwave lithotripsy.," *J. Acoust. Soc. Am.*, vol. 124, no. 4, pp. 2011–20, 2008.

[32] R J Browning, V Rajkumar, R B Pedley, *et al.*, "Prospects for enhancement of targeted radionuclide therapy of cancer using ultrasound," *J. Label. Compd. Radiopharm.*, vol. 57, pp. 279–284, 2014.

[33] G N Sankin and P Zhong, "Interaction between shock wave and single inertial bubbles near an elastic boundary," *Phys. Rev. E*, vol. 74, no. 046304, 2006.

[34] T Kodama, Y Tomita, Y Watanabe, *et al.*, "Cavitation Bubbles Mediated Molecular Delivery During Sonoporation," *J. Biomech. Sci. Eng.*, vol. 4, no. 1, 2009.

[35] R Browning and E Stride, "Microbubble-Mediated Delivery for Cancer Therapy," *Fluids*, vol. 3, no. 4, p. 74, 2018.

[36] M Vedadi, A Choubey, K Nomura, *et al.*, "Structure and Dynamics of Shock-Induced Nanobubble Collapse in Water," *Phys. Rev. Lett.*, vol. 105, no. 014503, 2010.

[37] A W Campbell, W C Davis, and J R Travis, "Shock Initiation of Detonation in Liquid Explosives," *Phys. Fluids*, vol. 4, no. 4, pp. 498–510, 1961.

[38] A W Campbell, W C Davis, J B Ramsay, and J R Travis, "Shock Initiation of Solid Explosives," *Phys. Fluids*, vol. 4, no. 4, p. 511, 1961.

[39] C L Mader, "Initiation of Detonation by the Interaction of Shocks with Density Discontinuities," *Phys. Fluids*, vol. 8, no. 10, pp. 1811–1816, 1965.

[40] D I A Millar, *Energetic Materials at Extreme Conditions*. PhD thesis, University of Edinburgh, 2012.

[41] R Menikoff, "Hot spot formation from shock reflections," *Shock Waves*, vol. 21, pp. 141–148, 2011.

[42] M M Chaudhri and J E Field, "The role of rapidly compressed gas pockets in the initiation of condensed explosives," tech. rep., 1974.

[43] N Bourne and J Field, "Collapsing cavities in reactive and non-reactive media," *Proc. SPIE - Int. Soc. Opt. Eng.*, vol. 1358, no. pt 2, 1991.

[44] J E Field, "Hot Spot Ignition Mechanisms for Explosives," *Acc. Chem. Res.*, vol. 25, pp. 489–496, 1992.

[45] R B Frey, "AD-A172 513: Cavity Collapse in Energetic Materials," tech. rep., US Army Ballistic Research Laboratory, Marlyland, 1986.

[46] S Roy, N K Rai, O Sen, *et al.*, "Modeling mesoscale energy localization in shocked HMX, Part II: training machine-learned surrogate models for void shape and void–void interaction effects," *Shock Waves*, vol. 30, no. 4, pp. 349–371, 2020.

[47] J E Field, N K Bourne, S J P Palmer, and S M Walley, "Hot-spot ignition mechanisms for explosives and propellants," *Philos. Trans. R. Soc. A*, vol. 339, pp. 269–283, 1992.

[48] J P Dear, J E Field, and A J Walton, "Gas compression and jet formation in cavities collapsed by a shock wave," *Nature*, vol. 332, no. 7, pp. 505–508, 1988.

[49] J P Dear and J E Field, "A study of the collapse of arrays of cavities," *J. Fluid Mech.*, vol. 190, no. 1944, p. 409, 1988.

[50] K Nugent, T Gureyev, D Cookson, *et al.*, "Quantitative Phase Imaging Using Hard X Rays," *Phys. Rev. Lett.*, vol. 77, no. 14, pp. 2961–2964, 1996.

[51] D J Chapman, D D Radford, M Reynolds, and P D Church, "Shock induced void nucleation during Taylor impact," *Int. J. Fract.*, vol. 134, pp. 41–57, 2005.

[52] D R Jones, D J Chapman, and D E Eakins, "A gas gun based technique for studying the role of temperature in dynamic fracture and fragmentation," *Local Inert. Eff. Dyn. Fragm. J. Appl. Phys.*, vol. 114, p. 322, 2013.

[53] S N Luo, B J Jensen, D E Hooks, *et al.*, "Gas gun shock experiments with single-pulse x-ray phase contrast imaging and diffraction at the Advanced Photon Source," *Rev. Sci. Instrum.*, vol. 83, no. 7, 2012.

[54] D E Eakins and D J Chapman, "X-ray imaging of subsurface dynamics in high-Z materials at the Diamond Light Source," *Rev. Sci. Instrum.*, vol. 85, no. 12, 2014.

[55] M P Olbinado, X Just, J L Gelet, *et al.*, "MHz frame rate hard X-ray phase-contrast imaging using synchrotron radiation," *Opt. Express*, vol. 25, no. 12, 2017.

[56] B J Jensen, A J Iverson, K J Ramos, *et al.*, "Dynamic Compression Experiments at the Advanced Photon Source," in *Work. Stud. Dyn. Compress. Matter with X-rays*, pp. 1–23, 2015.

[57] D J Flannigan and K S Suslick, "Plasma Line Emission during Single-Bubble Cavitation," *Phys. Rev. Lett.*, vol. 95, no. 044301, pp. 1–4, 2005.

[58] K S Suslick and D J Flannigan, "Inside a Collapsing Bubble : Sonoluminescence and the Conditions During Cavitation," *Annu. Rev. Phys. Chem.*, vol. 59, pp. 659–683, 2008.

[59] B P Barber, C C Wu, R Löfstedt, *et al.*, "Sensitivity of sonoluminescence to experimental parameters," *Phys. Rev. Lett.*, vol. 72, p. 1380, 1994.

[60] W C Moss, D B Clarke, J W White, and D A Young, "Sonoluminescence and the prospects for table-top micro-thermonuclear fusion," *Phys. Lett. A*, vol. 9601, pp. 69–74, 1996.

[61] R P Taleyarkhan, C D West, J S Cho, *et al.*, "Evidence for Nuclear Emissions During Acoustic Cavitation," *Science (80-.).*, vol. 295, p. 1868, 2002.

[62] D Shapira and M Saltmarsh, "Nuclear Fusion in Collapsing Bubbles – Is It There? An Attempt to Repeat the Observation of Nuclear Emissions from Sonoluminescence," *Phys. Rev. Lett.*, vol. 89, p. 104302, 2002.

[63] Y T Didenko and K S Suslick, "The energy efficiency of formation of photons, radicals and ions during single-bubble cavitation," *Nature*, vol. 418, pp. 394–397, 2002.

[64] N Zoghi-Foumani and R Sadighi-Bonabi, "Investigating the possibility of Sonofusion in Deuterated acetone," *Int. J. Hydrogen Energy*, vol. 39, pp. 11328–11335, 2014.

[65] M J Stokmaier, A G Class, and T Schulenberg, "Optimising Acoustic Resonators for Sonofusion Experiments with Evolutionary Algorithms," in *20th Int. Conf. Appl. Comput. Sci. Math. Archit. Civ. Eng.*, no. July, pp. 20–22, 2015.

[66] R Sadighi-bonabi and M Gheshlaghi, "Laser induced sonofusion : A new road toward thermonuclear reactions Laser induced sonofusion : A new road toward thermonuclear reactions," *AIP Adv.*, vol. 6, no. 035218, pp. 1–10, 2016.

[67] P A Anderson, N A Hawker, M Betney, *et al.*, "Experimental characterisation of light emission during shock-driven cavity collapse," *Proceeding Meet. Acoust.*, vol. 19, no. 075039, 2013.

[68] N A Hawker, P Anderson, M R Betney, *et al.*, "Plasma Confinement via Shock-Driven Cavity Collapse," in *41st EPS Conf. Plasma Phys.*, (Berlin), 2014.

[69] P A Anderson, M R Betney, H W Doyle, *et al.*, "Characterizing shock waves in hydrogel using high speed imaging and a fiber-optic probe hydrophone," *Phys. Fluids*, vol. 29, no. 057101, 2017.

[70] N A Hawker and Y Ventikos, "Interaction of a strong shockwave with a gas bubble in a liquid medium: a numerical study," *J. Fluid Mech.*, vol. 701, no. 6, pp. 59–97, 2012.

[71] O Reynolds, "On the dynamical theory of incompressible viscous fluid and the determination of the criterion," 1895.

[72] J D Jackson, "Osborne Reynolds: scientist, engineer and pioneer," *Proceeding R. Soc. London A*, vol. 451, pp. 49–86, 1995.

[73] W H Besant, *A treatise on hydrostatics and hydrodynamics*. Cambridge: Deighton, Bell and Co., 1859.

[74] L Rayleigh, "VIII. On the pressure developed in a liquid during the collapse of a spherical cavity," *Philos. Mag.*, vol. 34, no. 200, pp. 94–98, 1917.

[75] C E Brennen, *Cavitation and Bubble Dynamics*. Oxford University Press, 1995.

[76] M S Plesset, "The Dynamics of Cavitation Bubbles," *J. Appl. Mech.*, vol. 16, pp. 277–282, 1949.

[77] N Gaines, "A magnetostriction oscillator producing intense audible sound and some effects obtained," *J. Appl. Phys.*, vol. 3, no. 5, pp. 209–229, 1932.

[78] J M Mousson, "Pitting Resistance of Metals under Cavitation Conditions," *Trans. ASME*, vol. 59, pp. 399–408, 1937.

[79] P Haller, "Untersuchungen über die durch Kavitation hergerufenen Korrosionen," *Schweiz Bauzeit*, vol. 101, pp. 243–246, 1933.

[80] M Kornfeld and L Suvorov, "On the Destructive Action of Cavitation," *J. Appl. Phys.*, vol. 15, p. 495, 1944.

[81] M S Plesset and T P Mitchell, "On the Stability of the Spherical Shape of a Vapor Cavity in a Liquid," *Q. Appl. Math.*, vol. 13, no. 4, pp. 419–430, 1956.

[82] C Naudé and A T Ellis, "On the Mechanism of Cavitation Damage by Non-hemispherical Cavities Collapsing in Contact With a Solid Boundary," *J. Basic Eng.*, vol. 1, pp. 1–9, 1961.

[83] T B Benjamin and A T Ellis, "The collapse of cavitation bubbles and the pressures thereby produced against solid boundaries," *Philos. Trans. R. Soc. A*, vol. 260, pp. 221–240, 1966.

[84] M S Plesset and R B Chapman, "Collapse of an initially spherical Vapor Cavity in the Neighborhood of a solid Boundary," *J. Fluid Mech.*, vol. 47, no. 2, pp. 283–290, 1971.

[85] W Lauterborn and H Bolle, "Experimental investigations of cavitation-bubble collapse in the neighbourhood of a solid boundary," *J. Fluid Mech.*, vol. 72, no. 2, pp. 391–399, 1975.

[86] N K Bourne and J E Field, "Shock-induced collapse and luminescence by cavities," *Philos. Trans. R. Soc. London A*, vol. 3511, pp. 295–311, 1999.

[87] N K Bourne and J E Field, "Explosive ignition by the collapse of cavities," *Proc. R. Soc. A Math. Phys. Eng. Sci.*, vol. 455, no. 1987, pp. 2411–2426, 1999.

[88] I Hansson and K A Mørch, "The dynamics of cavity clusters in ultrasonic (vibratory) cavitation erosion," *J. Appl. Phys.*, vol. 51, no. 9, pp. 4651–4658, 1980.

[89] A B Swantek and J M Austin, "Collapse of void arrays under stress wave loading," *J. Fluid Mech.*, vol. 649, pp. 399–427, 2010.

[90] J c Isselin, A p Alloncle, and M Autric, "On laser induced single bubble near a solid boundary : Contribution to the understanding of erosion phenomena," *J. Appl. Phys.*, vol. 84, no. 10, pp. 5766–5771, 1998.

[91] A Vogel, W Lauterborn, and R Timm, "Optical and acoustic investigations of the dynamics of laser-produced cavitation bubbles near a solid boundary," *J. Fluid Mech.*, vol. 206, pp. 299–338, 1989.

[92] G J Ball, B P Howell, T G Leighton, and M J Schofield, "Shock-induced collapse of a cylindrical air cavity in water: a Free-Lagrange simulation," *Shock Waves*, vol. 10, pp. 265–276, 2000.

[93] E Johnsen and T Colonius, "Numerical simulations of non-spherical bubble collapse," *J. Fluid Mech.*, vol. 629, pp. 231–262, 2009.

[94] C K Turangan, A R Jamaluddin, G J Ball, and T G Leighton, "Free-Lagrange simulations of the expansion and jetting collapse of air bubbles in water," *J. Fluid Mech.*, vol. 598, pp. 1–25, 2008.

[95] Z Ding and S M Gracewski, "The behaviour of a gas cavity impacted by a weak or strong shock wave," *J. Fluid Mech.*, vol. 309, pp. 183–209, 1996.

[96] N K Bourne and A M Milne, "The temperature of a shock-collapsed cavity," *Proc. R. Soc. London A*, vol. 459, no. 2036, pp. 1851–1861, 2003.

[97] X Ma, X Li, X Zheng, *et al.*, "Crack initiation and potential hot-spot formation around a cylindrical defect under dynamic compression," *J. Appl. Phys.*, vol. 122, no. 185104, 2017.

[98] N K Rai, M J Schmidt, and H S Udaykumar, "High-resolution simulations of cylindrical void collapse in energetic materials: Effect of primary and secondary collapse on initiation thresholds," *Phys. Rev. Fluids*, vol. 2, no. 043202, 2017.

[99] M P Kroonblawd and R A Austin, "Sensitivity of pore collapse heating to the melting temperature and shear viscosity of HMX," *Mech. Mater.*, vol. 152, no. November 2020, p. 103644, 2021.

[100] N K Rai and H S Udaykumar, "Three-dimensional simulations of dynamics of void collapse in energetic materials," *Phys. Rev. Fluids*, vol. 3, no. 033201, 2018.

[101] B Hejazialhosseini, D Rossinelli, and P Koumoutsakos, "Vortex dynamics in 3D shock-bubble interaction," *Phys. Fluids*, vol. 25, no. 11, 2013.

[102] N Grilli, C A Duarte, and M Koslowski, "Dynamic fracture and hot-spot modeling in energetic composites," *J. Appl. Phys.*, vol. 123, no. 065101, 2018.

[103] N K Rai, M J Schmidt, and H S Udaykumar, "Collapse of elongated voids in porous energetic materials: Effects of void orientation and aspect ratio on initiation," *Phys. Rev. Fluids*, vol. 2, no. 043201, 2017.

[104] M A Meyers, "Shock Waves," in *Dyn. Behav. Mater.*, ch. 4, pp. 98–122, New York: John Wiley & Sons, Inc., 1994.

[105] N R Barton, N W Winter, and J E Reaugh, "Defect evolution and pore collapse in crystalline energetic materials," *Model. Simul. Mater. Sci. Eng.*, vol. 17, no. 035003, 2009.

[106] R A Austin, N R Barton, J E Reaugh, and L E Fried, "Direct numerical simulation of shear localization and decomposition reactions in shock-loaded HMX crystal," *J. Appl. Phys.*, vol. 117, p. 185902, 2015.

[107] M D Nelms, M P Kroonblawd, and R A Austin, "Pore collapse in single-crystal TatB under shock compression," *AIP Conf. Proc.*, vol. 2272, 2020.

[108] M A Wood, D E Kittell, C D Yarrington, and A P Thompson, "Multiscale

modeling of shock wave localization in porous energetic material," *Phys. Rev. B*, vol. 97, no. 014109, 2018.

[109] M Armstrong, E Bukovsky, W Shaw, *et al.*, "Time-resolved X-ray Imaging of Void Collapse in Silicone and TNT," tech. rep., Lawrence Livermore National Lab.(LLNL), Livermore, CA (United States), 2018.

[110] M R Armstrong, R Austin, E Bukovsky, *et al.*, "Time-resolved x-ray imaging of void collapse at 10 micron length scales," tech. rep., 2019.

[111] D Ranjan, J Oakley, and R Bonazza, "Shock-Bubble Interactions," *Annu. Rev. Fluid Mech.*, vol. 43, no. 1, pp. 117–140, 2011.

[112] J H J Niederhaus, J A Grennough, J G Oakley, *et al.*, "A computational parameter study for the three-dimensional shock-bubble interaction," *J. Fluid Mech.*, vol. 594, pp. 85–124, 2019.

[113] W Jacobs, "Shock-induced mixing of a light-gas cylinder," *J. Fluid Mech.*, vol. 234, pp. 629–649, 1992.

[114] J Lindl, "Development of the indirect-drive approach to inertial confinement fusion and the target physics basis for ignition and gain," *Phys. Plasmas*, vol. 2, no. 3933, 1995.

[115] A Kapahi and H S Udaykumar, "Three-dimensional simulations of dynamics of void collapse in energetic materials," *Shock Waves*, vol. 25, pp. 177–187, 2015.

[116] M A Meyers, V F Nesterenko, J C Lasalvia, and Q Xue, "Shear localization in dynamic deformation of materials: microstructural evolution and self-organization," tech. rep., 2001.

[117] Q Xue, M A Meyers, and V F Nesterenko, "Self organization of shear bands in stainless steel," *Mater. Sci. Eng. A*, vol. 384, no. 1-2, pp. 35–46, 2004.

[118] M A Meyers, "Shear Bands (Thermoplastic Shear Instabilities)," in *Dyn. Behav. Mater.*, ch. 15, pp. 448–486, 1994.

[119] S M Walley, "Shear Localization: A Historical Overview," *Metall. Mater. Trans. A*, vol. 38A, no. 2629-2654, 2007.

[120] D E Grady and M E Kipp, "The growth of unstable thermoplastic shear with application to steady-wave shock compression in solids," Tech. Rep. 1, 1987.

[121] T W Wright and J W Walter, "On stress collapse in adiabatic shear bands," *J. Mech. Phys. Solids*, vol. 35, no. 6, pp. 701–720, 1987.

[122] T W Wright and H Ockendon, "A scaling law for the effect of inertia on the formation of adiabatic shear bands," Tech. Rep. 7, 1996.

[123] A Molinari, "Collective behavior and spacing of adiabatic shear bands," *J. Mech. Phys. Solids*, vol. 45, no. 9, pp. 1551–1575, 1997.

[124] V F Nesterenko, M A Meyers, and T W Wright, "Self-organization in the initiation of adiabatic shear bands," *Acta Metall.*, vol. 46, no. 1, pp. 327–340, 1998.

[125] A Cohen, D Levi-Hevroni, P Fridman, *et al.*, "In-situ radiography of a split-Hopkinson bar dynamically loaded materials," *J. Instrumentationm*, vol. 14, no. T06008, 2019.

[126] Z Lovinger, D Rittel, and Z Rosenberg, "Modeling spontaneous adiabatic shear band formation in electro-magnetically collapsing thick-walled cylinders," 2018.

[127] P Cloetens, R Barrett, J Baruchel, *et al.*, "Viewpoint on Phase objects in synchrotron radiation hard x-ray imaging," *J. Phys. D. Appl. Phys.*, vol. 29, pp. 133–146, 1996.

[128] S W Wilkins, T E Gureyev, D Gao, *et al.*, "Phase-contrast imaging using polychromatic hard X-rays," *Nature*, vol. 384, pp. 335–338, nov 1996.

[129] M Sánchez del Río and R J Dejus, "XOP 2.1 — A New Version of the X-ray Optics Software Toolkit," *AIP Conf. Proc.*, vol. 705, pp. 784–787, 2004.

[130] T Weitkamp, D Haas, D Wegrzynek, and A Rack, "ANKAphase: Software for single-distance phase retrieval from inline X-ray phase-contrast radiographs," *J. Synchrotron Radiat.*, vol. 18, no. 4, pp. 617–629, 2011.

[131] A Rack, S Zabler, B R Müller, *et al.*, "High resolution synchrotron-based radiography and tomography using hard X-rays at the BAMline (BESSY II)," *Nucl. Instruments Methods Phys. Res. Sect. A Accel. Spectrometers, Detect. Assoc. Equip.*, vol. 586, pp. 327–344, feb 2008.

[132] K Fezzaa and Y Wang, "Ultrafast X-ray phase-contrast imaging of the initial coalescence phase of two water droplets," *Phys. Rev. Lett.*, vol. 100, no. 10, pp. 1–4, 2008.

[133] Y Wang, X Liu, K S Im, *et al.*, "Ultrafast X-ray study of dense-liquid-jet flow dynamics using structure-tracking velocimetry," *Nat. Lett.*, vol. 4, pp. 305–309, 2008.

[134] J San Lee, B Mook Weon, S Ji Park, *et al.*, "Size limits the formation of liquid jets during bubble bursting," *Nat. Commun.*, vol. 2, no. 367, pp. 1–7, 2011.

[135] N D Parab, Z Guo, M C Hudspeth, *et al.*, "Dynamic fracture behavior of single and contacting Poly(methyl methacrylate) particles," *Adv. Powder Technol.*, vol. 28, no. 11, pp. 2929–2939, 2017.

[136] N D Parab, Z A Roberts, M H Harr, *et al.*, "High speed X-ray phase con-

trast imaging of energetic composites under dynamic compression," *Appl. Phys. Lett.*, vol. 109, no. 13, 2016.

[137] T M Willey, K Champley, R Hodgin, *et al.*, "X-ray imaging and 3D reconstruction of in-flight exploding foil initiator flyers," *J. Appl. Phys.*, vol. 119, no. 23, 2016.

[138] B J Jensen, S N Luo, D E Hooks, *et al.*, "Ultrafast , high resolution , phase contrast imaging of impact response with synchrotron radiation Ultrafast , high resolution , phase contrast imaging of impact," *AIP Adv. 2*, vol. 2, no. 012170, 2012.

[139] B J Jensen, C T Owens, K J Ramos, *et al.*, "Impact system for ultrafast synchrotron experiments," *Rev. Sci. Instrum.*, vol. 84, no. 1, 2013.

[140] J A Hawreliak, J Lind, B Maddox, *et al.*, "Dynamic Behavior of Engineered Lattice Materials," *Sci. Rep.*, vol. 6, no. 28094, 2016.

[141] B Branch, A Ionita, B E Clements, *et al.*, "Controlling shockwave dynamics using architecture in periodic porous materials," *J. Appl. Phys.*, vol. 121, no. 13, 2017.

[142] J Lind, B J Jensen, M Barham, and M Kumar, "In situ dynamic compression wave behavior in additively manufactured lattice materials," *J. Mater. Res.*, vol. 34, no. 1, pp. 2–19, 2019.

[143] K B Wagner, A Keyhani, A K Boddorff, *et al.*, "High-speed x-ray phase contrast imaging and digital image correlation analysis of microscale shock response of an additively manufactured energetic material simulant," *J. Appl. Phys.*, vol. 127, jun 2020.

[144] B J Jensen, K J Ramos, a J Iverson, *et al.*, "Dynamic experiment using IMPULSE at the Advanced Photon Source," *J. Phys. Conf. Ser.*, vol. 500, p. 042001, 2014.

[145] B J Jensen, F J Cherne, M B Prime, *et al.*, "Jet formation in cerium metal to examine material strength," *J. Appl. Phys.*, vol. 118, no. 19, 2015.

[146] T Weitkamp, P Tafforeau, E Boller, *et al.*, "Status and evolution of the ESRF beamline ID19," *AIP Conf. Proc.*, vol. 1221, no. 2010, pp. 33–38, 2010.

[147] A Rack, M Scheel, L Hardy, *et al.*, "Exploiting coherence for real-time studies by single-bunch imaging," *J. Synchrotron Radiat.*, vol. 21, pp. 815–818, 2014.

[148] M P Olbinado, V Cantelli, O Mathon, *et al.*, "Ultra high-speed x-ray imaging of laser-driven shock compression using synchrotron light," *J. Phys. D. Appl. Phys.*, vol. 51, no. 055601, pp. 1–11, 2018.

[149] D Yanuka, A Rososhek, S Theocharous, *et al.*, "Multi frame synchrotron

radiography of pulsed power driven underwater single wire explosions," *J. Appl. Phys.*, vol. 124, no. 153301, 2018.

[150] D J Miller, R S Crum, M A Homel, *et al.*, "Hugoniot Measurements Utilizing In Situ Synchrotron X-ray Radiation," *J. Dyn. Behav. Mater.*, 2019.

[151] M Jäcklein, K Kappe, A Pfaff, *et al.*, "Dynamic compression of 3D printed metallic mesostructures with in-situ X-ray imaging," *Int. Symp. Impact Eng.*, no. February 2020, 2019.

[152] L Farbaniec, D J Chapman, J R Patten, *et al.*, "In-situ visualisation of dynamic fracture and fragmentation of an L-type ordinary chondrite by combined synchrotron X-ray radiography and microtomography," *Icarus*, vol. 359, p. 114346, may 2021.

[153] M E Rutherford, D J Chapman, T G White, *et al.*, "Evaluating scintillator performance in time-resolved hard X-ray studies at synchrotron light sources," *J. Synchrotron Radiat.*, vol. 23, no. 3, pp. 685–693, 2016.

[154] M E Rutherford, D J Chapman, J G Derrick, *et al.*, "Probing the early stages of shock-induced chondritic meteorite formation at the mesoscale," *Sci. Rep.*, vol. 7, may 2017.

[155] J G Derrick, M E Rutherford, D J Chapman, *et al.*, "Investigating shock processes in bimodal powder compaction through modelling and experiment at the mesoscale," *Int. J. Solids Struct.*, vol. 163, pp. 211–219, 2019.

[156] E M Escauriza, A Rack, E Synchrotron, *et al.*, "Ultra high-speed indirect X-ray imaging system with versatile spatio-temporal sampling capabilities," *Appl. Opt.*, vol. 57, no. 18, pp. 5004–5010, 2018.

[157] E M Escauriza, J P Duarte, D J Chapman, *et al.*, "Collapse dynamics of spherical cavities in a solid under shock loading," *Sci. Rep.*, vol. 10, pp. 1–16, may 2020.

[158] N K Rai, E M Escauriza, D E Eakins, and H S Udaykumar, "Mechanics of shock induced pore collapse in poly(methyl methacrylate) (PMMA): Comparison of simulations and experiments," *J. Mech. Phys. Solids*, vol. 143, 2020.

Chapter 2

Methods

Here is presented a summary of the experimental and analytical methods for this project. Large portions of the methods sections from the radiographic results Scientific Reports paper [1] in Chapter 4 and the simulations comparison JMPS paper [2] in Chapter 5 have been moved to this Chapter and expanded significantly. For the Applied Optics paper [3] on imaging instrumentation, in Chapter 3, the substance of the paper is the methodology and analysis of the system's performance. As such, the methods of that paper are presented in that Chapter in full. In the present Chapter, additional analytical methods are also presented, on image processing and edge detection, parameter extraction and Fourier analysis. Lastly, the key details of the simulations package SCIMITAR3D are given, adapted from publications on this research code.

2.1 Gas gun systems

Gas-driven impact systems, known as 'gas guns', offer a reliable and safe solution for high strain-rate studies, without the need for powder explosives or electromagnetic pulse power [4]. For gas gun experiments, a projectile (henceforth referred to as the 'sabot') is impacted against a target, which is typically contained

within a target chamber. There are many gas gun designs [5–7], with variations in breech configuration, as well as the number of 'stages' of acceleration for the system [5]. Additional stages increases the impact velocity, but the final size of the sabot is greatly reduced. The techniques behind this principle will be explained in further detail below, in Section 2.1.2.

The shock compression of cavity collapse in solid media presents a scenario for which gas gun loading is ideally suited, because of the need to generate a planar shock to interact with the cavity. However, the range of loading conditions achievable with a given gas gun is determined largely by the range of impact velocities. Therefore, for the present work two systems are used, each allowing access to a different range of impact velocities. A single-stage system was used to study cavity collapse at lower velocities in the sub-km/s range and a two-stage system was used to study higher velocity impacts, between $\sim$1.5-4.5 km/s. Details of these systems, along with their relative advantages and disadvantages, are presented in the following sections.

2.1.1 Single-stage gas gun

Photographs of the single-stage gas gun system can be seen in Figs. 2.1a&b, which was taken in the experimental hutch of ESRF beamline ID19. The breech and target chamber are connected by the gun barrel, known as the 'launch tube', and the whole system is mounted on an aluminium frame. When the personnel are cleared from the lead-lined room and the main beamline shutter is opened, the X-rays emerge from a window. As shown by the arrow in Fig. 2.1b, the gas gun system is oriented so the X-ray beam is normal to the direction of impact, providing a side-on projection of the impacts. The aluminium frame is mounted on adjustable feet that allow the system to be raised so that the mid-point of the mounted target is level with the X-ray beam. Side flanges are mounted on the target chamber, which contain small circular holes where Mylar windows can be

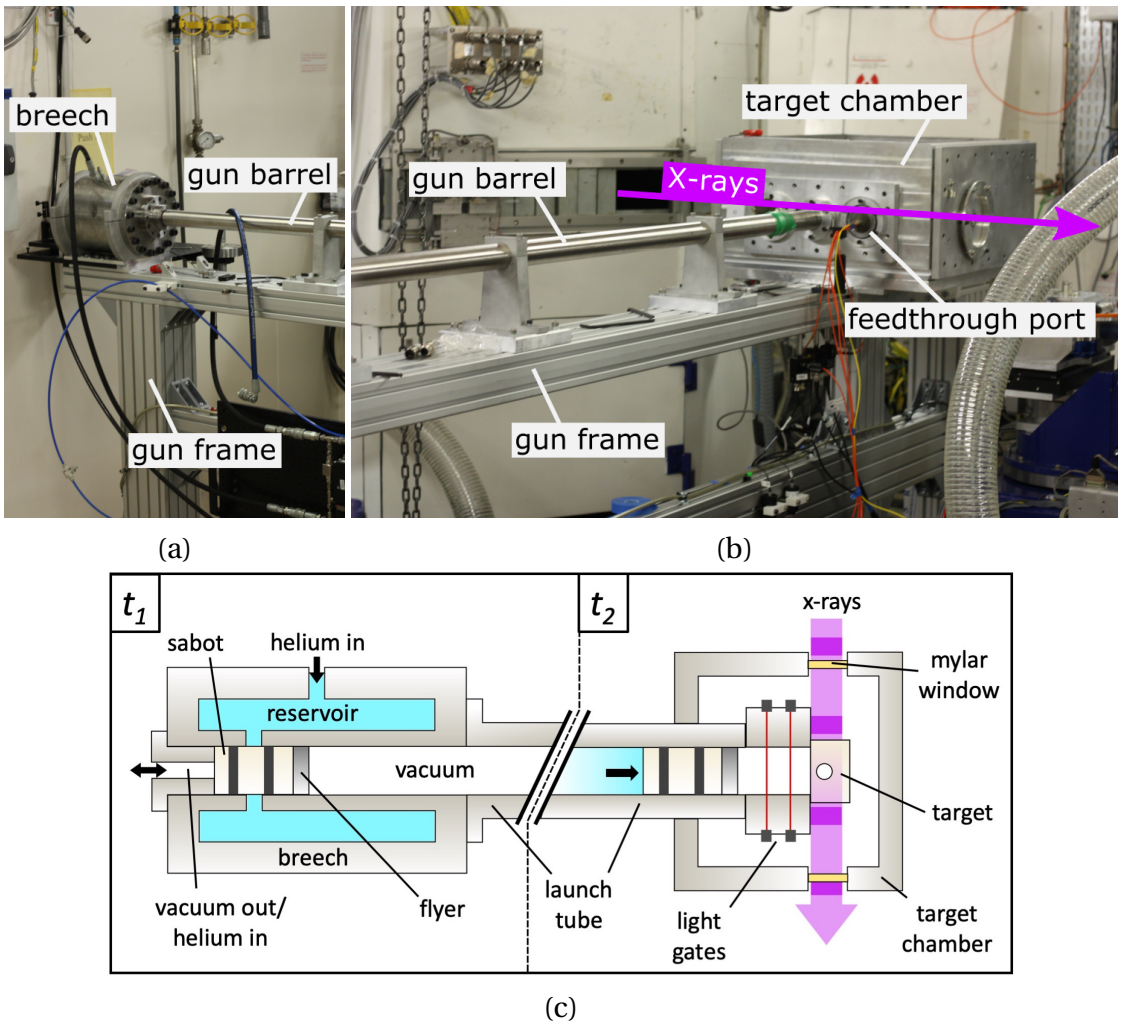
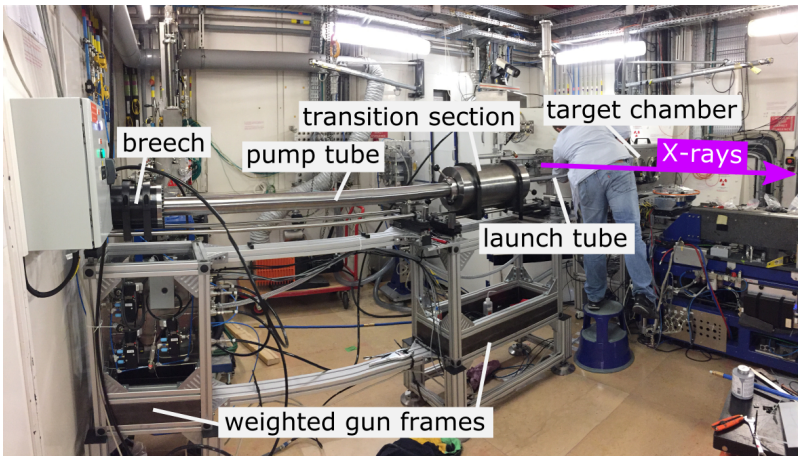


Figure 2.1: The single-stage gas gun system. (a) Photo of the breech end of the gun, which is mounted on a frame. (b) Photo of the opposite end of the gun, connected by the launch tube and also mounted on the frame. The target chamber contains the target and some of the diagnostics, which are fed into the chamber via a vacuum-sealed port. The synchrotron X-rays pass through Mylar windows attached to the side of the target chamber. (c) Schematic diagram showing the internal workings of the single-stage gas gun system at different times.

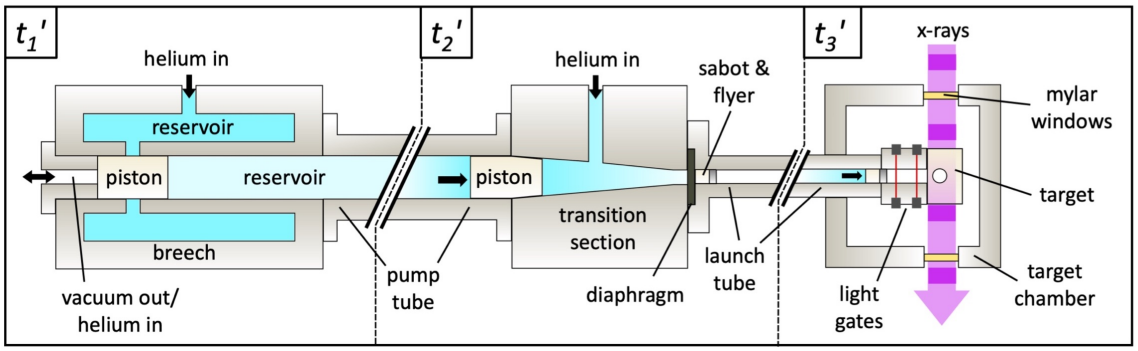
mounted with an o-ring, thus allowing a vacuum to be maintained. Since the Mylar sheets are thin ($\sim$100 μm) compared to the target chamber walls, and the polymer material has a low molecular weight, attenuation of the X-rays is minimised, producing a brighter illumination for capturing radiographs [8].

A schematic diagram of the single-stage gun system can be seen in Fig. 2.1c (not drawn to scale). Designed by Eakins and Chapman, the gas gun is based on the system used in earlier experiments at the Diamond synchrotron [9]. However, the newer version is distinct in that, rather than utilising a piston, the breech has a 'wrap-around' design, in which a reservoir surrounding the sabot is filled with helium gas at the desired firing pressure before firing [7]. The sabot is held in place by a vacuum in the space behind it, which is at a lower pressure than the vacuum in the region of the connected 25 mm bore launch tube, and target chamber (shown at time t_1 in Fig. 2.1c). The vacuum of the launch tube and target chamber drastically increases the impact velocity by decreasing air resistance. The gas from the reservoir is prevented from leaking around the sabot by an o-ring either end of the projectile.

Upon firing, the vacuum line behind the projectile, which is also connected to the high pressure gas through a valve, is blanked at the junction of the vacuum and then flushed with high-pressure gas. After the sabot moves past point of the breech inlet, the helium gas in the reservoir is released behind the sabot and continues to propel it forward. The reservoir substantially increases the total volume of helium, thus extending acceleration of the projectile. At time t_2 in Fig. 2.1c we see the sabot approaching the target chamber; two parallel light gates separated by 12 mm are directed normal to the sabot path, mounted in the muzzle, in order to measure the impact velocity before impact. The target is mounted on the end of the gun barrel, sitting proud of the muzzle. As mentioned above, the X-rays pass through the experiment region through Mylar windows mounted in the target chamber side flanges.



(a)



(b)

Figure 2.2: The two-stage gas gun system. (a) Photograph of the gun, which is mounted on a weighted frame to reduce movement when firing. The target chamber contains the target and some of the diagnostics, and has windows to allow the synchrotron X-rays to pass through the side flanges with minimal attenuation. (b) Schematic diagram showing the internal workings of the two-stage gas gun system at different times.

2.1.2 Two-stage gas gun

Figure 2.2 shows the two-stage gas gun setup. A wide-angle photograph of the system is shown in Fig. 2.2a. The system was designed and built by post-doctoral researcher Dr João-Pedro Duarte at Imperial College London between 2013 and 2017, as part of the EPSRC project EP/K028707/1. It is mounted on an aluminium frame and weighed down with steel rods, which reduces the misalignment caused by recoil when the gun is fired. As with the single-stage system, the breech has a wrap-around design and is charged with high-pressure helium. The additional 'stage' of acceleration is mediated with a transition section, which acts as a second breech. A 50 mm bore barrel, the 'pump tube', connects the breech and tran-

sition section, and a 10 mm launch tube connects the transition section and target chamber.

The principle behind the increased impact velocity, compared to the single-stage system, is demonstrated in Fig. 2.2b. At time t_1' the breech is charged in the same way as the single stage system, with the first sabot, known as the 'piston' because it is not impacted, held in place. However, distinct from the single-stage process, the pump tube is first evacuated of air and then filled with helium to a pressure of $\sim$1 bar, which is stopped from passing between the transition section and launch tube by a diaphragm and o-ring. The launch tube and target chamber are held under vacuum, again to increase the impact velocity. The sabot and mounted flyer plate are placed in front of the diaphragm before the breech is charged, and the sealed diaphragm stops gas from advancing the sabot down the launch tube, which is held under vacuum with the target chamber.

At time t_2' the vacuum is blanked and the line behind the piston flushed with high pressure helium, releasing the piston and launching it toward the transition section. As the piston advances it rapidly compresses the helium in the pump tube until it reaches the transition section. The tapered bore of the transition section deforms the piston and halts its advancement. Simulations by Dr Duarte predict that a peak pressure of up to $\sim$5 kbar is generated during the helium compression. This sudden spike in pressure bursts the diaphragm and the released gas launches the flyer down the launch tube at velocities up to $\sim$5 km/s. At lower breech pressures a 0.25 mm Mylar diaphragm is used, and at breech pressures above 80 bar a 0.9 mm stainless steel 'petal' design diaphragm is used. As the sabot approaches the target, shown at time t_3', light gates in its path record the impact velocity. Similar to the single-stage system, Mylar windows in the chamber allow synchrotron X-rays to pass through the target region minimally attenuated, travelling perpendicular to the axis of impact.

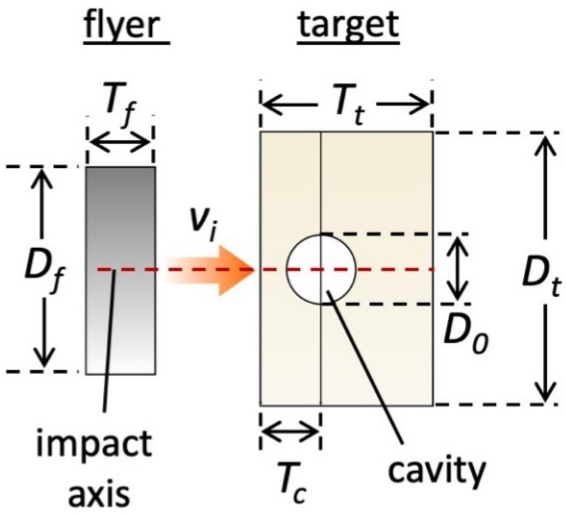


Figure 2.3: Schematic diagram showing the flyer and target design.

2.1.3 Flyer and target design

A schematic diagram showing the flyer impacting the target is shown in Fig. 2.3. For simplicity, the sabot is not included in the diagram. The flyer plate is a cylindrical disc of material, with thickness T_f and diameter D_f, which moves towards the target at impact velocity v_i. The value of D_f is limited to be less than the barrel diameter, and T_f is similarly limited by the need to reduce the weight, since higher impact velocities can be accessed with a lighter projectile. Aluminium 2024 flyers are used for the single-stage experiments, with $T_f = 5\,\mathrm{mm}$ and $D_f = 25\,\mathrm{mm}$, impacted with v_i ranging between 0.165 and 0.750 km/s. For the two-stage experiments polycarbonate flyers are used, with $T_f = 2\,\mathrm{mm}$ and $D_f = 9\,\mathrm{mm}$, with v_i values between 1.973 and 4.697 km/s. Polycarbonate is chosen because, with the smaller sabot size of the two-stage gun, small reductions in flyer weight greatly increases the maximum achievable impact velocity. Furthermore, in the event of a flyer becoming detached, using metal flyers risks irreparably damaging the launch tube interior. Two additional impacts are performed in a 'reverse' configuration with the single-stage system, at v_i of 0.719 km/s and 0.795 km/s, by mounting the cavity target onto a sabot and impacting it against a stainless steel anvil. In doing so, intermediate shock pressures are achieved that cannot be accessed with the standard single- and two-stage impact configura-

tions (this principle is explained in more detail below).

The choice of flyer materials is explained in Fig. 2.4, which shows the p-u_p Hugoniots for the range of materials and impact velocities studied, where p is the shock pressure generated by an impact and u_p is the particle velocity behind the shock. Figure 2.4a shows the Hugoniots for the single-stage experiments, whereas those of the two-stage experiment are shown in Fig. 2.4b. The value of p for a given u_p can be calculated as the product of u_p and the shock 'impedance', $Z = \rho_0 u_p$, which gives,

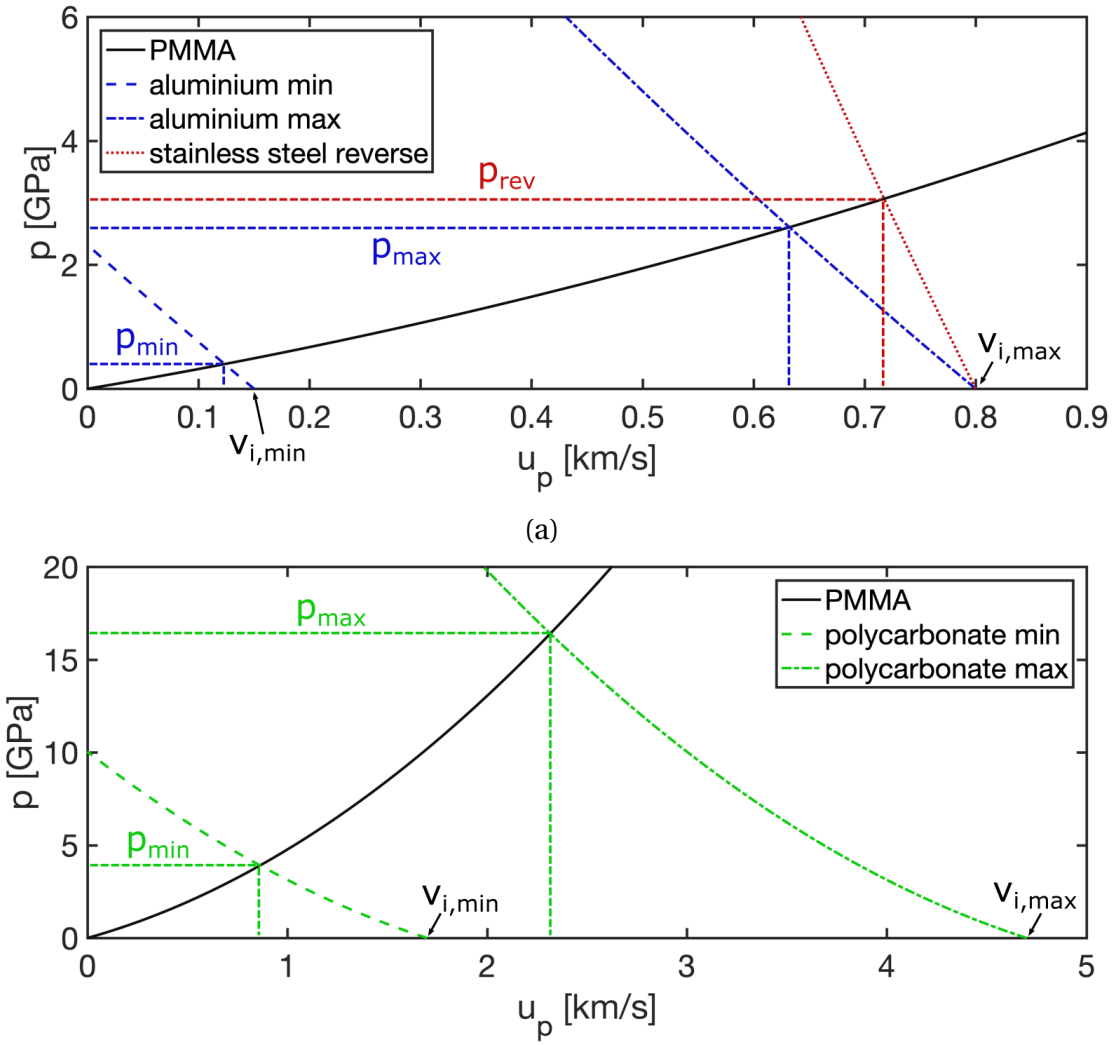
$$p = \rho_0 U_s u_p \tag{2.1}$$

where ρ_0 is the initial density of material and U_s is the shock velocity [10]. For most materials, U_s is linearly dependent on u_p, such that,

$$U_s = S u_p + C_0, \tag{2.2}$$

where S is the slope of the line and C_0 is the y-axis intercept [10, 11]. Therefore the p-u_p slope is a quadratic in u_p.

Through a method known as 'impedance matching', the p and u_p generated by an impact can be calculated through conservation of momentum, which states that the u_p of an impactor and target must be equal at the instant after impact [10]. Therefore, the values are given by the intercept of the Hugoniot lines of the target and impactor in the p-u_p plane. This principle is most clearly demonstrated in Fig. 2.4b: the solid black line is the Hugoniot for the PMMA target, which is the locus of all possible pressure states generated by impact. The Hugoniot slope for the polycarbonate flyer at the maximum impact velocity generated, $v_{i,max} = 4.697\,\mathrm{km/s}$, is shown by the green dashed and dotted line. Since the slopes are drawn in the target's frame of reference, the flyer slows down during impact, and the pressure generated is dependent on this decrease, which is why the slope points in this opposite direction. The pressure generated is the value



(a)

(b)

Figure 2.4: Plots showing the p-u_p Hugoniots for the range of materials and impact velocities, v_i, studied. The generated u_p and p values are indicated with vertical and horizontal lines, respectively. (a) Hugoniots for minimum and maximum v_i generated with the single stage gas gun, for aluminium flyers. For the two experiments conducted in against a steel anvil, the Hugoniot is shown from the PMMA flyer's frame of reference. (b) Hugoniots for minimum and maximum v_i generated with the two stage gas gun, for polycarbonate flyers.

at the intercept of the two Hugoniot curves, indicated by the dashed horizontal green line, labelled p_{max}, and is calculated to be 16.60 GPa – this corresponds to $u_p = 2.30\,\mathrm{km/s}$.

The same procedure is followed for the minimum impact velocity generated, v_{min}. By looking at Figs. 2.4a&2.4b, we can see the range of shock states that can be accessed with the two gas gun systems: 0.60-3.08 GPa for the single stage experiments and 4.80-16.60 GPa for the two-stage system. Polycarbonate is chosen at the flyer material because of its light weight and machinability, and because the barrel will not be damaged if the flyer detaches from the sabot. However, the lack of steepness in the Hugoniot curve for polycarbonate, which is very similar to the curve for PMMA, means that very high shock pressures cannot be reached. This is not an issue for the purposes of our study on PMMA, since, as we shall see in the results, the upper limit of 16.60 GPa is well beyond the strength limit.

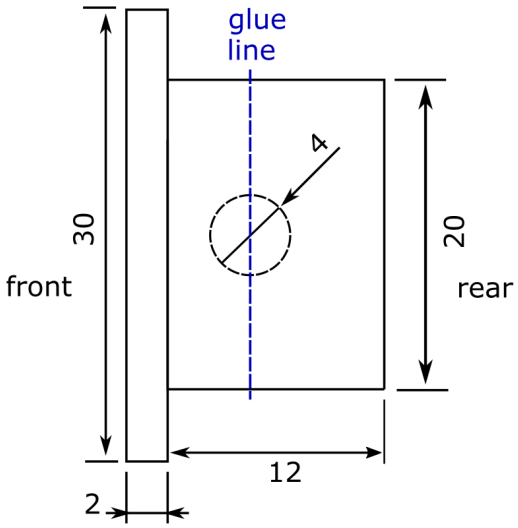
To access lower shock states, the single stage system is used, with aluminium flyer plates. The larger sabot design for this system means a larger flyer can be used without concern of increasing the total weight of projectile. Relative to its low density, aluminium has a steep Hugoniot curve compared to PMMA, as can be seen in 2.4b: the solid black curve is the PMMA Hugoniot and the blue dashed and dashed-dotted lines are the aluminium Hugoniots at the approximate minimum and maximum v_i generated, respectively. The range of p that can be accessed are between 0.49-2.44 GPa. The dotted red line shows the Hugoniot for the reverse impact against the steel anvil, with the line shown in the mounted PMMA target's frame of reference. Here we can see the benefit of the benefit of mounting the target as the flyer: at the same highest impact velocity, a higher shock state is generated, because of the steepness of the stainless steel Hugoniot curve. This would not be possible if the impact were performed directly, because of the high density of stainless steel – the increased projectile mass significantly lowers the impact velocity. By using a reverse setup, an intermediate state, with

with $p_{rev} = 3.08\,\mathrm{GPa}$, can be accessed, between the pressures generated by the direct impact with the single-stage and two-stage setups.

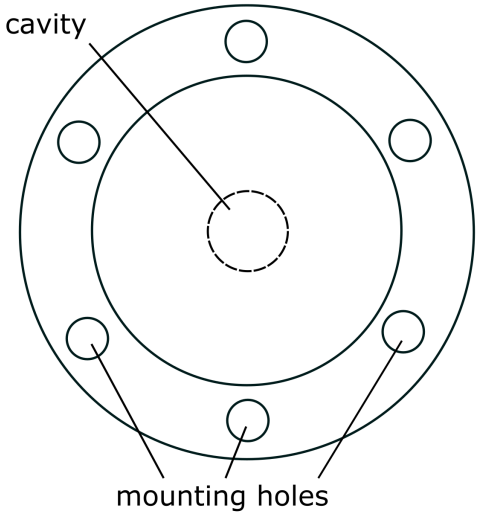
Also shown in Fig. 2.3 is the target design, which is likewise a cylindrical structure, with thickness T_t and diameter D_t, containing a spherical cavity in its centre, of diameter D_0. The targets are constructed from cast PMMA, purchased from commercial supplier RS Components UK. The offset between the cavity centre and impact surface, T_c, is chosen to be small to maximise the 1D shock region – as a conservative guide, the 1D region is assumed to shrink at an angle of ∼45°, since the lateral release wave travels in ward at approximately the same speed as the shock [12]. Therefore, having the cavity closer to the impact face reduces the effect of release on the collapse process.

The target is constructed from two cylindrical sections drilled with a concentric hemisphere, glued together with a polymer glue. During setup the target is positioned normal to the impact direction and concentrically aligned, such that there is cylindrical symmetry about the axis of impact, with machining tolerances of $\sim 10\,\mu\mathrm{m}$ on the gun and target components, which greatly increases the likelihood of normal impact. However, other factors can change the angle of impact, such as if the flyer becomes slightly detached, or if there is free flight of the sabot after leaving the barrel. In such cases, the shock will appear tilted relative to the normal. Even so, in the present work shock tilt did not present as a significant problem.

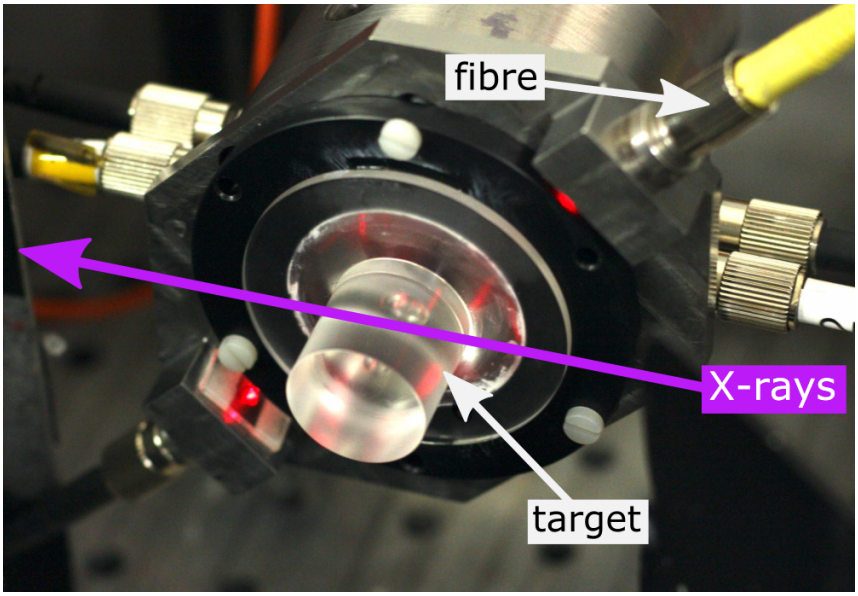
The specific design of the targets for the single-stage experiments can be seen in Fig. 2.5, for which cavity sizes of 4 and 6 mm are studied. In Fig. 2.5a the side view of the cylindrical design is shown, with the dimensions shown in mm. The blue dashed line indicates the gluing plane for the target. The front view in Fig. 2.5b shows the position of the holes for mounting the target, and in Fig. 2.5c a photograph can be seen of a target mounted on the muzzle at the end of the single-stage gas gun launch tube. In this case the target is glued to a mounting ring. The



(a) Side view.



(b) Front view.



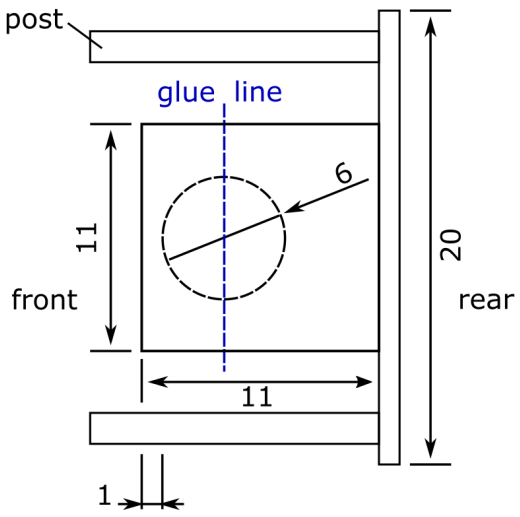
(c) Mounted target.

Figure 2.5: The target used for the single-stage experiments, with a side view and front view schematic diagram of a 4 mm cavity shown in (a) and (b), respectively. Units are in mm. A photograph of a mounted 4 mm cavity target is shown in (c).

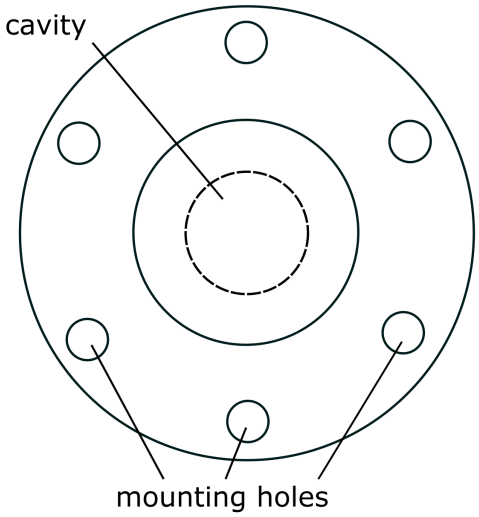
ring is then attached to the barrel with nylon screws, to prevent damage to the screw threading of the holes in the muzzle mount during impact. Also visible in the photograph are the light gate fibre-coupled lasers, which screw directly into the muzzle. In this setup a third light gate is added, seen as the pair of near fibres tilted at 45-degrees to the horizontal.

Figure 2.6 shows the design and mounting procedure of the targets for the two-stage experiments. Cavity diameters of 3, 4 and 6 mm are studied. The smaller flyer diameter compared to the single-stage setup is shown in Fig. 2.6a, which is (9 mm instead of 25 mm). For this reason, to reduce the distance between the cavity and impact face to just 1 mm, and thus minimise the effects of lateral release [12], the targets are mounted using posts and the mounting ring is placed on the rear side of the target. However, even with this adjustment it is not possible to study such large cavities and remain in the 1D planar shock zone. This is especially true for the 6 mm cavity shown in the diagram, which is large relative to the width of the target, and is therefore more affected by lateral release during shock interaction.

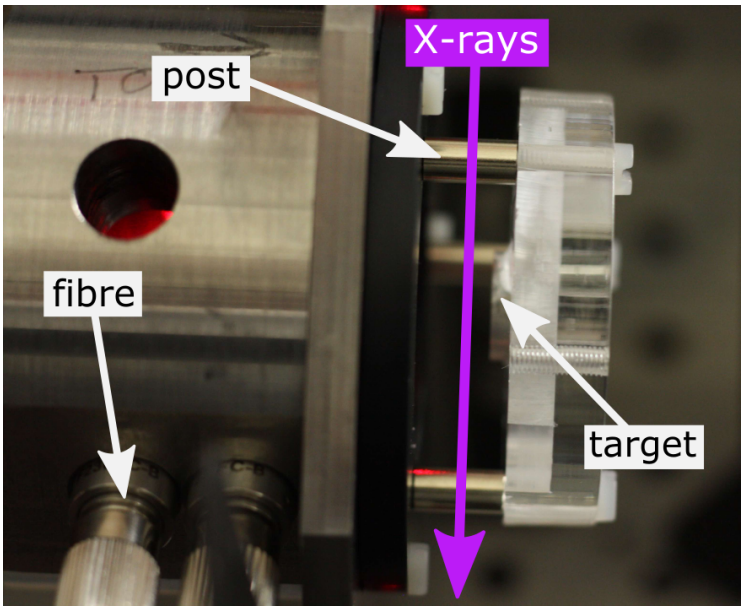
Nylon screws are inserted through the mounting holes in Fig. 2.6b, and then post are used to separate the target from the muzzle surface. A photograph of setup is not available, but a picture from an entirely different study on spall is shown in Fig. 2.6c to demonstrate the principle. The small disc of material under study is seen attached to the ring. As in the present work, the metallic posts separate the target from the muzzle and place it in free space, thus allowing the X-rays to pass through the target area with minimal attenuation. Also visible in the image are the connecting points for the light gate optical fibres.



(a) Side view.



(b) Front view.



(c) Mounted target with posts.

Figure 2.6: The target used for the two-stage experiments, with a side view and front view schematic diagram of a 6 mm cavity shown in (a) and (b), respectively. Units are in mm. A photograph of a mounted target using posts is shown in (c), taken from a different study.

2.2 Synchrotron imaging

Presented in this section are the details of the imaging system, synchrotron specifications, and synchronisation apparatus of the experiments at ESRF beamline ID19. The details are discussed in the context of the costs, advantages and trade-offs that must be made when choosing how to perform such a complex experiment. As with all synchrotron experiments, before opening the shutter which allows X-rays to enter the beamline 'hutch' (the lead-lined room in which the experiments take place), all personnel must vacate to the control room outside the hutch. This therefore presents the additional challenge of ensuring all components in the experiment can be controlled remotely.

2.2.1 Indirect X-ray imaging

A 'direct' X-ray detector records the intensity of the X-ray photons at a given position through an array of pixels placed directly in the X-ray beam. For these systems, the X-ray photons are detected (either by counting or integration) by photodiode pixels, which convert the photon energy into an electrical signal through ionisation [13]. Though offering a high quantum efficiency, direct detection systems are typically limited to coarse pixel sizes, and direct exposure to the X-rays leads to heating and damage over time, which can be costly [13]. Another limiting factor is the upper limit of frame rates for direct detectors, of up to around 10,000 frames per second [13]. This is too low for the use of macroscopic shock studies, which require frame rates of the order 1 M, since interfaces are often moving at multiple mm/μs. Furthermore, X-ray lens systems, to change magnification, are more complex and specialist than their visible light (optical) counterparts [14].

An alternative is to record the X-rays 'indirectly' with an optical imaging system, which requires first converting the X-ray photons into visible light with a scintillating medium placed in the X-ray beam path. The excitations in the scintillator

decay via emission in the visible part of the spectrum, and, importantly, the relative intensity of the X-rays at a given location is maintained [14]. Thus the spatial information of the absorbed X-rays is preserved. For high-speed imaging studies, some thin wafer crystal scintillators offers a very short emission, of around 100 ns, making them well suited for shock studies [15]. There are many advantages for choosing an indirect imaging system. Firstly, only the scintillator needs to be placed in the beam path, along with a mirror to reflect the optical light toward the lenses and camera, which are placed some distance away. Although scintillators must be replaced when damaged, the cost is much lower than repairing or replacing a damaged sensor [14].

Second, the scintillator allows more than one camera to capture images simultaneously, since the optical emission can be relayed and further split with commercial optical components. Furthermore, since the scintillator emits light from both of it's faces, emission of can be captured twice, thus doubling the light yield, by reflecting the visible light emitted back toward the X-ray source, using a pellicle mirror made from a thin polymer membrane (the X-ray attenuation of the membrane is negligible) [16]. A final advantage is the choice of magnification that an optical system offers, by simply changing the lens configuration. Combined with multiple cameras, this allows for different regions of interest to be recorded simultaneously [16]. The specifics of the scintillator used for the experiment will be given below in the sub-section on the imaging system, and more information on scintillator performance for dynamic radiography can be found in the work of previous PhD student in our group, Dr Michael Rutherford [15, 17]. Details of additional modifications, and the versatility of such a system, is presented in the instrumentation paper in Chapter 3.

2.2.2 The ESFRF synchrotron

The radiographic imaging studies are performed at the ESRF synchrotron's beamline ID19. The beamline was originally developed for tomographic imaging of palaeontological and archaeological samples, and this is still the main application of the beamline [18, 19]. For this purpose, the X-ray beam size is large compared to other beamlines, with an elliptical profile of nominal width of 45 mm and a height of 15 mm [19]. This large beam size offers a distinct advantage for high-speed imaging, since fast-moving object can be captured in both zoomed and wide fields of view, increasing the versatility of imaging systems used to capture the experiments. However, the most important aspect of high-speed imaging is having a sufficiently bright illumination source, which is captured by a parameter called Brilliance, defined as the flux per unit source area and unit solid angle [8],

$$\text{Brilliance} = \frac{\text{photons/second}}{(\text{mrad}^2)(\text{mm}^2 \text{ source area})(0.1\% \text{ bandwidth})}. \tag{2.3}$$

All other factors being equal, peak Brilliance is determined by the total X-ray flux. The flux is in turn determined by the energy of the electrons in the storage ring. For the ESRF, at the time when the experiments are performed, the storage ring energy is approximately 6 GeV. For comparison, the energy at the UK's brightest synchrotron, DLS, the energy is 3 GeV. This two-fold increase in energy corresponds to a sixteen-fold increase in flux (and therefore brightness), since the flux is proportional to the fourth power of electron energy [8]. A visual representation of the Brilliance of various undulator, accelerator and free electron laser (FEL) X-ray sources can be seen in the plot of Fig. 2.7. The ESRF is among the brightest in the world for synchrotron sources, which, when coupled with the continuously pulsed feature of synchrotron radiation, makes it an ideal place to conduct dynamic imaging experiments. Furthermore, the 'hard', i.e. high-energy, X-rays produced by undulator sources are well suited for studying solid materials, due

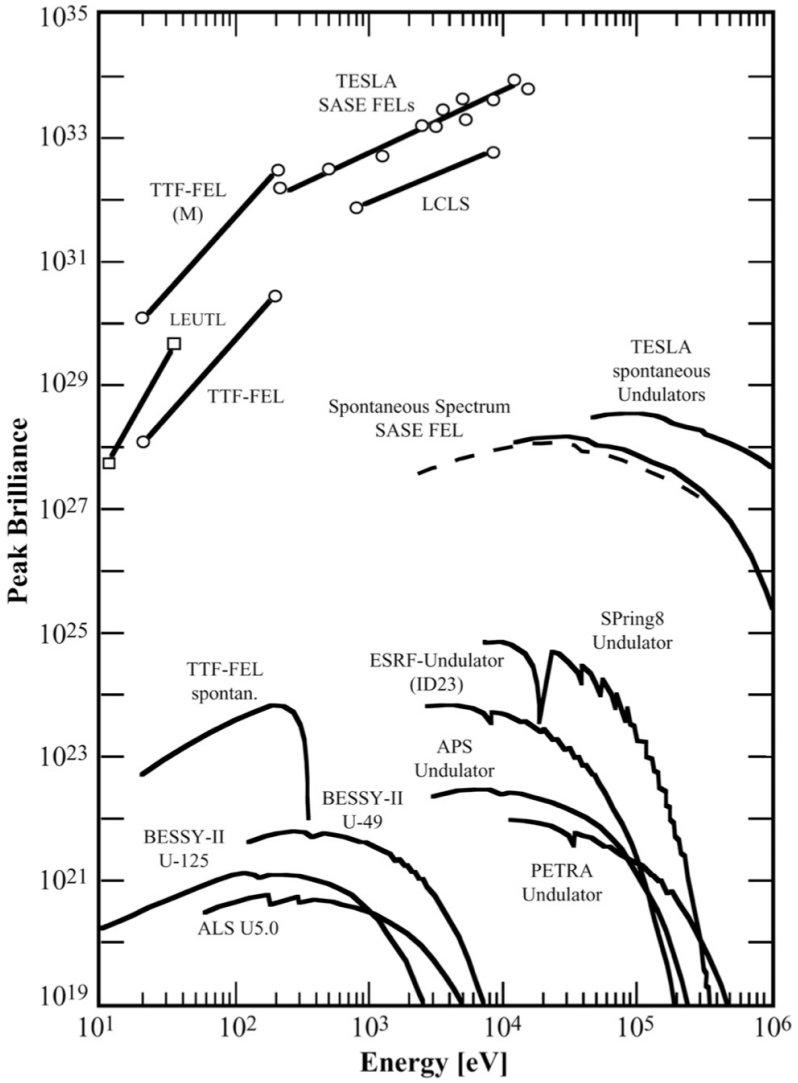


Figure 2.7: Plot from O'Shea & Freund [20] comparing the peak brilliance of various FEL and undulator sources.

to their penetrating power.

A second feature that makes the ESRF suitable for imaging studies is the so-called 'bunch structure', which refers to how the electrons are distributed around the storage ring. As the electrons orbit the ring, they are directed in a looped path with magnets, and naturally form distinct packets, known as 'bunches', in a self-correcting process [8]. The number of bunches can be finely controlled by the radio frequency (RF) voltage of the power supply, which evenly distribute around the ring (in time and space) so long as the RF is constant, since the electrons propagate along the ring at a fixed velocity. (For example, if the time taken for

one cycle is 1 μs and the RF supply is 500 MHz, 500 bunches will be generated [8].) At the ESRF, a single bunch has a temporal length of ∼100 ps, which is many orders of magnitude less than the time taken for a bunch to orbit the storage ring, approximately 2.8 μs, and short enough in duration to freeze even very fast moving interfaces in a shock experiment. For example, a shock front moving at 10 km/s would move 1 μm during the exposure. The effective pixel size (determined by the magnification) must therefore be greater than this displacement to avoid blurring in the images. In the present work the pixel size is 32 μm, meaning blurring is not an issue when illumination is from a single X-ray pulse.

At the ESRF there are three primary bunch structures [21, 22]: (i) 4-bunch, (ii) 16-bunch, and (iii) 'continuous fill', which is actually 992 bunches (other more complex modes are sometimes used, but they are not relevant here). Choosing which bunch structure to use for the experiments involves determining how to obtain the maximum number of frames without 'ghosting' appearing in the radiographs, which is caused by a camera capturing the scintillator emission from more than one X-ray pulse illumination (the additional illuminations appear as 'ghost' outlines in the radiograph when interfaces are moving significantly between frames). This is not simply a matter of having the inter-frame time less than the time between bunches, since the scintillator has a characteristic emission decay time of 30 ns [15], far greater than the 100 ps length of an individual X-ray pulse, and close to the time between bunches (of the order 100 ns for high-speed imaging applications). In the present study, 16-bunch mode is chosen, as the time between each electron bunch in the lab reference frame, and therefore each X-ray pulse also, is 176 ns [21, 22]. This means that frame rates over 1 Mfps can be captured while also being able to avoid ghosting between frames — by contrast, the inter-bunch time in 992 bunch continuous fill mode is 2.8 ns, which would cause significant ghosting if used to illuminate shock studies.

A third advantage the ID19 beamline has for imaging studies is the high level of

phase contrast enhancement that can be achieved, due to large the source-to-sample distance of approximately 150 m [19], compared to the source size of approximately 135 μm×25 μm [19]. This results in a high level of spatial coherence, which is required for PCI. As demonstrated by the images of a hair by Rack et al. [23] in the literature review (Section 1.2.7 of Chapter 1), the contrast at edges and interfaces in a radiograph are enhanced by interference between the X-rays after phase changes have occurred while interacting with the material [24, 25]. This form of PCI is known as propagation-based PCI, since all that is required to achieve edge enhancement is the propagation of the X-rays in the first Fresnel diffraction zone after passing through an object [26]. This principle is further explained by a diagram in Fig. 2.8 from Wilkins et al. [25]. In diagram a of Fig. 2.8a an object Ω is illuminated with a parallel beam of X-rays, which, as shown in diagram b, causes a phase difference $\phi(x)$ at location x in the plane normal to the X-rays. Diagram c shows the first derivative $\partial\phi/\partial x$ (thin line) and second derivative $\partial^2\phi/\partial x^2$ (thick line). Most notable is the sharp increase in $\partial^2\phi/\partial x^2$ at the spatial locations corresponding to the edge of Ω. This is a key result, since, in the Fresnel diffraction region, the X-ray intensity after interacting with object is dependent only on the second derivative of $\phi(x)$ [26]. Therefore, sharp changes in density are enhanced simply by the X-rays propagating in free space. The effect of this is demonstrated in Fig. 2.8b, which shows the size of the interference fringes at the edge increasing with detector distance from the object Ω.

To achieve optimum edge enhancement with propagation-based PCI, the sample-to-detector distance must be tuned, based on the mean X-ray energy λ and pixel size of the detector [27]. In the first Fresnel diffraction zone, interference fringes that form have a characteristic spacing D, given by,

$$D \approx \sqrt{\lambda z}, \tag{2.4}$$

where λ is the X-ray wavelength and z is the propagation distance. For the ex-

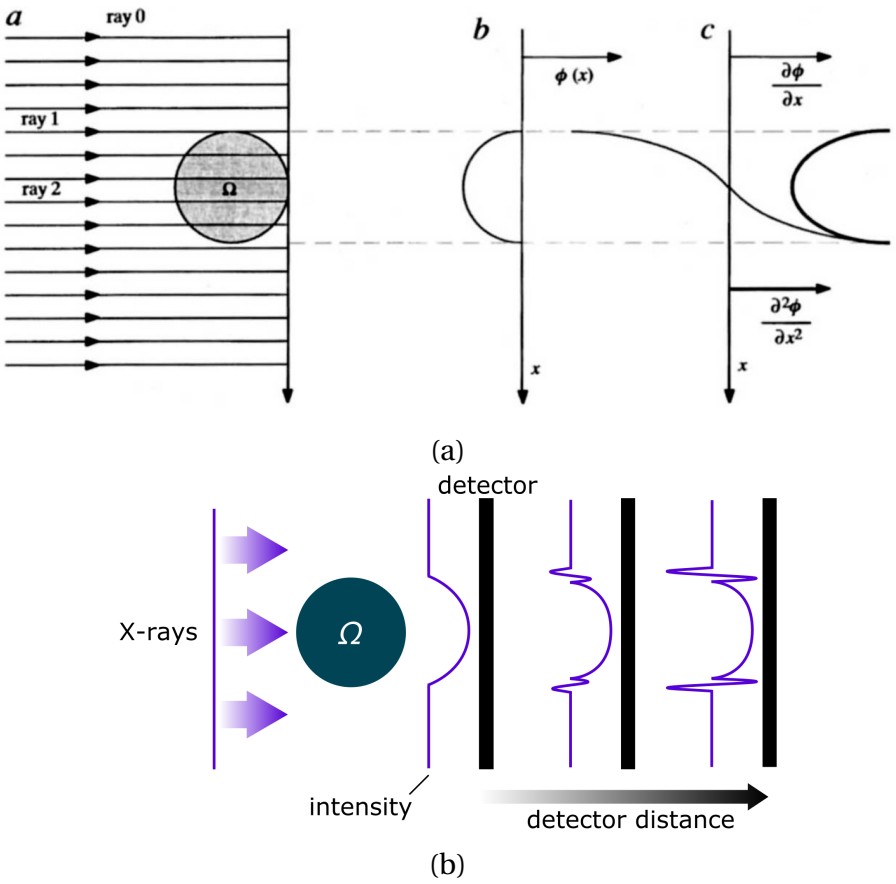


Figure 2.8: (a) Diagram of polychromatic X-ray PCI, from Wilkins et al. [25]. *a* An object Ω is illuminated with a parallel beam of X-rays. *b* The phase $\phi(x)$ of the X-rays at spatial locations x, after interacting with the object. *c* First derivative (thin line) and second derivative (thick line) of $\phi(x)$. (b) A diagram showing how edge contrast of an X-ray image of object Ω is enhanced by increasing the sample-to-detector distance is increased.

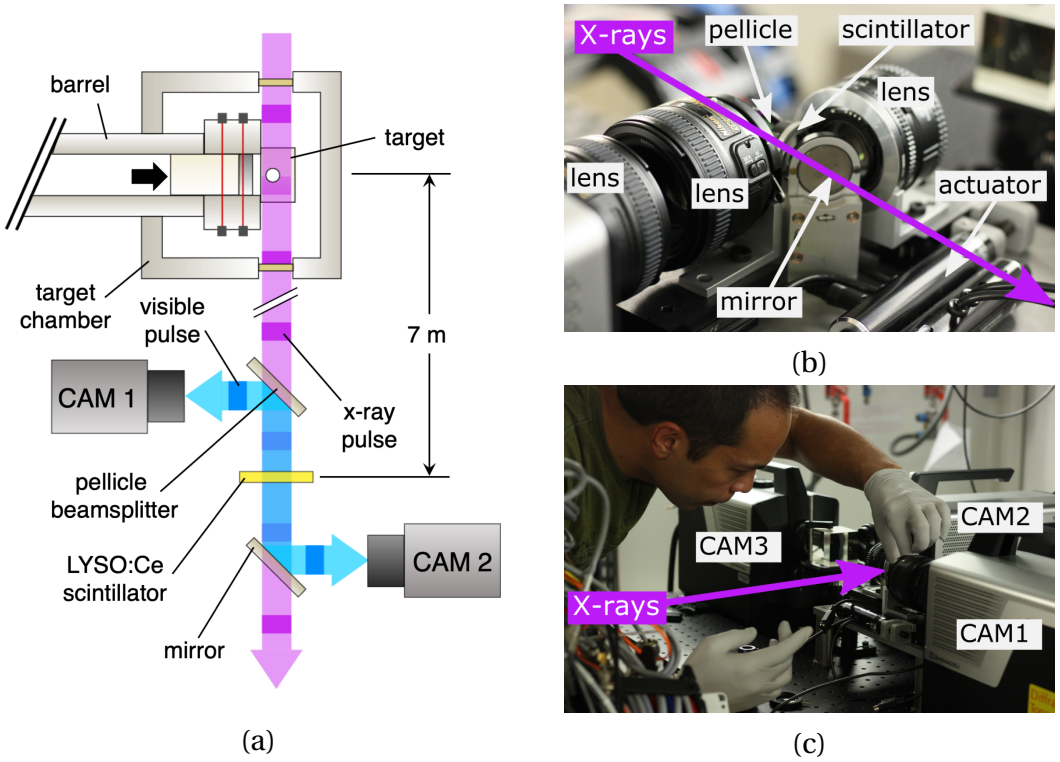
periments, a z value of 7 m is chosen and the mean λ for the polychromatic X-ray source is 0.28 Å (see spectrum in Chapter 3). This gives a D of approximately 14 µm, which, as we shall see in the following Section, is significantly less than the detector pixel size of 32 µm. Therefore, large distortions of edges that can occur when the interference fringe spacing is large relative to the detector pixel size are avoided [24, 25].

2.2.3 The imaging system

Due to the evolving complexity of the imaging system, different imaging systems are used for the single-stage and two-stage gas gun experiments. The final iteration of the system, along with further modifications and technical assessment, are presented in the instrumentation paper, in Chapter 3. Presented here is a more detailed specification of the imaging system used for the two sets of gas gun experiments.

The Shimadzu HPV-X2 camera is used to record the experiments, which is well suited for capturing highly dynamic experiments like shock impact. The camera has a high-speed CMOS burst image sensor, with a 400×250 pixel array and a 32×32 µm pixel size [28]. However, even with this camera it is not possible to capture every consecutive X-ray pulse when the synchrotron is operating in 16-bunch mode. This is because the maximum frame rate of the camera is 2 Mfps when in adjustable mode, equal to an inter-frame time of 500 ns, with inter-frame times higher than this adjustable in 10 ns increments. There is a 10 Mfps (100 ns) operating mode, but this is fixed. Based on the inter-bunch time constraint of 176 ns, it is chosen to operate the camera at an inter-frame time of 530 ns, which is within 2 ns of the time between three bunches/X-ray pulses of 528 ns (3×176 ns). The consequences of this drift with regards to ghosting effects are discussed below.

An HPV-X2 camera is permanently on-site at ESRF beamline ID19, and is used



(a) (b) (c)

Figure 2.9: The imaging system used for the dynamic radiography experiments. (a) A schematic diagram of the setup (not drawn to scale), (b) a close-up photograph of the components around the scintillator, and (c) a photograph of the three-camera arrangement.

for the single-stage gas gun experiments. For the two-stage gun experimental campaign, a second camera is borrowed from First Light Fusion Ltd., one of the co-sponsors of this project. Figure 2.9a shows a schematic diagram of the two-camera arrangement: the X-rays pass through the target chamber and through the cavity target region normal to the direction of impact, and propagate a further 7 m, where a portion of the X-rays are absorbed and re-emitted in the blue part of the the visible spectrum by a LYSO:Ce (Ce-doped $Lu_{1.8}Y_{0.2}SiO_5$, Hilger Crystals UK) scintillator, which has a decay time of 41 ns [15]. The emission in the downstream direction (direction of X-ray propagation) is folded away from the X-ray beam path with a 1' Thorlabs PF10-03-P01 silvered planar mirror and captured by Camera 1, and the upstream emission is likewise folded toward Camera 2, instead with a 1' Thorlabs BP145B5 300-400 nm pellicle beam splitter. For the single-stage experiments only Camera 2 is used.

Annotated photos of the 3-camera setup (discussed in Chapter 3) are shown in Figs. 2.9b&c. The lenses used are Nikon f/1.4 (0.36 NA) 50 mm, and are arranged in pairs for each camera in a 1:1 configuration, giving a field-of-view equal to the sensor dimensions of 12.8 mm$\times$8.0 mm. Focusing on the image plane is achieved through the fine adjustment of the lens that is not attached to the camera, via the remote control of an actuator. Each camera captures 128 frames with an exposure of 200 ns (the minimum at that frame rate) and, as mentioned above, an inter-frame time of 530 ns. However the inter-frame time of the captured images is that of the illumination frequency, 528 ns. Thus, the image sequences captured with a single camera have a frame rate of 1.89 Mfps and the two camera sequences – once interleaved – have dual frame rates of 2.84 Mfps and 5.68 Mfps, since every third X-ray illumination is not captured.

A consequence of the 2 ns $(530 - 128)$offset, is that there is a drift in the 'phase', ϕ, between the cameras and X-ray pulses, that changes by 2 ns every frame. This principle is explained in the diagram of Fig. 2.10, which shows how the camera

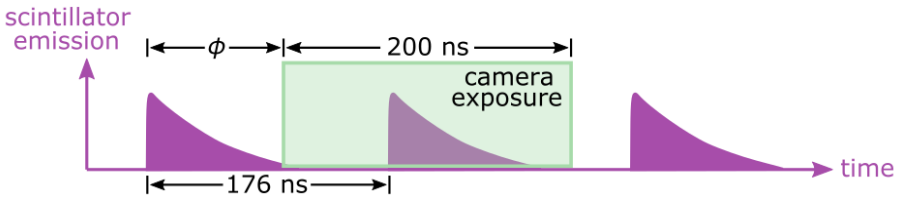


Figure 2.10: Diagram showing the phase difference ϕ between the start of each scintillator emission and the camera exposure.

exposure aligns the scintillator emissions, which have a decay time ~40 ns. The diagram demonstrates the ideal case, in which the 200 ns exposure window primarily captures the emission from a single scintillator emission. However, over the 128 frames, the phase ϕ will shift by over 250 ns, meaning the exposure window will slide along and capture the emission from a second scintillator. The proportion of the sharing of signal between the emissions, which varies between a ratio of ~99:1 and 50:50, will determine the level of ghosting in the radiograph. The exposures must be aligned to the emissions at the time when the event is expected to take place, thus keeping the ghosting ratio high for the frames that contain important data. This is achieved through a synchronisation system, as explained in the following Section. Further details on the imaging system are given in Chapter 3.

For one of the two-stage gas gun experiments, an additional Invisible Vision UHSi-24 framing camera is employed for the purpose of imaging the rear of the target (opposite the impact face). This allows the optical emission from cavity collapse to be captured, which occurs in the strong shock regime when a toroidal plasma forms. The camera is focused on the target's rear using a mirror, and the target surface is polished to ensure the emission is unobscured. The results of this additional imaging, along with the cavity collapse radiography results and analysis, is presented in Chapter 4.

2.2.4 Synchronisation

For imaging slow-moving phenomena at low frame rates, it is possible to treat the synchrotron X-rays as a continuous source, without having to take into account ghosting effects. This is the case so long as interfaces move less than approximately one pixel per frame. However, capturing high-speed radiography using the illumination of X-ray pulses from a single electron bunch, and when interfaces are moving around 1 km/s or more, it is important for each frame to primarily capture the scintillator emission from a single X-ray pulse. In this way ghosting between frames is avoided.

In order to understand the importance of synchronisation for capturing the experiments, it is first instructive to consider the timeline of events. An overview of the timeline is shown in the diagram of Fig. 2.11 (not been drawn to scale). The experiment is initiated by triggering the system, that opens a shutter inside the experimental hutch, known as the 'fast' shutter because of its quick response time. The main 'slow' shutter, which is not linked to the triggering system, is opened before this and can only be operated once the experimenters have evacuated the experimental hutch. The fast shutter remains open for 350 ms to allow time to capture the experiment, but not so long as to impose a significant heat load on the scintillator ot target. The gas gun system is fired approximately 50 ms later, by which time the fast shutter has fully opened. After the projectile breaks the light gate, impact of the target marks the start of the event, lasting between 10-20 μs depending on the experiments. The continuously produced pulsed X-rays from the synchrotron are let in to the hutch when the shutters are open, with each pulse separated by 176 ns. The scintillator emissions are therefore at the same rate. The imaging system is triggered when the light gate signal is broken, and is synchronised to the scintillator emission pulses with a signal provided by the synchrotron: the 'radio frequency 16' (RF16) gives the rate of X-rays pulses when the synchrotron is operating in 16-bunch mode. This signal allows

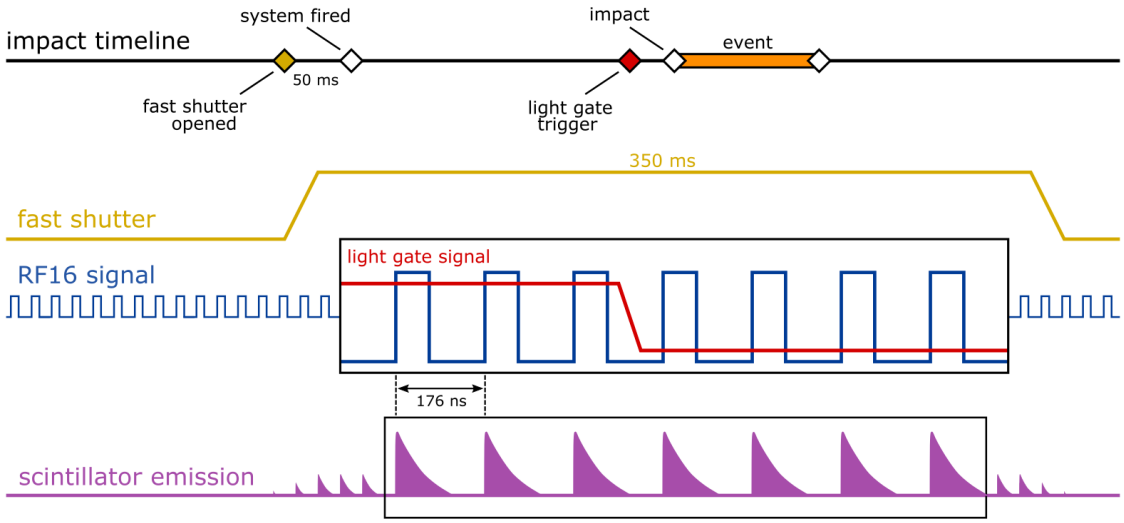


Figure 2.11: Diagram giving an overview of the experimental timeline. The fast X-ray shutter is opened upon triggering the system, followed by a 50 ms delay before the gun system is fired. The fast shutter closes automatically after 350 ms, during which time impact occurs and the event is recorded. The RF16 signal and scintillator emission are both pulsed at intervals of 176 ns, and the breaking of the light gate signal before impact triggers the synchronisation system.

fine-tuning of the synchronisation between the imaging system and scintillator emission. In this Section, the setup and operation of the synchronisation system is explained.

Synchronisation poses a technical challenge, requiring a system of oscilloscopes and delay generators. A schematic diagram of the cabling for this system is shown in Fig. 2.12, with the connections between components denoted by lines and the directionality of the signals indicated with arrows. All of the cabling used to connect between components is BNC coaxial. The setup shown is the particular arrangement for the two-stage gas gun experimental campaign, where two Shimadzu cameras record the radiographs (X-CAM1 and X-CAM2), and one camera records the visible light emission from the rear of the cavity (V-CAM).

Image acquisition is timed relative to (i) the time just before projectile impact, which is measured by a light gate trigger some distance away from the impact face (10s of mm), and (ii) the fixed time reference of the synchrotron RF time period. As mentioned above, RF16 is the signal indicating the rate of X-ray pulses in

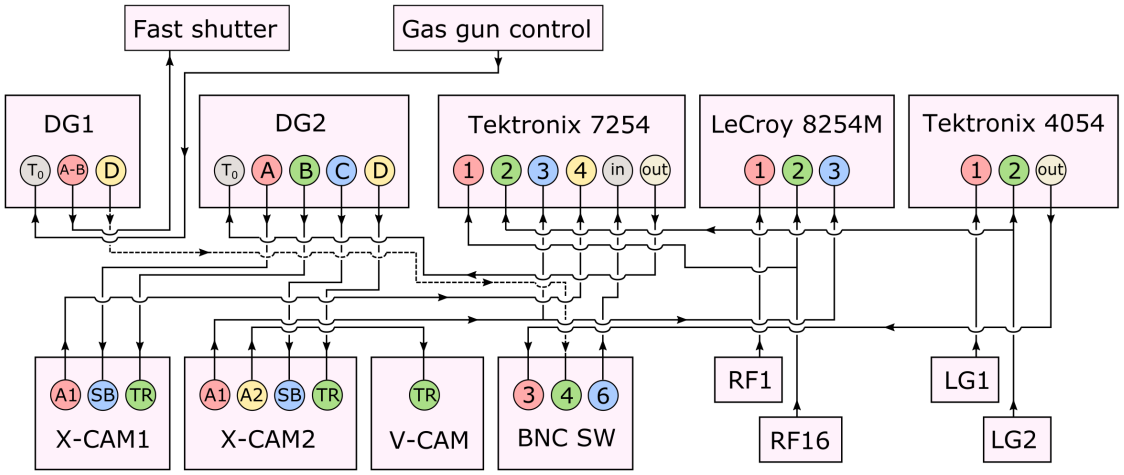


Figure 2.12: Schematic wiring diagram of the systems used to synchronise the cameras to the X-ray pulses, and the instruments used to record experimental data. The dashed line from the delay generator DG1 port D to BNC SW port #4 is the cable for simulating a trigger generated by the breaking of light gate 2 (LG2).

16-bunch mode. There is also another useful signal for the rate of a given bunch to circle the storage ring, known as 'RF1', since it is the time between X-ray pulses for 1-bunch mode. The signals for both of these RFs in beamline ID19 is delivered by optical fibres into the bunch clock delay unit (BCDU), and are denoted in Fig. 2.12. The $\sim$1 ms uncertainty of the gas gun firing, is vastly greater than the RF signal and synchronisation components, which are of the order nanoseconds.

The diagram of Fig. 2.12 shows the key components of the system for synchronisation. Three oscilloscopes are used: the Tektronix 4054 (1 GHz, 5 GS/s), Tektronix 7254 (2.5 GHz, 40 GS/s) and LeCroy 8254M (2.5 GHz, 40 GS/s). The oscilloscopes record traces of signals from the three cameras, two light gates (LG1 and LG2) and RFs (RF1 and RF16). In order to precisely capture the timeline of events, it is necessary to have the same signal recorded on multiple oscilloscopes. Thus the cable from LG2 to Tektronix 4054 port #2 is branched to Tektronix 7254 port #2. Moreover, the cable from RF16 to LeCroy 8254M port #2 is branched to Tektronix 7254 port #1. In this way the timing of each oscilloscope relative to the others can be determined to within a few ns of uncertainty. Input and output signals with delays can be generated using oscilloscopes only, but it is more compact

and cheaper to use delay generators (DGs) for this purpose. For the setup shown, two are used, DG1 and DG2. A photograph of the system, as constructed for the two-stage gas gun experiments, can be seen in Fig. 2.13, which has an additional small and portable oscilloscope ('scope'), for testing signals inside and outside of the experimental hutch. When the gas gun is fired from 'gas gun control', a signal is sent to DG1 port T_0, which outputs two signals after pre-determined time delays. Port A-B outputs a signal to the fast shutter, allowing X-rays to enter the hutch.

A trigger level of approximately 50% is set on the signal of LG2, which is recorded on Tektronix 4054 port #2 and triggered when the light gate is obscured by the projectile leaving the gun barrel. Port 'out' subsequently gives a signal to the Tektronix 7254 oscilloscope via the BNC switch box (BNC SW), for which the logic is controlled in LabVIEW. The LeCroy 8254M oscilloscope is triggered from port #3 when a signal is received from the X-CAM1 Aux 1 ('A1') port at the start of its recording. The logic of synchronising the X-ray cameras to the X-ray pulses is performed in the Tektronix 7254, which also receives the RF16 signal, and then outputs a signal to DG2 port T_0. Ports A and C output signals to X-CAM1 and X-CAM2 to their 'SB' ports to initiate standby, followed by a further delayed signal from ports B and D for their triggers via ports'TR'. X-CAM1 and X-CAM2 output monitor signals from their A1 ports, which are recorded on the Tektronix 7254 port #4 and LeCroy 8254M port #3, respectively. V-CAM is triggered by the signal from X-CAM2's A2 port and has no monitoring signal in this setup. Frame times for this camera are therefore calculated relative to X-CAM2. Frame rates and additional delays may be given to the cameras on the computers controlling them. To test trigger the system, a cable is connected from DG1 port D to Tektronix 7254 port 'in', via BNC SW to mimic the firing of the gas gun control system. The logic for BNC SW is changed such that the incoming signal is from port #4 (instead of #3 during the experiments), which then outputs the usual signal to the Tektronix 7254 port 'in', which initiates the camera triggering.

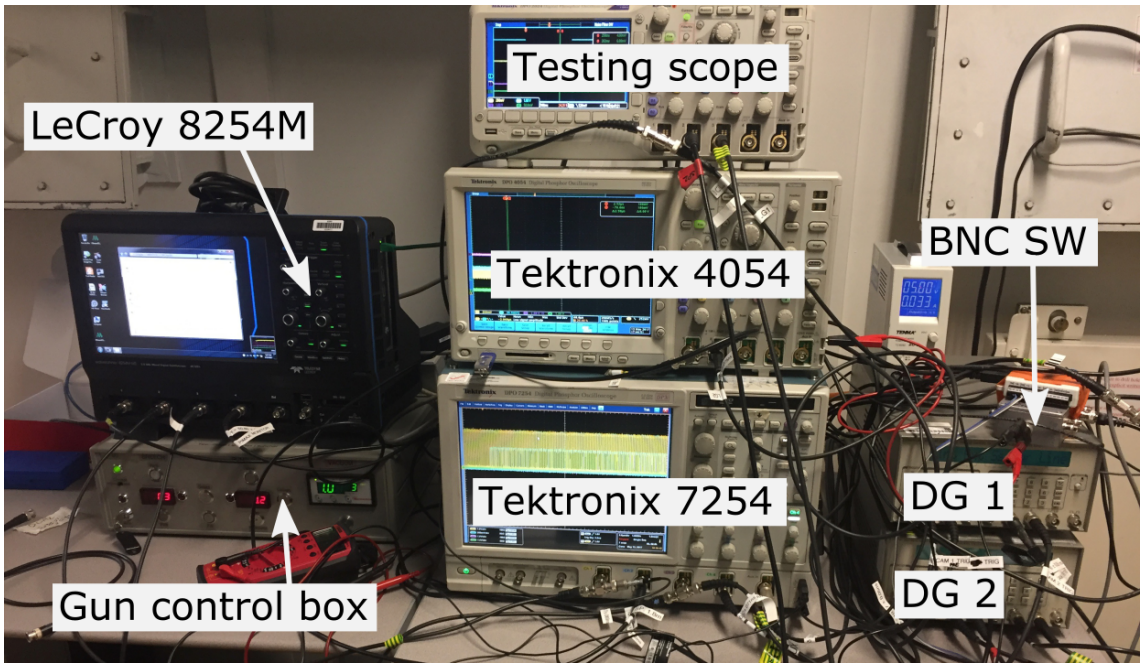


Figure 2.13: Photograph of the synchronisation system at beamline ID19, with the gas gun control box, oscilloscopes ('scopes'), delay generators (DGs) and BNC switch (BNC SW).

The time taken for a signal to travel along a BNC cable, known as the 'cable delay' is calculated beforehand to within 0.01 ns, and is approximately 5 ns per metre of BNC cabling. Internal delays of the oscilloscopes, delay generators and cameras are also measured beforehand. Thus, timing in the experiment can be determined to within a few ns if needed. However, in the present work, the key timing is the relative time between radiographs captured, which, as discussed above, is determined by the RF.

A considerable technical challenge for this experiment is the complexity of the organisation, transportation and setup of the various gas gun and synchronisation components. With the exception of the LeCroy 8254M oscilloscope and some of the BNC cabling, all of the equipment is taken from the home UK lab to the ESRF in France. Upon arrival, in collaboration with the beamline ID19 researchers headed by Dr Alexander Rack, the systems must be constructed, tested and calibrated. This process must be repeated for each experimental campaign, since the equipment is returned to the UK after the experiments are completed.

The experiments are conducted in a tight window of time over a period of days, which are allocated by the ESRF beforehand. As the X-rays are produced 24 hours per day, experimenters work in shifts around the clock to obtain as much data as possible. This study on dynamic cavity collapse is one of many such experiments conducted during the campaigns, under the supervision of group head Dr Daniel Eakins.

2.3 Analytical methods

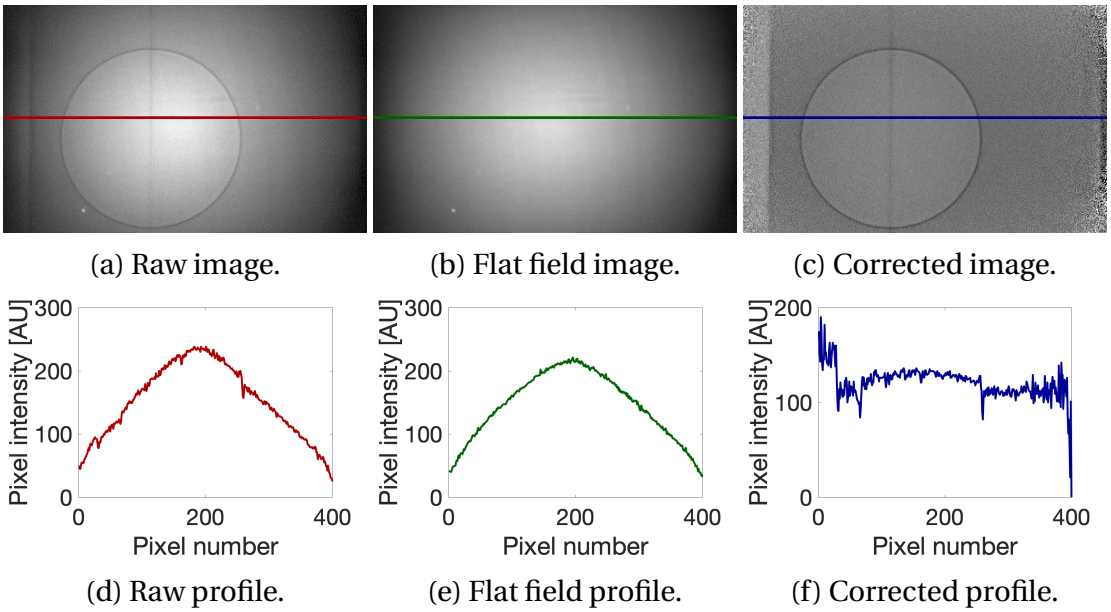
2.3.1 Image processing and data extraction

In its raw format, the radiographic image data obtained from the experiments is simply a greyscale 2D matrix of numbers that represent the value of light intensity recorded at a given pixel location. To extract meaningful information from the images, it is necessary to process the images and then apply transformations and algorithms like edge detection. In this section these processes are explained.

Flat field correction

Flat field correction is a process to correct for intensity from non-uniform illumination and sensor artefacts (from malfunctioning pixels, for example), which increases the quality of extracted data. The process to go from a raw image R to a corrected image C is achieved by taking a dark field image D, without an object or any illumination, and a flat field image F, with illumination but no object. By taking image D, the baseline of the pixels are accounted for, and by taking F non-uniform illumination and artefacts are accounted for. The following expression is used to produce the corrected image,

$$C = \frac{(R - D) * m}{(F - D)}, \tag{2.5}$$



(a) Raw image. (b) Flat field image. (c) Corrected image.

(d) Raw profile. (e) Flat field profile. (f) Corrected profile.

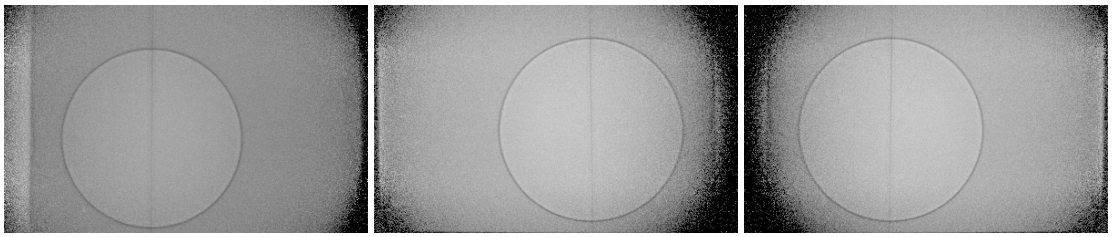
Figure 2.14: Images of a stationary 6 mm diameter cavity showing the benefit of flat field correction. The first column shows the raw image and line profile across the middle of the image. Similarly, the second and third columns show the image and line profile for the flat field and corrected image, respectively.

where m is an average value of the difference $(F - D)$ [8]. The subtractions and division are performed pointwise. The Shimadzu HPV-X2 camera used for the experiments has an in-built feature whereby the dark field is removed before the raw file is output. This means that the process of removing the dark field, which is usually used for image processing, is not necessary, and the expression is simplified to,

$$C = \frac{R}{F} * m. \tag{2.6}$$

Figure 2.14 shows the effect flat fielding has on the intensity profile of an image. The line profile of the raw image and flat field image have a similarly bell-shaped profile. This is due to the larger intensity at the centre of the X-ray beam, a standard feature of synchrotron radiation [8].

After dividing the raw image by the flat field image, the appearance of the corrected image is altered compared to the original raw data. The clearest expression of this is the removal of the vignetting at the edges, which is the result of the uneven illumination. This is reflected in the line profile of the corrected image,



(a) Camera 1 image. (b) Camera 2 image. (c) Camera 2 image flipped.

Figure 2.15: Images of a stationary 6 mm diameter cavity showing the left-right flipping transform, which must be performed on all of the camera 2 images. In (a) is shown a camera 1 image for reference, and (b) and (c) show the camera 2 image before and after the transform, respectively.

which now gives the true relative intensity. The precise values of the intensity, which are determined by the factor m, are not important for the image analysis used in the present work, namely edge detection. The disadvantage of using flat field correction is the introduction of noise, which is especially evident in the regions of low intensity in the raw image, namely the lateral edges. This means there is an increase in noise in some regions of the images. Fortunately, in the vast majority of the data recorded the size of the cavity and cavity position relative to the noisy regions is such that extracting data from edge positions is possible.

Image transforms

When more than one camera is used, the field of view for each camera is slightly different, despite great effort made to focus each camera on the same region of the scintillator. Since the frames from these cameras are interleaved in time, extracting displacements between frames requires transforming the images from one of the cameras (or more if using more than two cameras) relative to the camera designated as the 'reference' frame. Figure 2.15 shows a necessary first step sometimes required: flipping the image left-right. Camera 2 captures frames flipped in this way relative to camera 1 because it observes the opposite side of the scintillator.

After flipping all of the camera 2 images, they must be registered relative to cam-

era 1 such that the features in the image are spatially matched. The necessity of this process is shown in Fig. 2.16a, which shows a 'false-colour' representation of a camera 1 image and camera 2 image overlapped. The cavity perimeter is shifted significantly, which would render quantitative analysis erroneous. An affine 2D transformation is performed on the 'moving' camera 2 images, in order to align them relative to the 'fixed' camera 1 images. This transformation is represented by the matrix T,

$$T = \begin{bmatrix} s_x & 0 & 0 \\ 0 & s_y & 0 \\ t_x & t_y & 0 \end{bmatrix}, \tag{2.7}$$

where s_x and s_y are scale factors, and t_x and t_y are the displacements, in the x- and y-directions, respectively. By having 0 in the (3, 1) and (3, 2) components, it is assumed that there are no shear effects from the differences in image projection. The 0 components in (2, 1) and (1, 2) likewise assume there are no rotations. These assumptions are validated by the accuracy of the registration. The scale parameters are extracted by establishing the extreme perimeter positions in the x- and y-directions along the cavity edge, from the edge-extracted images of the cavity in a frame before deformation has started (details on edge extraction are given in the following section). From these coordinates, the following expressions are used to calculate the transform parameters.

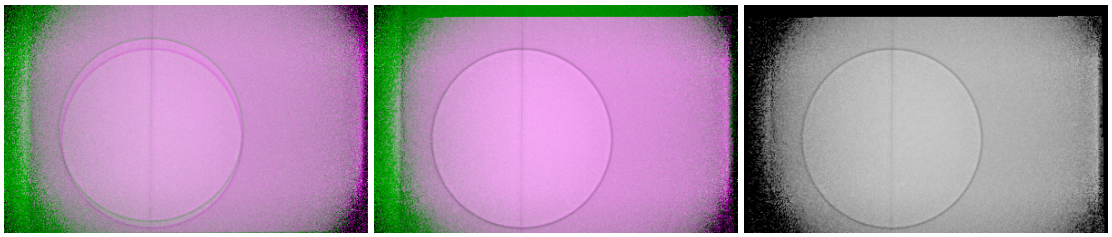
$$s_x = \frac{x_{max,f} - x_{min,f}}{x_{max,m} - x_{min,m}} \tag{2.8}$$

$$s_y = \frac{y_{max,f} - y_{min,f}}{y_{max,m} - y_{min,m}} \tag{2.9}$$

$$t_x = x_{max,f} - s_x.x_{max,m} \tag{2.10}$$

$$t_y = y_{max,f} - s_y.y_{max,m} \tag{2.11}$$

The f and m subscripts denote the fixed and moving image coordinates, respectively. The scripts to process the images are written in Matlab, with the registra-



(a) Pre-registration alignment.

(b) Camera 2 registered image.

(c) Post-registration radiograph.

Figure 2.16: Images of a stationary 6 mm diameter cavity showing the registration of the flipped camera 2 images with respect to the camera 1 images. The pink regions in (a) and (b) show areas of agreement, whereas the green regions show areas of large difference. In (c) the black region at the top are regions of the image lost in the registration process.

tion transformation performed using the `imwarp()` function [29].

After registration, the cavity perimeters are aligned, as demonstrated in Fig. 2.16b. However, there is a cost to this process: regions of data are lost when the image is transformed. This is seen as a black strip along the top perimeter of the image, as in Fig. 2.16c. Fortunately, this did not impact the extraction of data in the present work, as the cameras are already close to alignment and the cavity perimeter did not occupy the blackened region in any of the experiments. A different transform matrix T is calculated for each experiment, to allow for slight changes in camera alignment. The matrix elements are obtained from a stationary frame, before the cavity undergoes deformation, and then applied to the other frames of that experiment.

Edge detection

To track the time evolution of interfaces in the radiographs, it is necessary to use an edge detection algorithm. The `edge()` function in Matlab fulfils this purpose, and the 'Canny' method [30] is chosen. Although many other methods exist, the Canny method is an established and reliable. In the Canny algorithm, a Gaussian filter is applied to smooth the image and prevent the detection of false edges. A negative consequence of this is the suppression of weak but real edges, but this



(a) Low threshold. (b) High threshold. (c) Appropriate threshold.

Figure 2.17: Examples of a of a stationary 6 mm diameter cavity radiograph image after being processed with the Canny edge detection algorithm. In (a) the threshold is set too low, whereas in (b) it is set too high. In (c) we see the appropriate threshold to resolve the cavity perimeter.

is not an issue when applied to the phase-contrast enhanced edges in the radiographs. Next, the intensity gradients in the image are identified, after which weak edges are suppressed and then a threshold applied to identify the remaining edges. An upper and lower threshold is applied, from which 0.4 times that value is automatically taken as the lower threshold.

The output of the `edge()` function is a binary image of the same dimensions as the input image, with zeros (black) at the pixel locations where no edge is detected and ones (white) where an edge is found. Figure 2.17 shows the output with different threshold values. Too low a threshold, as in Fig. 2.17a, and the number of edges detected is too high, producing a noisy output that obscures in features of interest. The opposite is seen in Fig. 2.17b, where the threshold is too low. In this case the cavity interface has not been detected at all. At appropriate threshold, as in Fig. 2.17c, the cavity interface has been detected and there are a small number of features that can be cropped out or removed with little effort. The appropriate threshold level varies from experiment to experiment, and must be judged by eye.

2.4 Computational methods

Numerical simulations of the cavity collapse experiments are performed using two codes. Firstly, in Chapter 4 a small number of simulations are performed us-

ing the code Hytrac, to investigate the dynamics when material strength is not accounted for, since it does not contain a strength model. Second, in Chapter 5 the code SCIMITAR3D – which does contain a strength model – is used to simulate the experiments, along with simulations of cavity collapse in additional materials.

Both codes employ an underlying Eulerian grid that is modelled with a hyperbolic solver to capture the behaviour of the material away from edges. They also both use a separate Lagrangian technique to capture material interfaces and edges, but differ in the method to do so. The individual interface capturing schemes for each code and other unique aspects will be detailed at the end of this Section. First, the common features will be covered,

2.4.1 Governing equations

For high strain rate applications, the stress can be written as the sum of the volumetric (dilatational) and shear (deviatoric) components:

$$\sigma_{ij} = S_{ij} - P\delta_{ij}, \tag{2.12}$$

where S_{ij} is the shear stress tensor, P is the hydrostatic pressure and δ_{ij} is the Kronecker delta. Consequently, the response of the material can be split into two sets of governing equations [31]: (i) the volumetric response is determined by an equation of state (EoS), such as the Mie-Grüneisen [32] or Tillotson [33] EoS's; (ii) the shear response obeys a conventional flow theory of plasticity, such as the Johnson-Cook model [34], developed by G. R. Johnson and W. H. Cook [35]. Hytrac does not contain a strength model, and therefore only uses an EoS.

In an Eulerian formulation, the material points are not followed, meaning, in addition the EoS and plasticity theory, the flow of the material also needs to be calculated. This material flow, along with the axisymmetric shear deformation, is

determined from a set conservation laws, whereas the volumetric stress is obtained from the EoS [31]. However, front tracking is performed in the front's frame of reference, meaning the Lagrangian form of the conservation must still be considered. The differential form of these conservation laws, cast in both the Eulerian and Lagrangian reference frames, are as follows [2, 36].

Conservation of mass

Eulerian form:
$$\frac{\partial \rho}{\partial t} + \frac{\partial (\rho u_i)}{\partial x_i} = 0 \tag{2.13}$$

Lagrangian form:
$$\frac{D\rho}{Dt} + \rho \frac{\partial u_i}{\partial x_i} = 0 \tag{2.14}$$

Here ρ is the density, u_i are the components of velocity, t is time and x_i are the spatial coordinates. The 'total derivative' in the Lagrangian form, is denoted by D/Dt instead of d/dt, to avoid confusion with the partial time derivative $\partial/\partial t$. The full expression of the total derivative in index notation is,

$$\left(\frac{D}{Dt}\right)_L = \left(\frac{\partial}{\partial t}\right)_E + u_i \frac{\partial}{\partial x_i}, \tag{2.15}$$

where the $_E$ and $_L$ subscripts denote the Eulerian and Lagrangian derivative forms, respectively [36].

Conservation of momentum

Eulerian form:
$$\frac{\partial (\rho u_i)}{\partial t} + \frac{\partial (\rho u_i u_j - \sigma_{ij})}{\partial x_j} = 0 \tag{2.16}$$

Lagrangian form:
$$\rho \frac{Du_i}{Dt} - \frac{\partial \sigma_{ij}}{\partial x_j} = 0 \tag{2.17}$$

In addition to the previously defined variables, the stress tensor σ_{ij} is used.

Conservation of energy

Eulerian form:
$$\frac{\partial(\rho E)}{\partial t} + \frac{\partial(\rho E u_j - \sigma_{ij} u_i)}{\partial x_j} = 0 \tag{2.18}$$

Lagrangian form I:
$$\rho \frac{DE}{Dt} + \rho E \frac{\partial u_j}{x_j} - \frac{\partial \sigma_{ij} u_i}{\partial x_j} = 0 \tag{2.19}$$

Lagrangian form II:
$$\frac{dE}{dt} + P\frac{dV}{dt} = 0 \tag{2.20}$$

Finally, the specific total energy $E = e + \frac{1}{2} u_i u_i$ is introduced, where e is the specific internal energy. The second Lagrangian form is obtained by considering the first law of thermodynamics and assuming a reversible adiabatic process ($dS/dt = 0$) [36].

2.4.2 Hytrac

The front-tracking aspect of Hytrac is based on an previously developed front-tracking code, FronTier [37], which has been successfully applied to shock-cavity interactions in a liquid, in both 2D and 3D [38, 39]. For the present work, 2D axisymmetric simulations of shock-induced cavity collapse in PMMA are performed. In Hytrac, a lower-dimensional Lagrangian grid is defined as a series of vertices joined together by piecewise linear interpolation, and laid over the Eulerian mesh, with each point on the front having two thermodynamic states either side of the front [39]. The code solves each iteration in two steps, treating the Eulerian and Lagrangian aspects separately. For more details on Hytrac and FronTier, see Hawker & Ventikos [39] and Glimm et al. [37]. The specifics of the Hytrac simulation setup and equation of state used to model the cavity collapse

experiments are given in Chapter 4.

2.4.3 SCIMITAR3D

Both 2D plane strain and 3D simulations are performed in SCIMITAR3D, a simulation code developed by Prof. H. S. Udaykumar and his group at the University of Iowa. SCIMITAR3D was developed specifically to model phenomena that occur during impact, namely large deformations, nonlinear wave propagation, and shocks, while still being able to capture the constitutive properties and resolve multiple interfaces interacting during impact [31, 40–42]. The code has already been successfully used to model cavity collapse [43–46].

To be able to handle high-velocity impact scenarios and void-material interface regions, such as the study of shock-induced cavity collapse in the present work, a mixed Eulerian-Lagrangian approach is employed. As for Hytrac, the Eulerian grid is fixed, but rather than an interpolated series of nodes for the interface, Lagrangian particles are distributed along interfaces between materials (and voids) to capture the interfaces and ensure they remain sharp [40]. Further details of the code can be found in works by Udaykumar et al. [40], Tran & Udaykumar [31] and Sambasivan et al. [42]. In Chapter 5 the material models and geometries used in the SCIMITAR3D simulations are presented.

2.5 References

[1] E M Escauriza, J P Duarte, D J Chapman, *et al.*, "Collapse dynamics of spherical cavities in a solid under shock loading," *Sci. Rep.*, vol. 10, pp. 1–16, may 2020.

[2] N K Rai, E M Escauriza, D E Eakins, and H S Udaykumar, "Mechanics of shock induced pore collapse in poly(methyl methacrylate) (PMMA): Comparison of simulations and experiments," *J. Mech. Phys. Solids*, vol. 143, 2020.

[3] E M Escauriza, A Rack, E Synchrotron, *et al.*, "Ultra high-speed indirect X-ray imaging system with versatile spatio-temporal sampling capabilities," *Appl. Opt.*, vol. 57, no. 18, pp. 5004–5010, 2018.

[4] M A Meyers, "Experimental Techniques: Methods to Produce Dynamic Deformation," in *Dyn. Behav. Mater.*, ch. 12, pp. 296–321, 1994.

[5] S L Milora, S K Combs, M J Gouge, and R Kincaid, "Quickgun: An Algorithm for Estimating the Performance of Two-Stage Light Gas Guns," *ORNL/TM–II561*, 1990.

[6] S K Combs, C R Foust, D T Fehling, *et al.*, "Repetitive two-stage light gas gun for high-speed pellet injection," *Rev. Sci. Instrum.*, vol. 1978, 1991.

[7] S A Sheffield and A R Martinez, "New LANL group M-7 two-stage gun: Double diaphragm and wrap-around gas breech," Tech. Rep. 9, 1992.

[8] P Willmott, "Synchrotron Physics," in *An Introd. to Synchrotron Radiat.*, ch. 3, pp. 39–86, John Wiley & Sons, Ltd, 2011.

[9] D E Eakins and D J Chapman, "X-ray imaging of subsurface dynamics in high-Z materials at the Diamond Light Source," *Rev. Sci. Instrum.*, vol. 85, no. 12, 2014.

[10] M A Meyers, "Shock Waves," in *Dyn. Behav. Mater.*, ch. 4, pp. 98–122, New York: John Wiley & Sons, Inc., 1994.

[11] S P Marsh, "LASL Shock Hugoniot Data," tech. rep., University of California Press, 1980.

[12] G R Gathers, "Rarefaction Waves," in *Shock Wave Phys. Equ. State Model.*, pp. 65–95, 1994.

[13] T Hatsui and H Graafsma, "X-ray imaging detectors for synchrotron and XFEL sources," *IUCrJ*, vol. 2, pp. 371–383, 2015.

[14] A Rack, F García-Moreno, L Helfen, *et al.*, "Hierarchical radioscopy using polychromatic and partially coherent hard synchrotron radiation.," *Appl. Opt.*, vol. 52, no. 33, pp. 8122–7, 2013.

[15] M E Rutherford, D J Chapman, T G White, *et al.*, "Evaluating scintillator performance in time-resolved hard X-ray studies at synchrotron light sources," *J. Synchrotron Radiat.*, vol. 23, no. 3, pp. 685–693, 2016.

[16] B J Jensen, "LANL DCS Activities, Highlights and Perspectives," in *DOE/NNSA DCS Rev. Sept. 20-21, 2016*, pp. 1–23, 2016.

[17] M E Rutherford and D E Eakins, "LuI 3 Scintillator Decay Measurements at ESRF (September 2016)," no. September, 2016.

[18] P Tafforeau, R Boistel, E Boller, *et al.*, "Applications of X-ray synchrotron microtomography for non-destructive 3D studies of paleontological specimens," *Appl. Phys. A Mater. Sci. Process.*, vol. 83, no. 2, pp. 195–202, 2006.

[19] T Weitkamp, P Tafforeau, E Boller, *et al.*, "Status and evolution of the ESRF beamline ID19," *AIP Conf. Proc.*, vol. 1221, no. 2010, pp. 33–38, 2010.

[20] P G O'Shea and H P Freund, "Free-electron lasers: Status and applications," *Science (80-.).*, vol. 292, no. 5523, pp. 1853–1858, 2001.

[21] R Dimper, H Reichert, P Raimondi, *et al.*, *The Orange Book: ESRF Upgrade Programme Phase II (2015-2022)*. 2015.

[22] "Characteristics of Beam Modes at the ESRF, www.esrf.fr/Accelerators/Operation/Modes," tech. rep.

[23] A Rack, S Zabler, B R Müller, *et al.*, "High resolution synchrotron-based radiography and tomography using hard X-rays at the BAMline (BESSY II)," *Nucl. Instruments Methods Phys. Res. Sect. A Accel. Spectrometers, Detect. Assoc. Equip.*, vol. 586, pp. 327–344, feb 2008.

[24] P Cloetens, R Barrett, J Baruchel, *et al.*, "Viewpoint on Phase objects in synchrotron radiation hard x-ray imaging," *J. Phys. D. Appl. Phys.*, vol. 29, pp. 133–146, 1996.

[25] S W Wilkins, T E Gureyev, D Gao, *et al.*, "Phase-contrast imaging using polychromatic hard X-rays," *Nature*, vol. 384, pp. 335–338, nov 1996.

[26] D M Paganin, "Coherent X-ray imaging," in *Coherent X-Ray Opt.*, ch. 4, pp. 228–340, 2006.

[27] T Weitkamp, D Haas, D Wegrzynek, and A Rack, "ANKAphase: Software for single-distance phase retrieval from inline X-ray phase-contrast radiographs," *J. Synchrotron Radiat.*, vol. 18, no. 4, pp. 617–629, 2011.

[28] Y Tochigi, K Hanzawa, Y Kato, *et al.*, "A Global-Shutter CMOS Image Sensor with Readout Speed of 1Tpixel/s Burst and 780Mpixel/s Continuous," *IEEE J. Solid-State Circuits*, vol. 48, no. 1, pp. 329–337, 2013.

[29] MATLAB, *9.9.0.1495850 (R2020b)*. Natick, Massachusetts: The MathWorks Inc., 2020.

[30] J Canny, "A Computational Approach To Edge Detection," *IEEE Trans. Pattern Anal. Mach. Intell.*, vol. 8, no. 6, pp. 679–714, 1986.

[31] L B Tran and H S Udaykumar, "A particle-level set-based sharp interface cartesian grid method for impact, penetration, and void collapse," *J. Comput. Phys.*, vol. 193, no. 2, pp. 469–510, 2004.

[32] M A Meyers, "Shock Waves: Equations of State," in *Dyn. Behav. Mater.*, ch. 5, pp. 124–151, 1994.

[33] J H Tillotson, "Metallic equations of state for hypervelocity impact," *Gen. At. Rep. GA-3216*, 1962.

[34] T J Holmquist and G R Johnson, "Determination of Constants and Comparison of Results for Various Constitutive Models," *Le J. Phys. IV*, vol. 01, no. C3, pp. C3–853–C3–860, 1991.

[35] G R Johnson and W H Cook, "A constitutive model and data for materials subjected to large strains, high strain rates, and high temperatures," *Proc. Seventh Int. Symp. Ballist.*, pp. 541–547, 1983.

[36] M A Meyers, "Differential form of conservation equations and numerical solutions," in *Dyn. Behav. Mater.*, ch. 6, pp. 152–178, New York: John Wiley & Sons, Inc., 1994.

[37] J Glimm, M J Graham, J Grove, *et al.*, "Front tracking in two and three dimensions," *Comput. Math. with Appl.*, vol. 35, no. 7, pp. 1–11, 1998.

[38] M R Betney, B Tully, N A Hawker, and Y Ventikos, "Computational modelling of the interaction of shock waves with multiple gas-filled bubbles in a liquid," *Phys. Fluids*, vol. 27, no. 3, 2015.

[39] N A Hawker and Y Ventikos, "Interaction of a strong shockwave with a gas bubble in a liquid medium: a numerical study," *J. Fluid Mech.*, vol. 701, no. 6, pp. 59–97, 2012.

[40] H S Udaykumar, L Tran, D M Belk, and K J Vanden, "An Eulerian method for computation of multimaterial impact with ENO shock-capturing and sharp interfaces," *J. Comput. Phys.*, vol. 186, pp. 136–177, 2003.

[41] A Kapahi, S Sambasivan, and H S Udaykumar, "A three-dimensional sharp interface Cartesian grid method for solving high speed multi-material impact, penetration and fragmentation problems," *J. Comput. Phys.*, vol. 241, pp. 308–332, 2013.

[42] S Sambasivan, A Kapahi, and H S Udaykumar, "Simulation of high speed impact, penetration and fragmentation problems on locally refined Cartesian grids," *J. Comput. Phys.*, vol. 235, pp. 334–370, 2013.

[43] N K Rai, M J Schmidt, and H S Udaykumar, "Collapse of elongated voids in porous energetic materials: Effects of void orientation and aspect ratio on initiation," *Phys. Rev. Fluids*, vol. 2, no. 043201, 2017.

[44] N K Rai and H S Udaykumar, "Void collapse generated meso-scale energy localization in shocked energetic materials: Non-dimensional parameters, regimes, and criticality of hotspots," *Phys. Fluids*, vol. 31, no. 016103, 2019.

[45] P Zhao, S Lee, T Sewell, and H S Udaykumar, "Tandem Molecular Dynamics and Continuum Studies of Shock-Induced Pore Collapse in TATB," *Propellants, Explos. Pyrotech.*, vol. 45, no. 2, pp. 196–222, 2020.

[46] N K Rai, O Sen, and H S Udaykumar, "Macro-scale sensitivity through mesoscale hotspot dynamics in porous energetic materials: Comparing the

shock response of 1,3,5-triamino-2,4,6-trinitrobenzene (TATB) and 1,3,5,7-tetranitro-1,3,5,7-tetrazoctane (HMX),” *J. Appl. Phys.*, vol. 128, no. 085903, p. 85903, 2020.

Chapter 3

Ultra-high-speed indirect X-ray imaging system with versatile spatio-temporal sampling capabilities

This chapter is based on the paper published in Applied Optics, "E M Escauriza, M P Olbinado, M E Rutherford, D J Chapman, J C Jonsson, A Rack and D E Eakins, *Ultra-high-speed indirect X-ray imaging system with versatile spatio-temporal sampling capabilities*, Applied Optics **57**, 8 (2018)" [1]. The experiments were performed by all of the authors, and all of the authors edited the manuscript. The aluminium lattice samples were provided by Fraunhofer EMI. From the ESRF, Dr Benoît Roche provided bunch current data and Dr Paul Tafforeau gave advice on the spectrum calculations. Dr David Paganin from the Monash University gave comments on versions of the paper manuscript. The gas gun and imaging systems were designed by Dr D E Eakins and Dr D J Chapman. The author performed spectral simulations, processed the images, created the figures and wrote the manuscript, under the supervision of Dr D E Eakins.

Paper abstract

A new generation of cameras has made ultra high-speed X-ray imaging at synchrotron light sources a reality, revealing new details of sub-surface transient phenomena. We introduce a versatile indirect imaging system capable of capturing – for the first time – hundreds of sequential X-ray pulses in 16-bunch mode at the European Synchrotron Radiation Facility, recording over dozens of microseconds at 5.68 Mfps , with an effective exposure of 100 ps. The versatile multiplex camera construction of the system allows for various arrangements, including different scintillator configurations, and simultaneous imaging with different resolutions and regions of interest. Image results from a gas gun impact experiment, in which an additive manufactured aluminium lattice was dynamically compressed, is presented as a demonstration of the system's capabilities.

3.1 Introduction

The demand for ultra high-speed (UHS) X-ray imaging (XRI) has come primarily from research fields that require *in-situ* X-ray measurements of ultra-fast processes. Here, UHS is defined as recording imaging data at greater than 1 million frames per second (fps) – for a general overview of UHS imaging, refer to [2]. Examples include direct measurements of sub-surface shock dynamics in diamond [3] and high-Z materials, such as additively manufactured (AM) stainless steel lattices [4]; shockwave distributions in granular materials [5]; explosion by plasma expansion during electric arc ignition in a fuse [6]; and crack propagation in glass [6, 7]. Tracking real-time changes in these experiments requires high temporal and spatial resolutions, as well as a high frame rate to capture the physical and chemical changes that evolve over the ns to ms timescales. A detailed

account of UHS XRI and its applications is given by Olbinado et al. [6].

For XRI experiments, there is a choice to be made between direct and indirect detection. Direct detectors offer a comparatively high quantum efficiency, and very low level of noise. However, direct detectors lack versatility and typically have a fixed coarse pixel size [8]. Furthermore, direct detectors are prone to heat and radiation damage from direct exposure in the X-ray beam path. Indirect detection systems offer an alternative solution, by utilising a scintillating screen that re-emits absorbed X-ray photons as visible photons, which are captured by a visible light detector [9]. The optical light path is frequently folded by a mirror away from the X-ray beam path toward lenses and a detector, such that they are not directly in the path of the X-rays (see diagram (a) of Fig. 3.1). The lack of direct X-ray exposure means the electronics of indirect systems avoid radiation damage. Another advantage of indirect detectors is their versatility: different magnifications can be achieved by simply changing the configuration of the optical lenses. Thus, with minimal adjustment, a large range of spatial resolutions can be achieved with a single indirect detector.

The steady pulse of high-intensity X-rays produced by the accelerated electrons in a synchrotron provide an ideal source for performing time-resolved XRI experiments, due to the high brilliance and partial spatial coherence that can be achieved. When operating in one of the so-called 'timing modes', the X-ray pulses are evenly spaced, due to the distribution of the electrons into tight 'bunches' around the synchrotron's storage ring. This bunching effect is caused by the timing of the energy boost they receive from the radio frequency power supply [10]. The number of electron bunches around the ring is denoted by the 'filling mode'. Current image sensor and scintillator technology allows the X-ray pulses originating from a single bunch to be captured, giving rise to the name 'single-bunch' XRI. The minimum effective exposure of a recorded XRI image is thus determined by the duration of a single X-ray pulse, which is given by the bunch

duration of ∼100 ps, and the maximum acquisition frame rate is determined by the separation time between consecutive bunches in a given filling mode (e.g. 153 ns in 24-bunch mode at the Advanced Photon Source (APS) [11] and 176 ns in 16-bunch mode at the European Synchrotron Radiation Facility (ESRF) [12]). Consequently, the maximum frame rate of an XRI image sequence recorded at a synchrotron is equal to the synchrotron's X-ray pulse repetition rate in a given filling mode.

Commercially available cameras used for UHS imaging include those with gated image intensifier charge-coupled device (ICCD) sensors. Such devices are capable of recording scintillator emissions from a single synchrotron X-ray pulse, with very short sensor exposure times (< 500 ps). However, at UHS frame rates, ICCD-based cameras are limited to a two-frame storage limit [13]. Cameras using a complementary metal oxide semiconductor (CMOS) sensor architecture are also capable of single-bunch imaging, but are limited to sub-100 kfps recording [7]. New-generation UHS cameras, which are capable of recording at rates exceeding 1 Mfps for multiple frames, employ *in-situ* storage to overcome the limitations of sensor read-out speeds. Using a new-generation UHS camera in combination with 16-bunch filling mode at ESRF beamline ID19, Olbinado et al. performed a single-bunch phase contrast imaging study to capture a 1.9 Mfps sequence of laser-induced shockwave propagation and cavity formation in water [6]. With a similar arrangement, Parab et al. recorded > 1 Mfps sequences of dynamic fracture in poly(methyl methacrylate) particles at APS beamline 32-ID-B [14].

To capture many sequential X-ray pulses using XRI at a synchrotron facility, a multiplex arrangement is necessary for both gated ICCD and new-generation cameras. Jensen et al. have used a multiplex setup consisting of four gated ICCD cameras – each capable of storing two images – to capture up to eight sequential single-bunch frames in 24-bunch filling mode at the APS dynamic compres-

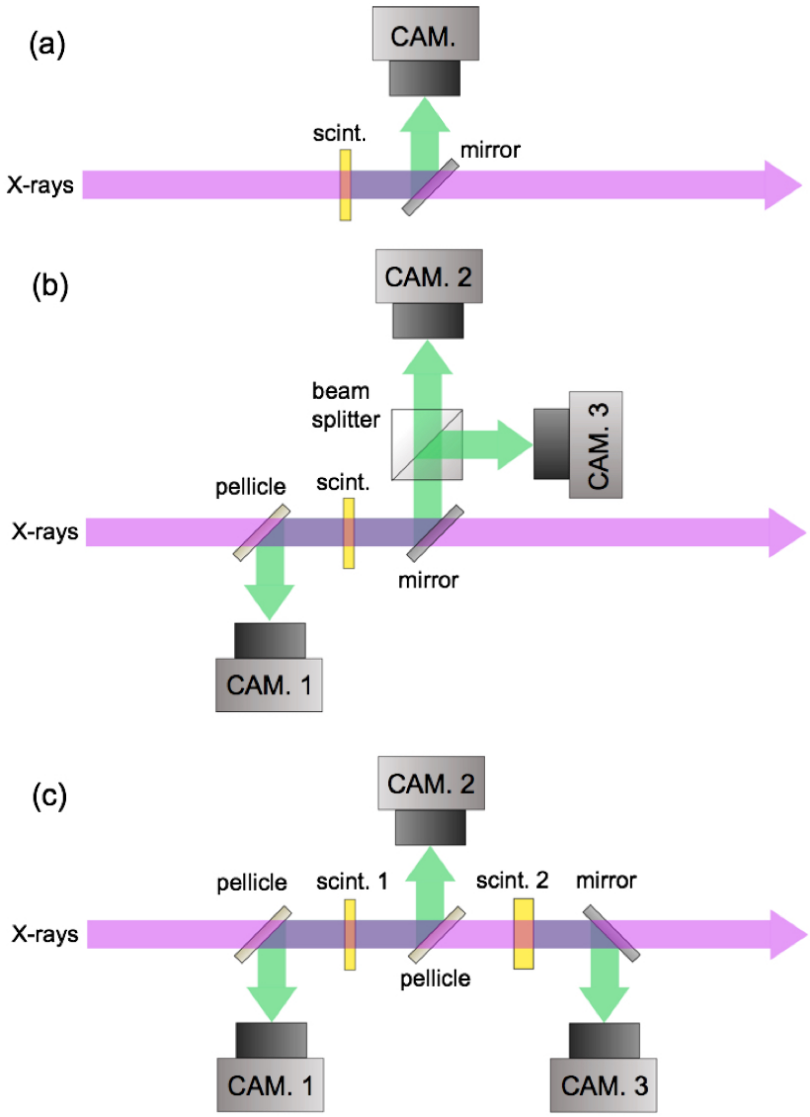


Figure 3.1: Diagrams showing three possible camera configurations for performing UHS XRI. (a) A single camera indirectly captures the luminescence from a single scintillator. (b) A three-camera configuration captures the luminescence from a single scintillator. The rear-surface luminescence is split into two optical beams with a 50:50 beam splitter. (c) The configuration used during the experiment presented in this article: a three-camera configuration utilising a 250 μm LYSO:Ce scintillator (scint. 1) and a 500 μm LYSO:Ce scintillator (scint. 2), placed 100 mm downstream of the first. The front- and rear-surface luminescence of the upstream scintillator is captured with two cameras via pellicle beam splitters, and the rear-surface luminescence of the downstream scintillator is captured with a third camera via a mirror.

sion sector (DCS) beamline 35-ID [15]. Their system also allows the simultaneous imaging of experiments at multiple magnifications, by using different lens configurations on each camera.

In this Chapter, we present a UHS XRI system consisting of three CMOS-based new-generation cameras. The system's unprecedented capabilities allow up to 384 single-bunch frames to be captured, with an inter-frame time equal to the inter-bunch time, when using 16-bunch mode at the ESRF. The versatile multiplex construction means it can also be used to simultaneously capture different magnifications and different scintillator emissions. Details of the system implementation and possible configurations are given in section 3.2 and example XRI images from a gas gun impact experiment of a dynamically compressed AM aluminium lattice are presented in section 3.3, with conclusions given in section 3.4.

3.2 Instrumentation

In order to capture sequential single-bunch images in 16-bunch mode at the ESRF, a multiplex camera system is used, consisting of three Shimadzu Hyper Vision HPV-X2 cameras. Each camera has a high-speed CMOS burst image sensor, with a 400×250 pixel array and a 32×32 μm pixel size [16]. In the maximum frame rate operation mode, the HPV-X2 camera is fixed to an inter-frame time of 200 ns (5 Mfps), and in adjustable frame rate mode the minimum inter-frame time is 500 ns (2 Mfps), adjustable in 10 ns increments. The inter-bunch time is 176 ns, meaning synchronisation between the cameras and the bunches is only possible if the inter-frame time for each camera is matched to an integer multiple of the inter-bunch time that is greater than 500 ns. Thus, with three HPV-X2 cameras, it is possible to capture every sequential bunch if each camera is triggered in sequence, with the inter-frame time set to 530 ns, which is close to the three-bunch separation time of 528 ns. The three sets of images are combined to

produce an image sequence with an effective frame rate of 5.68 Mfps. A possible arrangement of the three cameras can be seen in diagram (b) of Fig. 3.1, with the emission from a single scintillator shared between the cameras by exploiting its isotropic luminescence. The upstream scintillator luminescence is folded perpendicular to the X-ray path with a weakly attenuating thin-membrane pellicle beam splitter, toward the first camera (here, we define 'upstream' relative to the direction of X-ray propagation). The downstream luminescence is folded likewise with an optical mirror, then split by a 50:50 beam splitter and captured by the second and third cameras. A consequence of the 50:50 beam splitter arrangement is that the second and third cameras receive less than half of the light compared to the first, meaning signal in those images may be insufficient when imaging materials with higher levels of attenuation.

The arrangement used in the present study can be seen in diagram (c) of Fig. 3.1. Compared to the arrangement in diagram (b), the total light yield is increased by using a second in-line scintillator. For the experiment, two LYSO:Ce (Ce-doped $Lu_{1.8}Y_{0.2}SiO_5$, Hilger Crystals, UK) scintillators were used: one of 250 µm thickness, and a second of 500 µm thickness, placed 100 mm downstream from the first. LYSO:Ce has a comparatively short characteristic decay time, $\tau \approx 40$ ns, making it suitable for imaging high-speed XRI experiments. Other scintillators used for high-speed XRI are GAGG:Ce (Ce-doped $Gd_3Al_2Ga_3O_{12}$) and YAG:Ce (Ce-doped $Y_3Al_5O_{12}$), with characteristic decay times of 60 ns and 96 ns, respectively (an overview of scintillator performance in time-resolved XRI is given by Rutherford et al. [17]). The upstream and downstream luminescence of the 250 µm scintillator is captured with two cameras, via two Thorlabs BP145B5 1" 300-400 nm pellicle beam splitters, of 5 µm thickness, placed in the X-ray beam path. The downstream luminescence of the 500 µm scintillator is captured with a third camera via a mirror. Each camera is focused with a motorised 1:1 lens system, consisting of two Nikon f/1.4 (0.36 NA) 50 mm lenses, giving a field-of-view equal to the sensor dimensions of 12.8 mm $\times$ 8.0 mm.

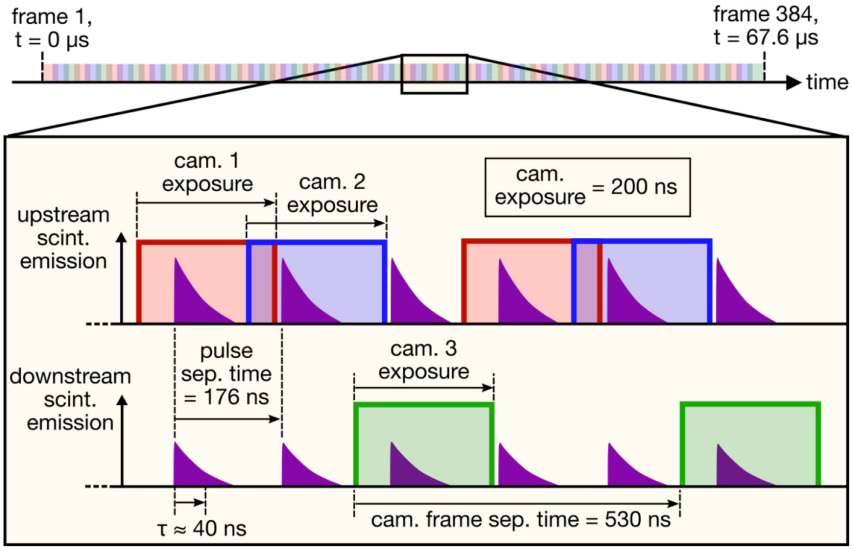


Figure 3.2: Diagram showing the timing and synchronisation between the three cameras and the two scintillator emissions. The combined 384-frame acquisition lasts for 67.6 µs, and is represented by the timeline at the top. An expanded section of the timeline shows the exposure times of the three cameras, which are all 200 ns, and how the intensity of the two scintillator emissions varies over time. Cameras 1 and 2 capture the front- and rear-surface emissions of the upstream scintillator, respectively, and camera 3 captures the front-surface emission of the downstream scintillator. The inter-bunch time of 176 ns, inter-frame time of 530 ns and the LYSO:Ce scintillator decay time of 40 ns are also shown.

A diagram showing the aforementioned three-camera sequencing, and synchronisation to the emissions of the two scintillators, can be seen in Fig. 3.2. A single acquisition records 384 frames for a total of 67.6 µs, with cameras 1 and 2 capturing the luminescence of the upstream scintillator and camera 3 capturing the luminescence of the downstream scintillator. The frame separation time of the cameras is set to 530 ns, such that each camera sequentially captures an image every third X-ray pulse.

The ESRF ID19 X-ray sources used are two U32 undulators operated at minimum gap widths of 11.1 mm and 11.5 mm, in order to maximise the spectral flux – a requirement for single-bunch XRI, as maximising the signal-to-noise ratio (SNR) is critical at such short exposures. A 1.4 mm diamond filter minimises the flux of X-rays with energies below 10 keV, thus limiting the heat load on the scintillators. The output spectrum after filtering can be seen in the plots (A1) and (B1) of Fig.

3.3. The mean photon energy is approximately 44 keV, with an integral photon flux density (IPFD) of 4.9×10^{15} photons/mm^2/s. The integral photon energy density (IPED) per X-ray pulse is 6.1×10^{-6} J/mm^2 (all calculations performed in XOP [18]).

The absorption and transmission spectra of the upstream 250 μm LYSO:Ce scintillator can be seen in plots (A2) and (A3) of Fig. 3.3, respectively. The mean absorbed energy is around 40 keV, and the absorbed IPFD is calculated to be 3.6×10^{15} photons/mm^2/s, giving an absorbed IPED per pulse of 4.1×10^{-6} J/mm^2. The absorption of the downstream 500 μm LYSO:Ce scintillator is shown in plot (A4) of Fig. 3.3. The mean energy of the downstream scintillator absorption spectrum is higher than for the upstream scintillator, at 55 keV. This increase is due to the 'beam hardening' effect, when lower-energy X-rays are absorbed by an object (in this case the upstream scintillator), which increases the mean energy of the transmitted spectrum relative to the incoming spectrum. The absorbed IPFD of the downstream scintillator is 1.0×10^{15} photons/mm^2/s, and the absorbed IPED per pulse is 1.5×10^{-6} J/mm^2. The consequences of the different absorption values of the two scintillators, with respect to the recorded XRI images, will be discussed in the following section.

3.3 Ultra high-speed radiography

The experiment, consisting of an impact target and gas gun projectile launcher, is placed approximately 150 m downstream from the source, with the impact direction perpendicular to the X-ray beam. The detector is placed a further 7 m downstream from the target, ensuring the images are in the propagation-based 'phase contrast' regime – interference between the X-rays after they pass through the target material increases the contrast of material edges and interfaces [19, 20]. As the X-rays propagate into the first Fresnel diffraction zone, interference fringes form, with a characteristic length given by $\sqrt{\lambda z} \approx 14$ μm (where $\lambda = 0.28$ Å

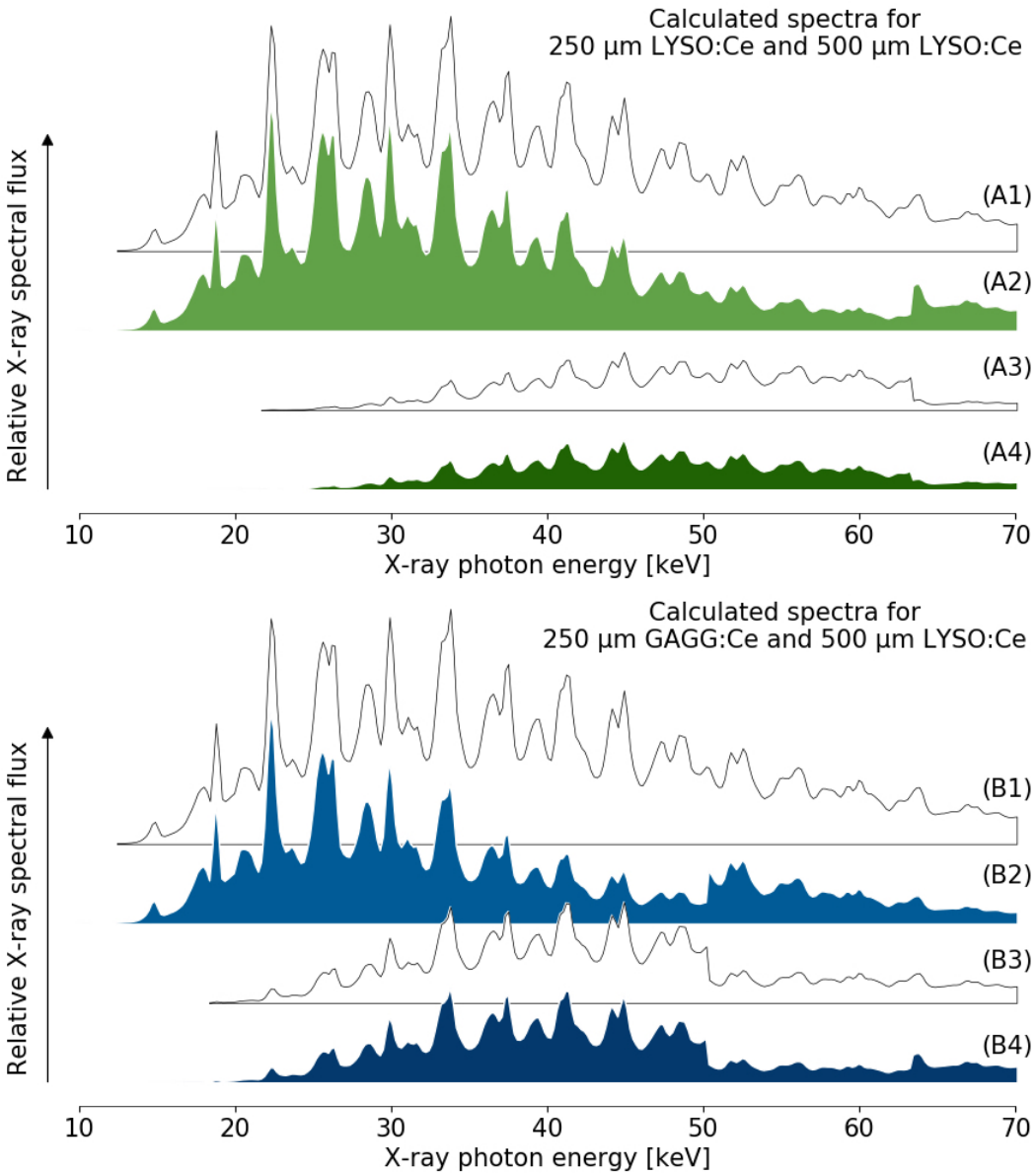


Figure 3.3: The predicted photon flux density spectra based on the absorption of filters and the LYSO:Ce and GAGG:Ce scintillators. All calculations have been performed using XOP [18]. Incoming spectra have been represented by a plot outline and absorbed spectra by a solid fill. Spectra A1 and B1 show the incoming source after filtering, spectra A2 and B2 show the absorption of the upstream scintillator, spectra A3 and B3 show the transmission of the upstream scintillator, and spectra A4 and B4 show absorption of the downstream scintillator.

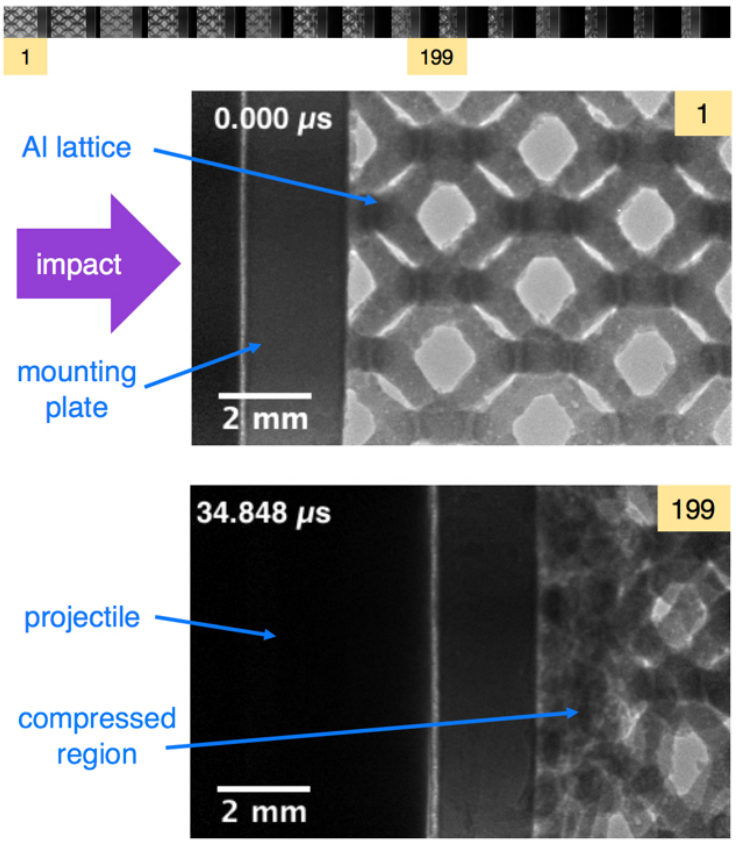


Figure 3.4: Single-bunch radiographs of the gas gun impact experiment, performed in 16-bunch mode at the ESRF. The images are taken from a 384-frame, 5.68 Mfps image sequence. The top row of smaller images are separated by 22 frames, starting from frame 1. The larger images show frames 1 and 199. Frame 1 shows the details of the target: an AM aluminium lattice built onto a 2 mm thick aluminium plate is impacted from the left at 160 m/s by a projectile tipped with a 3 mm thick aluminium flyer plate. Frame 199 shows the details of the impact: compression of the lattice is visible in the right of the images, and the darkened region on the left is the highly-attenuating projectile.

is the mean X-ray wavelength and $z = 7$ m is the target-to-detector distance). Therefore, with a pixel size of 32 μm, and with the main features of the object being significantly larger than the characteristic length, the edge contrast in the recorded images is enhanced, while preserving the attenuation projection of the target.

The example application shown in this Chapter is a dynamic compression experiment, in which an AM aluminium lattice was impacted with a gas gun projectile. Such an experiment typically involves *in-situ* optical and surface measurements, and *ex-situ* analysis of the target after impact. Synchrotron UHS XRI systems

now enable the *in-situ* tracking of subsurface phenomena, with a 100 ps effective exposure per image. Hawreliak et al. [21] and Branch et al. [22] performed UHS XRI impact studies on AM polymer lattices at APS, capturing up to eight frames per impact. Our three-camera system extends the capabilities of UHS XRI, with each camera capturing up to 128 frames per experiment. The combined 384-frame image sequence has an inter-frame time of 176 ns (equivalent to 5.68 Mfps), allowing the tracking of phenomena as they evolve over dozens of μs. As well as gas gun impact studies, other applications for this versatile imaging system include laser shock [23], crack propagation [6, 7] and laser powder bed fusion [24].

Single-bunch radiographs from the experiment are shown in Figs. 3.4&3.5, taken from a 384-frame, 5.68 Mfps image sequence. The images have been normalised to highlight features, meaning grey levels should not be taken to represent absolute intensity. Phase-contrast is evident in the images as bright fringes at material interfaces. The time stamps are relative to the first image, and are separated by the inter-bunch time of 176 ns. Fig. 3.4 shows the details of the impact: the lattice target, which is shown stationary in frame 1, is built onto a 2 mm thick aluminium plate. The target is impacted from the left with a 3 mm thick aluminium flyer plate at 160 m/s. Deformation at a later time can be seen in frame 199. Changes between the images evolve slowly, with the fastest details in the material crossing approximately one of the 32 μm pixels every image (equivalent to a velocity of 180 m/s).

Recalling diagram (c) of Fig. 3.1, Fig. 3.5 shows three sequential radiographs, each captured with a different camera. Frames 67 and 68, captured with cameras 1 and 2 via the thinner upstream scintillator, show similar levels of contrast and signal. The contrast in frame 68 is approximately twice the contrast in frame 69, which was captured with camera 3 via the thicker downstream scintillator. This is due to the beam hardening effect discussed in the previous section. The

X-ray spectrum that reaches the second scintillator experiences lower attenuation from the target material, because of its higher average energy. Thus, the contrast between the sample and the unattenuated sections is lower in the resulting images. Furthermore, the noise level in frame 69 is higher than in frames 67 and 68, due to a ∼63% decrease in the absorbed energy of the downstream scintillator relative to the upstream scintillator. This is represented in the images captured via the different scintillators – the average pixel count of frame 69 is ∼64% less than in frame 68. According to the statistics of the Poisson noise in the images, the SNR scales with $\sqrt{N}$, where N is the number of visible photons detected (this scales with the total energy of X-ray photons absorbed by the scintillator). Our SNR measurements confirm this to be the case, with a ∼43% decrease in SNR when comparing frame 68 to frame 69. Despite this drop, the SNR in frame 69 is sufficient to distinguish features in the radiographs. However, for as the thickness or Z-value for a chosen sample increase, there will be a point where insufficient signal can be obtained to produce an image.

The two-scintillator multiplex arrangement has the advantage of fully utilising the X-ray flux, with ∼75% of the spectrum first attenuated by the 250 µm scintillator, after which ∼80% of the remaining, harder spectrum is attenuated by the 500 µm scintillator. This results in ∼95% total X-ray absorption. Furthermore, the pellicle beam splitters allow the isotropic luminescence of the scintillators to be exploited without further attenuating the X-rays, thus maximising the total signal yield for each image. This setup is therefore ideal for single-bunch imaging of ultra-fast processes when the maximum light yield is desired. Diagram (b) of Fig. 3.1, where every camera captures the emission from a single scintillator, would be suitable for experiments where it is required to have the same incoming X-ray spectrum for each image. This setup would also be suitable in experiments for which light yield is not a concern, e.g. for weakly attenuating samples or for longer exposures.

With both the two-scintillator and single-scintillator arrangements, it is possible to incorporate a fourth camera. In the former case, by capturing the front-surface luminescence of the second scintillator, and in the latter case, by splitting the upstream emission with a 50:50 beam splitter. In principle, it is also possible to incorporate more cameras, through further splitting of the optical beams, as demonstrated by Jensen et al. [15], with their four-camera, gated ICCD arrangement. They also showed an additional capability of a multiplex imaging system: the magnification of each camera can be customised by altering its lens configuration, allowing simultaneous UHS XRI of processes with multiple resolutions and regions of interest. This 'hierarchical' approach has also been demonstrated by Rack et al. [25].

The plots (B1)-(B4) of Fig. 3.3 show the predicted spectra for an alternative scintillator arrangement, in which a 250 μm GAGG:Ce scintillator replaces the 250 μm LYSO:Ce upstream scintillator. The IPED absorbed by GAGG:Ce per pulse is ∼26% less than LYSO:Ce, and the K-edge positions for GAGG:Ce and LYSO:Ce are 50 keV and 64 keV, respectively. These two factors result in an approximate ∼65% increase in photon energy absorption of the downstream scintillator for the GAGG-LYSO setup, when compared to the LYSO-LYSO setup used during the experiment. Additionally, the difference in absorbed IPED per pulse of the two scintillators is smaller for the new setup, with the upstream scintillator absorbing 3.0×10^{-6} J/mm^2 and the downstream scintillator absorbing 2.5×10^{-6} J/mm^2. From the ∼18% decrease in signal that this expected to produce (relative to the upstream scintillator), we predict that the decrease in SNR will be ∼9% for the GAGG-LYSO setup. This is a significant improvement when compared to the signal and SNR differences of ∼64% and ∼43%, respectively, for the LYSO-LYSO setup used in the experiment.

Furthermore, we predict that the difference in contrast between the images obtained on the different scintillators will be smaller, because the predicted mean

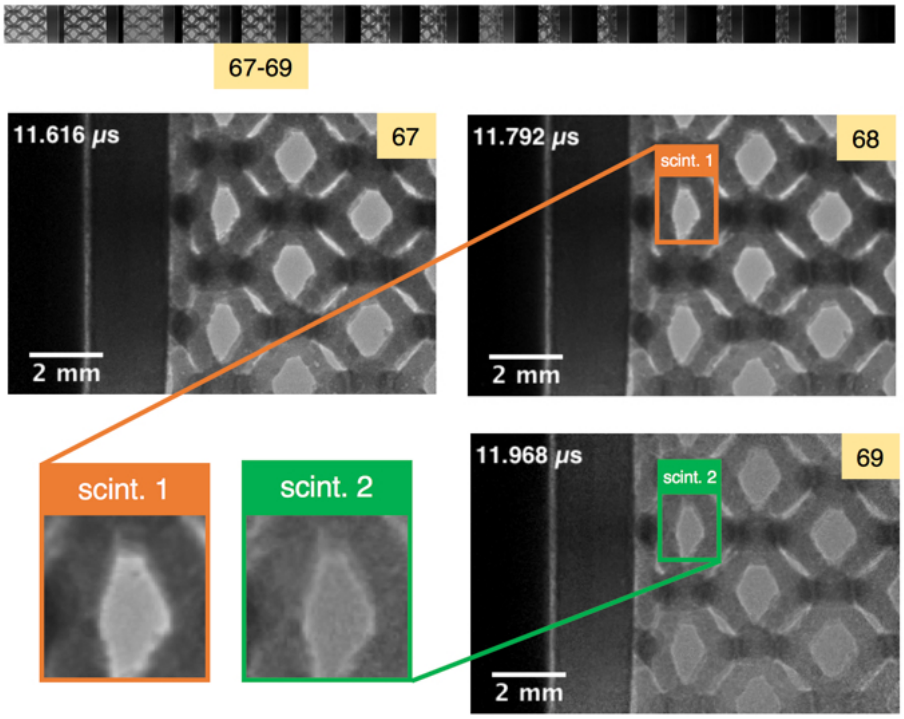


Figure 3.5: Single-bunch radiographs from the experiment. The top row of smaller images are separated by 22 frames, starting from frame 1. The larger images show frames 67-69. The inter-frame time is equal to the inter-bunch time of 176 ns. Frames 67 and 68 were captured by cameras 1 and 2, respectively, via the upstream 250 μm scintillator. Frame 69 was captured with camera 3 via the downstream 500 μm scintillator. Sections from frame 68 and 69 have been enlarged to highlight the difference in contrast from the two scintillators.

energy absorption between the two scintillators in the GAGG-LYSO setup is less, at 11 keV, compared to 15 keV in the LYSO-LYSO case. The improvements in SNR difference and contrast will likely result in combined radiograph sequences with a more uniform image response, which is key in experiments that require higher levels of consistency between the images, such as when looking at thicker samples with lower signal. It should be noted, however, that in the images captured via the GAGG:Ce scintillator, there is the potential introduction of ghosting effects. This would be due to the longer characteristic decay time of the GAGG:Ce luminescence, when compared to LYSO:Ce [17].

Another potential advantage of a two in-line scintillator arrangement is the hardened X-ray spectrum observed by the second scintillator, which could also be used in studying composite materials with high-Z inclusions. Different scintilla-

tor combinations may be used to increase this difference. With the lower-energy portion of the transmitted spectrum removed by the first scintillator, higher levels of transmission through high-Z regions of the sample will be visible in the images recorded via the second scintillator. Using two scintillators of varying composition also presents the opportunity to generate two images of a dynamic event simultaneously, with different absorption characteristics. For experiments involving attenuation measurements, such as density calculations, this arrangement would increase the amount of information recorded per event.

In the experiment presented, the extended recording time of the imaging system has been demonstrated, with the impact spanning the majority of the frames. The extended recording capability will also be beneficial when investigating the onset of rapid (<1 μs) failure processes in brittle materials, such as the fracture of ceramics [26] and adiabatic shear band formation [27], where, due to the complexity of the system the impact-to-failure time may be uncertain. In such cases, a full 384-frame recording can be made, centred on the predicted event time, thus increasing the probability of capturing the event.

However, the 5.68 MHz frame rate capability is not fully demonstrated by the presented experiment, since only small changes are visible between frames. Experiments involving events with faster time evolution will exploit the high frame rate, when it is crucial to use a single bunch per image, because of blurring that occurs if two X-ray pulses are captured per camera exposure (e.g. blurring of size 176 μm will occur for an object travelling at 1 km/s). Examples of faster processes that could be imaged with this system include crack wave propagation in silicon [28] and supersonic jet formation in aluminium [29]. Though, as the speed of objects imaged increases, the portion of the frames providing data will decrease (e.g. an object travelling at 2 km/s will cross the field of view in 34 frames). Future advances in scintillator and detector technology may allow single-bunch imaging in 'uniform' fill mode at the ESRF, which operates with 992 bunches and an

inter-bunch time of 2.8 ns. This would give a frame rate of 352 MHz, and allow for the extended recording of objects travelling many km/s.

For synchrotron imaging, vast improvements in resolution and frame rate can be made before the limit of the 100 ps effective exposure is reached. This is because, at present, there is a three orders of magnitude difference between the 176 ns inter-bunch time and the 100 ps effective exposure. For example, the detector resolution would have to approach 1 μm for blurring to be significant, if imaging an object moving at 10 km/s. It is also worth mentioning that, with a frame rate of 5.68 MHz, the system is also compatible with the timing of the bunch-trains at the European XFEL (Hamburg, Germany) where fs-short X-ray pulses are available at a frequency of 4.5 MHz [30].

3.4 Conclusions

We have demonstrated a newly-developed indirect UHS XRI system with a highly versatile multiplex construction. With this imaging system, it is now possible to capture sequential bunches over extended periods in 16-bunch mode at the ESRF. The three-camera, two-scintillator setup is capable of producing image sequences at 5.68 Mfps for 67.6 μs, recording a maximum of 384 frames. As a proof-of-concept, results from a gas gun experiment using the imaging system have been presented, in which an AM aluminium lattice was dynamically compressed. The limitations of the system and the scope for future improvements in synchrotron UHS XRI have been considered in the context of the image results.

The pros and cons of the two-scintillator setup have been discussed, with comparisons between the radiographs from each scintillator. Despite a reduction in SNR and contrast in the images recorded from the second scintillator, the values were still sufficient to provide data on the compression dynamics of the lat-

tice structure. To address the issue in contrast from the second scintillator in the LYSO-LYSO setup, an alternate GAGG-LYSO set-up was also discussed, with the predicted spectra showing closer levels of absorption between the two scintillators, which we expect will produce more uniformity between the images. This setup could also be used to simultaneously obtain image data from multiple spectra, a useful capability for studying heterogeneous samples.

Looking toward the future of UHS XRI, the 'Extremely Brilliant Source' (EBS) upgrade to the ESRF will provide orders of magnitude increases in X-ray flux density, thus increasing the range of configurations for this imaging system, beyond those already mentioned, by allowing for the scintillator emission to be further split and more cameras incorporated [31]. These developments will greatly increase the range of experimental applications for this system.

3.5 References

[1] E M Escauriza, A Rack, E Synchrotron, *et al.*, "Ultra high-speed indirect X-ray imaging system with versatile spatio-temporal sampling capabilities," *Appl. Opt.*, vol. 57, no. 18, pp. 5004–5010, 2018.

[2] K Tsuji, "History of Curiosity," in *Micro-World Obs. by Ultra High-Speed Cameras* (K Tsuji, ed.), ch. 1, pp. 3–5, Cham: Springer, 1 ed., 2018.

[3] A Schropp, R Hoppe, V Meier, *et al.*, "Imaging Shock Waves in Diamond with Both High Temporal and Spatial Resolution at an XFEL," *Sci. Rep.*, vol. 5, no. 11089, pp. 1–8, 2015.

[4] D E Eakins and D J Chapman, "X-ray imaging of subsurface dynamics in high-Z materials at the Diamond Light Source," *Rev. Sci. Instrum.*, vol. 85, no. 12, 2014.

[5] M E Rutherford, D J Chapman, J G Derrick, *et al.*, "Probing the early stages of shock-induced chondritic meteorite formation at the mesoscale," *Sci. Rep.*, vol. 7, may 2017.

[6] M P Olbinado, X Just, J L Gelet, *et al.*, "MHz frame rate hard X-ray phase-contrast imaging using synchrotron radiation," *Opt. Express*, vol. 25, no. 12, 2017.

[7] A Rack, M Scheel, L Hardy, *et al.*, "Exploiting coherence for real-time studies by single-bunch imaging," *J. Synchrotron Radiat.*, vol. 21, pp. 815–818, 2014.

[8] T Hatsui and H Graafsma, "X-ray imaging detectors for synchrotron and XFEL sources," *IUCrJ*, vol. 2, pp. 371–383, 2015.

[9] S M Gruner, M W Tate, and E F Eikenberry, "Charge-coupled device area x-ray detectors," *Rev. Sci. Instrum.*, vol. 73, no. 101, pp. 2815–6023, 2002.

[10] P Willmott, "Synchrotron Physics," in *An Introd. to Synchrotron Radiat.*, ch. 3, pp. 39–86, John Wiley & Sons, Ltd, 2011.

[11] A Miceli, "Application of Pixel array detectors at X-ray synchrotrons," *J. Instrum.*, vol. 4, 2009.

[12] M Wulff, F Schotte, G Naylor, *et al.*, "Time-resolved structures of macromolecules at the ESRF: Single-pulse Laue diffraction, stroboscopic data collection and femtosecond flash photolysis," *Nucl. lnstrurnents Methods Phys. Res. A*, vol. 398, pp. 69–84, 1997.

[13] "PI-MAX4:1024i-RF Rev. P1," tech. rep.

[14] N D Parab, Z Guo, M C Hudspeth, *et al.*, "Dynamic fracture behavior of single and contacting Poly(methyl methacrylate) particles," *Adv. Powder Technol.*, vol. 28, no. 11, pp. 2929–2939, 2017.

[15] B J Jensen, "LANL DCS Activities, Highlights and Perspectives," in *DOE/NNSA DCS Rev. Sept. 20-21, 2016*, pp. 1–23, 2016.

[16] Y Tochigi, K Hanzawa, Y Kato, *et al.*, "A Global-Shutter CMOS Image Sensor with Readout Speed of 1Tpixel/s Burst and 780Mpixel/s Continuous," *IEEE J. Solid-State Circuits*, vol. 48, no. 1, pp. 329–337, 2013.

[17] M E Rutherford, D J Chapman, T G White, *et al.*, "Evaluating scintillator performance in time-resolved hard X-ray studies at synchrotron light sources," *J. Synchrotron Radiat.*, vol. 23, no. 3, pp. 685–693, 2016.

[18] M Sánchez del Río and R J Dejus, "XOP 2.1 — A New Version of the X-ray Optics Software Toolkit," *AIP Conf. Proc.*, vol. 705, pp. 784–787, 2004.

[19] S W Wilkins, T E Gureyev, D Gao, *et al.*, "Phase-contrast imaging using polychromatic hard X-rays," *Nature*, vol. 384, pp. 335–338, nov 1996.

[20] P Cloetens, R Barrett, J Baruchel, *et al.*, "Viewpoint on Phase objects in synchrotron radiation hard x-ray imaging," *J. Phys. D. Appl. Phys.*, vol. 29, pp. 133–146, 1996.

[21] J A Hawreliak, J Lind, B Maddox, *et al.*, "Dynamic Behavior of Engineered Lattice Materials," *Sci. Rep.*, vol. 6, no. 28094, 2016.

[22] B Branch, A Ionita, B E Clements, *et al.*, "Controlling shockwave dynamics using architecture in periodic porous materials," *J. Appl. Phys.*, vol. 121, no. 13, 2017.

[23] M P Olbinado, V Cantelli, O Mathon, *et al.*, "Ultra high-speed x-ray imaging of laser-driven shock compression using synchrotron light," *J. Phys. D. Appl. Phys.*, vol. 51, no. 055601, pp. 1–11, 2018.

[24] C Zhao, K Fezzaa, R W Cunningham, *et al.*, "Real-time monitoring of laser powder bed fusion process using high-speed X-ray imaging and diffraction," *Sci. Rep.*, vol. 7, no. 3602, 2017.

[25] A Rack, F García-Moreno, L Helfen, *et al.*, "Hierarchical radioscopy using polychromatic and partially coherent hard synchrotron radiation.," *Appl. Opt.*, vol. 52, no. 33, pp. 8122–7, 2013.

[26] T Camacho and M Ortizt, "Computational Modelling of Impact Damage in Brittle Materials," *Int. J. Solids Struct.*, vol. 33, no. 2, pp. 2899–2938, 1996.

[27] Z Zhang, D E Eakins, and F P E Dunne, "On the formation of adiabatic shear bands in textured HCP polycrystals," *Int. J. Plast.*, vol. 79, pp. 196–216, 2016.

[28] D Massy, F Mazen, S Tardif, *et al.*, "Fracture dynamics in implanted silicon," *Appl. Phys. Lett.*, vol. 107, no. 092102, 2015.

[29] J M Foster, B H Wilde, P A Rosen, *et al.*, "Supersonic jet and shock interactions," *Phys. Plasmas*, vol. 9, no. 5, pp. 2251–2263, 2002.

[30] A Aghababyan, C Bohm, P Gessler, *et al.*, "XFEL Timing System Specifications Version 2.2," tech. rep., Hamburg, 2013.

[31] R Dimper, H Reichert, P Raimondi, *et al.*, *The Orange Book: ESRF Upgrade Programme Phase II (2015-2022).* 2015.

Chapter 4

Collapse dynamics of spherical cavities in a solid under shock loading

This Chapter is based on the paper published in Scientific Reports, "E. M. Escauriza, J. P. Duarte, D. J. Chapman, M. E. Rutherford, L. Farbaniec, J. C. Jonsson, L. C. Smith, M. P. Olbinado, J. Skidmore, P. Foster, T. Ringrose, A. Rack and D E Eakins, *Collapse dynamics of spherical cavities in a solid under shock loading*, Scientific Reports **10**, 8455 (2020)" [1]. New Fourier-based analysis has been added to the results, in Section 4.3.7, with the corresponding methods added to Section 4.2.2. The experiments were conceived by the author, and all of the authors performed the experiments and edited the manuscript. The PMMA cavity targets were designed by the author and manufactured by First Light Fusion Ltd. The single-stage gas gun and imaging systems were designed by Dr D E Eakins and Dr D J Chapman, and the two-stage gas gun system was designed by Dr J P Duarte. The author processed the images, performed the simulations, analysed the data, created the figures and wrote the manuscript, under the supervision of Dr D E Eakins.

Paper abstract

Extraordinary states of highly localised pressure and temperature can be generated upon the collapse of impulsively driven cavities. Direct observation of this phenomenon in solids has proved challenging, but recent advances in high-speed synchrotron radiography now permit the study of highly transient, sub-surface events in real time. We present a study on the shock-induced collapse of spherical cavities in a solid poly(methyl methacrylate) medium, driven to shock states between 0.49 and 16.60 GPa. Utilising multi-MHz phase contrast radiography, extended sequences of the collapse process have been captured, revealing new details of interface motion, material failure and jet instability formation. Results reveal a rich array of collapse characteristics dominated by strength effects at low shock pressures and leading to a hydrodynamic response at the highest loading conditions.

4.1 Introduction

The importance of the cavity collapse phenomenon was first recognised by Lord Rayleigh, among others, who in 1917 attempted to explain the progressive damage experienced by screw propellers in water. By assuming the cavity is sufficiently far from the propeller surface, Rayleigh analytically modelled a spherical void collapsing under hydrostatic pressure. The results revealed an extraordinary increase in pressure at the instant of collapse, far in excess of the strength of materials used at the time [2]. Subsequent investigations revealed that, if the collapse occurs near a solid boundary, a jet instability forms which impacts the solid boundary [3, 4]. For both the jetting and non-jetting cases, deterioration of the propeller surface is caused by the accumulation of the actions of many individual collapsing cavities. In the modern context, cavity collapse plays an

important role in several applications, including the *in-situ* destruction of kidney and gall stones through shock lithotripsy [5, 6], targeted drug delivery [7–9], and the cleaning of surfaces exposed to ultrasonic fields in liquids [10–12].

More recently, there has been interest in the collapse of cavities in solid media, particularly in relation to hot spot formation and ignition mechanisms in energetic materials [13–15]. Although more stable under ambient fluctuations, these cavities may be driven to collapse under intense pressure waves, such as those produced under shock loading. Depending on the magnitude of the shock relative to the strength of the solid, the dynamics of the collapse process vary significantly. For the strongest shocks, hydrodynamic collapse is expected [16], and energy is localised during the formation of a high-speed jet and toroidal vortex that forms after jet impact [17]. Other mechanisms become dominant at lower shock pressures, when the deviatoric strength of the solid medium is significant relative to the stresses generated during the impact [16]. This also corresponds to an increase in the complexity of the collapse process, due to presence of failure and other strength-related phenomena. Simulations have been performed to model cavity collapse in a solid, in both the hydrodynamic [18, 19] and strength [20, 21] shock pressure regimes, but the precise effect that strength has on the collapse process and the mechanisms of energy dissipation is not known.

While hydrodynamic shock-induced cavity collapse has been observed experimentally in gaseous [17, 22, 23] and liquid media [24–26], direct observation in solid media has thus far proved challenging, primarily due to the opacity of most solids to visible light. Even for optically transparent solids, large refractive effects coupled with severe deformations in shock loading serve to either distort or obscure entirely details of the evolving sub-surface interfaces. A recent optical imaging study by Ma et al. [27], looking at weak shock-cavity interactions in polymethyl methacrylate (PMMA), partly addressed this issue by cutting cylindrical holes from blocks of PMMA. This provided a two-dimensional (2D) cavity

geometry that avoided the issues of optical refraction. Comparisons to 2D simulations gave predictions for the temperature field around the cavity during hot spot formation. Stronger shock loading, sufficient to induce collapse of a solid cavity, has yet to be observed.

For the probing of 3D cavities fully embedded in a solid, X-ray imaging (XRI) offers distinct advantages, as the higher transmission of X-rays provides direct access to the sub-surface details of the collapse process. Furthermore, compared to high-speed optical imaging, XRI benefits from reduced spatial distortion due to the negligible refraction of X-rays. Recent advancements in XRI techniques at synchrotron facilities mean it is now possible to image the sub-surface dynamics of materials at ultra-high-speed (UHS) rates of over 1 M frames per second (fps), with each image created from a single 100 ps X-ray pulse [28–34]. These techniques have been used to study shockwave dynamics and jet formation in shock-compressed polymer lattices by Branch et al. [35], and shock-induced collapse of hollow spherical glass cavities in silicone and TNT by Armstrong et al. [36]. The latter study found evidence of higher temperatures in the collapsed cavity region. However, due to the sub-millimetre cavity sizes and constraints imposed by the electron bunch spacing of the synchrotron, only a single frame could be captured per collapse.

Motivated by the dearth of currently available experimental data — in both the hydrodynamic and strength regimes — this study presents direct observations of shock-cavity interactions in a solid medium. Single-stage and two-stage gas gun plate impact experiments are performed at the European Synchrotron Radiation Facility (ESRF) to generate planar shocks in PMMA targets containing spherical cavities. A bespoke UHS XRI system is employed to capture dynamic radiographs of collapsing cavities at rates exceeding 1 Mfps [33]. Fluid-dominated dynamics are studied, as well as the previously unobserved strength-dominated and transition regimes, by exploring a wide range of stress states.

4.2 Methods

Specifications of the gas gun system, flyer and target design, and imaging system have been moved to Chapter 2. Remaining in this Chapter are the methods of extracting parameters from the radiographs, and the details of the simulation code Hytrac, which is used to test the hypothesis that constant cavity interface acceleration is observed during hydrodynamic cavity collapse.

4.2.1 Extracting parameters

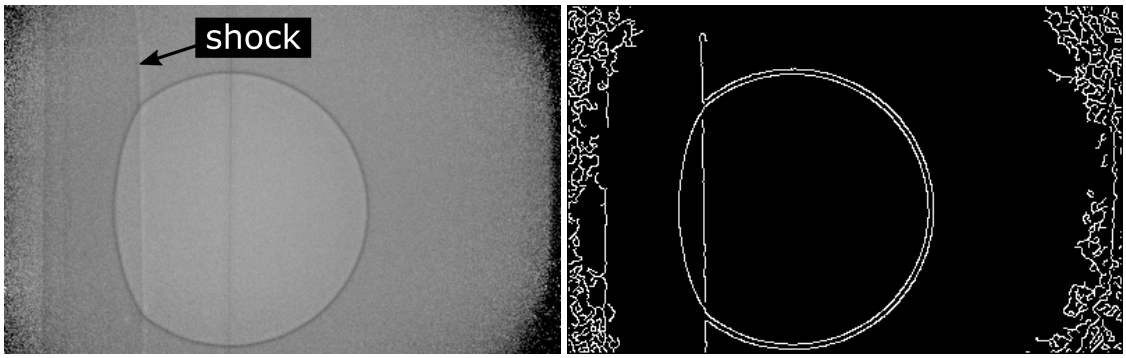
The edge-detected images can be used to extract information from the radiographs, thus allowing the time evolution of the cavity collapse process to be compared between experiments. First an objective measure of time is established, after which parameters, such as enclosed cavity area and interface displacement, can be extracted.

Frame times

It is important to have an objective measure of time when comparing the evolution of extracted parameters between experiments. In the present study, the zero-time, $t_0 = 0\,\mu s$ is chosen to be the time at which the shock front first interacts with the cavity interface. The time of the first 'dynamic' frame, *after* the shock reaches the cavity, is determined by measuring the shock front position and using the calculated shock speed, such that,

$$t_1 = \frac{d_s}{U_s}, \tag{4.1}$$

where t_1 is the time of the first dynamic frame relative to t_0, d_s is the shock displacement past the cavity interface, and U_s is the shock speed. For a steady shock, the speed of the shock front is a constant [16], and can be obtained analytically from the U_s-u_p Hugoniot relationship, $U_s = C_0 + Su_p$. A further assumption is that the shock has not greatly suffered from attenuation once it has interacted

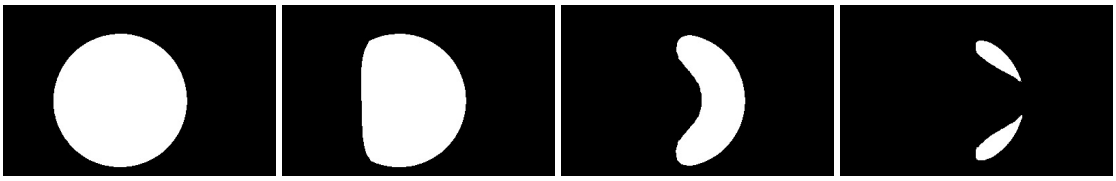


(a) Processed radiograph with shock front. (b) Edge detected shock front.

Figure 4.1: Example of edge detection with the purpose of extracting the shock front position, for a 6 mm diameter cavity impacted with a 12.38 GPa shock. In (a) is shown the flat field corrected radiograph, and in (b) is the output of the edge detection algorithm.

with the cavity, which is supported by observations based on the three dimensional geometry of the cylindrical target: there are regions of the shock front that have not yet been affected by the release, either from the target edge or cavity interface, and it is that which we see as the most advanced regions of the shock front. In Fig. 4.1a can be seen an example of a radiograph with the shock front interacting with a cavity. The radiograph is from Camera 1, so has been flat-field corrected but not transformed for registration. Curvature in the shock front can be seen at the top of the frame, due to lateral release at the target edge. Note also that the shock front in the region of the image occupied by the cavity is, due to cylindrical symmetry, in a region of the target on the same projected line as the cavity (as opposed to in the cavity region itself, since it is a void).

Phase contrast enhancement (see explanation in Chapter 2) of the radiographs combined with the large and steep density change along the shock front, means the front is clearly visible in the radiographs. Thus, as for the cavity interface, the shock front position can be determined using edge detection. Figure 4.1b shows an image that has been processed with the edge detection algorithm for the purposes of detecting the front. A lower threshold is used to capture the weaker edge of the shock compared to the cavity interface, resulting in a secondary edge of the cavity being detected, as well as noise in the peripheral regions. The shock posi-



(a) t = 0 μs (b) t = 0.33 μs (c) t = 0.86 μs (d) t = 1.21 μs

Figure 4.2: Filled in images after edge detection, from the 6 mm diameter cavity, 12.38 GPa shock pressure experiment, showing the decreasing projected cavity area over time.

tion is then obtained by cropping the pixels along the shock front and obtaining the average pixel coordinate in the x-direction, x_s. The displacement d_s is then calculated as,

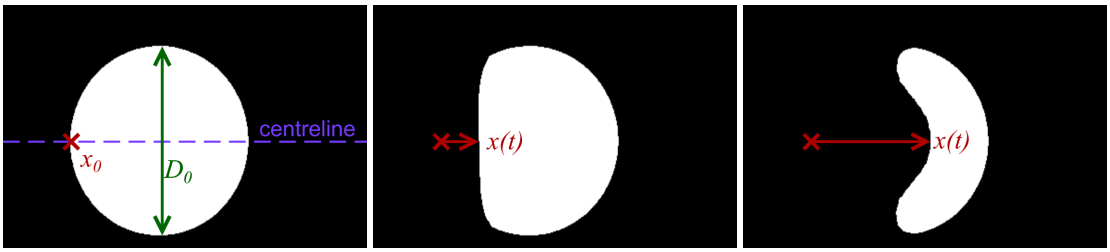
$$d_s = x_s - x_c, \tag{4.2}$$

where x_c is the x-coordinate of the left-most pixel of the cavity interface (left because the shock is moving from left to right in the frame). This d_s value, along with the calculated shock speed, U_s is used to find t_1 with Eq. 4.1. Every frame time thereafter is determined from the inter-frame time in the camera settings for that experiment. As confirmed by the camera signal oscilloscope traces, the error in camera timing is very small, at approximately 1 ns, which corresponds to a few μm of displacement at the highest shock speeds generated. By contrast, the error associated with measuring displacements by edge detection is taken to be the pixel size of 32 μm. The camera error is therefore not considered. Furthermore, for the purposes of investigating the scaling of cavity diameter, D_0 and longitudinal sound speed of the medium in which the cavity is situated, C_L, the latter of which is a material-dependent parameter, a dimensionless time t' is introduced, where,

$$t' = t\frac{C_L}{D_0}. \tag{4.3}$$

Cavity projected area

During interaction with the shock, the cavity is deformed and compressed, decreasing the volume enclosed within the cavity interface. The cavity seen in the



(a) t = 0 µs (b) t = 0.33 µs (c) t = 0.86 µs

Figure 4.3: The displacement of the cavity interface along the centreline axis of symmetry, for a 6 mm diameter cavity impacted with a 12.38 GPa shock.

2D radiographs is a projection of the 3D spherical cavity. Thus, the change in projected area can be measured, which is simply the number of pixels contained within the cavity perimeter in the edge-detected images. The projected area is a metric that has be commonly used in previous experimental [25, 26] and computational [37, 38] studies on shock-cavity interactions. This is achieved by first using the `imfill()` function in Matlab, which fills in enclosed region in the edge-detected binary image with ones, leaving the region outside as zeros. The enclosed area is then simply the number of non-zero elements, calculated using the `nnz()` function. This pixel area can then, if needed, be converted to mm^2 with an image of an object of known size. The output of this calculation is a time-dependent area, $A(t)$, which can be normalised by it's initial value, A_0, to give a dimensionless area, $A'(t)$, for comparing between experiments,

$$A'(t) = \frac{A(t)}{A_0} \tag{4.4}$$

Figure 4.2 shows an example of the images after edge detection and filling in of the cavity region; the images are from the 6 mm diameter cavity, 12.4 GPa shock pressure experiment, and the frame times given have been calculated with Eq. 4.1. Clearly we see that the area decreases as time progresses and the cavity undergoes deformation.

Cavity kinematics

The edge detected images can also be used to track the dynamics of the cavity interface. Of particular interest in the present work is the maximal horizontal displacement, which, due to the spherical symmetry and the planar shock, is the displacement along the horizontal centreline axis of symmetry. This is shown in Fig. 4.3a, which also shows the initial x-coordinate of the cavity interface along the centreline, x_0, as well as the initial cavity diameter, D_0. The displacement after the shock interaction commences, $x(t)$, is annotated in Fig.4.3b&c. This displacement can also be scaled, to produce the dimensionless centreline displacement,

$$x'(t) = \frac{x(t)}{D_0}, \tag{4.5}$$

which again allows scaling laws to be investigated.

The centreline displacement can then be used to calculate the centreline velocity, $v(t)$, with a dimensionless velocity,

$$v'(t) = \frac{v(t)}{C_L}, \tag{4.6}$$

where, as before, C_L is the longitudinal sound speed of the medium. Likewise, the acceleration of the interface is $a(t)$, with the dimensionless form,

$$a'(t) = a(t)\frac{D_0}{{C_L}^2}. \tag{4.7}$$

For some of the experiments above a threshold loading pressure (and so also above a certain impact velocity), the acceleration of the interface is constant. The validity of this assumption is assessed in the results, in Section 4.3.6. If we then integrate the a twice with respect to time, we obtain quadratic expressions for the displacement, which are, in both dimensional and dimensionless forms,

$$x(t) = v_0 t + \frac{1}{2}at^2, \tag{4.8}$$

$$x'(t) = v_0' t' + \frac{1}{2} a' t'^2, \tag{4.9}$$

where the additional constant v_0 is the initial velocity, i.e. the release velocity of the shock at the cavity interface, and the primes represent the dimensionless variables defined above. Using Eq 4.9, a quadratic is fit to plots of $x'(t)$ vs. t', in order to extract the constants a' and v_0', which enables the comparison of acceleration and release velocity with parameters like loading pressure. The fitted acceleration and release velocity allows us to determine the velocity for a given time (again in dimensional and dimensionless forms) with,

$$v(t) = at + v_0 \tag{4.10}$$

$$v'(t) = a' t' + v_0'. \tag{4.11}$$

These two expressions can then be used to find the velocity of the interface when it reaches the far position of the cavity. This velocity will be referred to as the 'jet velocity', v_{jet}, since, as was discussed in the introduction of this Chapter, for hydrodynamic shock-driven cavity collapse, the interface forms a jet instability [39, 40]. The two forms of this velocity are determined from the following expressions,

$$v_{jet} = at|_{x=D_0} + v_0 \tag{4.12}$$

$$v_{jet}' = a' t'|_{x'=D_0'} + v_0'. \tag{4.13}$$

The variation of jet velocity with shock loading pressure can thus also be compared.

The parameters extracted and expressions presented above can equally be applied to simulations of cavity collapse. In the following Chapter, a head-to-head comparison between experiments and the output of simulations performed in SCIMITAR3D is presented.

4.2.2 Shear banding analysis

Covered in this section are the methods for extracting quantitative information on the spacing of perturbations that appear on the cavity surface at lower shock pressures.

Extracting radial lineouts

In the lower shock pressure regime, when the material strength of the PMMA medium is not overwhelmed by the shock loading, perturbations form along the cavity interface. As discussed in Chapter 1, simulations have shown that these perturbations originate from localised shear, known as 'shear bands'. In the following Chapter, simulations of these experiments confirm this to be the case. As can be seen in Fig. 4.4a, at the location of these perturbations, there are also cracks. Figure 4.4b shows the process by which the coordinates of the cavity perimeter are obtained, to produce a 'radial lineout'. The displacement from the cavity centre is obtained from the pixel coordinate locations of the perimeter in the mask cavity image (the process for mask creation is described above in the section on edge detection). The 'centre' is defined as the mean value of the x- and y-coordinates of the non-zero pixel values in the mask image before impact, i.e. the 'centre of mass' (CoM) of the cavity at t_0. Since the cavity in Fig. 4.4b is for a frame captured after impact, the cavity has deformed toward the CoM position predominantly on its left side. By choosing the CoM as the reference point of the radial lineouts, the reference point is fixed in the lab frame of reference. An alternative would be to use the CoM of each given frame as the reference point, but this increases the complexity of analysis, since the CoM would move as the cavity is deformed, and is therefore not chosen. There is, however, an issue of having more than one perimeter point along a radial line, which can occur when the cavity is severely deformed. For this reason, the lineouts are only extracted for earlier times, when the deformation is not so advanced as to have overlapping boundaries.

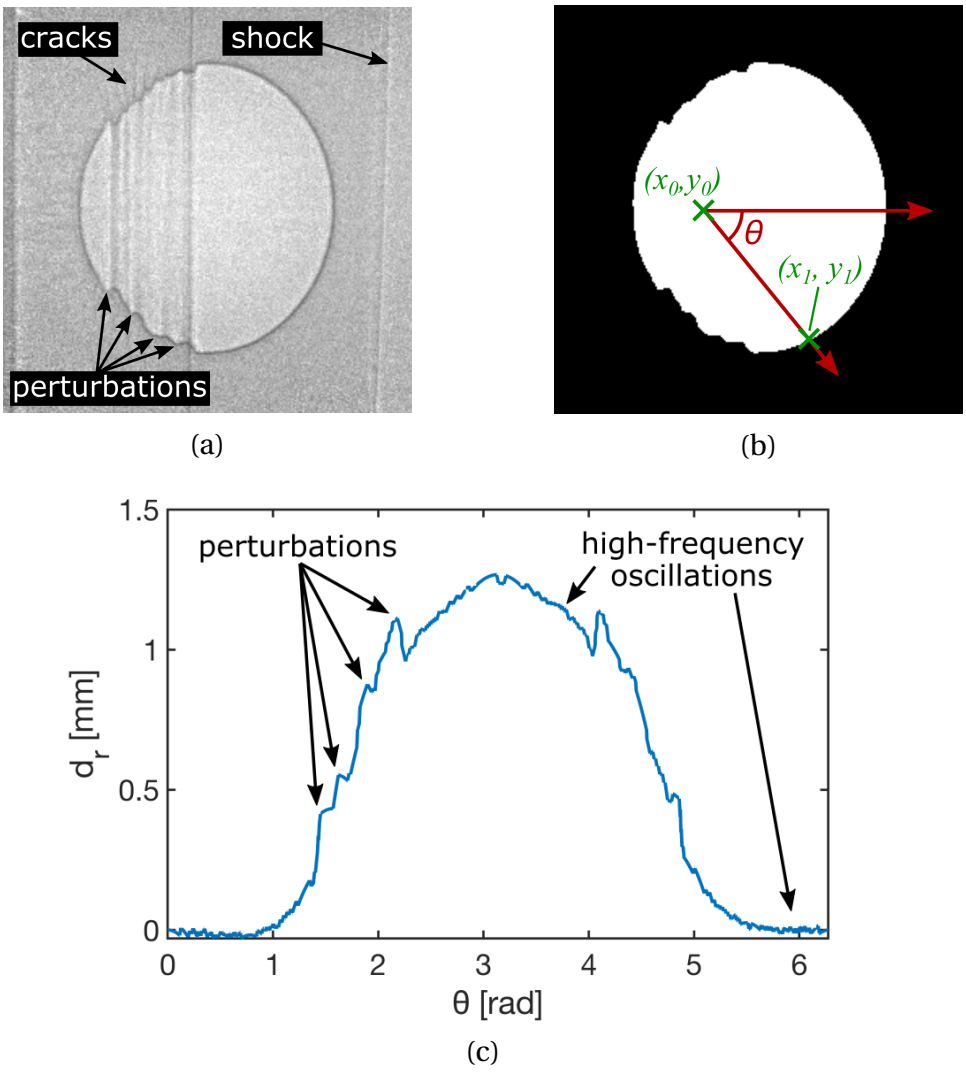


Figure 4.4: The method used to obtain radial lineouts from the cavity collapse images. The example shown is a 6 mm diameter cavity impacted with a 0.59 GPa shock. (a) The processed image before edge detection, with the perturbations and cracks annotated. (b) The mask image created with edge detection, and the coordinate positions for finding the radial and angular displacements of the cavity perimeter. (c) The lineout of radial displacement d_r vs. angular displacement θ, where d_r has been scaled to mm and zeroed relative to the initial average value before impact. The perturbation positions and regions of high-frequency oscillations are annotated.

The radial displacement, d_r is calculated from coordinates (x_0, y_0) and (x_1, y_1). This displacement can be converted from its pixel unit value into mm from the known pixel size, and then zeroed relative to the initial value before impact, such that the displacement starts at approximately zero and is in the direction toward the origin. Using the same coordinates, the angle of the lineout θ, which can be thought of as the 'angular displacement', is then calculated as the inverse tangent. The appropriate transformation is given to θ depending on which quadrant of the image the lineout is in. Furthermore, when the lineout lies either on the horizontal or vertical, the value must be assigned (0, $\pi/2$, π or $3\pi/2$), as the tangent function tends to infinity at these values. All of the calculations are performed using scripts written in Matlab [41].

The final output of d_r vs. θ for the example is shown in Fig. 4.4c. The radial displacement has been converted into mm and zeroed, and the angular displacement is in radians. The perturbations on the cavity surface are captured by the lineout, visible as 'peaks' and 'valleys', where peaks are local maxima and valleys are local minima — a discussion of the mathematical criteria for peak and valley identification is given below. The regions extracted near the horizontal axis, where the cavity surface is smooth, have high frequency oscillations due to coarse changes when moving between pixels. The fineness of these oscillations is determined by the resolution of the detector.

Fourier analysis

The features present in the output of the radial lineout method in Fig. 4.4c can be filtered and analysed using the discrete Fourier decomposition methods. This quantitative characterisation of the perturbations allows comparison between cavity collapse results at different loading conditions.

Fourier processing is performed in Matlab, using functions available in the Signal Processing Toolbox [41]. The first step is to resample the signal with equally

spaced sampling, which is assumed by the fast Fourier transform (FFT) in Matlab, the `fft()` function, where 'fast' refers to the fact that the transform algorithm is much faster than its brute-force approach counterpart [42, 43]. The initial signal is not evenly sampled because the change in angular displacement along the x-axis, $d\theta$, is dependent of the pixel coordinates, which changes with every pixel jump. Furthermore, the number of pixels along the perimeter varies (usually decreases) as the cavity is deformed, meaning the signals must be resampled with the same number of points between 0 and 2π radians, if they are to be compared directly. The resampling, performed with a linear interpolation, is chosen to be at a much higher frequency than the average frequency of the original signals. A value of 3,600 samples is chosen, an approximate order of magnitude larger than the number of pixels in the perimeter (480 in the case of the example in Fig. 4.4). The raw and resampled signals are shown in Fig. 4.5a, with an inset showing the increase in sampling frequency.

The resampled signal can then be analysed using Fourier techniques. Firstly, the raw lineout signal, after resampling, is filtered using the `bandpass()` function in Matlab, which 'passes' the signal only between a defined range of frequencies, with an upper and lower limit. By passing the signal through a bandpass filter, the dominant low-frequency oscillations of the lineout, which is there by the very nature of the process advancing around a largely symmetric and circular shape, are suppressed. Furthermore, the high frequency noise (up to a maximum of $3600/2\pi = 573\,\mathrm{rad}^{-1}$) from the pixel oscillations and increased sampling frequency, are also suppressed, leaving a smoothed signal that preserves the pertinent features of the lineout, namely the peaks and valleys in the locations where cracks are observed. The minimum and maximum frequencies that provide the optimum filtering (judged qualitatively by eye), are $1.5\,\mathrm{rad}^{-1}$ and $20\,\mathrm{rad}^{-1}$, respectively. These two parameters are applied to all of the lineouts during processing. The signal of Fig. 4.5a and its bandpass filtered signal are both shown in Fig. 4.5b, which have both been normalised by their maximum respective val-

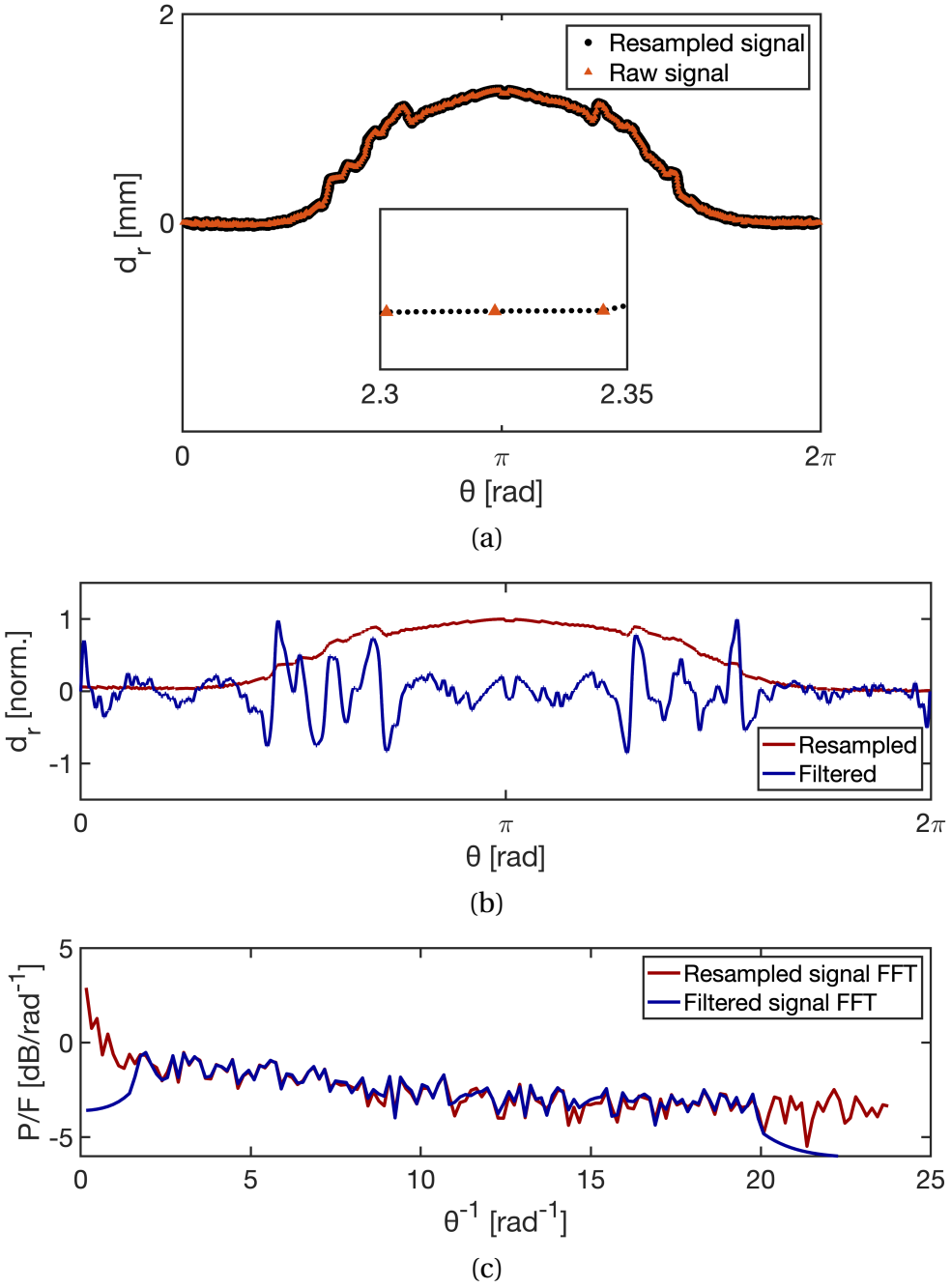


Figure 4.5: The process of analysing a lineout signal with Fourier techniques. (a) The raw signal is resampled to a finer and constant sampling rate. (b) The raw and bandpass filtered lineouts. Both lineouts have been normalised relative to the maximum value for the purposes of presentation. (c) The power spectral density spectra of the FFT raw and filtered lineouts.

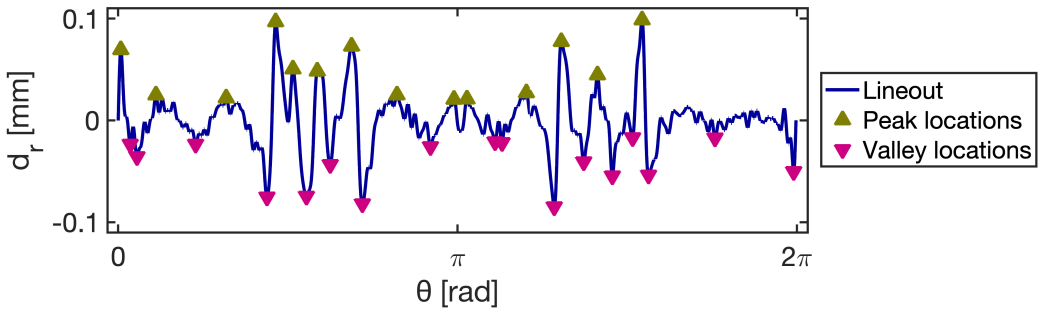


Figure 4.6: The peak and valley locations extracted from the radial lineout.

ues. Figure 4.5c shows the power spectral density of the resampled and bandpass filtered lineouts, where the effect of the cutoff frequencies can be seen on the filtered spectrum. The power spectral density, P/F, is defined as,

$$\frac{P}{F} = 2\frac{\Phi^2}{N f_s}, \tag{4.14}$$

where P is the spectral power, F is the frequency 'volume', Φ is the amplitude of the FFT values, N is the number of samples and f_s is the sampling frequency (3,600 and 573 rad^{-1}, respectively, in the present example). The factor of 2 accounts for the fact that signal is composed only of real values.

The bandpass filtered lineouts and power density plots contain quantitative information that can be tracked over time during the collapse process, and compared between experiments and simulations. Of interest to the study of shear banding phenomena, which the peaks and valleys in the cavity collapse lineouts are thought to indicate, is the spacing between bands. The average spacing of the peaks and valleys for the example radiograph in Fig. 4.4a can be obtained from the bandpass filtered lineout from Fig. 4.5b.

The output of the peak and valley detection method is shown in Fig. 4.6, with the peak and valley positions indicated with different colour markers. The positions are located with the `findpeaks()` function in Matlab [41], by splitting the signal into values above and below zero, respectively. Since the algorithm only locates maxima, the below zero signal is flipped above the x-axis to locate the po-

sitions, and then flipped back when making the plot. The parameter exploited is the peak 'prominence', which is a criteria for specifying whether a maxima is a peak or not, by comparing the horizontal distance from a given maxima to either ends of the signal, or another maxima. The prominence is specified with a decimal value between 0 and 1. In the present work, the peaks in the experimental lineouts are judged to be captured with a value of 0.55.

It should be noted that, for whichever value for peak prominence is chosen, the `findpeaks()` function will inevitably not recognise some peaks and valleys that are judged by eye to be so, and recognise others still that are thought to not be peaks or valleys. In the interest of not introducing additional observational bias, it is decided that, once the prominence parameter is chosen, the selected peak validity is not assessed further. In this sense, any procedural bias from the algorithm is spread as randomly as possible, and applied equally to all of the data. With this in mind, a single peak and valley spacing parameter, λ, is extracted from the peak and valley locations, as,

$$\lambda = \frac{\bar{\lambda}_p + \bar{\lambda}_v}{2}, \tag{4.15}$$

where $\bar{\lambda}_p$ and $\bar{\lambda}_v$ are the mean spacing of the peaks and valleys, respectively. The mean perturbation spacing λ is in radians, but may be converted into mm spacing by using the radial displacement of each perimeter point.

4.2.3 Hydrodynamic simulations

Two-dimensional axisymmetric simulations of the experiments are performed in Hytrac, a multi-material front-tracking Eulerian hydrocode which has been used in earlier studies to model dynamic flow instabilities in PMMA under shock compression [44]. As the code does not include material strength, these simulations provided a baseline understanding of the collapse within a fluid medium, allowing the effects of strength to be more clearly contrasted to fully hydrody-

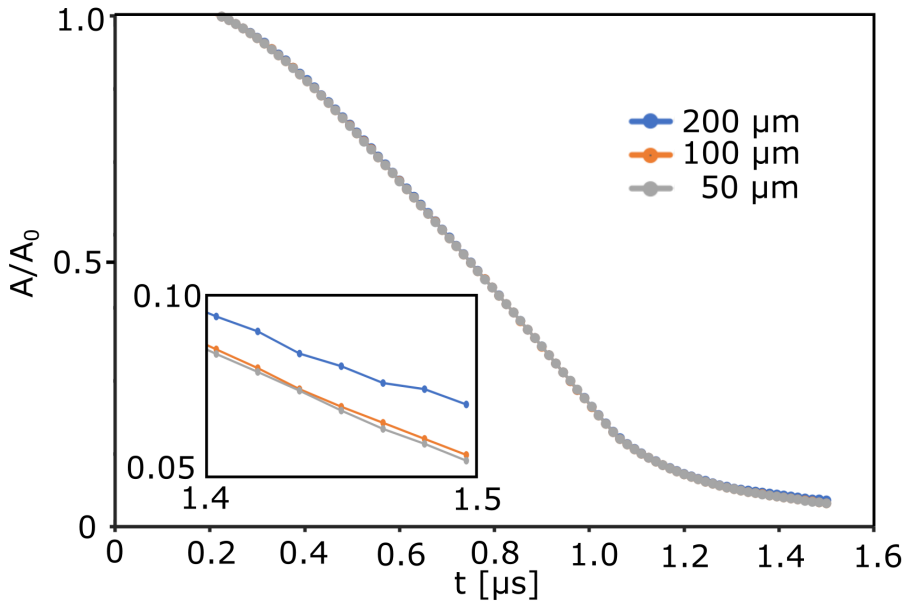


Figure 4.7: Normalised area vs. time for hydrodynamic simulations in Hytrac at grid cell sizes of 200 µm, 100 µm and 50 µm in the direction perpendicular to the direction of the shock. Simulation is of a 6 mm diameter cavity impacted with a 16.60 GPa shock.

namic behaviour. In the present work, a cell-based adaptive mesh refinement (AMR) scheme is used to balance computational resources with resolution requirements. Further details of Hytrac are given in the methods of Chapter 2.

For the PMMA targets and flyer materials a Frankfurt equation of state package is used to relate the pressure and specific internal energy to the density and temperature, producing a tabulated equation of state [45]. Two sets of simulations are performed, for the single-stage and two-stage experiments, with initial cell sizes of 100 µm and 137.5 µm, in the directions perpendicular and parallel to the shock direction, respectively. Convergence of the grid size can be seen in Fig. 4.7, which shows the decrease in normalised area after impact at different grid sizes. Convergence was judged to be complete at 100 µm in the perpendicular direction.

For both sets 4 levels of AMR are used, giving minimum cell sizes one eighth of the initial value. An axisymmetric half-domain is modelled with a central reflective boundary and transmissive boundaries along the other three edges. For the

Material	ρ_0(g/cm^3)	Hugoniot Relation	Ref.
PMMA ($u_p < 0.5$ km/s)	1.187	$U_s = 9.17{u_p}^3 - 9.47{u_p}^2 + 3.64u_p + 2.74$	[46]
PMMA ($u_p > 0.5$ km/s)	1.187	$U_s = 1.54u_p + 2.55$	[46]
Aluminium 2024	2.784	$U_s = 1.29u_p + 5.37$	[47]
Polycarbonate	1.193	$U_s = 1.20u_p + 2.92$	[47]
Stainless steel	7.910	$U_s = 1.49u_p + 4.58$	[47]

Table 4.1: The U_s-u_p Hugoniot for each material, used to calculate the shock pressure.

simulations of the two-stage experiments the whole flyer and target geometries are simulated because of the small size of the target and flyer. This ensures that effects from rarefaction waves at the edge of the projectile are accounted for. Due to the larger target and flyer sizes used in the single-stage experiments, release effects are not a concern. This allows the simulation setup to simply be a uniform domain of PMMA with a central cavity a fixed distance from the loading surface. To replicate the impact event, the loading surface is assigned the particle velocity corresponding to the shock state of interest.

4.3 Results

4.3.1 Shock state calculations

The pressure p generated upon impact is calculated from the Rankine-Hugoniot jump conditions, where the shock pressure is given by the product of the shock impedance, $Z = \rho_0 U_s$, and the particle velocity behind the shock, u_p, such that,

$$p = \rho_0 U_s u_p, \tag{4.16}$$

where ρ_0 is the initial density of the material and U_s is the shock velocity [16]. From the conservation of momentum jump condition, p and u_p must be contin-

uous at the interface between the flyer and target at the instant after impact. This allows respective values to be calculated at the intercept between the p-u_p Hugoniot projections for the target and flyer, with the initial particle velocity of the flyer given by the impact velocity v_i. The values of U_s in Eq. 4.16 for each material are calculated with the empirical U_s-u_p relationships found in the literature (Table 4.1). As the impact pressure is increased in PMMA there is a transition from a cubic to linear relationship at $u_p = 0.5\,\mathrm{km/s}$ [46, 47]. This transition has been attributed to a change in the mechanical response of polymers under shock compression, due to a large difference between forces along the polymer chain and forces between neighbouring chains [48].

D_0 (mm)	D_t (mm)	T_t (mm)	T_c (mm)	v_i (km/s)	u_p (km/s)	U_s (km/s)	p (GPa)
Single-stage gas gun, single-camera, 25 mm flyer diameter, 5 mm flyer thickness							
4	20	12	5	0.200 ± 0.001	0.16 ± 0.01	3.12 ± 0.10	0.60 ± 0.02
4	20	12	5	0.396 ± 0.002	0.32 ± 0.01	3.23 ± 0.10	1.21 ± 0.04
4	20	12	5	0.595 ± 0.003	0.47 ± 0.02	3.28 ± 0.10	1.86 ± 0.06
4	20	12	5	0.750 ± 0.004	0.59 ± 0.02	3.46 ± 0.11	2.44 ± 0.08
6	20	12	6	0.165 ± 0.001	0.13 ± 0.01	3.08 ± 0.10	0.49 ± 0.02
6	20	12	6	0.406 ± 0.002	0.32 ± 0.01	3.24 ± 0.10	1.25 ± 0.04
6	20	12	6	0.589 ± 0.003	0.47 ± 0.02	3.31 ± 0.10	1.84 ± 0.06
Single-stage gas gun, single-camera, reverse impact against stainless steel anvil							
4	25	13	6	0.719 ± 0.004	0.65 ± 0.02	3.54 ± 0.12	2.72 ± 0.09
4	25	13	6	0.795 ± 0.004	0.71 ± 0.03	3.65 ± 0.11	3.08 ± 0.10
Two-stage gas gun, two-cameras, 9 mm flyer diameter, 2 mm flyer thickness							
3	11	11	2.5	1.973 ± 0.010	0.99 ± 0.03	4.08 ± 0.13	4.80 ± 0.15
3	11	11	2.5	2.985 ± 0.015	1.48 ± 0.05	4.83 ± 0.15	8.49 ± 0.26
4	11	11	3	3.020 ± 0.015	1.50 ± 0.05	4.85 ± 0.15	8.63 ± 0.26
4	11	11	3	3.937 ± 0.020	1.94 ± 0.06	5.53 ± 0.17	12.71 ± 0.39
6	11	11	4	3.868 ± 0.019	1.90 ± 0.06	5.48 ± 0.17	12.38 ± 0.38
6	11	11	4	3.957 ± 0.020	1.95 ± 0.06	5.55 ± 0.17	12.80 ± 0.39
6	11	11	4	4.697 ± 0.023	2.30 ± 0.07	6.09 ± 0.19	16.60 ± 0.49

Table 4.2: Details of the results and the three setups used for the experiments. The values for u_p, U_s and p are calculated using Eq. 4.16 and the impedance matching method.

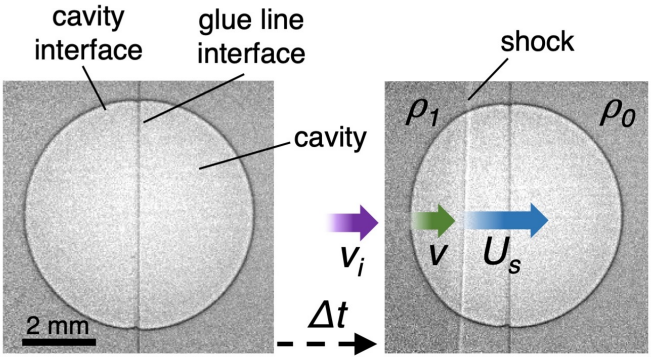


Figure 4.8: Radiographs of a 6 mm cavity. The left image shows the stationary cavity before impact. The right image shows the target after impact from the left by a 0.59 GPa shock, with the velocities and densities annotated.

It is also possible to measure U_s and u_p from the shock front and flyer positions in the radiographs. However, because of the small distance between the impact surface and cavity interface and the large shock velocity relative to the inter-frame time, it is not always possible to measure the shock front displacement before it has interacted with the cavity. Furthermore, the flyer interface during the early stages of compression cannot be accurately identified due to the poorer signal to noise ratio near the periphery of the radiographs. By contrast, the impact velocity v_i can be determined to within 1% uncertainty and the equations of state given in Table 4.1 are well established. For these reasons, the pressures measured from the radiographs are used only as a check against the pressures calculated using v_i and the impedance matching method. A summary of the key experimental details, and the results of the impedance matching calculations, can be seen in Table 4.2. As labelled in the gas gun diagram in Chapter 2, D_0 is the cavity diameter, D_t is the target diameter, T_t is the target thickness and T_c is the distance between the target impact face and the cavity centre. The uncertainties in u_p, U_s and p are calculated from the uncertainties associated with v_i and the $\sim 3\%$ uncertainty associated with the U_s-u_p equations of state for PMMA given in Table 4.1 [46].

4.3.2 Experimental data

Example radiographs showing a 6 mm cavity experiment can be seen in Fig. 4.8. The left-hand image shows the cavity stationary before impact, and the right-hand image shows the early interaction between the shock and the cavity after impact. The planar shock front, which propagates at velocity U_s, is visible as a phase contrast fringe separating the lighter uncompressed region and the darker compressed region of the target, which have densities ρ_0 and ρ_1, respectively. The shock releases at the free surface of the cavity interface and propagates in the direction of the shock with velocity v at time t after release. The cavity interface and glue line are also clearly visible because of the prominent dark phase contrast fringe. The projected area of the cavity is measured as the number of pixels enclosed by the cavity interface. The proportional change in area can thus be calculated as the ratio of the area in the images of the deformed cavity to the area before impact, providing a normalised and dimensionless measurement. The results of these calculations are presented in Section 4.3.5. Radiograph sequences from the experiments can be seen Fig. 4.9-4.11, which show shock-cavity interactions in different pressure regimes, from weak to strong shocks.

4.3.3 The strength regime

Radiographs from a single-stage gas gun experiment can be seen in Fig. 4.9, showing the features of strength-dominated collapse dynamics. In Fig. 4.9(a) a 6 mm diameter cavity is impacted from the left with an aluminium flyer, with an impact velocity of 0.165 km/s, producing a shock pressure of 0.49 GPa. The times given are relative to contact between the shock and the upstream cavity surface. At 0.369 µs there is visible deformation of the upstream cavity interface, with the shock front and glue line interface also visible. Perturbations and sites of crack initiation can be seen at 2.581 µs. At 11.029 µs a large amount of damage is visible, and there are axially aligned cracks. These features are qualitatively similar to the shear banding formed in the simulations of weakly shocked cavity collapse

in HMX [20, 21].

The radiographs in Figs. 4.9(b)&4.9(c) show cavities subjected to shock pressures of 0.59 GPa and 1.25 GPa, respectively. At these increased pressures the collapse behaviour is dominated by uniform deformation until later times, and the spacing of the surface perturbations that form is smaller. As can be seen in Fig. 4.10, this trend continues as the shock pressure is increased and the dynamics transition from a failure mode dominated by brittle fracture to one dominated by material flow. The images, which show experiments between 1.84 and 3.08 GPa, show uniform deformation dominating for a larger proportion of the collapse, with the shape similar to that of a bubble collapsing under hydrostatic compression. Note that the experiments shown in Figs. 4.10(b)&(c) are reverse impact, in which the cavity targets are impacted against a steel anvil.

4.3.4 The hydrodynamic regime

The radiograph sequences in Fig. 4.11 show fluid-dominated collapse dynamics. In all three sequences the cavity has been impacted with a polycarbonate flyer using a 2-stage gas gun. In this regime the formation of a pronounced jet can be seen, typical of strong shock-cavity interactions in a gaseous fluid. This feature is predicted by the simulations of shock-cavity interactions in a gaseous medium [49]. Experimentally it has been observed in spherical cavities in gas [22, 23] and cylindrical cavities in hydrogel [24, 25]. Pronounced jet formation is also predicted in simulations of shock-cavity interactions in HMX, for both cylindrical [21, 50] and spherical [19] cavity geometries.

For all three radiograph sequences in Fig. 4.11, after the cavity has completely collapsed the remaining hot gas and vapourised PMMA forms one or more visible tori, which propagate downstream. The tori are formed by the deposition of vorticity along the cavity surface during the jet impact [17]. The formation of tori is observed in 3D simulations of shocks interacting with micrometre-sized

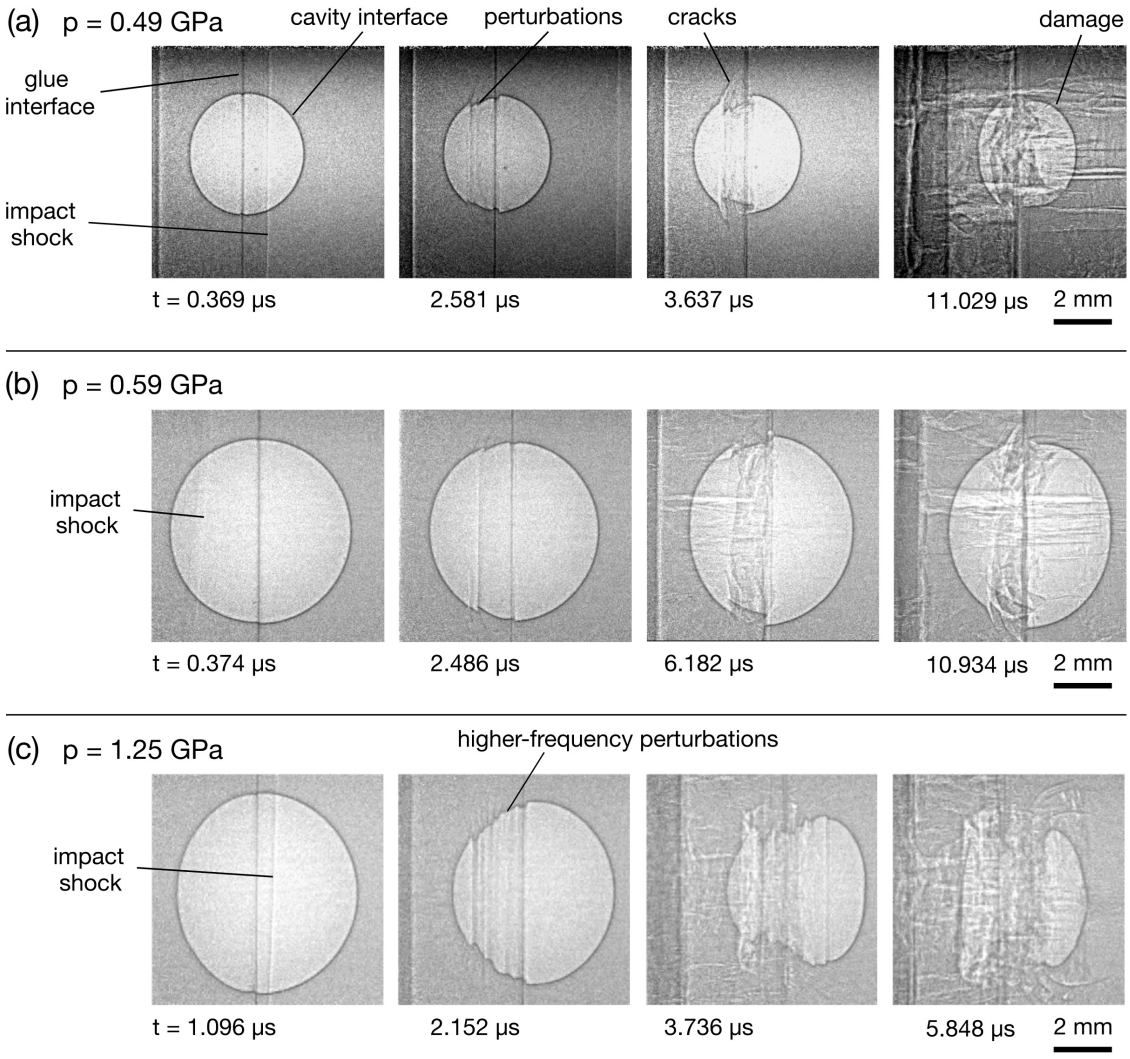


Figure 4.9: Radiograph sequences showing shock-cavity interactions in the strength-dominated regime. (a) A 4 mm cavity and 0.49 GPa shock. (b) A 6 mm cavity and 0.59 GPa shock. (c) A 6 mm cavity and 1.25 GPa shock.

spherical cavities in HMX [18, 19] and spherical helium cavities in air [51]. While experimental observation of tori formation has thus far been restricted to gaseous [22, 23] and liquid [25] media, this work has confirmed the phenomena extends to solids subjected to strong shock compression. Through simultaneous optical imaging, the toroidal plasma emission is captured through the transparent rear surface of the target. The early and late stages of the toroid formation can be seen in the optical imaging insets in Fig. 4.11(c), which have been matched to the approximate time in the radiographs.

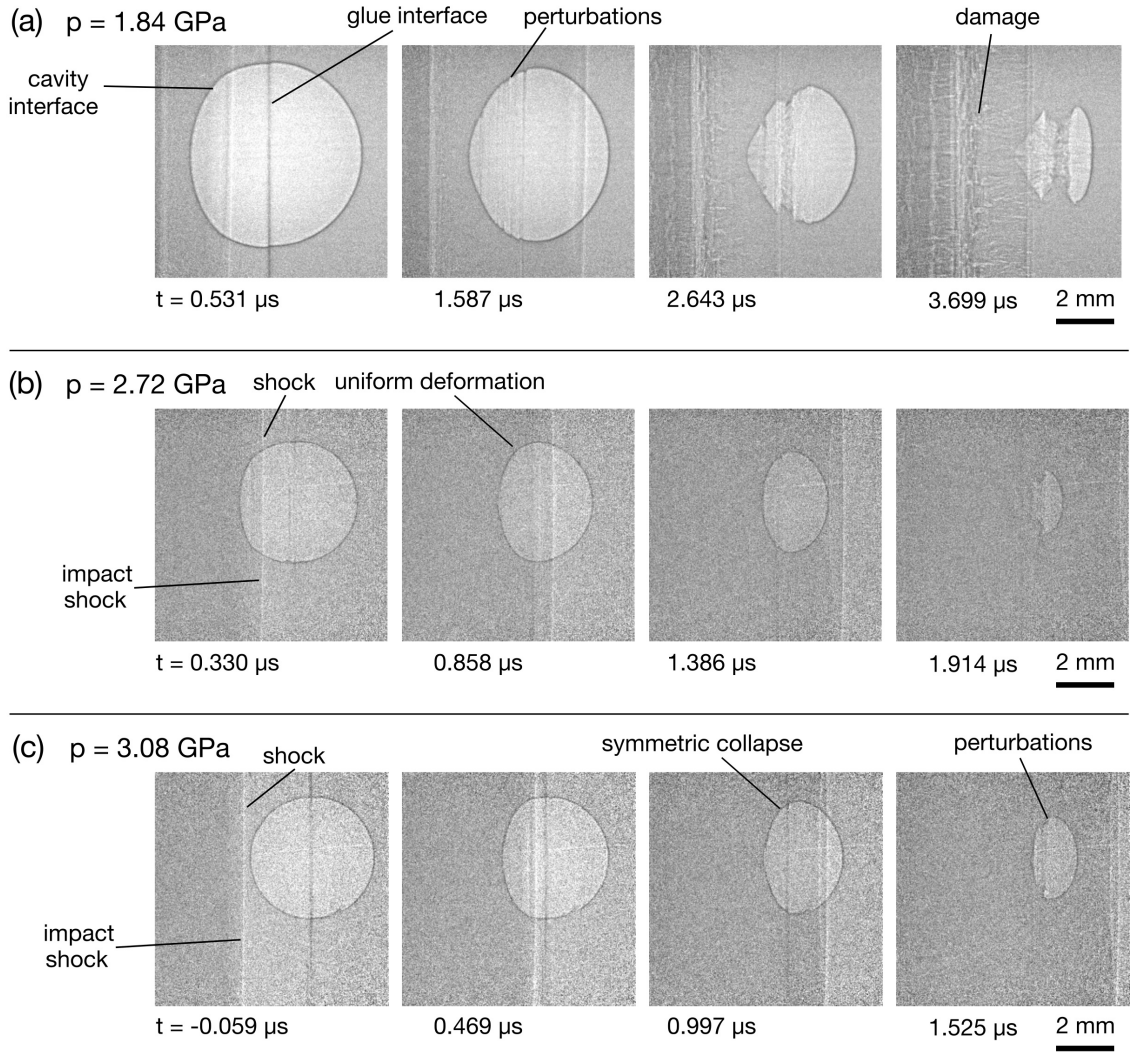


Figure 4.10: Radiograph sequences showing shock-cavity interactions in the transition regime. (a) A 6 mm cavity and 1.84 GPa shock. (b) A 4 mm cavity and 2.72 GPa shock. (c) A 4 mm cavity and 3.08 GPa shock.

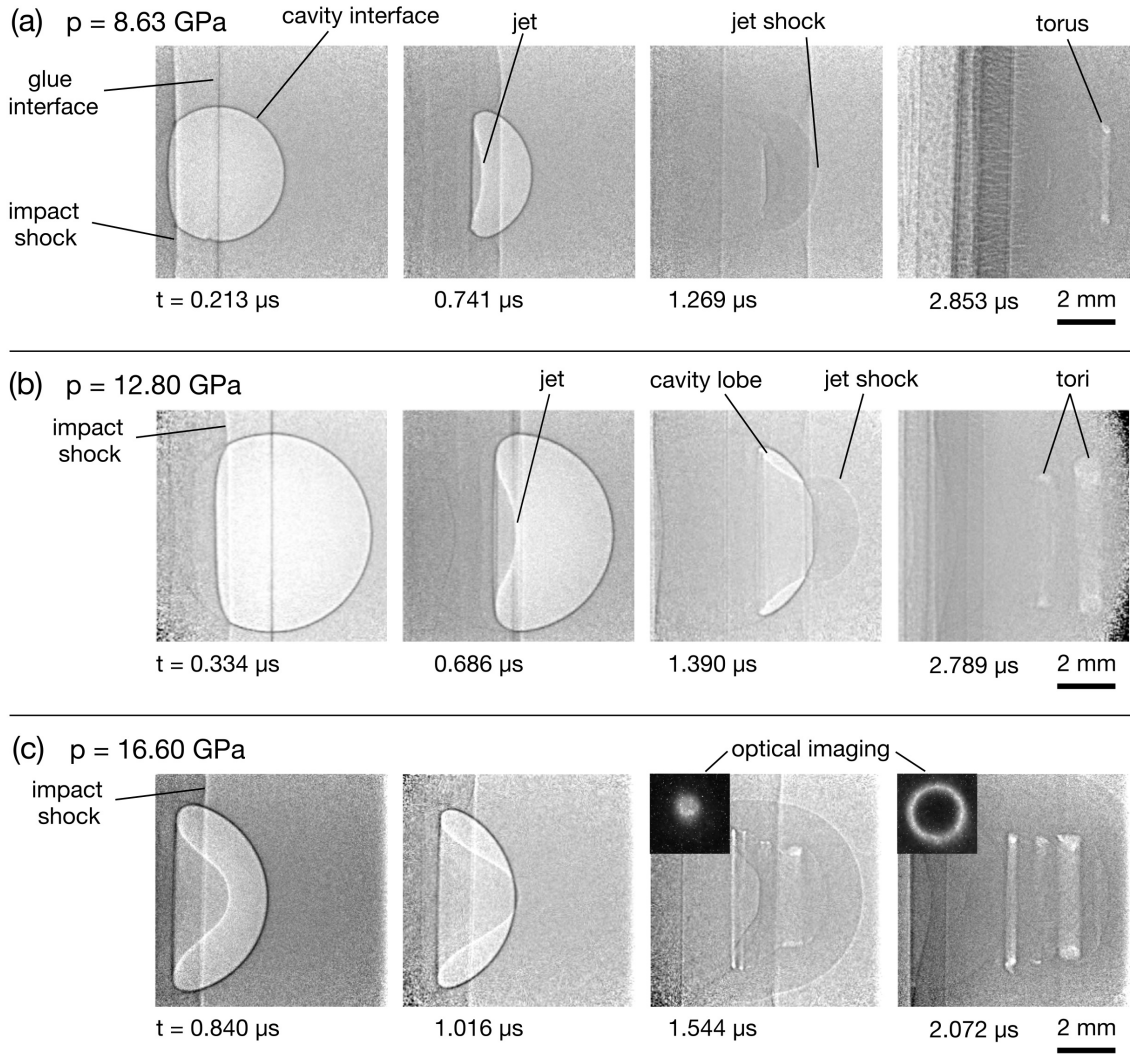


Figure 4.11: Radiograph sequences showing shock-cavity interactions in the hydrodynamic regime. (a) A 4 mm cavity and 8.63 GPa shock. (b) A 6 mm cavity and 12.80 GPa shock. (c) A 6 mm cavity and 16.60 GPa shock, with insets showing the rear-surface optical images of the toroidal plasma emission.

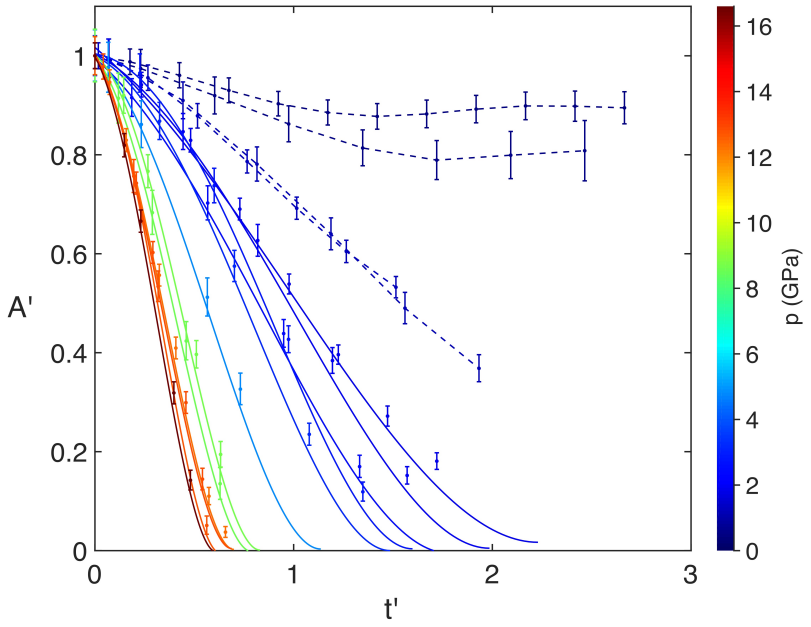


Figure 4.12: Plots of A' vs. t'. The colour bar shows the shock pressure p. In the low-pressure region the dashed lines show the trajectory of the projected area, with a piecewise linear interpolation between each point. In the higher-pressure region the solid lines show the fitting of each curve with Eq. 4.19.

4.3.5 Cavity collapse time evolution

The normalised projected cavity area $A' = A/A_0$, where A is the area at time t and A_0 is initial area, is a quantifiable parameter of cavity collapse. This metric has been used in both experimental [25, 26] and computational studies [38, 52, 53], which are performed with hydrogel and water as the surrounding medium, respectively. These earlier experiments consider cylindrical cavities, in which the cross section remains constant throughout the cavity, and the volume scales with normalised cavity area. In the present study the use of 3D spherical cavities means only the maximum projected area of the cavity can be directly measured from the radiographs, as the cross-sectional area varies with depth. The measured data can be seen in Fig. 4.12, which shows the time evolution of A', with each line representing a single experiment. The horizontal axis is presented in dimensionless time $t' = t/(D_0/C_L)$, where t is in microseconds, D_0 is the initial cavity diameter in millimetres and $C_L = 2.75\,\mathrm{mm/\mu s}$ is the longitudinal sound speed in PMMA [46]. A value of $t' = 1$ thus corresponds to the time taken for

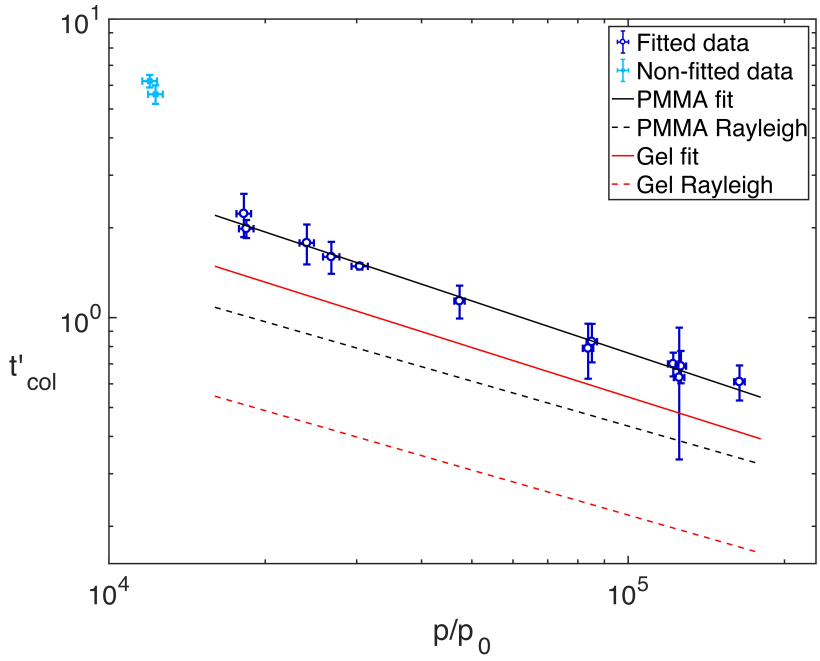


Figure 4.13: Logarithmic plot of t'_{col} vs. p/p_0 for shock-induced and Rayleigh collapse. The open circles show the collapse times obtained from curve fitting and the closed symbols show the collapse times estimated from the radiographs. The solid black line shows the fit for the data, with $p > 1.25\,\mathrm{GPa}$, $t'_{col} = 617(p/p_0)^{-0.58}$, and the solid red line shows the fit from the Swantek & Austin study, $t'_{col,SA} = 305(p/p_0)^{-0.55}$ [26]. The dashed black and red lines show the respective theoretical Rayleigh curves for PMMA, $t'^{R}_{col,PMMA} = 137(p/p_0)^{-0.5}$, and water, $t'^{R}_{col,gel} = 69(p/p_0)^{-0.5}$.

a longitudinal sound wave in PMMA to travel a distance of one cavity diameter. The time $t' = 0$ (which is at the same time as $t = 0$) is defined as the time at which the shock front first reaches the cavity interface. The colours in the plots represent a linear change in the initial shock pressure, from 0 to 16.6 GPa. As expected, there is a steepening of the gradient as the shock pressure increases due to the increased rate of collapse.

For cavities that undergo complete collapse (defined here as cases in which the cavity area is reduced to less than 5% of its initial value), we can define the collapse time t'_{col} as the time at which A' reaches its minimum value. It is not possible to obtain the precise collapse time from the area trajectories, as the exact instant of minimum area is not captured. For the data from the two-stage experiments, this is due to the short duration of the collapse process combined with

the limited frame-separation times of the image sequences from the two-camera imaging system, which are 0.176 μs and 0.352 μs. For example, the 6 mm cavity in Fig. 4.11(b), which is impacted with a 12.80 GPa shock, collapses in approximately 1.5 μs. This means a maximum of five frames can be recorded during the collapse, which doesn't guarantee capturing the final stage of the collapse. Furthermore, for the single-stage experiments, the increased level of fragmentation in the PMMA medium over time means that after a certain point it is no longer possible to quantitatively resolve the cavity interface. Therefore, for the cavities that do collapse, t'_{col} is found either by fitting the collapse curves or by estimating the collapse time from the radiographs (when fitting is not appropriate). These two processes are described below. At the two lowest shock pressures studied (0.49 GPa and 0.60 GPa) the cavities do not undergo complete collapse. Rather, failure along the cavity interface breaks up the cavity before total collapse can occur.

Complete collapse is observed at shock pressures of 1.25 GPa and above. Jet formation, jet impact and tori formation are observed at shock pressures greater than 8.49 GPa (Fig. 4.12). Between 1.84 GPa and 4.80 GPa, rather than forming a jet, the shape of the interface during collapse is more similar to the symmetrical shape produced by hydrostatic Rayleigh collapse. At these lower shock pressures, the pressure field forms around the cavity after the shock passes, akin to the hydrostatic pressure field in an extended fluid region. A similar result is observed in the simulations of Austin et al. [20], which includes the interaction between a 9.4 GPa shock and 1 μm cavity in HMX. They also note high levels of deviatoric stresses around the cavity, which causes highly localised temperature regions in the form of shear bands. The surface perturbations and crack formation visible in Fig. 4.9 also suggest the presence of this type of shear localisation.

For the experiments in which total collapse is observed, a non-linear relationship between the dimensionless collapse time t'_{col} and the shock pressure p is

observed. Such non-linearity is predicted in the analysis of Rayleigh collapse, which shows the dimensionless collapse time scales inversely with the square root of the pressure difference between the fluid pressure in the liquid medium far from the cavity and the vapour pressure of the gas inside the cavity [2, 54]. A similar scaling is found for the hydrostatic collapse of a cavity near a solid boundary, with an extra prolongation factor to account for the non-spherical shape of collapse [55]. An inverse square root dependency has also been found for numerical simulations of shock-induced collapse, showing remarkable similarities between Rayleigh collapse and shock-induced collapse, despite their notable differences [38, 56]. However, a deviation from this exponent is found by Swantek & Austin, who look at the collapse times of shock and stress wave induced hydrodynamic collapse of cylindrical cavities in agarose-GGB gel [26]. As in the present study, millimetre-sized cavities are used. Including data from a similar Dear & Field study [57], they found that the dimensionless minimum volume time against the pressure ratio p/p_0, where p_0 is the initial pressure of the surrounding medium, follows the power-law relationship,

$$t'_{col,SA} = 305\left(\frac{p}{p_0}\right)^{-0.55}, \tag{4.17}$$

where $t'_{col,SA}$ is the time to minimum volume found by Swantek & Austin [26].

In the present work, the dimensionless collapse time t'_{col} is determined from the plots in Fig. 4.12. As the exact collapse time for each cavity is not known, it is necessary to fit a function to each collapse curve to find the time of minimum area t'_{col}. A functional form is chosen with the boundary conditions that the area is initialised at a normalised value of 1, and decreases according to a square dependence on an effective radius, r^*,

$$A' = r^{*2} + c. \tag{4.18}$$

The constant c allows for cases when the area does not completely fall to zero. After comparing functional forms to hydrocode simulations run in Hytrac, the effective radius that most closely matched the simulation data is $r^{*2} = (1 - at' - bt'^2)$, where a, b and c are fitting parameters, yielding the following expression for normalised projected area,

$$A' = (1 - at' - bt'^2) + c. \tag{4.19}$$

For two of the experiments the cavities do not collapse. These can be seen as the two dashed lines in the top of the figure that increase in area after reaching a minimum. For the next two highest pressures, although the cavities do collapse, the functional form does not agree with the collapse times observed in the radiographs. These curves, which show the 1.21 GPa and 1.25 GPa experiments, are shown as the two blue dashed lines in the middle of Fig. 4.12. The collapse times are instead estimated from the radiographs. For all the fitted curves, shown as solid lines in the figure, the collapse times agreed well with the apparent collapse times observed from the radiographs. Using a p_0 value of 1 atm $= 1.01 \times 10^5$ Pa to determine the pressure ratio, the power-law relationship is determined from a linear fit of the p/p_0 vs. t'_{col} logarithmic plot, which is shown in Fig. 4.13. Rearranging the logarithmic form gives,

$$t'_{col} = 617\left(\frac{p}{p_0}\right)^{-0.58}, \tag{4.20}$$

with an R^2 value of 0.99 determined by the fitting. The two closed-symbol points in the top left of the figure show the collapse times estimated from the radiographs, for the 1.21 GPa and 1.25 GPa experiments, which are not used in the power-law fitting. This behaviour away from the power law is possibly explained either by a change in failure mode from cracking to flow, or because of release effects at later times. In terms of the power relationship, this is in strong agreement

with the Swantek & Austin finding in Eq. 4.17 [26]. This is perhaps unexpected given the differences between the experimental arrangements: in the present study spherical cavities are used, as opposed to cylindrical; the pressure ratios explored are an order of magnitude greater; and the initial state of the cavity medium is a solid, rather than a liquid. The closely matched exponents thus suggest a universal mechanism underlying the collapse of cylindrical and spherical cavities, in both liquid and solid media.

Also shown in Fig. 4.13 are dashed black and red lines, showing the collapse time vs. pressure ratio for Rayleigh collapse in PMMA and water respectively. The Rayleigh model [2, 54], which applies to the hydrostatic compression of a bubble in an infinite fluid, predicts a collapse time based on the density ρ and pressure p of the fluid, given by,

$$t^R_{col} = 0.4573 D_0 \sqrt{\rho/p}. \tag{4.21}$$

To plot the dimensionless Rayleigh collapse time, the same scaling is used as for the data, such that,

$$t'^R_{col} = t^R_{col}/(D_0/C_L) = 0.4573 C_L \sqrt{\rho/p}. \tag{4.22}$$

This gives respective expressions for PMMA and agarose-GG gel of,

$$t'^R_{col,PMMA} = 137(p/p_0)^{-0.5} \tag{4.23}$$

and

$$t'^R_{col,gel} = 69(p/p_0)^{-0.5}. \tag{4.24}$$

Despite the strong agreement in the exponents of experimental scaling laws for the present work and the Swantek & Austin study, there is a significant offset between the two lines, caused by a large difference in their multiplicative factors. Interestingly, for both shock-induced collapse (solid lines) and Rayleigh collapse

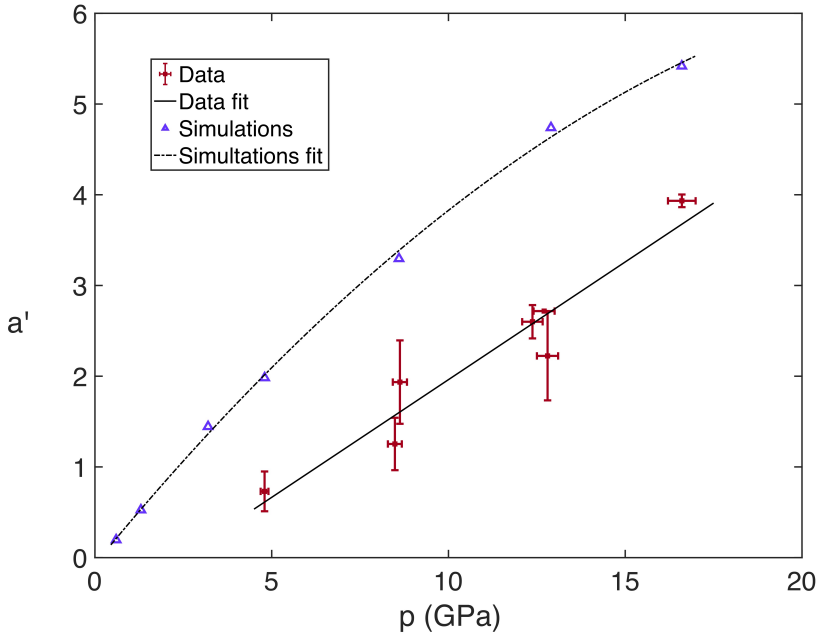


Figure 4.14: Plots of a' vs. p, with the data for the experiments with shock pressures of 4.80 GPa and above. The solid line shows the linear fit of the experimental data and the dashed line shows the quadratic fit for the simulations.

(dashed lines), the same ratio is observed between the factors for PMMA and the gel: $617/305 = 137/69 = 2.0$. This ratio can be explained by the difference in sound speed and density of the two materials, which are used to calculate the scaled collapse time for the Rayleigh expressions: $C_{L_{PMMA}}\sqrt{\rho_{PMMA}}/C_{L_{gel}}\sqrt{\rho_{gel}} = 2.0$, where the gel sound speed has been taken from Swantek & Austin and the gel density is assumed to be that of water.

4.3.6 Cavity interface dynamics

After the release of the shock at the upstream cavity interface, the centre of the interface moves downstream with displacement x. By introducing a dimensionless interface displacement $x' = x/D_0$, the dimensionless acceleration a', assuming constant acceleration, is determined by fitting the quadratic relationship,

$$x' = (a'/2)t'^2 + v_0't', \tag{4.25}$$

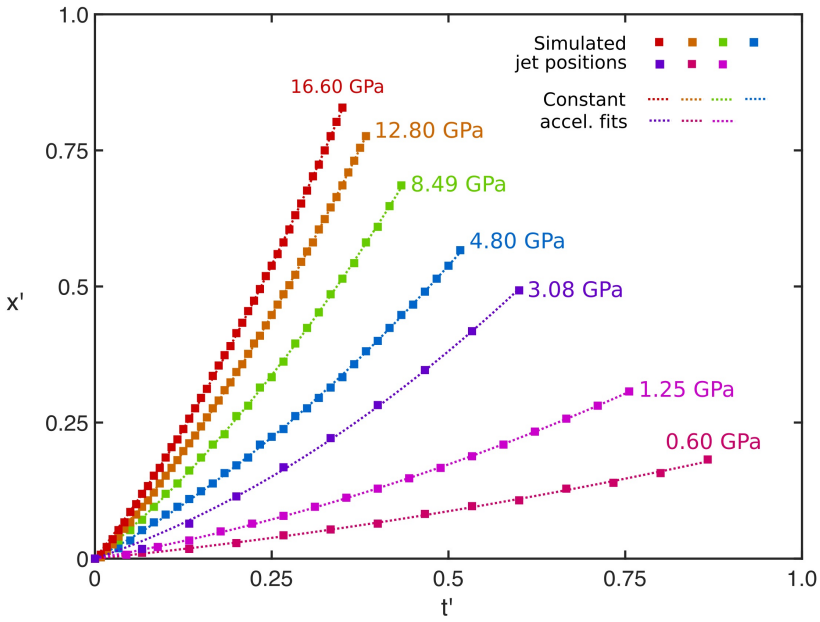


Figure 4.15: Plots of x' vs. t' extracted from simulations in Hytrac, with constant-acceleration quadratic fits.

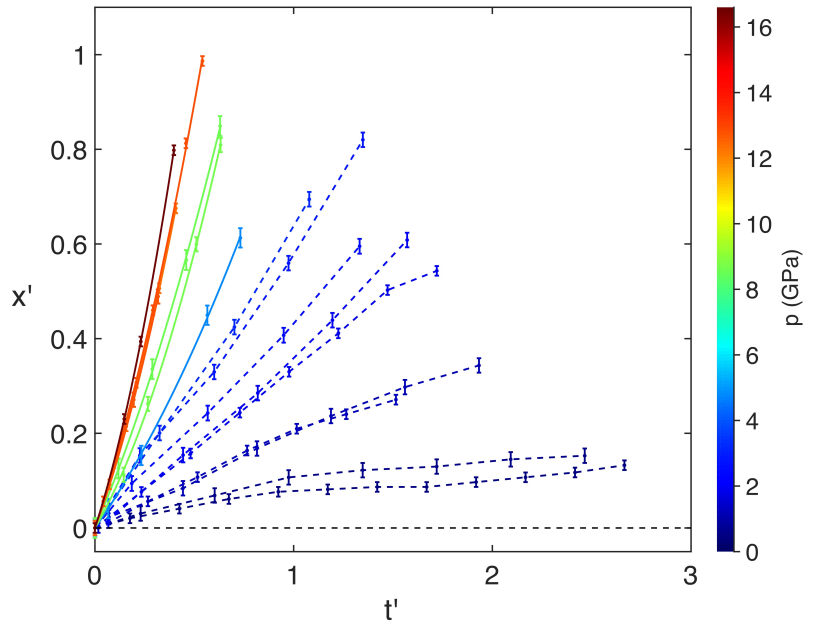


Figure 4.16: Plots of x' vs. t'. The solid lines show a quadratic fit for each interaction and a linear change in the initial shock pressure p is represented by the colour bar. The dashed lines show a piecewise linear interpolation of the low-pressure data.

where v_0' is the initial dimensionless velocity. This assumption is supported by analysis of x' vs. t' curves extracted from hydrodynamic Hytrac simulations over the full range of shock pressures studied experimentally, shown in Fig. 4.15. The quadratic fits of the seven curves have R^2 values in excess of 0.99, confirming constant jet acceleration is a characteristic of cavity collapse in fluids. The plots from the experimental data are shown in Fig. 4.16, where the colour bar represents a linear scaling of p. Contrasted to the simulation plots, for the weaker shocks below $p = 4.80\,\mathrm{GPa}$ the curves are not well-fitted by constant acceleration. The trajectories of these displacements are instead shown as dashed lines with piece-wise linear interpolation between the points. This demonstrates the assumption of constant acceleration is not valid in the strength regime.

Fig. 4.14 shows the results of the fitted acceleration parameter a' as a function of shock pressure p, for both the Hytrac simulations and the data extracted from the radiographs above $p = 4.80\,\mathrm{GPa}$. The simulation data is best fitted by a quadratic relationship given by,

$$a'_{sim} = -0.01p^2 + 0.48p - 0.07, \tag{4.26}$$

with an R^2 value of 0.99. However, the experimental data is adequately described by a linear relationship,

$$a'_{data} = 0.29p - 0.93, \tag{4.27}$$

with an R^2 value of 0.98. Notwithstanding the difference in dimensionality between the simulations and experiments (2D cylindrical vs. 3D spherical), the clearest source of the model deviating from the radiographic results is the lack of a strength model in the simulations. If the effects of strength were to abruptly disappear above the transition to fluid-like behaviour, we would expect the experimental curve to quickly converge with the simulations. Instead we see a consistent offset in the acceleration values, suggesting the effects of strength persist and influence the dynamics of cavity collapse in PMMA at shock pressures in ex-

cess of 16.60 GPa. These observations will be investigated in future work using simulations that include a strength model.

4.3.7 Fourier analysis of interface perturbations

As discussed in the methods Section of this Chapter, Fourier analysis is applied to the surface perturbations that form along the cavity interface at lower impact velocities. The results presented in this sub-section are additional and not in the published Scientific Reports paper. Of the experiments, seven are in the low-velocity range and exhibit perturbations, and for six of those the data is of sufficient quality to perform the analysis. For the 4 mm cavities, these are for the impacts that generated shock pressures of 0.60 GPa, 1.21 GPa and 1.86 GPa, and for the 6 mm cavities, shock pressures of 0.49 GPa, 1.25 GPa and 1.84 GPa.

The mean spacing λ is calculated for the frames in the experiments in which the perturbations are visible, for which the deformation is not so severe that the cavity interface has not collapsed beyond the initial 'centre of mass', and for which there are not multiple readings per lineout due to the interface overlapping during deformation. These restrictions mean that between two and four frames can be analysed per experiment. Each of these frames provides a λ value that can be tracked over time. The frames for which analysis could be performed are shown in Fig. 4.17 and Fig. 4.18, for the 4 mm and 6 mm cavity results, respectively. Of the four frames shown for each experiment, the analysed frames are highlighted. The highlight colour is the same as the colour for the extracted data points show in Fig. 4.19, where λ is plotted against time t, and the colour in turn represents the shock pressure p.

We see in Fig. 4.19 that the spacing λ is inversely dependent on both the impact velocity and time. The perturbations spacing decreases over time, as the cavity is further deformed, for two reasons. Firstly, more perturbations form in between existing perturbations. This effect is visible as the sudden drop from the first data

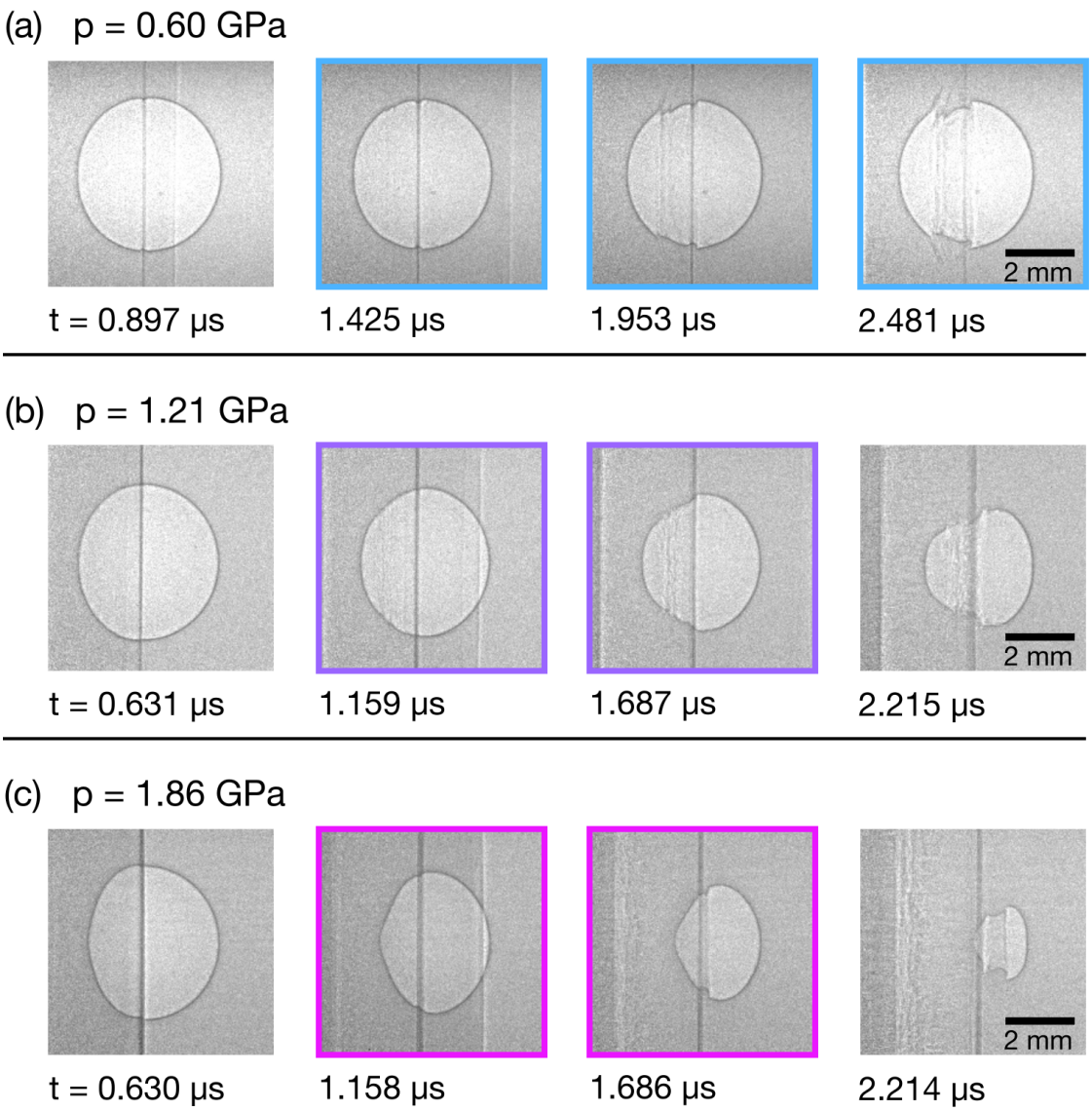


Figure 4.17: The 4 mm cavity radiographs in the low-pressure region. Perturbation analysis is performed on the highlighted frames, where the colours match the colour representation of the data points in Fig. 4.19, which corresponds to shock pressure p.

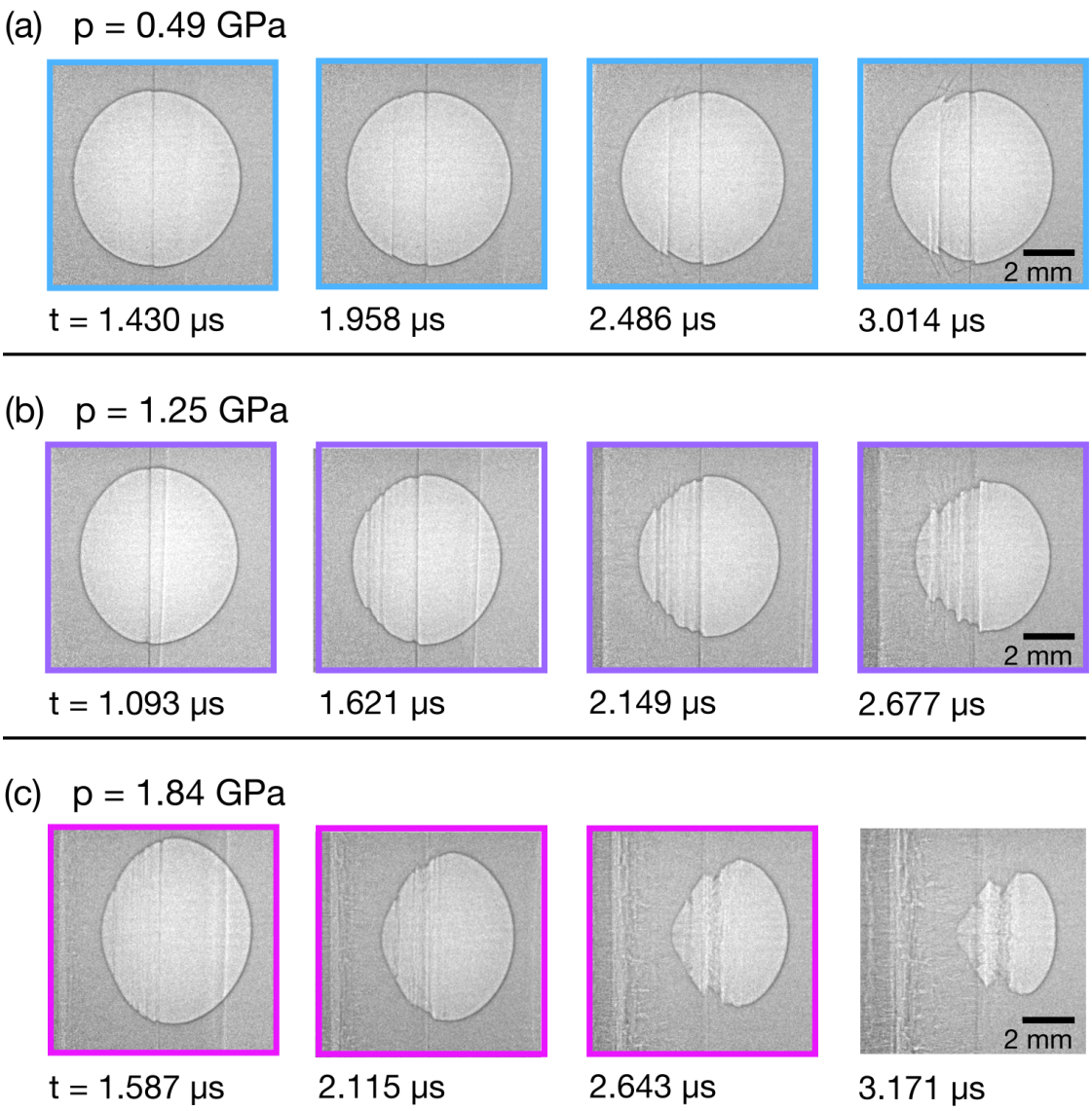


Figure 4.18: The 6 mm cavity radiographs in the low-pressure region. Perturbation analysis is performed on the highlighted frames, where the colours match the colour representation of the data points in Fig. 4.19, which corresponds to shock pressure p.

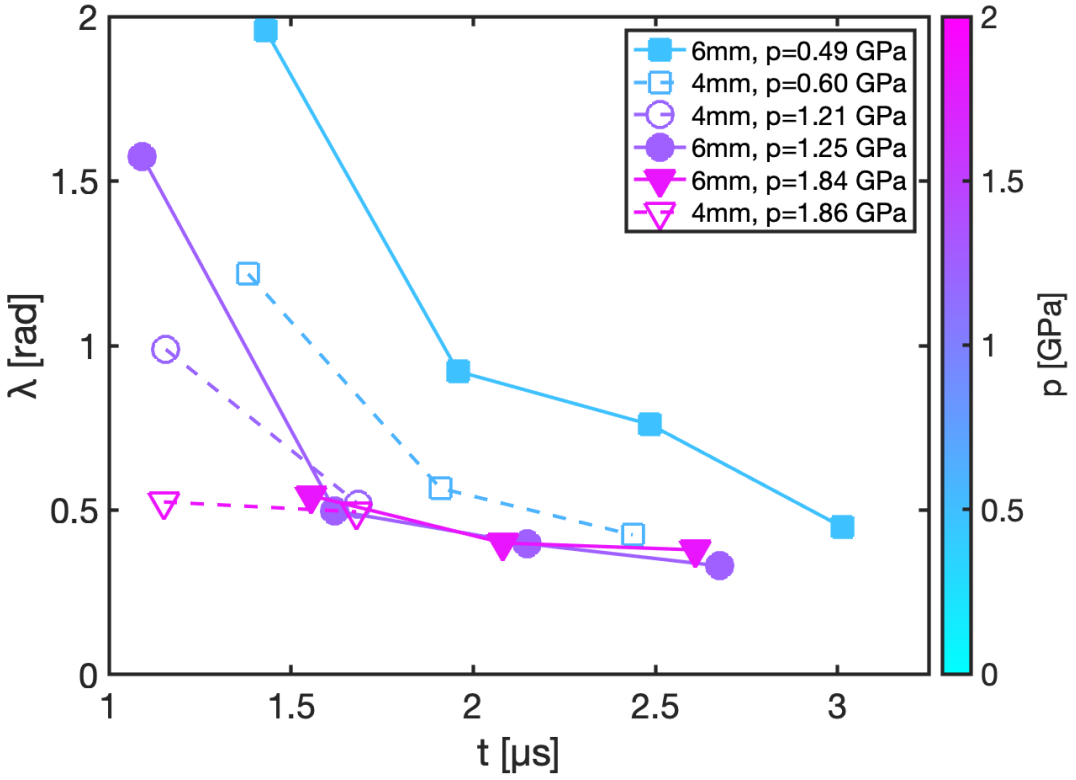


Figure 4.19: Plot showing the mean peak spacing λ vs. time t for the experiments that exhibit perturbations during collapse. The colour bar shows the shock loading pressure, p.

point for four of the lines in the plot. Secondly, the cavity perimeter decreases as the cavity collapses, thus compressing the perturbations closer together. This is the steady drop after the initial fall. For two of the experiments, the 4 mm cavities with shock pressures of 1.21 and 1.86 GPa, only two data points are available, meaning it is harder to draw conclusions about them. Nonetheless, the points lie within their expected values, given the other results.

Again from Fig. 4.19, we see the initial spacing is also initially less at higher particle velocities, due to the finer formation of shear banding, which is thought to be the origin of the perturbations [58, 59]. The increased pressure in the PMMA medium leads to a decrease in the spacing through the increase in bulk heating that occurs with higher shock pressures. The limit of this is that the bands become so fine as to not be detectable, at which point the deformation takes on a qualitatively hydrodynamic appearance, as is observed for shock pressures of

2.72 GPa and above. The pressure at which this transition occurs will vary greatly depending on the solid material a cavity or set of cavities is situated in.

4.4 Discussion

There is a visible transition in the radiographs of Fig. 4.9-4.11, from strength-dominated to fluid-dominated dynamics with increasing shock pressure. For the lowest shock pressures strength features are dominant in PMMA, with high levels of surface perturbations and damage. In the mid-range of pressures between 1.84 and 3.08 GPa material flow becomes the dominant deformation mechanism, with the collapse highly symmetric and qualitatively similar to the shape of hydrostatic Rayleigh collapse (see Fig. 4.10). The cavities are observed to collapse above 1.25 GPa, with those at 1.84 GPa and above obeying a power law relationship. The remarkable similarity to the relationship found by Swantek & Austin [26] suggests that cavity collapse in this regime can at least in part be described in terms of hydrodynamic scaling and points to an underlying universality of shock-induced cavity collapse, even for spherical cavities in solid media and at pressures ratios an order of magnitude greater. Furthermore, the offset between the PMMA data and the gel data can be explained by the differences in sound speed and density, for both the analytic Rayleigh collapse times and the experimental shock-induced data. Hydrodynamic simulations of the experiments, which do not include a strength model, predict a constant acceleration of the driven cavity interface. Analysis of cavity kinematics from the data show that the motion is not well described by constant acceleration until 4.80 GPa. This indicates that a transition to a hydrodynamic response between 3.08 GPa and 4.80 GPa.

Previous studies identify a change in the U_s-u_p Hugoniot equation of state, from a cubic to linear relationship, at a shock pressure of $\sim$2 GPa [46]. Drawing upon Pastine's equation of state model for polyethylene [60], Carter & Marsh explain

the non-linear region of the curve in terms of the molecular structure of amorphous polymers generally: the forces along the backbone of the polymer chain are an order of magnitude greater than the forces between neighbouring chains. The initial compression of the polymer is thus dominated by the inter-molecular forces in the planes orthogonal to the polymer backbone [48]. By ignoring the spatial dimension along the backbone, the $P(V)$ relationship is modelled in two dimensions, where V is the volume, and then transformed into the U_s-u_p plane. This reproduces the observed cubic shape in the low-pressure region of the Hugoniot. Using the same arguments, Carter & Marsh explain that the linear region above the cubic region in the U_s-u_p Hugoniot is initiated when the initial shock compression reaches a level at which the inter-molecular forces approach a significant value with respect to the forces along the chain. At this point the polymer behaves in the expected manner of a shocked isotropic solid [48].

It is interesting to note that different transitions have been observed within this pressure region in other experiments on the shock response of PMMA: (i) Lacina et al. [46] observe a change in the characteristic relaxation time constant in the rounding of the u_p wavefronts, which increases to a maximum value at 1 GPa before decreasing rapidly until 2 GPa; (ii) A sudden increase in the dielectric constant above 2 GPa is observed by Hauver [61] and Graham [62]; (iii) A similar increase in the temperature of shocked PMMA at this pressure is observed by Bloomquist & Sheffield [63, 64]; (iv) Jordan et al. [65] measure the dependence of the strength on impact pressure, combining their data with that of an earlier Millet & Bourne study [66]. They observe an approximate plateau in shear strength with increasing shock pressure above 2 GPa, indicative of a transition to hydrodynamic behaviour [16]. Although the precise mechanisms which underlie these phenomena have yet to be established, these studies point to a significant transition in the shock response of PMMA at shock pressures of $\sim$2 GPa. In the present work, this transition is manifest as a change in the collapse characteristics of cavities in PMMA, from a strength-dominated mode to a hydrodynamic

mode in which the collapse energy is either distributed throughout the cavity periphery, or concentrated within the jet. Interestingly, this is the approximate pressure at which the collapse times begin to fall on the power-law relationship curve (1.84 GPa and above), which extends into the hydrodynamic regime, suggesting this may correspond to a change in collapse dynamics and the onset of a transition to fluid-like behaviour. This transition demarcates distinct regimes of dynamic material behaviour differing in how shock energy is internalised, which furthermore can play an important role in driving processes that depend upon the precise distribution of energy.

One example of the importance of shock energy distribution lies in the impact initiation of energetic materials. Mesoscale simulations of shock-cavity interactions in HMX by Rai et al. [67] reveal similar collapse dynamics as observed in the present study: (i) the presence of perturbations and shear localisation in the weak shock regime; (ii) intermediate strength shocks producing weak jetting; and (iii) strong shocks generating pronounced jets and high levels of vorticity and mixing after collapse. The results also predicted a dependence between shock loading pressure and the size and shape of hot spots, key to yielding a sustained reaction, with the reaction threshold further linked to the ratio of shock strength to the yield stress of HMX.

In the present work, the presence of tori in the experiments for shock pressures 8.49 GPa and above also indicate high levels of vorticity (see the tori in the images of Fig. 4.11 (b)&(c)). This phenomenon, which has been observed in gaseous [22, 23] and liquid [25] media, indicates a high level of material mixing, which is necessary for prompt, non-diffusive mass transport of reactants [68]. Furthermore, the perturbations that occur during collapsing PMMA cavities appear to closely match those in the simulations of HMX cavities [20, 21, 67]. In these studies, localised heating in the form of shear band is identified as the cause of the perturbations, which leads to intense hotspot formation at the cavity closure

site. Therefore, a comparison between the experiments and simulations will further validate the capacity of numerical simulations to inform the conditions occurring during cavity collapse over a wide range of loading conditions.

The decrease in spacing between the perturbations is indicative of a decrease in the spacing between the shear bands, which leads to a greater proportion of melted material in the PMMA cavity medium. Spacing between the bands is related to the strain in a loaded material [59, 69, 70], which in turn increases with shock loading [16]. This may explain the decrease in perturbation spacing, since, as simulations on HMX have shown [20, 21], they are the seed sites of shear bands. At a certain point the spacing becomes so small that bulk melt has occurred and a transition to the hydrodynamic regime is complete. However, as we saw, the lingering effects of strength and viscosity likely still play an important role.

4.5 Summary

High-speed radiography has been used to reveal sub-surface the time evolution of features during shock-induced cavity collapse in a solid. These include surface perturbations and crack propagation for weaker shocks, and jet and tori formation for strong shocks. A transition from brittle fracture to material flow is observed, and, consistent with studies that have looked at shock-cavity interactions in liquids, analysis of the normalised projected cavity area vs. dimensionless collapse time reveal a power law relationship between the collapse time and shock pressure at 1.84 GPa and above. Surprisingly, this relationship holds across the shock regimes, from strength-dominated to hydrodynamic. Strength-free simulations performed in Hytrac exhibit constant jet acceleration during hydrodynamic collapse, suggesting this to be a common characteristic of fluids. However, the present experimental measurements reveal more complex collapse kinematics, with the onset of jet formation and constant acceleration be-

haviour occurring at pressures in excess of 4.80 GPa. Taken alone, these observations might imply a complete loss of strength at this critical pressure. The persistence of an offset between the measurements and the ideal fluid behaviour rather indicates the prevailing effects of strength well above this transition.

We present here previously unobserved features of shock-induced cavity collapse in a solid medium. The results showcase the latest developments in UHS synchrotron imaging capabilities, which allow sub-surface dynamics of transient events to be captured to an unprecedented level of detail. The quality of the data and its broad scope will be essential for the development and improvement of new models governing the dynamic behaviour of solids in both the strength and hydrodynamic regimes, as well the less-explored transition regime. Specifically, we expect the direct observations of hydrodynamic phenomena such as jet formation, impact and tori formation to be an invaluable resource for research into medical treatments where cavity collapse plays a central role. Additionally, new details on the richness and complexity of strength-mediated collapse, with perturbation and crack formation from localised heating and damage, will help guide the design of improved materials for harnessing and releasing energy.

4.6 References

[1] E M Escauriza, J P Duarte, D J Chapman, *et al.*, "Collapse dynamics of spherical cavities in a solid under shock loading," *Sci. Rep.*, vol. 10, pp. 1–16, may 2020.

[2] L Rayleigh, "VIII. On the pressure developed in a liquid during the collapse of a spherical cavity," *Philos. Mag.*, vol. 34, no. 200, pp. 94–98, 1917.

[3] M Kornfeld and L Suvorov, "On the Destructive Action of Cavitation," *J. Appl. Phys.*, vol. 15, p. 495, 1944.

[4] C Naudé and A T Ellis, "On the Mechanism of Cavitation Damage by Non-hemispherical Cavities Collapsing in Contact With a Solid Boundary," *J. Basic Eng.*, vol. 1, pp. 1–9, 1961.

[5] J E Field, "The physics of liquid impact, shock wave interactions with cav-

ities, and the implications to shock wave lithotripsy," *Phys. Med. Biol.*, vol. 36, no. 11, pp. 1475–1484, 1991.

[6] T Kodama and K Takayama, "Dynamic Behaviour of Bubbles During Extracorporeal Shock-Wave Lithotripsy," *Ultrasound Med. Biol.*, vol. 24, no. 5, pp. 723–738, 1998.

[7] G N Sankin and P Zhong, "Interaction between shock wave and single inertial bubbles near an elastic boundary," *Phys. Rev. E*, vol. 74, no. 046304, 2006.

[8] T Kodama, Y Tomita, Y Watanabe, *et al.*, "Cavitation Bubbles Mediated Molecular Delivery During Sonoporation," *J. Biomech. Sci. Eng.*, vol. 4, no. 1, 2009.

[9] R Browning and E Stride, "Microbubble-Mediated Delivery for Cancer Therapy," *Fluids*, vol. 3, no. 4, p. 74, 2018.

[10] C D Ohl, M Arora, R Dijkink, *et al.*, "Surface cleaning from laser-induced cavitation bubbles," *Appl. Phys. Lett.*, vol. 89, no. 074102, 2006.

[11] G L Chahine, A Kapahi, J K Choi, and C T Hsiao, "Modeling of surface cleaning by cavitation bubble dynamics and collapse," *Ultrason. Sonochem.*, vol. 29, pp. 528–549, 2016.

[12] B Verhaagen and D F Rivas, "Measuring cavitation and its cleaning effect," *Ultrason. Sonochem.*, vol. 29, pp. 619–628, 2016.

[13] A W Campbell, W C Davis, and J R Travis, "Shock Initiation of Detonation in Liquid Explosives," *Phys. Fluids*, vol. 4, no. 4, pp. 498–510, 1961.

[14] A W Campbell, W C Davis, J B Ramsay, and J R Travis, "Shock Initiation of Solid Explosives," *Phys. Fluids*, vol. 4, no. 4, p. 511, 1961.

[15] C L Mader, "Initiation of Detonation by the Interaction of Shocks with Density Discontinuities," *Phys. Fluids*, vol. 8, no. 10, pp. 1811–1816, 1965.

[16] M A Meyers, "Shock Waves," in *Dyn. Behav. Mater.*, ch. 4, pp. 98–122, New York: John Wiley & Sons, Inc., 1994.

[17] D Ranjan, J Oakley, and R Bonazza, "Shock-Bubble Interactions," *Annu. Rev. Fluid Mech.*, vol. 43, no. 1, pp. 117–140, 2011.

[18] A Kapahi and H S Udaykumar, "Three-dimensional simulations of dynamics of void collapse in energetic materials," *Shock Waves*, vol. 25, pp. 177–187, 2015.

[19] N K Rai and H S Udaykumar, "Three-dimensional simulations of dynamics of void collapse in energetic materials," *Phys. Rev. Fluids*, vol. 3, no. 033201, 2018.

[20] R A Austin, N R Barton, J E Reaugh, and L E Fried, "Direct numerical simulation of shear localization and decomposition reactions in shock-loaded HMX crystal," *J. Appl. Phys.*, vol. 117, p. 185902, 2015.

[21] H K Springer, S Bastea, A L Nichols, *et al.*, "Modeling The Effects of Shock Pressure and Pore Morphology on Hot Spot Mechanisms in HMX," *Propellants, Explos. Pyrotech.*, vol. 43, no. 8, pp. 805–817, 2018.

[22] J F Haas and B Sturtevant, "Interaction of weak shock waves with cylindrical and spherical gas inhomogeneities," *J. Fluid Mech.*, vol. 181, pp. 41–76, 1987.

[23] D Ranjan, M Anderson, J Oakley, and R Bonazza, "Experimental Investigation of a Strongly Shocked Gas Bubble," *Phys. Rev. Lett.*, vol. 20, no. 184507, 2005.

[24] J P Dear, J E Field, and A J Walton, "Gas compression and jet formation in cavities collapsed by a shock wave," *Nature*, vol. 332, no. 7, pp. 505–508, 1988.

[25] N K Bourne and J E Field, "Shock-induced collapse of single cavities in liquids," *J. Fluid Mech.*, vol. 244, pp. 225–240, 1992.

[26] A B Swantek and J M Austin, "Collapse of void arrays under stress wave loading," *J. Fluid Mech.*, vol. 649, pp. 399–427, 2010.

[27] X Ma, X Li, X Zheng, *et al.*, "Weak shock loadings induce potential hot spots formation around an intergranular pore," *J. Appl. Phys.*, vol. 121, no. 115102, 2017.

[28] B J Jensen, S N Luo, D E Hooks, *et al.*, "Ultrafast , high resolution , phase contrast imaging of impact response with synchrotron radiation Ultrafast , high resolution , phase contrast imaging of impact," *AIP Adv. 2*, vol. 2, no. 012170, 2012.

[29] B J Jensen, C T Owens, K J Ramos, *et al.*, "Impact system for ultrafast synchrotron experiments," *Rev. Sci. Instrum.*, vol. 84, no. 1, 2013.

[30] D E Eakins and D J Chapman, "X-ray imaging of subsurface dynamics in high-Z materials at the Diamond Light Source," *Rev. Sci. Instrum.*, vol. 85, no. 12, 2014.

[31] M P Olbinado, X Just, J L Gelet, *et al.*, "MHz frame rate hard X-ray phase-contrast imaging using synchrotron radiation," *Opt. Express*, vol. 25, no. 12, 2017.

[32] M E Rutherford, D J Chapman, J G Derrick, *et al.*, "Probing the early stages of shock-induced chondritic meteorite formation at the mesoscale," *Sci. Rep.*, vol. 7, may 2017.

[33] E M Escauriza, A Rack, E Synchrotron, *et al.*, "Ultra high-speed indirect X-ray imaging system with versatile spatio-temporal sampling capabilities," *Appl. Opt.*, vol. 57, no. 18, pp. 5004–5010, 2018.

[34] D J Miller, R S Crum, M A Homel, *et al.*, "Hugoniot Measurements Utilizing In Situ Synchrotron X-ray Radiation," *J. Dyn. Behav. Mater.*, 2019.

[35] B Branch, A Ionita, B E Clements, *et al.*, "Controlling shockwave dynamics using architecture in periodic porous materials," *J. Appl. Phys.*, vol. 121, no. 13, 2017.

[36] M Armstrong, E Bukovsky, W Shaw, *et al.*, "Time-resolved X-ray Imaging of Void Collapse in Silicone and TNT," tech. rep., Lawrence Livermore National Lab.(LLNL), Livermore, CA (United States), 2018.

[37] E Johnsen and T Colonius, "Shock-induced collapse of a gas bubble in shockwave lithotripsy.," *J. Acoust. Soc. Am.*, vol. 124, no. 4, pp. 2011–20, 2008.

[38] E Johnsen and T Colonius, "Numerical simulations of non-spherical bubble collapse," *J. Fluid Mech.*, vol. 629, pp. 231–262, 2009.

[39] R D Richtmyer, "Taylor Instability in Shock Acceleration of Compressible Fluids," *Commun. Pure Appl. Math.*, vol. 8, pp. 297–319, 1960.

[40] E E Meshkov, "Instability of the interface of two gases accelerated by a shock wave," *Fluid Dyn.*, vol. 4, pp. 101–104, sep 1969.

[41] MATLAB, *9.9.0.1495850 (R2020b)*. Natick, Massachusetts: The MathWorks Inc., 2020.

[42] J W Cooley and J W Tukey, "An Algorithm for the Machine Calculation of Complex Fourier Series," *Math. Comput.*, vol. 19, no. 90, p. 297, 1965.

[43] M Frigo and S G Johnson, "FFTW : An Adaptive Software Architecture for the FFT," *Proc. Int. Conf. Acoust. Speech, Signal Process.*, vol. 3, pp. 1381–1384, 1998.

[44] T J Ringrose, H W Doyle, P S Foster, *et al.*, "A hypervelocity impact facility optimised for the dynamic study of high pressure shock compression," *Procedia Eng.*, vol. 204, pp. 344–351, 2017.

[45] S Faik, A Tauschwitz, and I Iosilevskiy, "The equation of state package FEOS for high energy density matter," *Comput. Phys. Commun.*, vol. 227, pp. 117–125, 2018.

[46] D Lacina, C Neel, and D Dattelbaum, "Shock response of poly[methyl methacrylate] (PMMA) measured with embedded electromagnetic gauges," *J. Appl. Phys.*, vol. 123, no. 1855901, 2018.

[47] S P Marsh, "LASL Shock Hugoniot Data," tech. rep., University of California Press, 1980.

[48] W J Carter and S P Marsh, "Hugoniot Equationof State of Polymers," tech. rep., Report No. LA-13006-MS, Los Alamos National Laboratory, 1995.

[49] J H J Niederhaus, J A Grennough, J G Oakley, *et al.*, "A computational parameter study for the three-dimensional shock-bubble interaction," *J. Fluid Mech.*, vol. 594, pp. 85–124, 2019.

[50] N K Rai, M J Schmidt, and H S Udaykumar, "High-resolution simulations of cylindrical void collapse in energetic materials: Effect of primary and secondary collapse on initiation thresholds," *Phys. Rev. Fluids*, vol. 2, no. 043202, 2017.

[51] B Hejazialhosseini, D Rossinelli, and P Koumoutsakos, "Vortex dynamics in 3D shock-bubble interaction," *Phys. Fluids*, vol. 25, no. 11, 2013.

[52] G J Ball, B P Howell, T G Leighton, and M J Schofield, "Shock-induced collapse of a cylindrical air cavity in water: a Free-Lagrange simulation," *Shock Waves*, vol. 10, pp. 265–276, 2000.

[53] C K Turangan, A R Jamaluddin, G J Ball, and T G Leighton, "Free-Lagrange simulations of the expansion and jetting collapse of air bubbles in water," *J. Fluid Mech.*, vol. 598, pp. 1–25, 2008.

[54] C E Brennen, *Cavitation and Bubble Dynamics*. Oxford University Press, 1995.

[55] M Rattray, *Perturbation Effects in Cavitation Bubble Dynamics*. PhD thesis, California Institute of Technology, 1951.

[56] Z Ding and S M Gracewski, "The behaviour of a gas cavity impacted by a weak or strong shock wave," *J. Fluid Mech.*, vol. 309, pp. 183–209, 1996.

[57] J P Dear and J E Field, "A study of the collapse of arrays of cavities," *J. Fluid Mech.*, vol. 190, no. 1944, p. 409, 1988.

[58] D E Grady and M E Kipp, "The growth of unstable thermoplastic shear with application to steady-wave shock compression in solids," Tech. Rep. 1, 1987.

[59] Q Xue, M A Meyers, and V F Nesterenko, "Self-organization of shear bands in titanium and Ti-6Al-4V alloy," tech. rep., 2002.

[60] D J Pastine, "Volume Dependence of the Thermal Expansion of Polymers," *J. Appl. Phys.*, vol. 41, pp. 5084–5087, 1970.

[61] G E Hauver, "Shock-Induced Polarization in Plastics. II. Experimental Study of Plexiglas and Polystyrene," *J. Appl. Phys.*, vol. 36, pp. 2113–2118, 1965.

[62] R A Graham, "Shock-Induced Electrical Activity in Polymeric Solids. A Mechanically Induced Bond Scission Model," *J. Phys. Chem.*, vol. 83, no. 23, pp. 3048–3056, 1979.

[63] D D Bloomquist and S A Sheffield, "Shock-compression temperature rise in polymethyl methacrylate determined from resistivity of embedded copper foils," *Appl. Phys. Lett.*, vol. 38, no. 185, 1981.

[64] D D Bloomquist and S A Sheffield, "Thermocouple temperature measurements in shock-compressed solids," *J. Appl. Phys.*, vol. 51, no. 5260, 1980.

[65] J L Jordan, D Casem, and M Zellner, "Shock Response of Polymethylmethacrylate," *J. Dyn. Behav. Mater.*, vol. 2, pp. 372–378, 2016.

[66] J C F Millett and N K Bourne, "The deviatoric response of polymethylmethacrylate to one-dimensional shock loading," *J. Appl. Phys.*, vol. 88, no. 7037, 2000.

[67] N K Rai and H S Udaykumar, "Void collapse generated meso-scale energy localization in shocked energetic materials: Non-dimensional parameters, regimes, and criticality of hotspots," *Phys. Fluids*, vol. 31, no. 016103, 2019.

[68] D E Eakins and N N Thadhani, "Mesoscale simulation of the configuration-dependent shock-compression response of Ni + Al powder mixtures," *Acta Mater.*, vol. 56, pp. 1496–1510, 2008.

[69] Q Xue, M A Meyers, and V F Nesterenko, "Self organization of shear bands in stainless steel," *Mater. Sci. Eng. A*, vol. 384, no. 1-2, pp. 35–46, 2004.

[70] V F Nesterenko, M A Meyers, and T W Wright, "Self-organization in the initiation of adiabatic shear bands," *Acta Metall.*, vol. 46, no. 1, pp. 327–340, 1998.

Chapter 5

Mechanics of shock induced cavity collapse in poly(methyl methacrylate) (PMMA): Comparison of simulations and experiments

This chapter is based on the paper published in Journal of the Mechanics and Physics of Solids, "N K Rai, E M Escauriza, D E Eakins and H S Udaykumar, *Mechanics of shock induced pore* [cavity] *collapse in poly(methyl methacrylate) (PMMA): Comparison of simulations and experiments*, JMPS **143**, 104075 (2020)" [1]. The experiments were conceived by the author and performed by the author, Dr D E Eakins and other group members, along with scientists at the ESRF and First Light Fusion (see previous Chapter for full experimental authors list). Conceptualisation of the original paper, simulation methodology, and the simulation data and presentation came from Dr N K Rai. Processing, analysis and presenting comparisons of the simulation and experimental data was performed by the author, under the supervision of Dr D E Eakins. All of the listed authors edited the manuscript. As the original manuscript was conceived and the majority por-

tion of it written by Dr N K Rai, content written by him has been heavily adapted to ensure that the contributions included are from the author of the present thesis.

Paper abstract

Head-to-head comparisons are made between calculations and experimental data on shock-driven cavity collapse in the material poly(methyl methacrylate) (PMMA). Simulations are performed using SCIMITAR3D, a sharp-interface Eulerian multi-material code, while plate impact experiments are visualised using ultra-high speed X-ray imaging. The experiments and simulations are conducted over a range of loading conditions; from low strength loading regimes where adiabatic shear banding predominates all the way up to the regime where hydrodynamic cavity collapse is expected. PMMA is modelled using an isotropic rate-dependent plasticity model for the deviatoric stress response and a Tillotson equation of state for the pressure. Calculations are primarily done in 2D, to save computational effort, but a limited number of 3D calculations are also performed to assess the differences entailed by the dimensionality. The 2D calculations are in fairly good agreement with the experimental results, for the evolution of cavity shape. 3D calculations, while quite computationally intense, indeed produce better agreement with experimental data. The computations also agree well with the experiments in delineating the loading strength at which a transition from the strength-dominated to hydrodynamics-dominated cavity collapse occurs. This work provides confidence in the ability of Eulerian, sharp interface computational techniques to correctly represent and understand the mechanics of shock-loaded porous condensed phase materials over a range of loading conditions.

5.1 Introduction

Cavity collapse is an important mechanism for energy localisation in heterogeneous materials, i.e. materials that include regions of voids or other material inclusions. In liquids this localisation results in jet and vortex formation, which has been harnessed for applications in the medical sciences, such as targeted drug delivery [2, 3] and the destruction of kidney and gall stones through shock lithotripsy [4, 5], among others. In solid media, which is the focus of the present work, the energy localisation can be more complex, and has primarily been studied in relation to heterogenous energetic materials (HEMs). Cavity collapse in HEMs leads to energy localisation at hotspots primarily at high loading pressures, when the applied shock leads to pressures considerably exceeding the yield strength of the material. Closer to the yield stress and certainly below it, other mechanisms of energy localisation may play important roles. These may include adiabatic shear bands, plastic dissipation, friction etc. [6]. Numerical simulations must therefore accurately capture the variety of possible energy localisation mechanisms. In this work, we examine the mechanics of shock driven cavity collapse in a solid inert polymer material, poly(methyl methacrylate) (PMMA), under loading regimes where shear bands (at lower loading pressures) and jetting (at higher loading pressures) are the primary modes of energy localisation.

It is well known that cavity collapse in HEMs leads to intense hotspots that can grow into sustained reactive fronts that consume the surrounding solid material. In the case of a single cavity [7–14] or a field of cavities [12, 13, 15], the thermo-mechanics of cavity collapse has now been well studied using simulations. Benchmarking has been done to some extent [10, 16] and issues such as the resolution requirements to obtain reliable calculations of hotspot temperatures have been investigated [10]. However, even for a primarily hydrodynamic collapse, and even in well-studied energetic materials such as HMX and TATB,

comparison of numerical calculations against experimental data for wide range of loading conditions has not yet been achieved. Recent work by Duarte et al. [17] has shown good agreement with experimental data for cavity collapse in HMX in the weak shock loading regime, for a particle velocity behind the shock of 0.1 km/s. Some preliminary, qualitative comparisons for cavity collapse in HMX were also shown in Rai et al. [10] against the experimental cavity collapse interface outlines of Swantek and Austin [12]. However, a quantitative head-to-head comparison of calculated collapse behaviour and temperatures for wide range of loading scenarios against experiments is still lacking, which is a significant gap in the literature on hotspot formation in HEMs. Establishing the accuracy of numerical simulations, particularly as they relate to hotspot ignition and growth, is crucial to enhancing our ability to model and predict the sensitivity of shock-loaded HEMs.

The situation regarding dearth of quantitative comparison between models and experiments is not markedly better for other regimes of cavity collapse. For example, when the shock strength is lowered from pressures of several GPa (flyer impact velocities of km/s) to hundreds of MPa (flyer impact velocities of hundreds of m/s), the importance of inertial flow is diminished. Previous cavity collapse studies in HMX [7, 11, 18] have suggested there can be considerable energy localisation in shear bands emanating from cavity surfaces as the shock strength is lowered. These studies capture the localised plastic dissipation in the adiabatic shear bands using plasticity models that vary in sophistication from semi-empirical isotropic rate-dependent models for HMX [7, 18] to sophisticated – but computationally intensive – calculations using anisotropic crystal plasticity treatments [11]. Both types of calculations produce physically realistic shear band formation, irrespective of the complexity of the material model involved. Rate-dependent plasticity effects appear sufficient to obtain shear bands exhibiting significant temperature excursions (with maximum temperature approaching the melting point). The shock intensity which marks the transition between

inertia-dominated and shear-band dominated energy localisation is not precisely established in these models; the transition point is material dependent. In addition, while some interesting simulations of the shear banding phenomena have been shown [7, 11, 18], no direct comparison with experiments in any energetic material has yet been performed.

The present work addresses the above knowledge gaps by comparing numerical simulations of cavity collapse directly against sub-surface X-ray imaging experiments The head-to-head comparison is performed over a range of loading conditions spanning shock strengths for which shear bands predominate to those firmly in the hydrodynamic range. A sharp interface Eulerian level-set based approach [19–21] is used to calculate the dynamics of a single cavity embedded in a solid material matrix. The geometry used in the simulations mimics that used in experiments, allowing for direct comparison of the deformation of cavities at several time instants. The comparison is performed for the inert non-crystalline material PMMA, which facilitates visualisation in experiments due to its low X-ray attenuation, resulting from its relatively low atomic weight.

The paper is organised as follows. In Section 5.2, a brief summary of the numerical and experimental methods used in this work are presented. Section 5.3 presents the results of the cavity collapse simulations and comparison with experiments over the period of cavity deformation and collapse. 2D and 3D simulation results are compared to each other and to experiments to assess the error resulting from adopting the far more tractable 2D approximation. In Section 5.3.5 cavity collapse in additional materials is simulated to investigate a universal law for collapse time based only on the basic geometrical and material parameters. Section 5.4 summarises the main conclusions of this work.

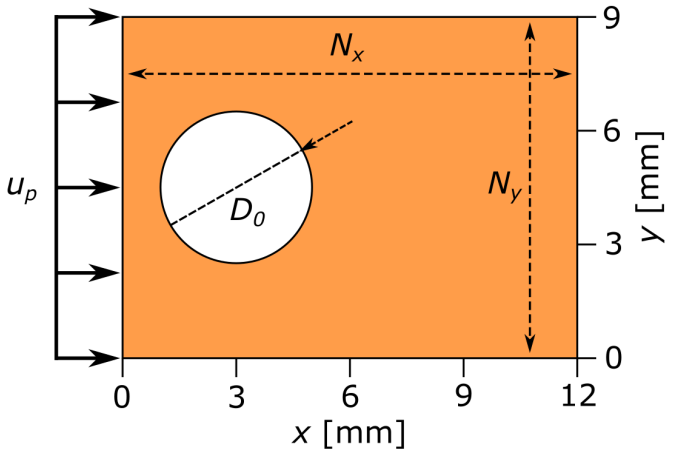


Figure 5.1: Diagram showing the domain setup of the simulations in SCIMITAR3D, with N_x and N_y points across the width and height, respectively. A velocity boundary condition u_p is applied to west face.

5.2 Methods

A detailed overview of the computational and experimental methods is given in the Methods section, in Chapter 2. This is a modification and abbreviation of the original methods in the published JMPS paper, on which this Chapter is based. Firstly, a more concise description of SCIMITAR3D is given, with the details of the material models used in the PMMA simulations. Second, a brief description of the experimental and imaging set-up is given as a recap, along with the relevant parameters used for the plots in the results. Lastly, the method for creating overlay images in the plots is explained.

5.2.1 Computational methods

The simulations are performed in SCIMITAR3D, a Cartesian grid Eulerian based sharp interface code. Cavity collapse in PMMA is modelled as a 2D plane strain (as opposed to axisymmetric) domain filled with PMMA, containing a single void of diameter D_0. A diagram of the domain setup can be seen in Fig. 5.1. A domain height of 9 mm and width 12 mm is used and cavities with D_0 values of 4 mm and 6 mm are modelled. The distance between the cavity and west face is 1 mm.

The grid points have a height and width of 12 µm, giving the number of points

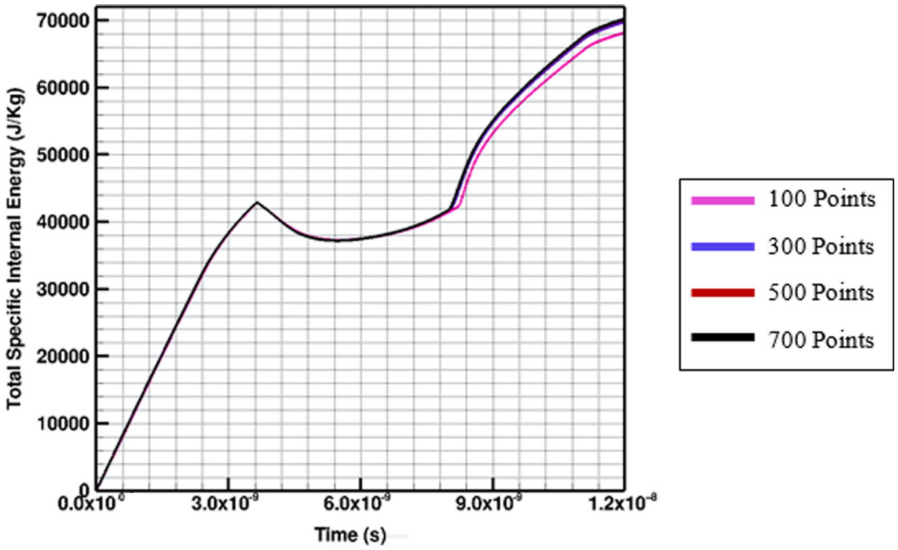


Figure 5.2: Grid convergence of the total specific internal energy varying over time, for a 10 µm cavity driven by a 500 m/s particle velocity shock impulse. Grid sizes of 100, 300, 500 and 700 points across the cavity diameter were studied [22].

across the width of the boundary, N_x, and across the height, N_y, as 1,000 and 750, respectively. The 'grid resolution' is defined as the number of points across the cavity diameter, which, for the 4 mm diameter cavities is 333, and is 500 for the 6 mm cavities. In previous work by Rai et al. [22], grid convergence for the total specific internal energy during cavity collapse is observed to occur between 300 and 500 points. This is demonstrated by the plot from that study in Fig. 5.2.

It is important to recall that experiments are performed on spherical cavities, meaning 3D simulations are necessary to completely recreate the experimental conditions. However, since simulations in 3D are computationally expensive, the behaviour of the spherical cavity is primarily simulated using 2D circular cavities of the same diameter as the spherical cavities. To assess the validity of the 2D approximation in the different loading regimes, two 3D simulations are performed, at low- and high-end of the shock pressure regimes studied experimentally, at $p = 1.25\,\mathrm{GPa}$ ($u_p = 0.32\,\mathrm{km/s}$) and $p = 16.60\,\mathrm{GPa}$ ($u_p = 2.30\,\mathrm{km/s}$), respectively. For the 3D simulations, the simulation setup is analogous to 2D analysis with top and bottom boundaries supplied with zero-gradient boundary, with the same grid dimensions and grid resolution.

A zero-gradient boundary condition is applied to the north, south and east boundaries. A particle velocity u_p is applied to the west boundary. For the simulations that are directly based on experiments, the u_p value is obtained, along with the shock pressure p, from the impedance matching calculations using Eq. 4.16 and detailed in Table 4.2, from Chapter 4. Additional simulations are performed with chosen u_p values. The velocity impulse boundary condition is a step wave of duration t_p,

$$t_p = \frac{2T_f}{U_s}, \tag{5.1}$$

where T_f is the flyer thickness and U_s is the shock speed (also listed in Table 4.2).

For modelling the PMMA medium, the Johnson-Cook plasticity model and Tillotson equation of state (EoS) are used. The PMMA material properties, along with the parameters for these models are listed in Table 5.1.

The isotropic rate dependent Johnson-Cook model is employed [23], in which the yield surface is defined as,

$$\sigma_Y = [A_{JC} + B_{JC}\epsilon_p^n][1 + C_{JC}\ln(\dot{\epsilon}^*)][1 - T^{*m}], \tag{5.2}$$

where σ_Y is the the yield stress, ϵ_p is the equivalent plastic strain, $\dot{\epsilon}^* = \dot{\epsilon}/\dot{\epsilon}_0$ is the dimensionless strain rate ($\dot{\epsilon}$ is the strain rate and $\dot{\epsilon}_0 = 1\,\mathrm{s}^{-1}$). The homologous temperature is $T^* = (T - T_{ref})/(T_{MELT} - T_{ref})$, where T is temperature of the material, T_{MELT} is the melting temperature and $T_{ref} = 298\,\mathrm{K}$ is the reference temperature. Parameters A_{JC}, B_{JC}, n, C_{JC}, m and T_{MELT} are constants, determined for PMMA by T. J. Holmquist et al. [24].

The isotropic rate dependent plastic behaviour of PMMA is modelled until the temperature reaches the melting temperature of PMMA. After melting, the deviatoric stress components, i.e. S_{ij} is set to 0. The mechanical behaviour of PMMA is then only governed by the pressure, which is determined by the Tillotson EoS, developed for high-velocity impact problems, where both low and high pressure

PMMA parameters	
Density, ρ (kg/m^3)	1187
Speed of sound, C_0 (km/s)	2.23
Shear modulus, G (GPa)	5.9
Isochoric specific heat capacity, C_v (J/kg/K) at 298 K	1466
Johnson-Cook (JC) model	
A_{JC} (MPa)	357
B_{JC} (MPa)	90
n	4
C_{JC}	0.077
m	0.74
T_{MELT} (K)	398
Tillotson equation of state	
a	0.85
b	0.0
E_0 (J/K)	7.95e6
A_T (GPa)	5.9
B_T (GPa)	19
α	0.0
β	0.0

Table 5.1: The material model parameters of PMMA used in the SCIMITAR cavity collapse simulations [24, 25].

states can be present [26]. In this formulation, the pressure p in the material is related to the specific total energy E and density ρ, which is contained in the two parameters $\eta = \rho/\rho_0$ and $\mu = 1 - \eta$, where ρ_0 is the initial density. There are two equations, depending on whether the material is under compression or expanding. Under compression with $\eta < 1$,

$$p_c = \left[a + \frac{b}{\frac{E}{E_0\eta^2} + 1}\right] \rho E + A_T\mu + B_T\mu^2, \tag{5.3}$$

where p_c is the pressure under compression, E is the specific internal energy, E_0 is the initial specific total energy, and a, b, A_T and B_T are constants. When the material is expanding, for $\eta < 1$, a different equation is used,

$$p_e = a\rho E + \left[\frac{b\rho E}{\frac{E}{E_0\eta^2} + 1} + A_T\mu e^{-\beta\mu}\right] e^{-\alpha\mu^2}, \tag{5.4}$$

where α and β are two additional constants [26]. The Tillotson constants for PMMA, which are obtained from an S.P. Marsh 1980 report [25], are listed in Table 5.1.

A constant value is used for the specific heat at constant volume, C_v. This is then used to compute the temperature T in the PMMA using,

$$T = T_{ref} + \frac{E - E_0}{C_v}, \tag{5.5}$$

where $T_{ref} = 298\,\mathrm{K}$ is the reference temperature and $C_v = 1466\,\mathrm{J/kg/K}$ [25]. In the present analysis, a constant value of C_v is used to calculate the temperature because a temperature and pressure dependent relation of C_v for PMMA is not available in the literature. The constant C_v assumption can lead to the overestimation of temperature. As a crude estimation, the upper and lower bound of C_v can be used to obtain the bounds on the temperature rise from the cavity collapse in PMMA. The lower bound of C_v at 298 K is used in the current analysis, i.e. $C_v^{298K} = 1466\,\mathrm{J/kg/K}$ and the classical limit (CL) of C_v given by Dulong-Petit law

[27] defines the upper bound of C_v, i.e. $C_v^{CL} = 3741\,\mathrm{J/kg/K}$. The upper bound of temperature, i.e. $T_{C_v^{298K}}$ is obtained using Eq. 5.5 with C_v^{298K}. On the other hand, the lower bound of temperature is given by $T_{C_v^{CL}}$, which is related to $T_{C_v^{298K}}$ as,

$$T_{C_v^{CL}} = T_{ref} + \frac{C_v^{298K}}{C_v^{CL}}(T_{C_v^{298K}} - T_{ref}). \tag{5.6}$$

The temperature data presented in the present work is given by $T_{C_v^{298K}}$, however, it is important to note that in reality the temperature rise from the cavity collapse is expected to vary between $T_{C_v^{CL}}$ and $T_{C_v^{298K}}$, depending on the specific loading conditions.

5.2.2 Experimental methods

The experiments are performed at beamline ID19 of the European Synchrotron Radiation Facility (ESRF), where both a single-stage and a two-stage gas gun are used to dynamically compress targets containing a single spherical cavity under a wide range of shock loading conditions. Figure 5.3 shows the experimental set-up used to study the behaviour of the cavities under shocks. The targets were constructed from PMMA, consisted of two cylindrical sections glued together – see Figure 5.3(b). Nine experiments were performed on the single-stage gas gun, which launched projectiles constructed from a flyer plate attached to the front of a sabot. The targets for these impacts contained cavities with diameters of 4 and 6 mm. A further eight experiments were performed on the two-stage gas gun, for which the sabot diameter was 10 mm. Polycarbonate flyer plates 9 mm in diameter were impacted against targets with cavities 3, 4 and 6 mm in diameter.

With reference to Figure 5.3(a), which shows the configurations for the experimental and imaging systems: to record the cavity deformation under applied loading, a custom indirect ultra-high-speed (UHS) x-ray imaging (XRI) system design was used. UHS is defined here as >1 million frames per second (fps). The

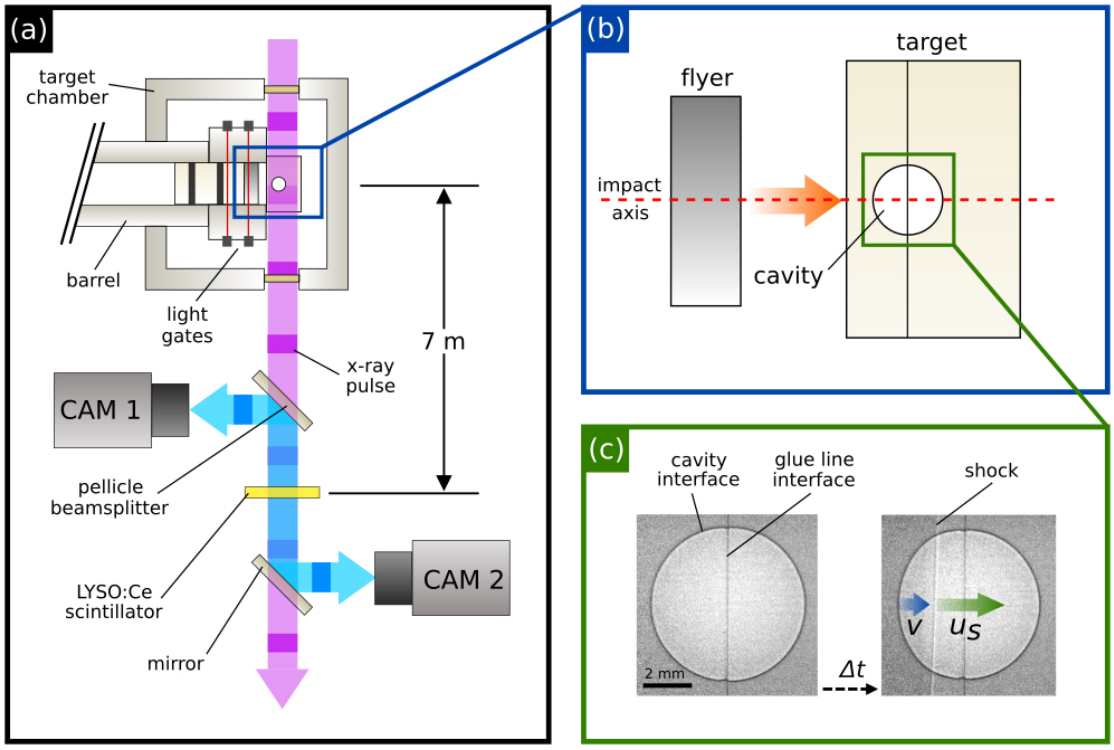


Figure 5.3: Schematic diagram showing details of the experimental setup. (a) The X-rays propagate through the target chamber normal to the impact direction. The imaging system is placed 7 m away from the target in the region of phase contrast enhancement. The X-rays are partially absorbed by the scintillator and re-emitted in visible light, which is captured with two high-speed cameras. (b) Section view of the impact between the flyer and cavity target, which is symmetric about the impact axis. The target is constructed from two cylindrical sections glued together. (c) Example radiographs showing a section view of the cavity before and during interaction with a 0.59 GPa shock from the left. The arrows indicate the cavity interface velocity, v, and the shock velocity, U_s.

Flyer material	D_0 [mm]	T_f [mm]	v_i [km/s]	u_p [km/s]	U_s [km/s]	p [GPa]
Aluminium	6	5	0.40 ± 0.01	0.32 ± 0.01	3.23 ± 0.10	1.25 ± 0.04
Aluminium	6	5	0.59 ± 0.01	0.47 ± 0.01	3.31 ± 0.10	1.84 ± 0.06
Polycarbonate	6	2	1.70 ± 0.01	0.84 ± 0.01	3.87 ± 0.10	4.10 ± 0.12
Polycarbonate	6	2	4.70 ± 0.01	2.30 ± 0.01	6.09 ± 0.19	16.60 ± 0.49

Table 5.2: Parameters for the four experiments chosen for the head-to-head simulation comparison.

imaging system configuration is also shown in Figure 5.3(a). The radiographs were recorded 'indirectly' using visible light cameras, by first absorbing the X-ray photons with a scintillator. The scintillator re-emits visible photons from its front and rear surfaces.

The imaging system for recording the X-rays was placed 7 m from the experiment. Based on the system's specifications, this ensured that the radiographs were recorded in the phase contrast regime. The phase contrast effect increases the contrast of material edges and interfaces, thus improving the visibility of tracking details during the impacts, such as the dynamics of the cavity interface and crack formation [28].

Using the experimental and imaging setups, the cavity collapse behaviour of the 3 mm, 4 mm and 6 mm diameter cavities under low to high speed impact is analysed. The results from the 17 experiments are presented in detail in the work of Escauriza et al. [29] (Chapter 4). In the present work, the underlying physics governing the collapse behaviour of a cavity of given diameter under different loading strengths is studied through simulations. For this purpose, four of the 6 mm diameter experiments, two from the single-stage experiments gun and two from the two-stage gun experiments, are analysed with the simulations in a head-to-head fashion using the same image processing and analysis techniques outlined in the Methods in Chapter 2. The experimental parameters for these four experiments are presented in Table 5.2.

5.2.3 Image processing and parameter extraction

For a given experiment, the UHS X-ray imaging setup records radiographs of the deformed cavity surface at different time instants. The recorded images are 2D projections of the spherical cavity target, as can be seen from Figures 5.3(b) and 5.3(c). Interfaces in the images, such as the glue line, cavity interface, and shock front, were enhanced by phase contrast interference fringes [30, 31].

As detailed in the Methods in Chapter 2, the images are processed using flat-fielding techniques, after which parameters are obtained from the images. Equations 4.1-4.13 in Methods detail how the parameters are extracted, and for brevity the relevant expressions for the present Chapter are listed as follows.

Dimensionless time t' is given by,

$$t' = t\frac{C_L}{D_0}, \tag{5.7}$$

where t is time in μs, C_L is the longitudinal sound speed in km/s (same as mm/μs) and D_0 is the initial cavity diameter in mm. The collapse time, t_{col} is scaled in the same manner to produce the dimensionless collapse time t'_{col}. The normalised time-dependent cavity area, $A'(t)$ is given by,

$$A'(t) = \frac{A(t)}{A_0}, \tag{5.8}$$

where $A(t)$ is the projected cavity area in mm^2 and A_0 is the initial area. The dimensionless displacement $x'(t)$ of the cavity interface along the centreline position is the following,

$$x'(t) = \frac{x(t)}{D_0}, \tag{5.9}$$

where $x(t)$ is the displacement in mm and D_0 has been defined above. The dimensionless velocity $v'(t)$ is scaled by,

$$v'(t) = \frac{v(t)}{C_L}, \tag{5.10}$$

where, $v(t)$ is the velocity in km/s and C_L is as above. Additionally, the dimensionless acceleration $a'(t)$ is,

$$a' = a\frac{D_0}{{C_L}^2}. \tag{5.11}$$

A quadratic relationship between $x(t)$ and a is used, with an initial 'release' ve-

locity v_0,

$$x'(t) = v_0' t' + \frac{1}{2} a' t'^2, \tag{5.12}$$

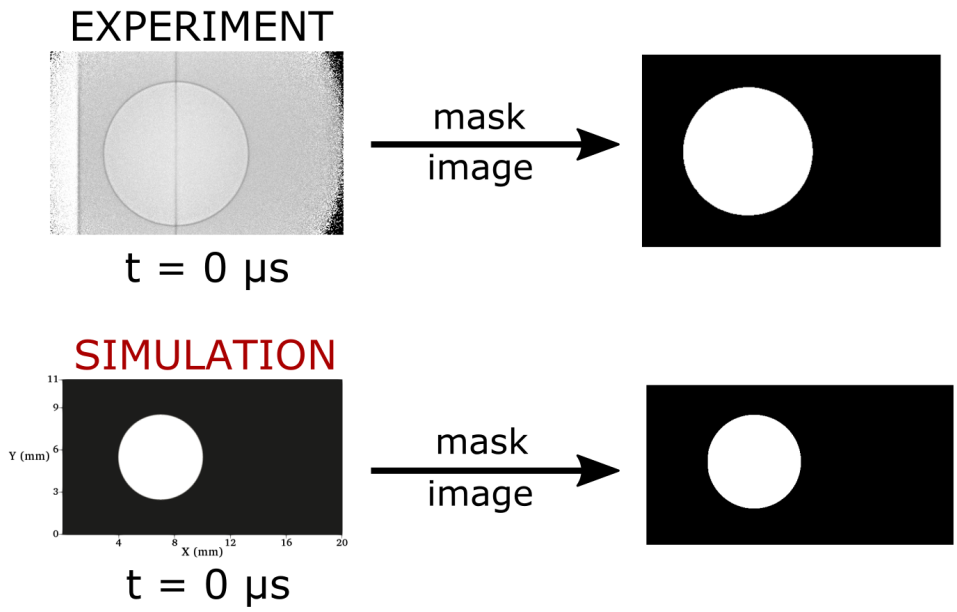
which assumes the acceleration is constant. As discussed in the previous Chapter, this assumption is only valid in PMMA for the data in the hydrodynamic regime, at pressures > 4.80 GPa. The 'jet' velocity, v_{jet} at the instant before collapse, which is also only valid in the hydrodynamic regime, is calculated with,

$$v_{jet} = at|_{x=D_0} + v_0, \tag{5.13}$$

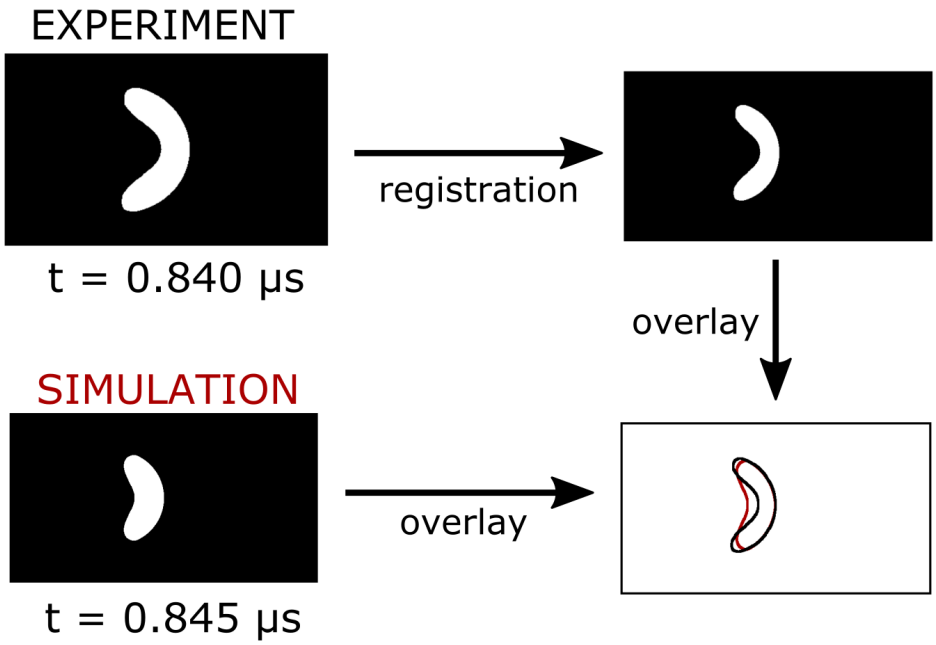
where $t|_{x=D_0}$ is the time at which the interface displacement equals the initial diameter of the cavity. It should be noted that, depending on the application, either the dimensional or dimensionless forms of these expressions can be used.

5.2.4 Creating overlay images

To visually compare the experimentally observed cavity collapse behaviour and numerical simulations, the cavity shapes are extracted at different times from the 2D radiographic images and are laid over the simulation cavity shapes. These overlay images are presented in the results below. A diagram demonstrating the steps taken to create the overlaid images can be seen in Figure 5.4. As can be seen in Figure 5.4a, the first step is to create binary 'mask' images from the experiment radiographs and simulation outputs. For the radiographs this is done with the edge detection and fill processes described previously in the methods in Chapter 2. For the simulations it is only required to crop the outputs and convert the image to a binary format, with the cavity 'void' area indicated by ones and material area with zeros. The next step, as shown in Figure 5.4b, is to transform the radiographic images to the same size as the simulation – this order, as opposed to the other way around, is chosen because the simulation images are higher resolution. Having the cavities the same size in their respective images then allows the images to be overlaid. To obtain the transformation matrix pa-



(a)



(b)

Figure 5.4: Schematic diagram showing the procedure to generate overlay plots between the experiment and simulation plots of cavity collapse. a) A mask image of the 6 mm diameter cavity is made from the experimental image and simulation image at initial time before impact, $t = 0\,\mu s$. These two images are used to obtain the registration transform parameters. (b) Each frame of the experimental mask images is transformed through image registration and an overlay image is created by matching to a simulation image mask at the same approximate time.

rameters (see Chapter 2), the mask images of the un-shocked cavity at $t = 0\,\mu s$ are chosen, because at this time before impact both the data and simulation images have the same cavity shape, i.e. projected circles. The result is two images with the same pixel dimensions, cavity size and cavity position.

The transformation parameters are then applied to all of the experiment images, producing a set of images for the experiment and simulation that are aligned and the same size. This is also demonstrated in Figure 5.4b, in which the top left experiment image is transformed to the top right image. Each experiment image is then paired with a simulation image that has an interaction time in the same neighbourhood (0.840 μs and 0.845 μs in the Figure 5.4b example). The final overlaid image is produced by taking the edge of the simulation mask image and registered experiment mask image and placing them overlaid on a white background. In the example shown, black and red lines are chosen for the experiment and simulation images, respectively.

5.3 Results and discussion

In the past, the influence of loading strength on the cavity collapse behaviour in a solid explosive (HMX) was analysed using numerical simulations [7, 11, 13, 18, 22]. For strong shocks, where 'strong' means the HMX material strength is overwhelmed and hydrodynamic behaviour is observed, collapse is characterised by the formation of a material jet [7, 22]. Jetting is also observed in the collapse of cavities in a liquid gel subjected to shock loading [8, 9, 12, 14]. For moderate to weak strength shocks, where the shock heating does not lead to bulk melting, the collapse of the cavity involves the formation of adiabatic shear bands [7].

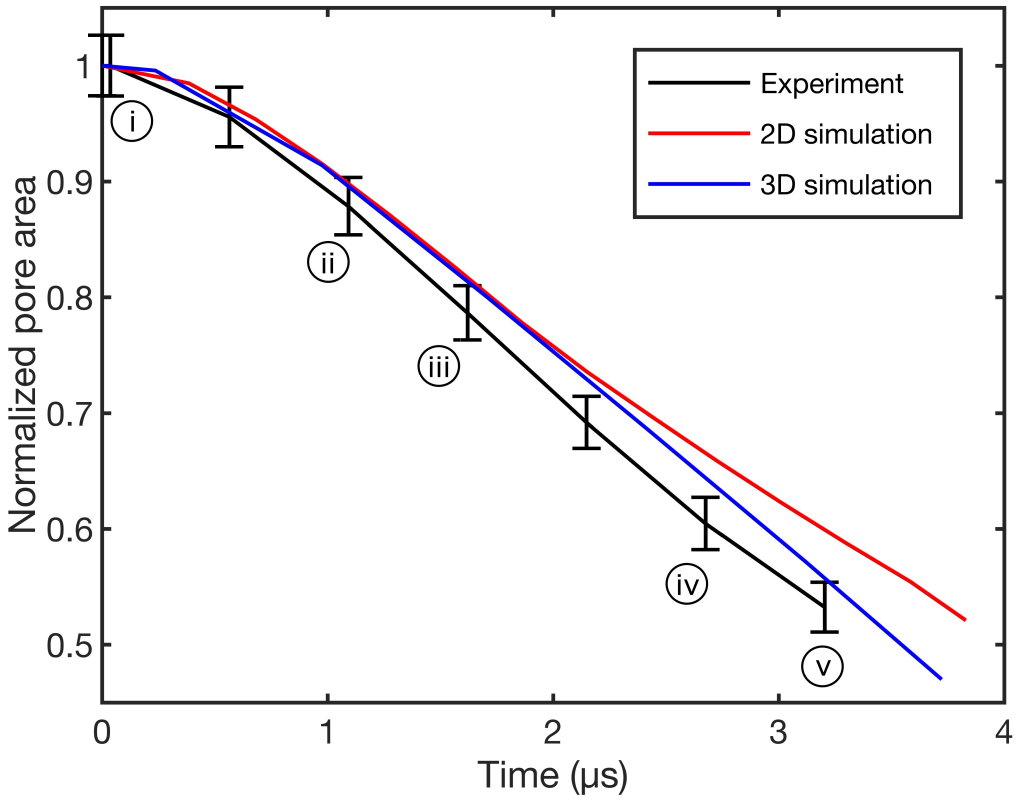
A head-to-head comparison is performed between the numerical simulations and experiments, from the strength-dominated to hydrodynamic lading regimes. Firstly, in Sections 5.3.1-5.3.3 a more detailed comparison will be covered on four

of the experiments, and their corresponding simulations, as listed in Table 5.2, for shock strengths of $p = 1.25$, 1.84, 4.10 and 16.60 GPa. Second, in Section 5.3.4 extracted parameters from all of the experiments and simulations are compared in plots, looking at the collapse time relationship to loading pressure, acceleration vs. pressure in the hydrodynamic regime, and the respective dependence of release velocity and jet velocity on particle velocity generated by the shock. Lastly, in Section 5.3.5 additional analysis is presented that is not featured in the original JMPS paper, detailing a comparison of the collapse times extracted from simulations on more materials in SCIMITAR3D (copper, aluminium and stainless steel).

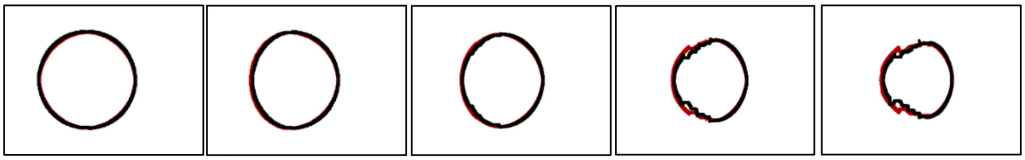
5.3.1 Cavity collapse under 1.25 GPa shock strength

First, we consider the collapse behaviour of a 6 mm diameter cavity for a low shock strength of 1.25 GPa. To assess the consequences of the 2D assumption, 3D cavity collapse is also simulated; these simulation results are compared against corresponding experimental data.

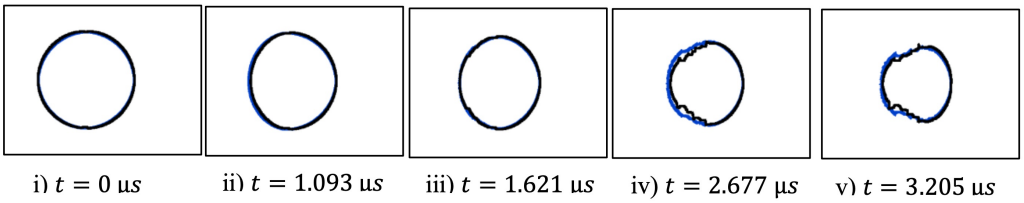
Figure 5.5a compares the time variation of the normalised area obtained from experiment, and 2D and 3D simulations. For the experiment and the 3D simulation, the area of the cavity is obtained for the central plane through the cavity perpendicular to the shock direction, as explained in Section 5.2.3. It is important to note that in Fig. 5.5a , the normalised area is shown up to a value of 0.5, i.e. corresponding to the halfway point of total cavity collapse. This is because, for the given loading condition, complete collapse of the cavity is not observed, since at this point of time in the experiment the glue layer between the target surfaces begins to separate. There is a divergence between the 2D and 3D lines after 2 μs, which, when extrapolated means the 3D simulation predicts a faster collapse time. The presence of an additional dimension may account for this, as it provides an extra component of material displacement and rotation, by which



(a) Experimental and simulation results comparison of the time evolution of the normalised cavity area for a 6 mm diameter cavity impacted with a 1.25 GPa shock.



(b) Comparison of cavity deformation obtained from the experiment and 2D simulation. Experimental cavity interfaces are shown by the black curves and the red curves show the 2D simulation results.



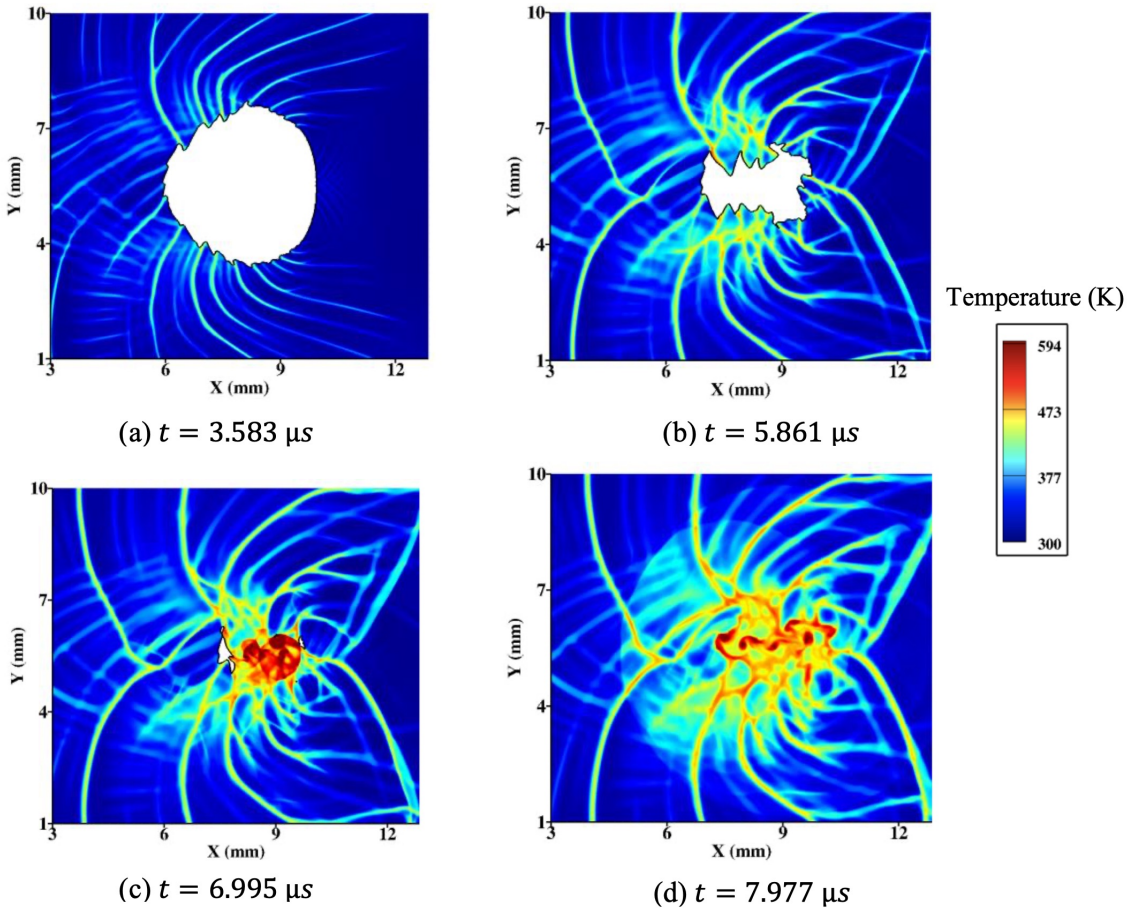
(c) Comparison of cavity deformation obtained from the experimental and 3D simulation. Experimental cavity shapes are shown by the black curves and the blue curves show the 3D simulation results.

Figure 5.5: Comparison of experimental and simulation results (2D and 3D) for the collapse of a cavity of diameter 6 mm in PMMA matrix impacted by a shock pressure of 1.25 GPa.

a more rapid acceleration of the cavity interface is produced.

To gain insights into the collapse behaviour, the transient cavity interfaces are extracted for direct comparison between the experiment and simulations data. The simulated cavity interfaces are shown overlaid on the experiment images in Figs. 5.5b&c at the different time instants numbered from (i)–(v) in Fig. 5.5a. The simulations are in close agreement with experimental results during collapse, with the 3D modelling showing subtle features of weak shock loading. The above comparison for the $p = 1.25\,\mathrm{GPa}$ case points out two general observations. Firstly, the deformed interfaces in Figs. 5.5b&c show the formation of irregular ridges on the cavity surface at later stages of the collapse, as can be seen in Fig. 5.5b(iv)&b(v). These ridges are observed in both simulations and experiment. Second, the interfaces at the various instants shown are predicted well by both the 2D and 3D simulations. To understand the physics governing the ridge formation and to assess the validity of the 2D modelling assumption in detail, the simulation results are further analysed.

The physical mechanism governing the ridge formation is analysed using the temperature contours at different times in the 2D simulation, as shown in Fig. 5.6. Figure 5.6a shows that the shock wave interaction with the cavity leads to the initiation of adiabatic shear bands at its upper and lower surfaces. These shear bands have been simulated by other researchers in both energetic crystals [7, 11] and metals [32–34]. In the present calculations, the shear bands in PMMA are captured using the rate-dependent Johnson Cook plasticity model [24]. The ridges on the cavity surface are formed by shear band initiation sites, as also seen in previous studies [7, 11, 33]. The shear bands initiate and grow from the cavity surface at an initial angle of $\sim$90° to the shock direction as can be seen from Fig. 5.6b. At later times, the bands turn along the direction of the shock and the tips of the bands grow at an angle of $\sim$45°. This shows that the growth of bands is favoured along the expected maximum shear stress plane, i.e. at 45° to the load-



(a) $t = 3.583\ \mu s$ (b) $t = 5.861\ \mu s$

(c) $t = 6.995\ \mu s$ (d) $t = 7.977\ \mu s$

Figure 5.6: 2D simulation of the temperature [K] evolution following the collapse of a 6 mm diameter cavity under shock pressure of 1.25 GPa from the left.

ing direction.

The localisation of the plastic dissipation in the bands leads to temperatures in excess of $\sim$400 K, the melting point of PMMA [24]. The PMMA material melts in the band, leading to liquid PMMA bands sandwiched between the solid PMMA material, as can be seen from Fig. 5.6b. The initiation and growth of the bands is accompanied by the shrinking and compression of the cavity from all directions under the pressurised material behind the shock front. Figure 5.6c shows that compression of the cavity eventually leads to its collapse, followed by the generation of a diverging circular re-shock wave. The re-shock propagates into the PMMA material and leads to further heating of the melted PMMA in the band causing temperature elevation of approximately 100 K, as can be seen in Fig. 5.6d. In this $p = 1.25\,\mathrm{GPa}$ case, a heated region forms after collapse, consisting of a network of adiabatic shear bands around the central heated core of the collapse site. The structure of this 'hotspot' has implications for initiation in reactive energetic materials where a similar combination of collapse induced re-shock wave formation and heating of the shear bands can be expected [35, 36]. It is also interesting to note the vertical non-asymmetry of the bands about the horizontal midline. This is because the simulations are run in plane-strain configuration, as opposed to an axisymmetric. As a result, the bands form at different times as the simulation rasters when iterating along the grid cells. Thus the bands form at different rates depending on where they are located in the grid, resulting in an asymmetrical band pattern.

From the above 2D analysis, the ridges on the cavity surface in experiments are identified as the initiation sites for the adiabatic shear bands. Similar to the 2D and experiment results, the 3D interfaces in Fig. 5.5b also show the formation of ridges on the cavity surface. To visualise the shear bands in 3D, Fig. 5.7 shows the iso-surface of the effective plastic strain coloured with the temperature contours. Along with the iso-surface of the effective plastic strain, the 2D projection of the

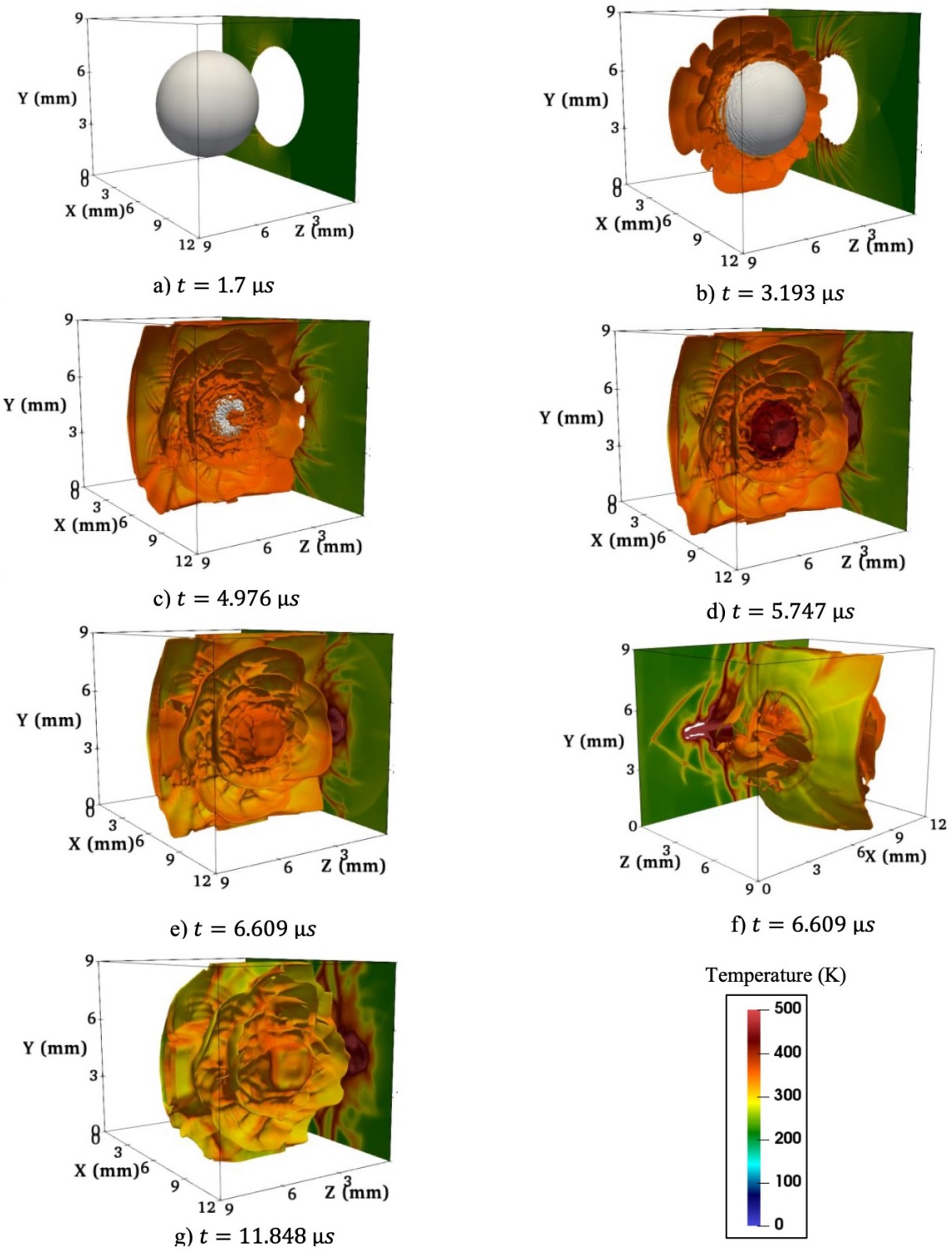


Figure 5.7: 3D simulation results for the collapse of a spherical cavity of diameter 6 mm in PMMA impacted by a shock of pressure 1.25 GPa from the left. Iso-surface of effective plastic strain coloured with temperature contours [K] are shown to visualise the adiabatic shear bands in 3D.

temperature on the centreline Z-axis plane and the deformed cavity surface are also shown. Figure 5.7a shows that the interaction between the shock wave and cavity surface leads to the initiation of adiabatic shear bands at sites coinciding with the ridges observed in Fig. 5.5b. As for the 2D case, the bands initiate at an angle of 90° and later grow along the maximum shear localisation plane at approximately 45° with respect to the incident shock direction, as can be seen from Fig. 5.7b&c.

This observation is consistent with the 2D results, except that in 3D, rather than the bands being 1D-like structures, multiple bands grow outward as concentric petal-like surface formations. Figure 5.7c shows the surfaces of the petals. The increase in temperature along the shear band surfaces melts the PMMA material. The cavity shrinks and eventually collapses, leading to the formation of a re-shock wave in Fig. 5.7d. The spherical re-shock propagates radially outward, leading to increases in the temperature of the band surface by approximately 100 K as shown in Figs. 5.7e-g. The initiation process and the adiabatic shear band outlines in the 2D and 3D analysis are qualitatively similar. However, the mass of the heated region from the plastic dissipation and the collapsing cavity is significantly higher in 3D.

The present analysis shows that the numerical simulations in both 2D and 3D can predict the experimentally observed cavity collapse behaviour. To evaluate the influence of material strength effects on the collapse behaviour, the collapse of a 6 mm diameter cavity under an increased shock of strength $p = 1.84\,\mathrm{GPa}$ is analysed in the next section.

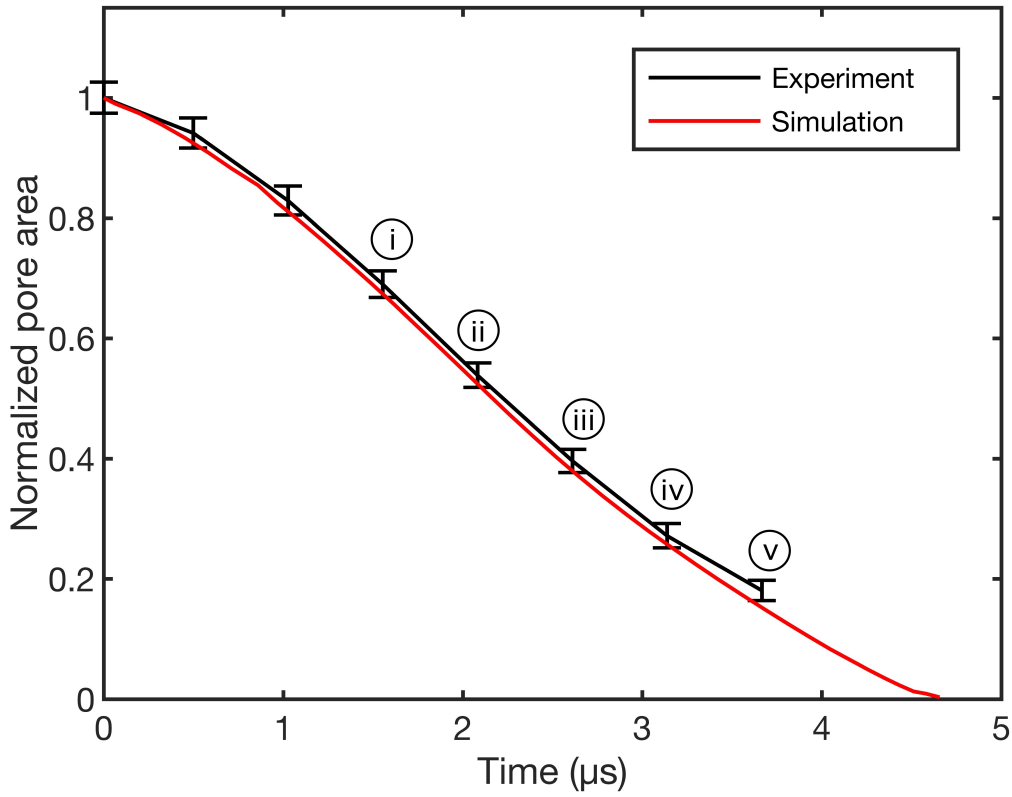
5.3.2 Cavity collapse under 1.84 GPa shock strength

Figure 5.8 compares the time evolution of the normalised cavity area of the experiment and 2D simulation for $p = 1.84\,\mathrm{GPa}$, and shows good agreement. At this higher pressure, the glue layer separation in the experimental results is not

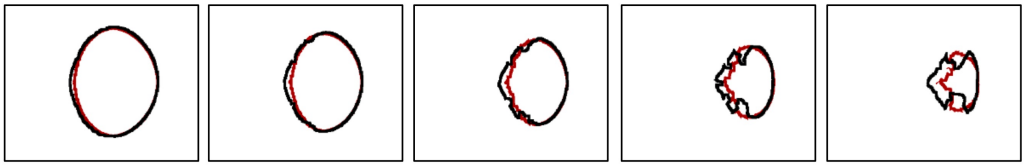
present, meaning the cavity deformation data is available for later stages of collapse. Figure 5.8b shows the overlaid plots of the cavity interfaces at different times, which are numbered (i)–(v) in Fig. 5.8a. The cavity interfaces predicted from the 2D simulation are in close agreement with the experimental results across different stages of collapse. It is interesting to note that, similar to the previous case of a 1.25 GPa shock, Fig. 5.8b shows the formation of ridges on the cavity surface. The ridge formation in both simulation and experiment is observed at a later stage of cavity collapse, i.e. $t > 2.6\,\mu s$. The approximate locations of the ridges also appear to match closely between the experiment and simulation results. For the experimental interface plot (black line) there is a 'pinching' of the interface in the vertical direction. Although this could be due to the presence of a glue layer in the target construction, the same pinching has been seen in simulations of cavity collapse in HMX in the strength regime [7, 11].

For this higher shock strength, the features of cavity collapse observed for the previous lower velocity case seem to largely hold true, as shown by the temperature contours in Fig. 5.9. The cavity deformation progresses, again with ridges forming along with the surface, leading to the complete cavity closure. In this case, however, the cavity closure generates a stronger re-shock wave that propagates radially outward from the collapse site, as shown in Fig. 5.9d. The re-shock wave leads to increase in temperature of the already melted bands by $\sim$150 K.

The mechanism of cavity collapse for the 1.84 GPa shock is similar to the 1.25 GPa case. For both these shock strengths, the collapse is dominated by strength effects and plastic dissipation. The resulting hotspot region consists of a network of shear bands surrounding a heated core region corresponding to the location of the final cavity closure site. Although there are similarities in the collapse mechanism for the two shock strengths, the locations of the band initiation sites and the morphology of the shear band network are significantly different between the two cases. First, for the 1.25 GPa shock, the adiabatic shear bands are initi-



(a) Experimental and simulation results comparison of the time evolution of the normalised cavity area for a 6 mm diameter cavity impacted with a 1.84 GPa shock.



i) $t = 1.587\ \mu s$ ii) $t = 2.115\ \mu s$ iii) $t = 2.643\ \mu s$ iv) $t = 3.171\ \mu s$ v) $t = 3.699\ \mu s$

(b) Comparison of cavity deformation obtained from the experiment and 2D simulation. Experimental cavity interfaces are shown by the black curves and the red curves show the 2D simulation results.

Figure 5.8: Comparison of experimental and simulation results for the collapse of a cavity of diameter 6 mm in PMMA matrix impacted by a shock pressure of 1.84 GPa.

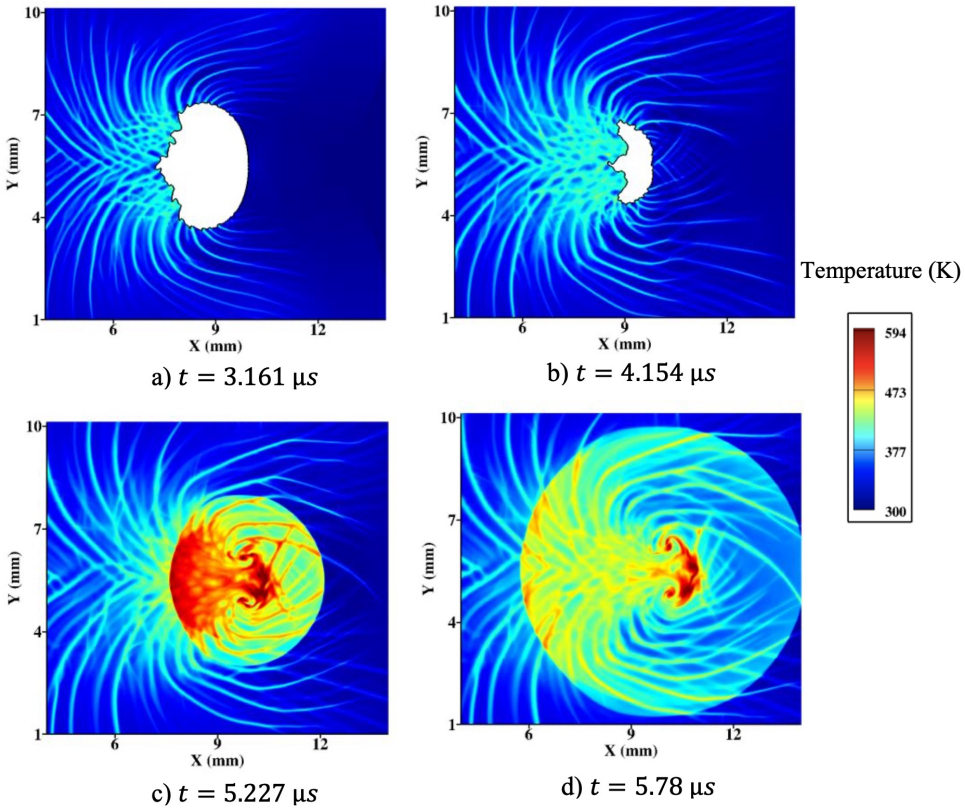


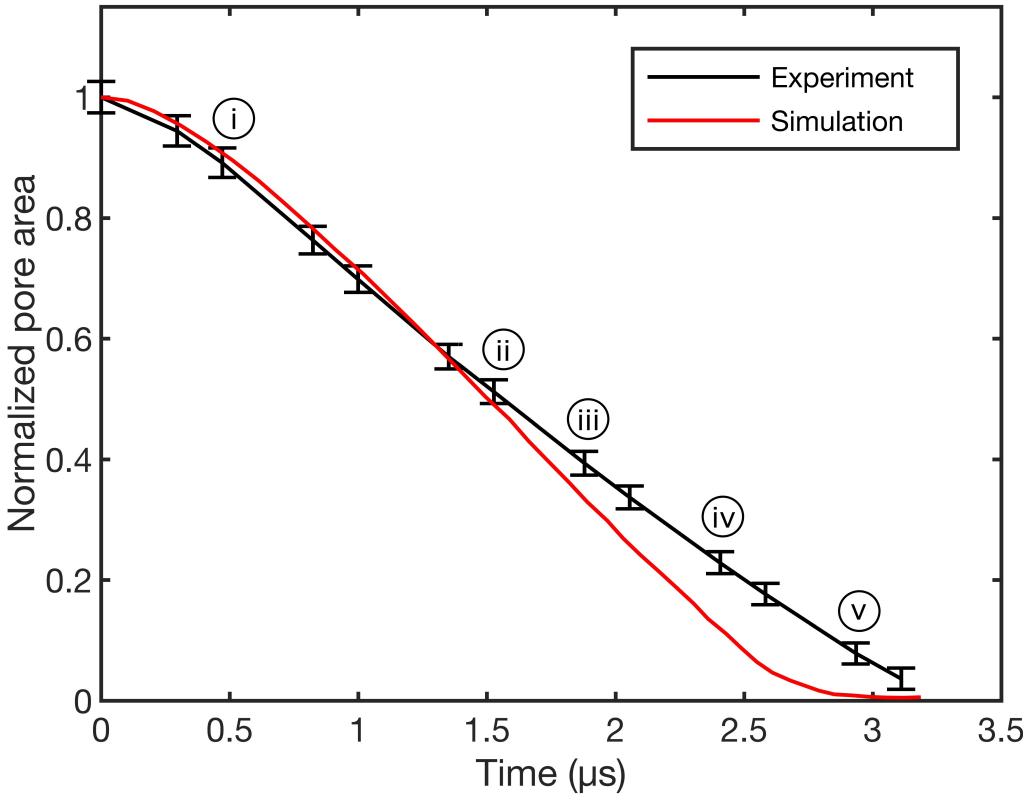
Figure 5.9: 2D simulation showing the temperature [K] evolution following the collapse of a 6 mm cavity under shock pressure of 1.84 GPa from the left.

ated near the equator on the upper and lower surfaces of the cavity and they initially start to grow at an angle of ∼90° to the cavity surface, as can be seen from Fig. 5.6b. On the other hand, as can be seen in Fig. 5.9a, for the 1.84 GPa case the adiabatic shear bands are seeded at an angle of ∼135° to the shock propagation direction. In addition, the band morphology for the two cases are also different. For the 1.84 GPa shock, the gaps between the adjacent bands at the cavity surface are observed to be less than the 1.25 GPacase. This leads to the formation of a finer band network, as can be seen by comparing Fig. 5.9b and Fig. 5.6b. Since the shear band density is higher for the 1.84 GPa case, the hotspot mass is also higher at this higher shock strength. In the case of energetic materials, this increase of hotspot mass can lead to faster hotspot reaction initiation and growth rates.

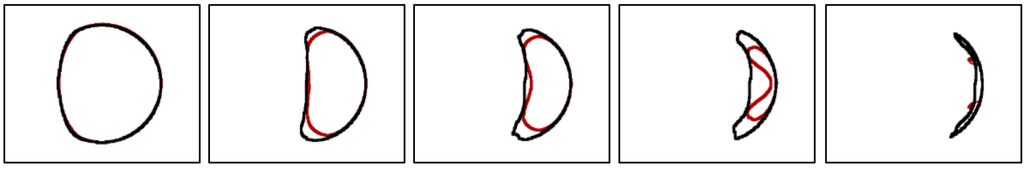
5.3.3 Cavity collapse under higher shock strengths, 4.10 GPa and 16.60 GPa

We now examine the dynamics of cavity collapse for higher shock strengths, in the regime where hydrodynamic behaviour is expected to dominate. For a shock of strength 4.10 GPa, Fig. 5.10a compares the time variation of the normalised area obtained from the 2D simulation and experiment. As seen in the figure, there is good agreement between the experiment and simulation observed during the initial stages of collapse, i.e. $t < 1.5\,\mu\text{s}$. However, the calculated cavity area deviates from the experimental results for $t > 1.5\,\mu\text{s}$. To understand this deviation, the deformed interfaces from simulation and experiment are overlaid in Fig. 5.10b at different instants numbered (i) through (v). Figure 5.10b(i)-(iii) show that for $t < 1.5\,\mu\text{s}$, the cavity interfaces from the simulation closely match the experimental results. At later times, as shown in Fig. 5.10b(iv)-(v), the simulated deformation of the cavity front surface along the centreline is higher; in the experiments, the front surface of the cavity is observed to be flatter, i.e. the jet formation is less prominent in the experiment. This difference in shape of the cavity in the later stages of collapse leads to the lower value of computed normalised area in Fig. 5.10a.

For the $p = 4.10\,\text{GPa}$ case, bulk shock heating in PMMA leads to a temperature rise of $\sim$450 K, and PMMA mostly melts under the incident shock load, as can be seen from Fig. 5.11a. In contrast to the previous $p = 1.25\,\text{GPa}$ and $p = 1.84\,\text{GPa}$ cases, the ridges that form on the cavity surface are extremely fine and hard to resolve. The collapse progresses in melted PMMA and the interaction of the incident shock with the cavity surface leads to the formation of a material jet, as shown in Fig. 5.11b. The shock focusing by the material jet causes larger deformation along the centreline of the cavity. Jet impact at the centreline leads to the generation of a re-shock wave and two symmetric lobes as can be seen from Fig. 5.11c. The lobes collapse under the combined influence of the



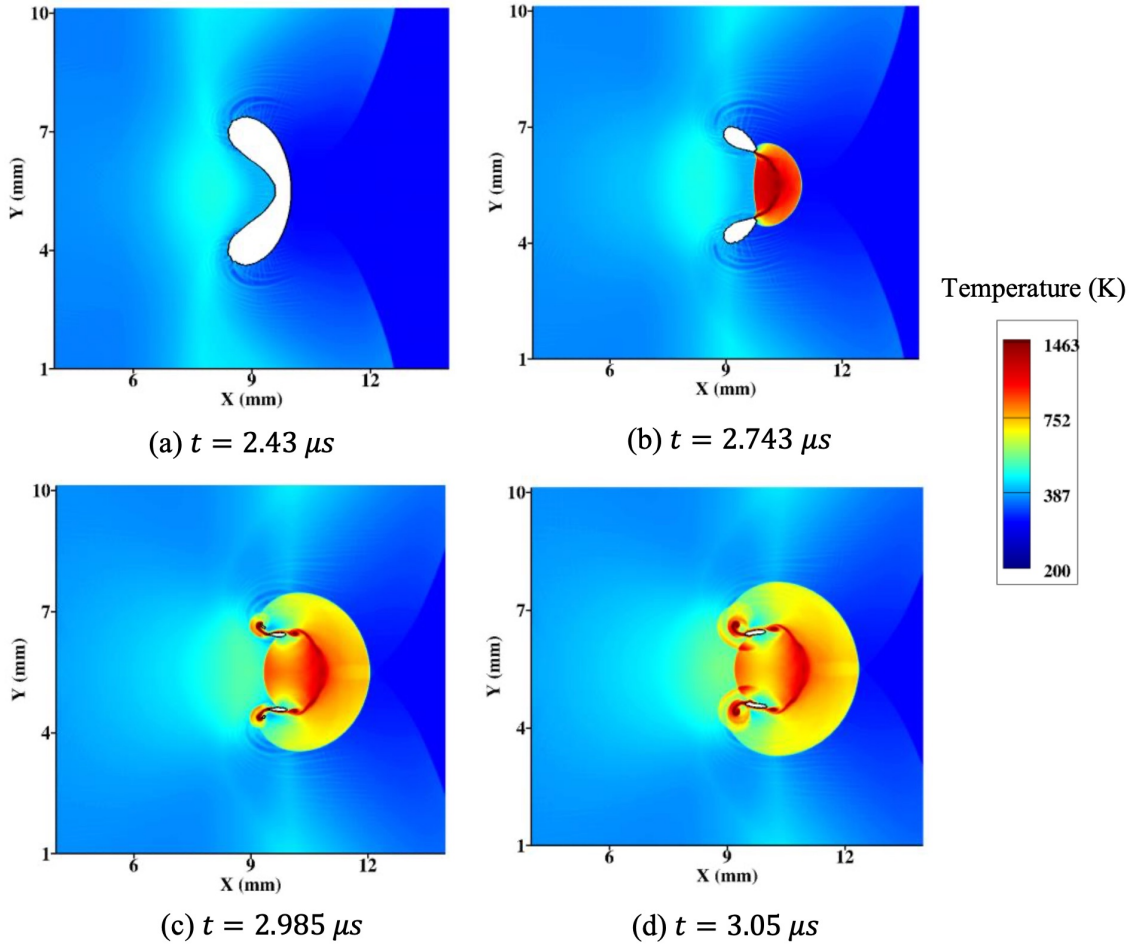
(a) Experimental and simulation results comparison of the time evolution of the normalised cavity area for a 6 mm diameter cavity impacted with a 4.10 GPa shock.



i) $t = 0.485\ \mu s$ ii) $t = 1.541\ \mu s$ iii) $t = 1.893\ \mu s$ iv) $t = 2.488\ \mu s$ v) $t = 2.949\ \mu s$

(b) Comparison of cavity deformation obtained from the experiment and 2D simulation. Experimental cavity interfaces are shown by the black curves and the red curves show the 2D simulation results.

Figure 5.10: Comparison of experimental and simulation results for the collapse of a 6 mm diameter cavity in PMMA impacted by a shock pressure of 4.10 GPa.



(a) $t = 2.43\ \mu s$ (b) $t = 2.743\ \mu s$

(c) $t = 2.985\ \mu s$ (d) $t = 3.05\ \mu s$

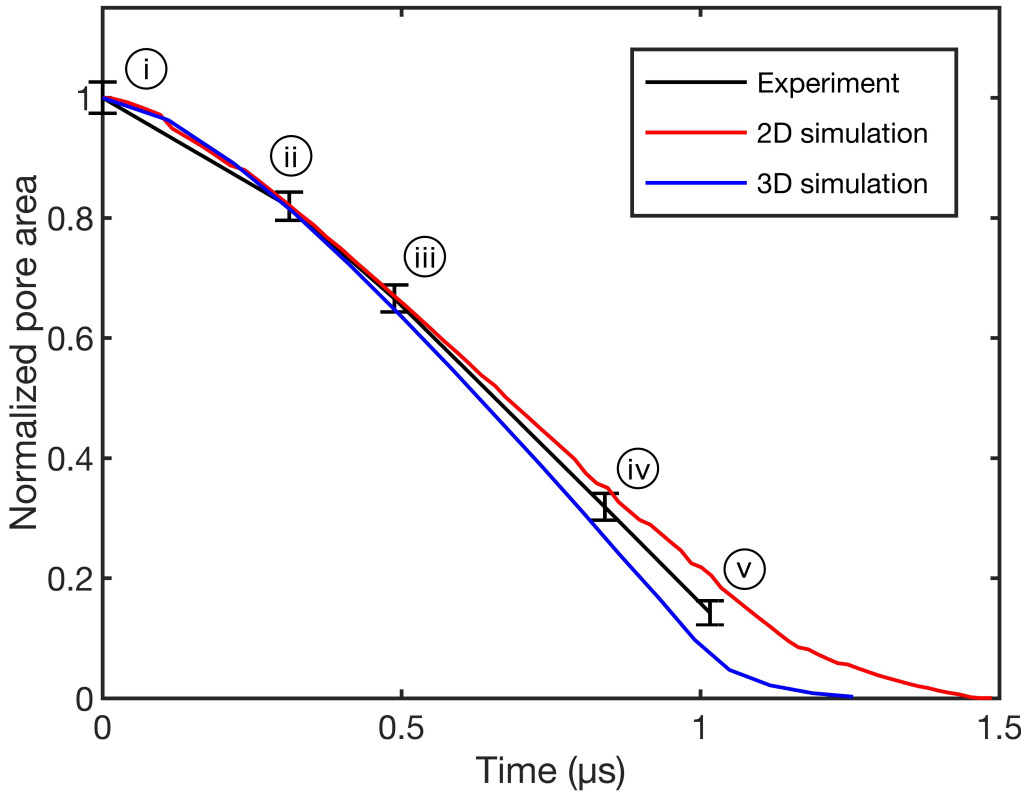
Figure 5.11: 2D temperature [K] evolution following the collapse of the cavity of diameter 6 mm under shock pressure of 4.10 GPa from the left.

re-shock and the incident shock. Figure 5.11c shows that the complete closure of the cavity leads to the formation of a mushroom-shaped intense hotspot. The peak temperature in the hotspot region is approximately 1,000 K higher than the $p = 1.84\,\mathrm{GPa}$; this can be seen by comparing Fig. 5.11d and Fig. 5.9d.

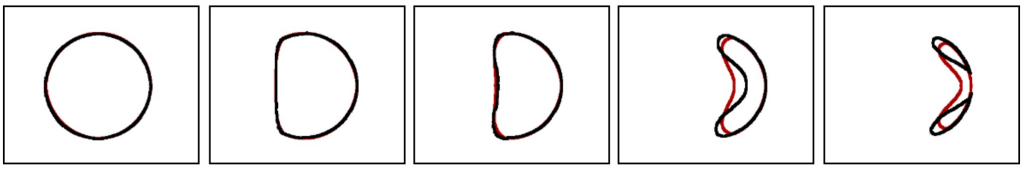
Simulation of the 4.10 GPa case above is seen to lead to a mode of collapse dominated by hydrodynamic behaviour. However, we see significant deviation from the experimental results in the interface comparison of Fig. 5.8b, where the jetting is far less pronounced. This suggests the transition to the hydrodynamic regime is more advance for the simulation at this pressure than the experiment, which exhibits more strength-dominated behaviour. To examine collapse at even higher velocities, we compare simulation and experimental results for the high-

est flyer velocity tested, corresponding to $p = 16.60\,\mathrm{GPa}$. In this case, as for the lowest velocity case of 1.25 GPa, both 2D and 3D calculations are performed to assess the impact of performing 2D as opposed to 3D calculations.

Fig. 5.12a shows the comparison between the experimental results and the 2D and 3D simulation results. The time evolution of the normalised cavity area calculated from the 2D simulation is in close agreement with the experimental data. This contrasts with the deviations observed in the 4.10 GPa case, which indicates the transition to the hydrodynamic regime is complete in both the experiment and 2D simulation. To further validate the collapse behaviour, we overlay deformed interface plots at time instants (i)-(v) in Fig. 5.12b; the corresponding instants on the cavity area versus time plot can be seen in Fig. 5.12a. Figures 5.12b(i)-(iii) show that for $t < 0.75\,\mu\mathrm{s}$, the deformed cavity interface obtained from the simulation is nearly identical to the experiment. At later stages, i.e. for $t > 0.75\,\mu\mathrm{s}$, the centreline deformation of the front cavity surface is lower than the experimental value. To understand the influence of spatial dimensionality on the deformed interface, a high-fidelity 3D simulation for a 6 mm diameter spherical cavity is performed. Fig. 5.12a shows the comparison of the normalised cavity area obtained from the 3D calculation with the experimental data. The normalised area predicted from the 3D simulation matches well with the experiments. Similar to the 2D overlaid plots, Fig. 5.12c shows the comparison between the deformed interfaces obtained from the 3D simulation with experimental results at the instants (i)-(v). The 3D interfaces are almost identical in the early as well as later stages of the collapse as can be seen from the overlays images in Fig. 5.12c. It is noteworthy that at later stages, unlike in the 2D simulations, the front surface of the cavity shows nearly the same deformation in 3D as experiments as shown in Figs. 5.12c(iv)-(v). Therefore, 3D simulations produce better agreement with the experiments in terms of the details of the cavity shape over the entire collapse process, when compared to the 2D simulations. However, gross measures, such as area and collapse time obtained from 2D cal-

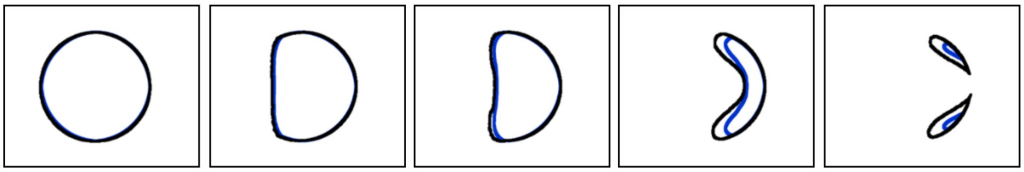


(a) Experimental and simulation results comparison of the time evolution of the normalised cavity area for 6 mm cavity diameter impacted with a 16.60 GPa shock.



i) $t = 0.0\ \mu s$ ii) $t = 0.312\ \mu s$ iii) $t = 0.488\ \mu s$ iv) $t = 0.840\ \mu s$ v) $t = 1.016\ \mu s$

(b) Comparison of cavity deformation obtained from the experiment and 2D simulation. Experimental cavity shapes are shown by the black curves and the red curves show the 2D simulation results.



i) $t = 0.0\ \mu s$ ii) $t = 0.312\ \mu s$ iii) $t = 0.488\ \mu s$ iv) $t = 0.840\ \mu s$ v) $t = 1.016\ \mu s$

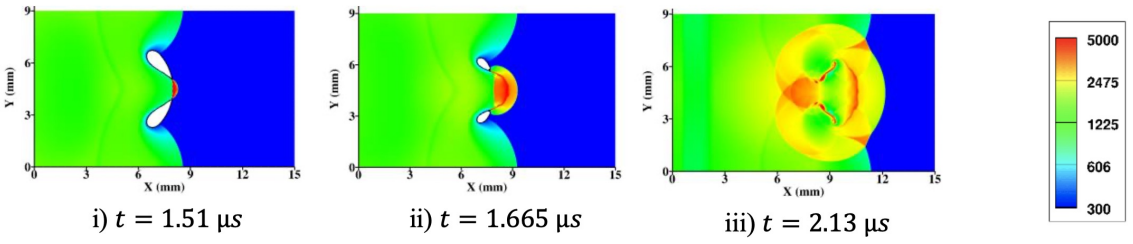
(c) Comparison of cavity deformation obtained from the experimental and 3D simulation. Experimental cavity interfaces are shown by the black curves and the blue curves show the 3D simulation results.

Figure 5.12: Comparison of experimental and simulation results (2D and 3D) for the collapse of a cavity of diameter 6 mm in PMMA matrix impacted by a shock pressure of 16.60 GPa.

culations are still in good agreement with experiments.

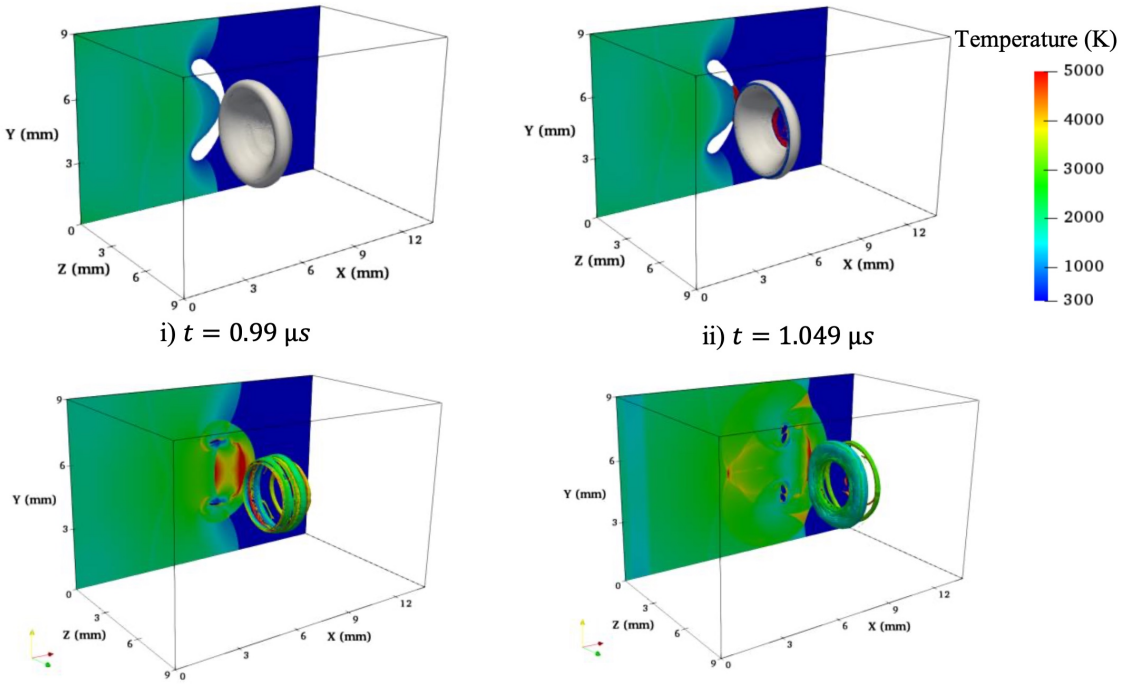
For the $p = 16.60\,\mathrm{GPa}$ case, Fig. 5.13 shows the temperature contours at different instants in the 2D and 3D simulations. The shock heating in the bulk of PMMA leads to the increase in temperature to $\sim$1200 K. The bulk PMMA material therefore melts entirely for the 16.60 GPa loading condition, and contrasted to the lower pressure cases, there is no appearance of shear banding since the collapse of the cavity progresses in an entirely liquid PMMA material. The shock interaction with the leads to the formation of a material jet, as can be seen from Fig. 5.13a(i). The jet impact at the centreline forms two side lobes and generates a re-shock wave that propagates radially outward from the impact location as shown in Fig. 5.13a(ii). Under the combined influence of the re-shock and incident shock, the lobes collapse leaving behind a mushroom-shaped heated region as can be seen from Fig. 5.13a(iii). Because of the misalignment in the pressure and density gradients during the collapse of the lobes, rotational vortices are generated. This draws the hotspot into a slender, convoluted shape. It is interesting to note that the hotspot shape is similar to the 4.10 GPa case, but with elevated temperature. Comparing the final hotspot shapes for the four different velocities used in this study, i.e. in Figs. 5.6d, 5.9d, 5.11d and 5.13a(iii), it can be seen that the hotspots have highly irregular, convoluted shapes and are surrounded by substantial areas of material at elevated temperatures. These characteristics of the hotspots have implications for the initiation and growth of hotspots in energetic materials.

In the 3D cavity collapse process, the mechanism of jet formation at the centreline surface is similar to the 2D case. The key difference lies in the collapse of the lobes where the barotropic vortices are formed, which can only occur in the three dimensions. To visualise these barotropic vortices in 3D, the iso-surface of the vorticity (i.e. isocontours of the second invariant of the rotation tensor, λ_2), coloured with the temperature contours, are shown at different instants in



i) $t = 1.51\ \mu s$ ii) $t = 1.665\ \mu s$ iii) $t = 2.13\ \mu s$

(a)



i) $t = 0.99\ \mu s$ ii) $t = 1.049\ \mu s$

iii) $t = 1.32\ \mu s$ iv) $t = 1.638\ \mu s$

(b)

Figure 5.13: Temperature [K] evolution following the collapse of the circular and spherical cavity of diameter 6 mm under a shock of strength 16.60 GPa from the left. (a) 2D simulation output showing temperature [K] contours. (b) 3D simulation output showing the iso-surface of λ_2 (for vorticity), with the centreline Z-plane coloured with temperature [K].

Fig. 5.13b. Along with the vortices contours, Fig. 5.13b shows the temperature contours along the centreline Z-plane and the deformed cavity surface. From Fig. 5.13b(i) we see that the incident shock deforms the spherical cavity and leads to the formation of a material jet along the centreline. The shock focusing because of material jetting leads to closure of the cavity at the centreline and generates a re-shock wave from the jet impact site. The combined effect of the re-shock and incident shock eventually leads to the complete closure of the cavity, with generation of the barotropic vortex rings as shown in Fig. 5.13b(iii). The core of the vortex rings coincides with the maximum temperature rise from the collapse. The rings translate along the shock direction and eventually disintegrate and dissipate leaving behind a mushroom shaped heated region in 3D.

The comparison between the 2D and 3D results shows that 2D simulations can qualitatively calculate cavity collapse in the hydrodynamic regime. However, the hotspot mass in 3D is higher which can lead to enhanced ignition and growth rates in 3D when compared to 2D. Furthermore, the higher centreline cavity deformation in 3D and experiments seen in Figs. 5.12b&5.12c indicates that the jet speed in 2D is under-predicted.

5.3.4 Parameter variation with loading pressure

In the previous sections, the collapse behaviour of the cavities in various loading regimes is analysed and explained using experiments and numerical simulations. In the present section, using the experimental and simulation data for various shock strengths, quantitative measures describing the collapse process and its relation to the loading strength is established.

As explained in Section 5.2.3, from the experiments and simulation results, various quantitative measures including normalised cavity area $A'(t)$ (Eq. 5.8) and displacement, $x'(t)$ of the cavity interface along the cavity centreline (Eq. 5.9) can be used to estimate time to collapse, velocity and acceleration of the cavity inter-

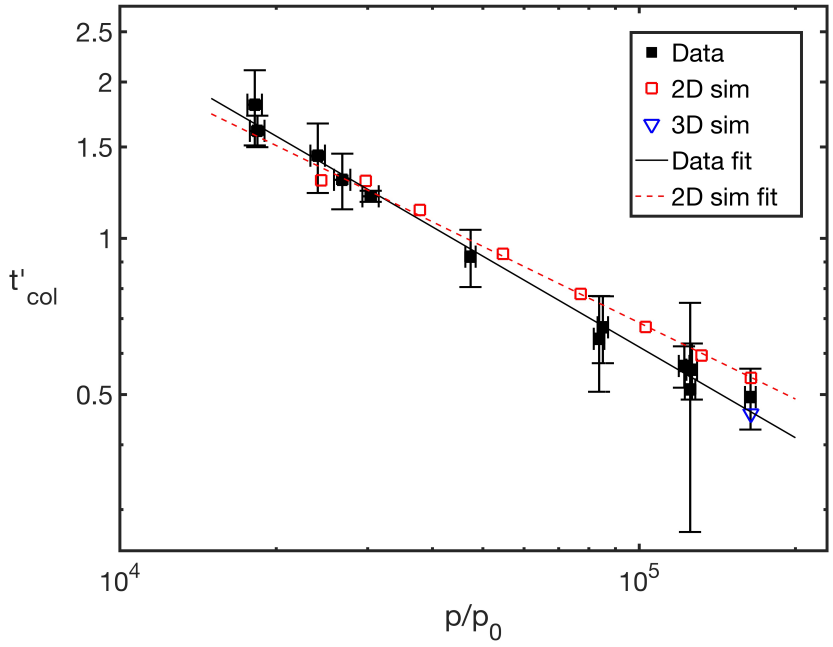


Figure 5.14: Variation of dimensionless collapse time with pressure ratio, in log-log space. Experiments shown as black closed symbols, with a solid black line for the fitting. The 2D simulation results are the red open symbols and a dashed red line for the fitting. The single 3D simulation is the blue triangle.

face. Using the method described earlier, these measures are obtained from the experiments and simulations data and scaling relations describing the collapse behaviour across wide range of loading regimes are established. In the past [12], such relations are reported for liquids and gels where the collapse mode is purely hydrodynamic. To compare the current results with the previously reported relations, and to obtain a reliable fit from the simulation results, four additional 2D cavity collapse simulations are performed (in the hydrodynamic regime) under shock loads corresponding to $u_p = 1.10$, 1.4, 1.70 and 2.0 km/s.

Figure 5.14 shows the variation of the dimensionless time to collapse with the incident shock pressure ratio, calculated from the simulations and experiments. The pressure ratio is dimensionless, and given by $p' = p/p_0$, where $p_0 = 1$ atm is the ambient atmospheric pressure, and the dimensionless time is as defined earlier in Eq. 5.7. The black line in the plot, which is log-log, shows the fit of the data analysed by Escauriza et al. [29]. It was found that above 1.85 GPa there is a power law relationship between t' and p' that, interestingly, spans the pressure

range from the strength regime to the maximum pressure studied in the hydrodynamic regime of 16.60 GPa. The relationship is given by the expression,

$$t'_{A,min,experiments} = 498p'^{-0.58}, \tag{5.14}$$

which is very similar to a relationship to that discovered by Swantek and Austin [12] in their study on dynamically loaded cylindrical cavities in hydrogel. The expression is also close to the analytic inverse root relationship between the collapse time and ambient fluid pressure for bubble collapse, derived by Rayleigh [37]. This collapse time, which is coupled with the jet dynamics described earlier, is related to the temperature and pressure states produces during collapse.

The collapse time power law curve calculated from the 2D simulations, which is shown in the plot as a dashed red line, is in close agreement with the experimental estimation for lower pressures. For higher pressures, the 2D simulations diverge and estimate higher collapse time as compared to the experiments. This was observed in Section 5.3.3 for the 2.3 km/s shock, where the less deformation along the cavity centerline in the 2D simulation was observed compared to the experiments. The collapse time estimation from 3D simulation and experiments for 2.3 km/s shock were observed to be in close agreement, and this is reflected in Figure 5.14. The fits from the experiments and simulations are obtained as,

$$t'_{A,min,2Dsims} = 191p'^{-0.49}. \tag{5.15}$$

It is interesting to note Swantek and Austin [12] obtained a similar relationship by performing experiments on a gel material under shock, with the collapse time scaling with the pressure ratio by a -0.55 exponent, i.e. close agreement with the current estimations for PMMA.

An additional metric to quantify the dynamics of the cavity collapse behaviour

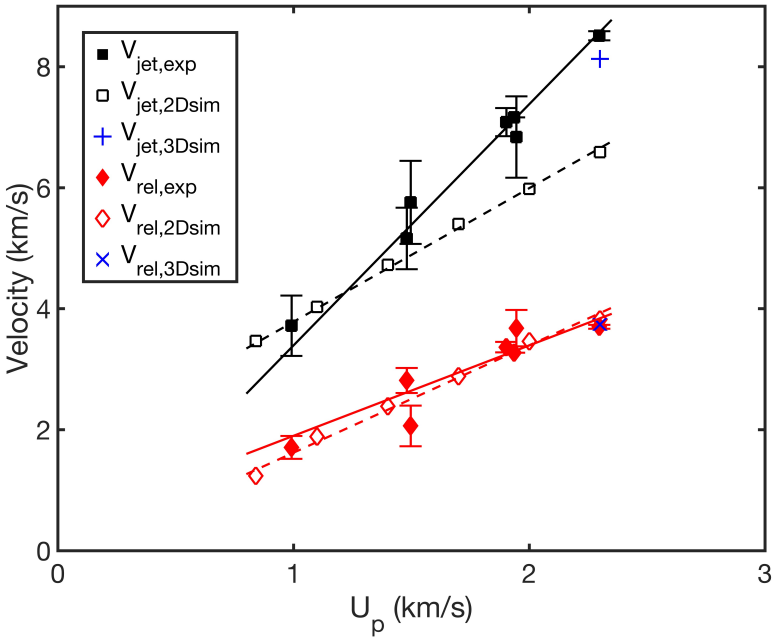


Figure 5.15: The variation of release and jet velocities with particle velocity behind the shock. Experiment values shown as closed symbols, with solid lines for the fitting. The 2D simulation results are the open symbols and have dashed lines for the fitting. The value from the 3D simulation is the blue cross.

as a function of the loading strength is the jet velocity and acceleration for the cavity interface along the centreline, which are calculated using Eqs. 5.7-5.13. As discussed in Section 5.2.3, the acceleration was only calculated for pressures $\geq 4.80\,\mathrm{GPa}$. Figure 5.15 shows that the acceleration of the cavity centreline varies linearly with the loading pressure for both experiments and simulations. The linear fits for normalised cavity interface acceleration for experiments and 2D simulations are obtained as,

$$a'_{experiments} = 0.38p - 0.93 \tag{5.16}$$

and

$$a'_{2Dsims} = 0.14p + 0.51. \tag{5.17}$$

Similar to the calculation of the centreline cavity interface acceleration, using Eq. 5.13, the jet velocity at the time of the cavity closure near the centerline is calculated for various shock strengths. Figure 5.16 shows the linear variation of the

jet velocity with respect to the particle velocity for both simulations and experiments. The linear fits for the jet velocity as a function of shock particle velocity are,

$$V_{jet,experiments} = 3.99u_p - 0.59 \tag{5.18}$$

and

$$V_{jet,2Dsims} = 2.21u_p + 1.58, \tag{5.19}$$

where V_{jet} is the jet velocity and u_p is the particle velocity.

Figure 5.16 also shows the initial release velocities of the interface from the experiments and simulations, as a function of particle velocity. There is good agreement for both the 2D simulations and the single 3D simulation data point in the range studied. The two equations for the fitted lines are,

$$V_{rel,experiments} = 1.49u_p + 0.40 \tag{5.20}$$

and

$$V_{rel,2Dsims} = 1.75u_p - 0.15, \tag{5.21}$$

where V_{rel} is the release velocity.

Figures 5.15 and 5.16 show that while the initial velocity of the interface is approximately equal, the jet velocity and acceleration of the centreline cavity interface is higher in experiments as compared to the 2D simulations. However, in the 3D simulation, for 2.30 km/s case, the results are in close agreement with the experiments. Therefore, the lower jet velocity and acceleration of the cavity interface in the 2D simulation is attributed because of the cavity geometry in 2D, i.e. cylindrical as opposed to spherical. Therefore, spherical cavity leads to higher jet focusing and eventually manifests in higher collapse temperatures and intense hotspots.

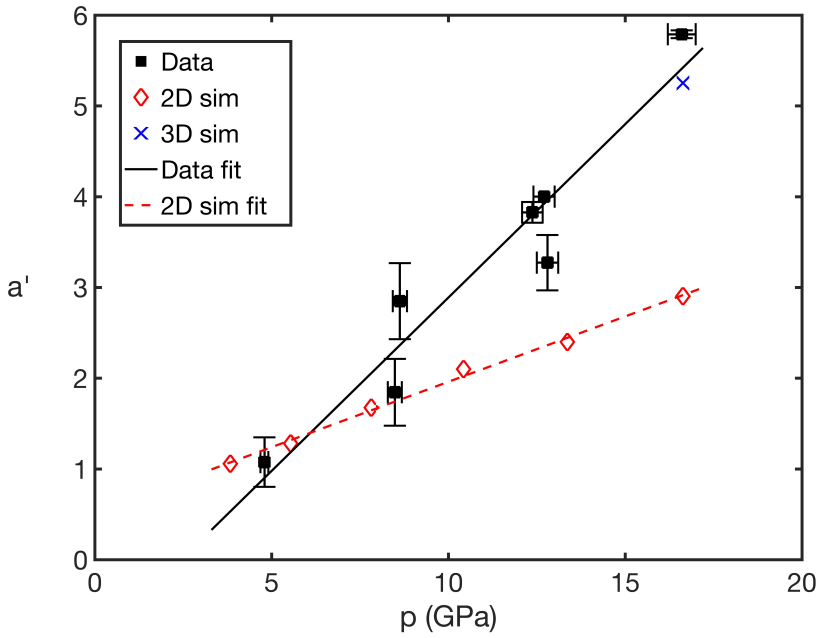


Figure 5.16: Variation of interface acceleration with loading pressure. Experiments shown as black closed symbols, with a solid black line for the fitting. The 2D simulation results are the red open symbols and a dashed red line for the fitting. The single 3D simulation is the blue cross.

5.3.5 Collapse time study on different materials

The studies on PMMA presented in the previous sections show that there is a relationship between parameters like collapse time, t_{col}, and loading pressure, p. From the study of Escauriza et al. [29], in which the experimental results in the present work were first presented, it is suggested that a more general empirical relationship may be found, between t_{col}, p, the longitudinal sound speed, C_L, cavity diameter, D_0, and the initial density, ρ, of the medium. This observation is further supported by the existence of a purely analytical expression for collapse time discovered by Lord Rayleigh, for the collapse of a spherical cavity in a fluid subjected to isotropic hydrostatic loading [37].

In the present section this theory is tested with 2D simulations in SCIMITAR3D on three additional materials: aluminium, copper and stainless steel. The basic Mie-Grüneisen equation of state is used [38], along with the same Johnson-Cook plasticity model [23] as is used to model PMMA. The parameters for these mod-

	Aluminium	**Copper**	**Stainless steel**
C_L (km/s)	6.36	4.76	5.77
Mie-Grüneisen equation of state			
γ_0	1.99	2.00	1.16
C_0 (km/s)	5.84	3.94	4.57
S	1.34	1.49	1.49
ρ (kg/m^3)	2,785	8,930	7,850
C_v (J/kg/K)	896	384	477
G (GPa)	26.0	43.3	81.8
Johnson-Cook model			
A_{JC} (GPa)	0.32	0.40	0.53
B_{JC} (GPa)	0.11	0.18	0.23
n	0.42	1.00	0.30
C_{JC}	0.002	0.025	0.030
m	1.34	1.09	1.00
T_{MELT} (K)	925	1,358	1,836

Table 5.3: Parameters for the aluminium, copper and stainless steel simulations. The C_L values are from a S. P. Marsh report on shock Hugoniot data [25], and the Mie-Grüneisen equation of state and Johnson-Cook plasticity model parameters are from the simulations study of Kapahi et al. [20].

D_0 (mm)	u_p (km/s)	p (GPa)	t_{col} (µs)
Aluminium			
4	0.2	3.04	5.10
4	0.6	10.25	2.28
4	1.0	18.74	1.62
4	1.5	30.87	1.23
4	2.0	43.87	1.01
Copper			
4	0.2	7.41	5.67
4	0.6	25.81	2.53
4	1.0	48.50	1.80
4	1.5	82.83	1.34
4	2.0	117.62	1.09
Stainless steel			
4	0.6	25.25	2.46
4	1.0	47.59	1.71
4	2.0	116.41	1.05

Table 5.4: The D_0 and u_p input values for the simulations on aluminium, copper and stainless steel, and the corresponding p and t_{col} generated by the impact.

els, from Kapahi et al. [20], are listed in Table 5.3, where the additional parameters are the initial Grüneisen coefficient, γ_0 and the gradient of the U_s-u_p Hugoniot slope, S (when assumed to be linear). The simulation geometry and setup is the same as in Fig. 5.1, but only 4 mm cavities are simulated. The particle velocities u_p simulated, and the corresponding shock pressures p generated, are listed in Table 5.4, along with the collapse time, t_{col}. Since the u_p value is inserted as the boundary condition, the p generated by each impact varied greatly for each material. For example, $u_p = 1.0\,\mathrm{km/s}$ in PMMA corresponds to $p = 4.83\,\mathrm{GPa}$, where as for aluminium, copper and stainless steel, the respective p values are 18.74, 48.50 and 47.59 GPa.

The area vs. time plots for the simulations are analysed using the same methods as for the PMMA experimental and simulation data, in order to extract the t_{col} and corresponding t'_{col} values. The same threshold for 'collapse' is used as for the experiments: that the cavity area drops below 5% of its initial value. The results of

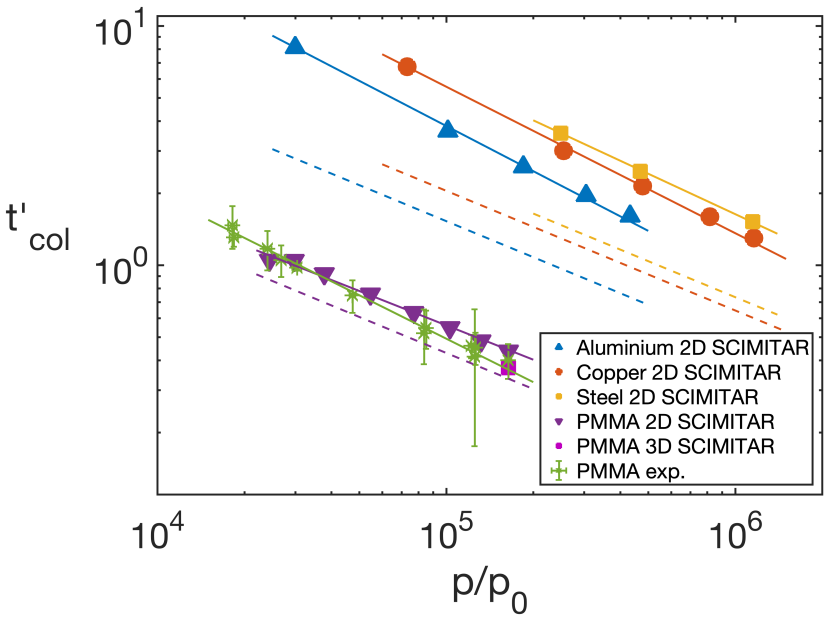


Figure 5.17: Log-log plot showing t'_{col} vs. p/p_0 for the experiments (asterisks) and simulations (close symbols) for which collapse was observed. The fittings for each set of data are shown by straight lines, the the theoretical Rayleigh collapse curves are shown as dashed lines.

this analysis is presented in Fig. 5.17, which shows t'_{col} vs. p/p_0, where, as before, $p_0 = 1\,\mathrm{atm}$ is the normalising pressure. The plot is base-10 logarithmic on both axes, and includes the three additional sets of SCIMITAR3D simulations, along with the PMMA simulations (closed symbols) and PMMA experimental results (asterisks).

Fitting of the lines are shown in Fig. 5.17 as solid lines, fitted using an equation of the form,

$$t'_{col} = \alpha \left(\frac{p}{p_0} \right)^{-\beta}, \tag{5.22}$$

where α and β are the fitting parameters. The fitting results for the additional set of simulations are as follows:

$$t'_{col,Al} = 5205 \left(\frac{p}{p_0} \right)^{-0.63}, \tag{5.23}$$

$$t'_{col,Cu} = 6390 \left(\frac{p}{p_0} \right)^{-0.61}, \tag{5.24}$$

and

$$t'_{col,SS} = 3794\left(\frac{p}{p_0}\right)^{-0.56}, \tag{5.25}$$

where the Al, Cu and SS subscripts correspond to aluminium, copper and stainless steel, respectively. These expressions confirm and generalise the observation that there is an approximate inverse relationship between the dimensionless collapse time and the root of the pressure (the relationship would be maintained even if p were not scaled by p_0, only α, the multiplicative factor, would be different). This was first predicted by Rayleigh's analytical study of spherical and hydrostatic collapse in water [37, 39], and later observed experimentally by Swantek & Austin (including data from Dear and Field) [12, 40], as well as being predicted in numerical simulations of cavity collapse in a fluid [41].

Rayleigh's expression provides a general expression for the cavity 'Rayleigh' collapse time in SI units, $t^R_{col,SI}$ [s], only in terms of its size D_0 [m], the density of the fluid ρ [kg/m^3] and the pressure in the fluid p [Pa],

$$t^R_{col,SI} = 0.4573 D_0 \sqrt{\frac{\rho}{p}}. \tag{5.26}$$

For the purposes of the present study, we recast the units of this expression to those that have been used in the shock-cavity interaction analysis, changing to D_0 [mm], ρ [g/cc] and keeping p [Pa], which results in t^R_{col} being in μs. Furthermore, to allow direct comparison of this expression to the shock collapse times, the pressure is replaced by $p = p_0(p/p_0)$, and $p_0 = 1.01 \times 10^5 \mathrm{Pa}$ is brought outside the surd and its value incorporated into the constant. This gives the final expression,

$$t^R_{col} = 45.44 D_0 \sqrt{\frac{\rho}{p_s}} \left(\frac{p}{p_0}\right)^{-0.5}, \tag{5.27}$$

where a 'scaling pressure', $p_s = 1\,\mathrm{Pa}$, has been kept to ensure the units in the expression are balanced. This is important when normalised the Rayleigh collapse time in the same way as for the shock case, by D_0 and C_L, i.e. $t' R_{col} = t^R_{col}(C_L/D_0)$.

Thus, we have,

$$t'^{R}_{col} = 45.44 C_L \sqrt{\frac{\rho}{p_s}} \left(\frac{p}{p_0}\right)^{-0.5}. \tag{5.28}$$

where again C_L is in mm/μs (same as km/s). An interesting consequence of this expression is that the dimensionless collapse time is directly proportional to the factor $C_L\sqrt{\rho}$. Interpretation of this product physically is simplified by the expression for sound speed in a material,

$$C_L = \sqrt{\frac{M}{\rho}}, \tag{5.29}$$

where M is the longitudinal modulus, the ratio of the axial stress to axial strain, when a material is in a uniaxial strain state, which is true of shock loading [42]. Rearranging this expression, we have $C_L\sqrt{\rho} = \sqrt{M}$, telling us the dimensionless collapse time is proportional to the root of the medium's longitudinal modulus, which is a measure of a material's 'stiffness'. Therefore, with a greater modulus a material will have higher collapse times when scaled for cavity size and when taking into account the material property of sound speed, which is as we would probably expect. As we will see below, this intuition is maintained for shock-cavity interactions also. It is also worth noting that M can be expressed in terms of the bulk modulus, K, and the shear modulus, G, as, $M = K + 4G/3$. For an inviscid fluid, G becomes zero, in which case M is simply K, and the sound speed expression becomes the Newton-Laplace equation, $C_L = \sqrt{K/\rho}$. From this we can see that the dimensionless collapse time of a solid or a fluid with viscosity is greater than the collapse time for an inviscid fluid of the same density, since $G \geq 0$. This is as we would expect, since the solid and viscous fluid have a higher stiffness than the inviscid fluid.

We can also express Eq. 5.28 in terms of two constants to give,

$$t'^{R}_{col} = \alpha_R \left(\frac{p}{p_0}\right)^{-\beta_R}, \tag{5.30}$$

where $\alpha_R = 45.44 C_L \sqrt{\rho/p_s}$ and $\beta_R = 0.5$. As we will see below, this is useful for comparing the dimensionless Rayleigh equation to the dimensionless simulation collapse time expressions in Eqs. 5.23-5.25. In Fig. 5.17 the theoretical collapse time curves for the four materials simulated are shown as dashed lines.

In theory, the Rayleigh expressions of Eqs. 5.27&5.28 apply to any material in its fluid state, which begs the question of whether such an expression can be obtained for shock-induced cavity collapse, even when the initial state is a solid. The conjecture proposed by Escauriza et al. [29], by comparing the collapse time equations of PMMA and hydrogel, for both their theoretical Rayleigh curves (by inputting the respective ρ and p values) and experimental results, is that the offset between the lines observed in log-log plot is determined by C_L and ρ only: the ratio of the multiplicative factor in their t'_{col} and t'^{R}_{col} equations are $617/305 = 137/69 = 2.0$. This is the same as the ratio of the factor $C_L\sqrt{\rho}$ present in the dimensionless Rayleigh expression in Eq. 5.28 – i.e. $C_{L_{PMMA}}\sqrt{\rho_{PMMA}}/C_{L_{gel}}\sqrt{\rho_{gel}}$ also equals 2.0.

It is thus investigated whether a general expression can be found relating t'_{col} and p/p_0 for any material. Furthermore, an effort is made to find a general expression that captures the exponent of p/p_0. For this purpose, an attempt is made to express the extracted α and β, from fitting from Eq. 5.22, in terms only of the cavity medium material parameters C_L and ρ, and the geometric parameter D_0. Inspired by the similarity of the α in the expression to the factor $45.44 C_L \sqrt{\rho/p_s}$ in the dimensionless collapse time Rayleigh form, Eq. 5.28, it is plotted against $C_L\sqrt{\rho/p_s}$. The constant p_s is again a scaling pressure of value 1 Pa in order to keep α in the final expression dimensionless. The resulting plot is shown in Fig. 5.18, where the experimental and simulation values are represented by closed and open symbols, respectively. Linear fitting is performed on the four 2D simulation data points only, but it is clear that the two experimental data points, on PMMA

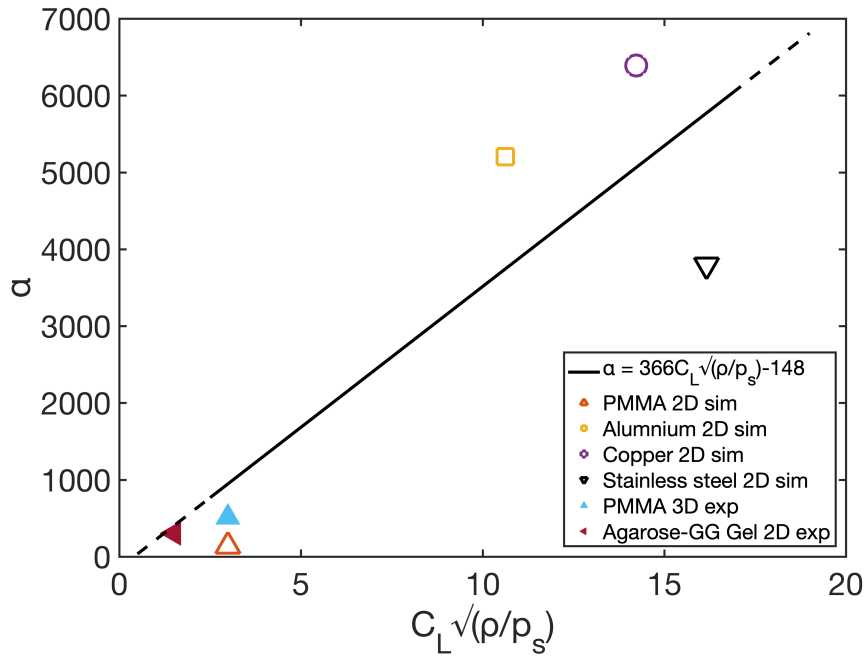


Figure 5.18: Plot showing α vs. $C_L\sqrt{\rho/p_s}$, with the open symbols for the simulations and closed symbols for the experiments. The solid line is the fitting for only the simulations, with the dashed line showing the linear extrapolation outside the fitting region.

and Agarose-GG gel, are in good agreement. The fit result is the expression,

$$\alpha = 366 C_L \sqrt{\frac{\rho}{p_s}} - 148. \tag{5.31}$$

Similarly, an expression for β is extracted, but with no form from the Rayleigh expression to follow, since its analytical form is always an inverse square root dependency. Since the sound speed C_L partly determines how fast an impulse transmits through a material, and thus how quickly the compression of the cavity may commence, it is chosen as the parameter to plot β against. Again in the interest of maintaining a dimensionless expression, C_L is divided by a scaling speed $C_s = 1\,\mathrm{km/s}$. As can be seen in Fig. 5.19, there does appear to be a proportional relationship, with a linear fit given by the black line. As in the α plot, the closed symbols are used for the experiments and the open for the simulation results. However, in this case the experimental data points do not lie closely to the line predicted by the fitting. Relative to their longitudinal sound speeds,

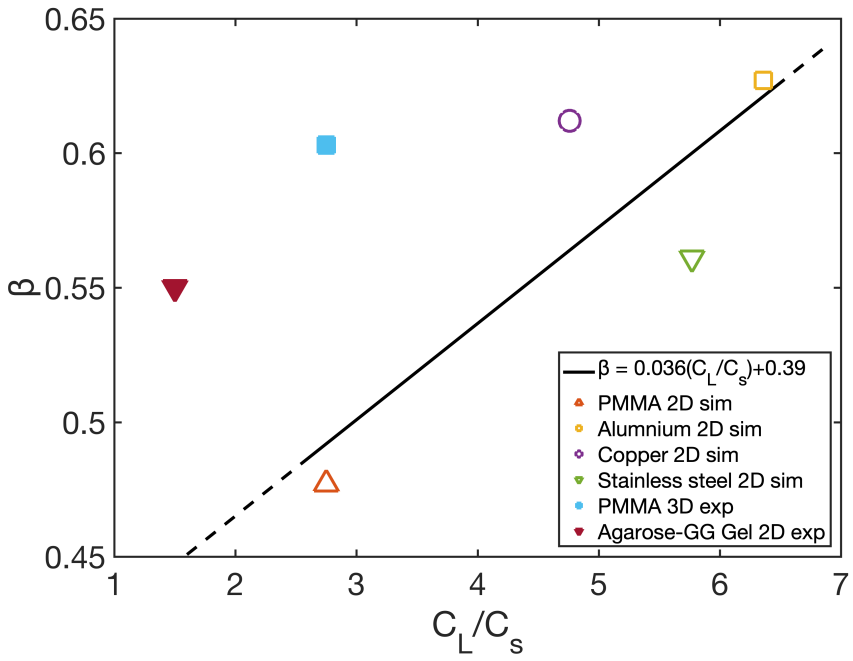


Figure 5.19: Plot showing β vs. C_L/C_s for the experiments and simulations, with the open symbols for the simulations and closed symbols for the experiments. The solid line is the fitting for only the simulations, with the dashed line showing the linear extrapolation outside the fitting region.

the higher experimental β values correspond to a steeper gradient in the log-log plot, and therefore a sharper decrease in collapse time as the loading pressure increases. The output of the fitting for the 2D simulations is,

$$\beta = 0.036\frac{C_L}{C_s} + 0.39. \tag{5.32}$$

A clear problem with the fitting to obtain Eqs. 5.31&5.32 is that only four materials have been simulated, and so only four data points are available for fitting. The result is respective R^2 values of 0.74 and 0.70, for α and β, which are too low to signify statistical accuracy. Simulations of more materials are needed, at a finer sampling of u_p values, and at different D_0 values to 4 mm, to be confident of the result. Nonetheless, there does appear to be a trend, and if we feed the two constants into Eq. 5.22, we obtain the general expression for the dimensionless col-

lapse time for an arbitrary material,

$$t'_{col} = t_{col}\left(\frac{C_L}{D_0}\right) = \left(366C_L\sqrt{\frac{\rho}{p_s}} - 148\right)\left(\frac{p}{p_0}\right)^{-\left(0.036\frac{C_L}{C_s}+0.39\right)}. \tag{5.33}$$

If we are to predict the collapse time in dimensional form, we simply multiply both sides by D_0/C_L, giving,

$$t_{col} = \left(366\sqrt{\frac{\rho}{p_s}} - 148\frac{1}{C_L}\right)D_0\left(\frac{p}{p_0}\right)^{-\left(0.036\frac{C_L}{C_s}+0.39\right)}. \tag{5.34}$$

It is instructive to consider the physical interpretation of the α and β factors inserted in the dimensionless expression in Eq. 5.33. All else being held equal, i.e. the cavity diameter and loading pressure, the α factor tells us that vertical placement of the dimensionless collapse time curve depends on the product $C_L\sqrt{\rho}$. As we saw for the dimensionless Rayleigh expression in Eq. 5.28, this means the shock-cavity interaction is related to the longitudinal modulus M, since $\sqrt{M} = C_L\sqrt{\rho}$. The expression mentioned above, $M = K + 4G/3$, may also explain the discrepancy between the acceleration of the cavity interface in the previous Chapter, where the simulations without a strength model under-predict the acceleration compared to the experiments. The effects of the shear modulus G may still play a non-significant role well into the hydrodynamic regime.

When we consider the equation for β, in Eq. 5.32, which is the exponent of the pressure ratio in Eqs. 5.33&5.34, the relationship is only in terms of the longitudinal sound speed C_L – in km/s – we see that a higher β value is predicted for high sound speeds, which in turn corresponds to a steeper negative gradient. This agrees with the intuition that an increase in sound speed leads to a decrease in the collapse time for a given loading pressure, since the shock will traverse the cavity more rapidly, and therefore exposes the cavity interface to loading at earlier times.

It is interesting to compare the dimensionless expression of Eq. 5.33 to the di-

mensionless Rayleigh expression in Eq. 5.28. The key similarity can be seen above between Eq. 5.22 and Eq. 5.30, respectively for shock and Rayleigh collapse, which have identical form: a multiplicative factor (α and α_R) and an exponent (β and β_R). After transforming the Rayleigh expression into the same units as the shock collapse expression, it is possible to determine the offset between the shock and Rayleigh constants, which allows transformation between the prediction of hydrostatic collapse and shock-induced collapse in a fluid. These transformations are,

$$\alpha = \alpha_R + 321 C_L \sqrt{\frac{\rho}{p_s}} - 148 \tag{5.35}$$

and,

$$\beta = \beta_R - 0.036 \frac{C_L}{C_s} + 0.11, \tag{5.36}$$

where again p_s and C_s values are there to ensure dimensionless expressions, and are equal to 1 Pa and 1 mm/μs, respectively. From these two expressions we are able to explain observations in Fig. 5.17. Firstly, the offset between the fitted shock simulation curves (solid lines) and Rayleigh curves (dashed lines) are regular, in that the order of the curves and approximate spacing between them is preserved. We also see that the collapse time for a shock interaction is longer than its corresponding time for Rayleigh collapse, i.e. the curve is above. This offset is captured by Eq. 5.35, since the magnitude of additional factor $(321 C_L \sqrt{\rho/p_s} - 148)$ is always > 1, since $321 > 148$ and $C_L \sqrt{\rho/p_s} > 1$. This finding is in agreement with simulations on shock-induced cavity collapse by Johnsen & Colonius [41], who found that cavity collapse under shock loading is greater than Rayleigh collapse, because of the time taken for the shock to propagate past the cavity, which is of the same order as dimensionless time unit of 1 ($t' = t \times C_L/D_0 \approx (D_0/U_s) \times (C_L/D_0) \sim 1$). For example, using the t'^R_{col} expression (Eq. 5.28) and general t'_{col} expression (Eq. 5.34) to predict the collapse time of a cavity of in aluminium of arbitrary size (D_0 does not appear in the dimensionless expressions) under a load of $p = 50\,\mathrm{GPa}$, we obtain $t'^R_{col,Al} = 0.69$ and $t'_{col,Al} = 1.12$, respec-

tively. For copper at the same pressure these values would be $t'^{R}_{col,Cu} = 0.92$ and $t'_{col,Cu} = 3.22$, and for stainless steel $t'^{R}_{col,SS} = 1.05$ and $t'_{col,SS} = 2.28$.

Second, the transformation in Eq. 5.36 tells us that the exponent β remains in the vicinity of $\beta_R = 0.5$ for the materials studied, varying between ∼0.45-0.6. This is reflected in the similar gradients of the shock simulation lines in Fig. 5.17. Furthermore, as discussed above, the β becomes more negative for higher sound speeds, meaning a sharper decrease in collapse time when the loading strength is increased.

These simulation results indicate the existence of a general collapse time scaling law for a cavity in an arbitrary solid material under shock impact, much as the Rayleigh expression is for an arbitrary liquid under a isometric and hydrostatic load. Interestingly, as observed for PMMA in the experimental results of Escauriza et al. [29], it appears that a full transition to hydrodynamic behaviour is *not* necessary for the scaling law to apply. A partial transition and full collapse of the cavity are sufficient. To assess the exact shock pressure for each material at which the scaling law begins to apply, and to assess whether this pressure is also related to the material properties, will require a large number of simulations for each material, over a large number of p and D_0 values, from strength-dominated up to hydrodynamic.

As discussed above, the main limitation of the general collapse time equations, Eqs. 5.33&5.34, is the small number of data points to obtain the fits, each of which is an individual material (aluminium, copper, PMMA and stainless steel). To improve the statistics and determine whether a strong trend truly exists, a large number of materials must be simulated. Multiplied by the number of simulations needed for each material, this comes to a significant computational cost. Therefore, there is clear motivation to build an analytical model for collapse time during shock loading of a cavity. At present, it does not appear that any such model exists. Nonetheless, the analysis presented in this work highlights a wide

array of avenues to be explored both experimentally and computationally in the field of shock-cavity interactions.

5.4 Conclusions

A detailed head-to-head comparison between experiments and simulations has been performed to analyse the shock-induced cavity collapse behaviour in the solid medium PMMA. The numerical simulations are performed using the Eulerian based sharp-interface code SCIMITAR3D. The experiments are performed at the ESRF using single and two-stage gas guns, with ultra-high-speed X-ray imaging used to obtain experimental data and visualisation of the cavity during the collapse process. The numerical simulations approximate the experimental spherical geometry by using a 2D circular cavity of the same diameter as in experiments, i.e. 6 mm. Since 3D simulations are expensive, high resolution spherical cavity collapse simulations are performed for only 2 shock strengths, of 1.25 and 16.60 GPa.

A detailed comparison is conducted at four selected shock pressures, of 1.25, 1.84, 4.10 and 16.60 GPa. For all four shock strengths, the predicted cavity interface outlines from simulations are in close agreement with experiments. The numerical framework can capture the mechanics of cavity collapse for the different loading regimes with good physical fidelity. For 1.25 GPa and 1.84 GPa shock strengths, the experiments show asymmetric collapse with the formation of ridges on the cavity surface. Using the numerical simulations, the ridges are identified as the locations of the initiation sites of the adiabatic shear bands that emanate from the surface. The collapse under low shock strengths is dominated by rate-dependent plastic dissipation. For higher shock strengths, i.e. 4.10 GPa and 16.60 GPa, both experimental and simulation results show a symmetric collapse shape with no ridge formation. Under strong shock loading, the PMMA melts because of shock heating and the cavity effectively collapses in a liquid

PMMA material, in a hydrodynamic mode with jet formation and generation of barotropic vortices. Between the two loading extremes, the collapse transitions from a strength-dominated regime to a hydrodynamic regime. This transition is observed to begin in the current analysis for loading pressure greater than 4.10 GPa. The prediction of the transition regime in the numerical simulation is dependent on: (i) the accuracy of the melting temperature, which is a function of pressure; and (ii) the temperature and pressure dependent specific heat value; more accurate models for melting temperature and specific heat will be required to pinpoint the transition load. The transition point may also depend on cavity size. These issues remain matters of future investigation.

In the two different loading regimes, i.e. strength-dominated and hydrodynamic, the key differences between the 2D and 3D simulations are analysed. The 2D simulations are observed to capture the qualitative behaviour of collapse in both loading regimes. For the lowest shock strength compared head-to-head, at the shock pressure of 1.25 GPa, in 3D the adiabatic shear bands are formed in the form of concentric disks around the cavity surface. As the bands grow, a complex hotspot structure forms with a central heated core corresponding to the collapse site. The collapse site is surrounded by what appear to be layers of adiabatic shear band surfaces. On the other hand, for the 16.60 GPa shock, the centreline deformation is observed to be higher in 3D and in experiments than 2D. Overall, the 3D simulations are in closer agreement with experiments; however, 2D simulations are far less computationally expensive and therefore allow for exploration of parameter spaces for cavity collapse and for construction of surrogate models, as done in previous work [43, 44].

For a quantitative comparison between the simulation and experiments data, scaling relations governing the cavity collapse and shock strength are obtained and compared for a wider set of loading pressures. The experimental data comprises the full set obtained by Escauriza et al. [29]. The empirical relations for the

time to collapse and cavity surface acceleration as a function of input pressure are obtained. The quantitative relationships from the simulations are in close agreement with experiments for PMMA. Furthermore, a useful scaling relationship between the hydrodynamic collapse jet speed and the imposed particle velocity is computed.

Finally, to determine whether a general equation for collapse time exists, in terms of basic material and geometric parameters, additional simulations in SCIMITAR3D are performed for cavity collapse in aluminium, copper and stainless steel mediums. Along with the PMMA simulations, the results suggest such an expression does exist, which agrees with previous comparisons of shock-induced cavity collapse to Rayleigh collapse: the dimensionless time to collapse for shock interactions is approximately one unit more than for Rayleigh collapse, and is related to the product of the sound speed and the square root of the material density, which, in fluid dynamics, is the square root of the bulk modulus, which is a measure of the materials stiffness.

The present study establishes confidence in the numerical simulations to study the physics governing the collapse behaviour in solids over a wide range of loading conditions. Further ongoing work is directed towards clarifying the detailed physics of shear band emergence at the cavity surface and the late-stage coarsening, bending and curvature of the shear bands. We are also investigating the way in which the energy content and temperature distribution in the hotspot depends on the occurrence or non-occurrence (in the hydrodynamic regime) of shear bands; the implications of these hotspot characteristics are expected to be significant for their initiation and growth and therefore for the sensitivity of energetic materials. In addition, an effort will be made to increase the confidence in the general collapse time equation, either through simulations of more material, or by pursuing an analytical expression from foundational arguments.

5.5 References

[1] N K Rai, E M Escauriza, D E Eakins, and H S Udaykumar, "Mechanics of shock induced pore collapse in poly(methyl methacrylate) (PMMA): Comparison of simulations and experiments," *J. Mech. Phys. Solids*, vol. 143, 2020.

[2] J E Field, "The physics of liquid impact, shock wave interactions with cavities, and the implications to shock wave lithotripsy," *Phys. Med. Biol.*, vol. 36, no. 11, pp. 1475–1484, 1991.

[3] T Kodama and K Takayama, "Dynamic Behaviour of Bubbles During Extracorporeal Shock-Wave Lithotripsy," *Ultrasound Med. Biol.*, vol. 24, no. 5, pp. 723–738, 1998.

[4] G N Sankin and P Zhong, "Interaction between shock wave and single inertial bubbles near an elastic boundary," *Phys. Rev. E*, vol. 74, no. 046304, 2006.

[5] R Browning and E Stride, "Microbubble-Mediated Delivery for Cancer Therapy," *Fluids*, vol. 3, no. 4, p. 74, 2018.

[6] J E Field, N K Bourne, S J P Palmer, and S M Walley, "Hot-spot ignition mechanisms for explosives and propellants," *Philos. Trans. R. Soc. A*, vol. 339, pp. 269–283, 1992.

[7] H K Springer, S Bastea, A L Nichols, *et al.*, "Modeling The Effects of Shock Pressure and Pore Morphology on Hot Spot Mechanisms in HMX," *Propellants, Explos. Pyrotech.*, vol. 43, no. 8, pp. 805–817, 2018.

[8] L Michael and N Nikiforakis, "The evolution of the temperature field during cavity collapse in liquid nitromethane. Part I: inert case," *Shock Waves*, vol. 29, pp. 153–172, 2019.

[9] L Michael and N Nikiforakis, "The evolution of the temperature field during cavity collapse in liquid nitromethane. Part II: reactive case," *Shock Waves*, vol. 29, pp. 173–191, 2019.

[10] N K Rai, M J Schmidt, and H S Udaykumar, "Collapse of elongated voids in porous energetic materials: Effects of void orientation and aspect ratio on initiation," *Phys. Rev. Fluids*, vol. 2, no. 043201, 2017.

[11] R A Austin, N R Barton, J E Reaugh, and L E Fried, "Direct numerical simulation of shear localization and decomposition reactions in shock-loaded HMX crystal," *J. Appl. Phys.*, vol. 117, p. 185902, 2015.

[12] A B Swantek and J M Austin, "Collapse of void arrays under stress wave loading," *J. Fluid Mech.*, vol. 649, pp. 399–427, 2010.

[13] A Kapahi and H S Udaykumar, "Dynamics of void collapse in shocked en-

ergetic materials: Physics of void-void interactions," *Shock Waves*, vol. 23, no. 6, pp. 537–558, 2013.

[14] N K Bourne and J E Field, "Shock-induced collapse of single cavities in liquids," *J. Fluid Mech.*, vol. 244, pp. 225–240, 1992.

[15] X C Mi, L Michael, E Ioannou, *et al.*, "Meso-resolved simulations of shock-to-detonation transition in nitromethane with air-filled cavities," *ArXiV*, vol. 125, p. 245901, 2019.

[16] M Armstrong, E Bukovsky, W Shaw, *et al.*, "Time-resolved X-ray Imaging of Void Collapse in Silicone and TNT," tech. rep., Lawrence Livermore National Lab.(LLNL), Livermore, CA (United States), 2018.

[17] C A Duarte, A Hamed, J D Drake, *et al.*, "Void Collapse in Shocked β - HMX Single Crystals: Simulations and Experiments," *Propellants, Explos. Pyrotech.*, pp. 243–253, 2020.

[18] D B Hardin and J O Mares, "Temperature rise from collapsing pores," *AIP Conf. Proc.*, vol. 1979, no. 180003, 2018.

[19] S Sambasivan, A Kapahi, and H S Udaykumar, "Simulation of high speed impact, penetration and fragmentation problems on locally refined Cartesian grids," *J. Comput. Phys.*, vol. 235, pp. 334–370, 2013.

[20] A Kapahi, S Sambasivan, and H S Udaykumar, "A three-dimensional sharp interface Cartesian grid method for solving high speed multi-material impact, penetration and fragmentation problems," *J. Comput. Phys.*, vol. 241, pp. 308–332, 2013.

[21] N K Rai, A Kapahi, and H S Udaykumar, "Treatment of contact separation in Eulerian high-speed multimaterial dynamic simulations," *Int. J. Numer. Methods Eng.*, vol. 100, pp. 793–813, 2014.

[22] N K Rai, M J Schmidt, and H S Udaykumar, "High-resolution simulations of cylindrical void collapse in energetic materials: Effect of primary and secondary collapse on initiation thresholds," *Phys. Rev. Fluids*, vol. 2, no. 043202, 2017.

[23] G R Johnson and W H Cook, "A constitutive model and data for materials subjected to large strains, high strain rates, and high temperatures," *Proc. Seventh Int. Symp. Ballist.*, pp. 541–547, 1983.

[24] T J Holmquist, J Bradley, A Dwivedi, and D Casem, "The response of polymethyl methacrylate (PMMA) subjected to large strains, high strain rates, high pressures, a range in temperatures, and variations in the intermediate principal stress," *Eur. Phys. J. Spec. Top.*, vol. 225, pp. 343–354, 2016.

[25] S P Marsh, "LASL Shock Hugoniot Data," tech. rep., University of California Press, 1980.

[26] J H Tillotson, "Metallic equations of state for hypervelocity impact," *Gen. At. Rep. GA-3216*, 1962.

[27] M Blackman, "The theory of the specific heat of solids," *Reports Prog. Phys.*, vol. 8, no. 1, pp. 11–30, 1941.

[28] E M Escauriza, A Rack, E Synchrotron, *et al.*, "Ultra high-speed indirect X-ray imaging system with versatile spatio-temporal sampling capabilities," *Appl. Opt.*, vol. 57, no. 18, pp. 5004–5010, 2018.

[29] E M Escauriza, J P Duarte, D J Chapman, *et al.*, "Collapse dynamics of spherical cavities in a solid under shock loading," *Sci. Rep.*, vol. 10, pp. 1–16, may 2020.

[30] S W Wilkins, T E Gureyev, D Gao, *et al.*, "Phase-contrast imaging using polychromatic hard X-rays," *Nature*, vol. 384, pp. 335–338, nov 1996.

[31] P Cloetens, R Barrett, J Baruchel, *et al.*, "Viewpoint on Phase objects in synchrotron radiation hard x-ray imaging," *J. Phys. D. Appl. Phys.*, vol. 29, pp. 133–146, 1996.

[32] V F Nesterenko, M A Meyers, and T W Wright, "Self-organization in the initiation of adiabatic shear bands," *Acta Metall.*, vol. 46, no. 1, pp. 327–340, 1998.

[33] Q Xue, M A Meyers, and V F Nesterenko, "Self-organization of shear bands in titanium and Ti-6Al-4V alloy," tech. rep., 2002.

[34] N A Kudryashov, P N Ryabov, and A S Zakharchenko, "Self-organization of adiabatic shear bands in OFHC copper and HY-100 steel," *J. Mech. Phys. Solids*, vol. 76, pp. 180–192, 2015.

[35] N K Rai and H S Udaykumar, "Void collapse generated meso-scale energy localization in shocked energetic materials: Non-dimensional parameters, regimes, and criticality of hotspots," *Phys. Fluids*, vol. 31, no. 016103, 2019.

[36] S Roy, N K Rai, O Sen, *et al.*, "Modeling mesoscale energy localization in shocked HMX, Part II: training machine-learned surrogate models for void shape and void–void interaction effects," *Shock Waves*, vol. 30, no. 4, pp. 349–371, 2020.

[37] L Rayleigh, "VIII. On the pressure developed in a liquid during the collapse of a spherical cavity," *Philos. Mag.*, vol. 34, no. 200, pp. 94–98, 1917.

[38] M A Meyers, "Shock Waves: Equations of State," in *Dyn. Behav. Mater.*, ch. 5, pp. 124–151, 1994.

[39] C E Brennen, *Cavitation and Bubble Dynamics*. Oxford University Press, 1995.

[40] J P Dear and J E Field, "A study of the collapse of arrays of cavities," *J. Fluid Mech.*, vol. 190, no. 1944, p. 409, 1988.

[41] E Johnsen and T Colonius, "Numerical simulations of non-spherical bubble collapse," *J. Fluid Mech.*, vol. 629, pp. 231–262, 2009.

[42] M A Meyers, "Dynamic Deformation and Waves," in *Dyn. Behav. Mater.*, ch. 1, pp. 1–22, 1994.

[43] A Nassar, N K Rai, O Sen, and H S Udaykumar, "Modeling mesoscale energy localization in shocked HMX, part I: machine-learned surrogate models for the effects of loading and void sizes," *Shock Waves*, 2018.

[44] O Sen, N K Rai, A S Diggs, *et al.*, "Multi-scale shock-to-detonation simulation of pressed energetic material: A meso-informed ignition and growth model," *J. Appl. Phys.*, vol. 124, p. 085110, 2018.

Chapter 6

Conclusions and research outlook

Summarised here are the research motivations and the overall conclusions of this work. Firstly, the technical challenges of performing and capturing the experiments are discussed, from the methods in Chapter 2 and the imaging system paper in Chapter 3. Second, the experimental results and conclusions from the paper in Chapter 4 are summarised. Third, highlights of the simulations comparison Chapter 5, based on a collaborative paper, are given. These summaries are presented below in Section 6.1. Lastly, in Section 6.2 the applications of this work and possible future developments are discussed.

6.1 Conclusions

Motivated by the need to understand cavity collapse in many fields of research, ranging from medical science to nuclear fusion, this work sheds light on a form of the phenomenon that has proven particularly difficult to capture experimentally: cavity collapse in a solid medium. To achieve this, it is necessary to generate the correct loading conditions for collapse to occur – in the case of solids, a shock must be generated in the cavity medium. Gas gun systems provide a reliable and safe solution for this purpose, and by using both a single-stage gas gun

and two-stage gas gun, a wide range of shock pressures can be accessed.

For visualising the collapse process *in-situ*, high-speed synchrotron radiography offers the combination of short-pulsed, bright and hard X-rays, which makes it highly favourable for capturing dynamic phenomena like crack formation, explosions and, as for the present work, shock-cavity interactions. To minimise X-ray attenuation, the material PMMA is chosen, because of its relatively low atomic weight. PMMA has also historically been used as a window material in shock studies, meaning it has been extensively studied under shock loading, and understanding its behaviour in the context of cavity collapse is relevant to research into dynamic physics more broadly.

In order to maximise the amount of data obtained during each cavity collapse experiment, it is necessary to capture radiographs using single pulses of the synchrotron X-rays. As discussed in Chapters 2&3, achieving this is a great technical challenge, due to the synchronisation between the gas gun system, imaging system and synchrotron X-rays. Furthermore, the equipment is transported from the UK to France and the experiments are conducted in a tight window of time. For this purpose, building upon previous work at other synchrotrons, a multi-camera system is developed: with a configuration of three cameras, the maximum acquisition rate is attained (5.68 Mfps in 16-bunch mode at the ESRF), with the cameras providing up to 384 frames per acquisition. In this particular setup, a second, thicker in-line scintillator is employed, to maximise the signal obtained by the three cameras.

As is presented in Chapter 3, an additively manufactured aluminium lattice is impacted to test the capabilities of the system, and it is found that high image quality is obtained for all of the images. For those images captured with the upstream scintillator, the signal-to-noise ratio is higher than for the downstream scintillator, due to the increase in mean X-ray energy for the spectrum transmitted through the upstream scintillator. By using the measured spectrum of ESRF

beamline ID19's undulator source, simulations of the attenuation of the spectrum by the two scintillators confirm this observation. Through further simulations, it is found that an alternative scintillator arrangement may address the disparity in signal-to-noise between the two scintillators. This is possible because of the high adaptability of the imaging system, which also makes is it versatile and well-suited for future advances in scintillator and synchrotron technology.

Two configurations of the imaging system are used to capture shock-induced cavity collapse in PMMA, with a single camera used to capture the single-stage gas gun experiments and a two-camera system capturing the two-stage gas gun experiments, through the emission of a single scintillator. The results from these two sets of experiments, presented in Chapter 4, reveal new observations of cavity collapse in a solid. As predicted by simulations on cavity collapse in solid materials like HMX, distinctly different collapse behaviour is observed over a range of shock pressures. At the lowest pressure generated, 0.49 GPa and 0.60 GPa, full collapse does not occur, and large fragments are formed by damage. At pressures above 0.60 GPa, full collapse is observed. Also observed at the lower shock pressures are perturbations, which form along the cavity interface during loading. From previous simulation studies, these perturbations are known to be caused by localised bands of shear, and this is confirmed by the simulations in Chapter 5. As the shock pressure is increased, we see that the spacing between these bands appears to decrease. Quantitative Fourier analysis shows this to be the case, with the initial mean spacing between bands decreasing with loading pressure.

As demonstrated by previous work on cavity collapse in solids and on shear banding, this decrease in spacing signifies a transition from strength-dominated to hydrodynamic behaviour. At the intermediate shock pressures studied, between 2.44 and 3.08 GPa, the perturbation spacing is not detectable with the resolution of the images, and the dynamics more closely resemble that of hydrostatic

compression of a cavity in a fluid medium. At 4.10 GPa and above, the onset of jetting is seen, which is associated with shock-cavity interactions in fluids. This pressure also demarcates the onset of constant acceleration of the cavity interface, which simulations performed in Hytrac confirm is a feature when cavity collapse is simulated without a strength model. However, the greater values of acceleration predicted by the Hytrac simulations, compared to the experimental simulations, suggests that strength may still play a significant role well into the hydrodynamic regime. At the highest shock strengths studied, up to 16.60 GPa, a pronounced jet is formed, impacting the far cavity interface and producing a secondary shock front ahead of the initial shock front. Rotational forces generated by the collapse cause the formation of toroidal vortices that propagate in the direction of the shock. Capture of the optical emission through the rear of the cavity target with a visible light camera verifies the formation of a plasma inside the tori. Observation of these tori match the prediction of many simulations on shock-cavity interactions in fluids, confirming one of the major mechanisms of energy localisation, since very large spikes in pressure and temperature are generated in the toroidal lobes.

Inspired by previous work on shock-cavity interactions in hydrogel, the dimensionless collapse time is plotted against the pressure ratio in log-log space. The fitted equation is an exponential expression, with a multiplicative factor and exponent. The results verify the fitting applies for PMMA also, with an expression very similar to that of hydrogel, as well as that predicted by the Rayleigh theory of hydrostatic collapse. Although it is observed that complete collapse is a necessary criteria to lie on the curve, also required is sufficient progression into the hydrodynamic regime.

A final aspect of this work is the head-to-head comparison of the experimental results to simulations performed in SCIMITAR3D, discussed in Chapter 5. Using parameters for PMMA from the literature, simulations of the same cavity ge-

ometry and loading conditions as the experiments are performed, including a strength model, mostly in plane-strain 2D, with two additional simulations in 3D. At four selected pressures, of 1.25, 1.84, 4.10 and 16.60 GPa, the projected area and cavity interface outline are closely compared. Despite the assumption that heat capacity is constant – not physically accurate for a polymer like PMMA – the features of collapse in the 2D simulations closely match those observed in the experiments. There is even closer agreement for the two 3D simulations, but the finer features like perturbation and shear band formation are still captured by the 2D modelling. The 3D simulation of the 1.25 GPa shock reveal that the shear bands appear as concentric, petal-like formations emanating from the cavity surface. The simulations also show that the network of shear banding elevates the temperature in the PMMA medium, which is further heated by the later re-shock after collapse, leading to the formation of an intense hot spot.

At 1.25 GPa the temperature increase from the re-shock is found to be approximately 100 K, whereas for the 1.84 GPa shock the increase is 150 K. There is also a difference in angle at which the shear bands emanate from the cavity surface, with the angle tilted in the direction of the shock for the stronger 1.25 GPa case. At the higher shock strengths studies, of 4.10 and 16.60 GPa, the hydrodynamic modes of collapse are observed. However, at 4.10 GPa the simulations predict a stronger jet, thus suggesting a more advanced transition to a fluid-like state. This may be due to the constant heat capacity value over-predicting the temperature rise in the PMMA medium. However, the collapse time closely aligns with the experiment at this pressure. The maximum temperature predicted by the simulations at this shock pressure is around 1,500 K.

At the highest shock pressure, 16.60 GPa, the formation of rotational vortices are also present in the 2D and 3D simulations, forming a toroid in the 3D case. The bulk temperature of the bulk PMMA medium rises to 1,200 K, far higher than the PMMA melt temperature, and the spike in temperature after collapse leads to hot

regions in excess of 5,000 K. The optical emission observed in the experiment validates the very intense hot spot seen in the simulations. As for the lower-pressure simulations in 2D and 3D, there is closer agreement between the experiment and 3D simulation in the collapse time. It is thought the extra dimension produces a more energetic collapse, though the precise mechanism for how this occurs is not known. Across the pressures studied, the close agreement of the cavity interface outline to the experiments provides further confidence in the prediction of parameters that are difficult to measure *in-situ*, such as temperature and local pressure and density.

In addition to this analysis, for a larger number of simulations the cavity dynamics are obtained, with collapse time, interface acceleration, and jet and release velocities are determined as a function of loading condition. These extracted values are compared to the experiments and broad agreement is found, but again the single 3D simulation is in closer agreement (the 1.25 GPa simulation is not included in this analysis). The biggest divergence between experiments and simulations is seen in the interface acceleration – at the highest pressures the simulations significantly under-predict the acceleration, again suggesting that the dimensionality plays a key role in the kinematics generated by the shock.

Additional simulations of cavity collapse are performed, in aluminium, copper and stainless steel media. This is motivated by the hypothesis in Chapter 4 that the placement of the collapse time vs. pressure ratio curve may be dependent on material properties like density and longitudinal sound speed, and that the dimensionless Rayleigh collapse time equation can be expressed in terms of a material's stiffness. The results, though limited, suggest the collapse time due to shock loading can be predicted with an analytic expression, dependent only the shock pressure, density, cavity diameter and longitudinal sound speed. This relationship appears to hold regardless of whether the transition to hydrodynamic behaviour is complete, extending well into the strength-dominated re-

gion. Though promising, the small number of data points for the plots means that more experiments and simulations are needed before any firm conclusions on this aspect can be drawn. This also motivates the development of a collapse time expression from purely physical arguments. This will be useful for scenarios where cavity collapse time is informative, such as in the modelling of distributions of cavities of varied size in a energetic material, where the closure time is related to the activation time.

6.2 Research outlook

The results of this work represent a significant experimental advancement in the study of the cavity collapse phenomenon, and are relevant to the many fields of research interested in shock-induced collapse, in both solids and fluids. As we saw in the motivation Section in Chapter 1, understanding the mechanisms of cavity collapse is a key factor in the development of medical technologies – specifically, where the ability to reveal the mechanisms of dynamic collapse may help identify the correct ultrasound pulse energy needed to achieve sufficient penetration into cancerous tissue during targetted drug delivery, while minimising collateral damage. We also saw that in the development of energetic materials, cavity collapse plays a key role in initiation, for which there is little direct experimental data available. Therefore, having data to test and improve the models is a important outcome for such research, which this work provides in unique detail.

There is also the direct relevance to the development of novel fusion techniques, where it has been shown that the conditions during cavity collapse are extreme enough to generate nuclear fusion. The toroidal plasma captured in this work further validates this prediction. Furthermore, the research fields detailed in the literature review show that this work is relevant beyond cavity collapse research. This includes the study of the shear banding phenomenon, which is difficult to

capture experimentally *in-situ*. The results of this work thus showcase the range of phenomena that can be captured utilising high-speed synchrotron radiography, from the interaction of shock front with defects, to shear band, jet and tori formation.

Although the impact and significance of this work is clear, there are still many avenues left to explore in this work on cavity collapse in a solid medium. There are clear improvements that can be made to the imaging system, made possible by the recent 'Extremely Bright Source' (EBS) upgrade at the ESRF, which promises increased X-ray flux, and therefore illumination power. Furthermore, continued improvements in scintillator decay times and high-speed camera sensor sensitivity and frame rates will eventually enable single-bunch imaging while using the ESRF's 992-bunch 'continuous fill' mode. This will produce image sequences at approximately 350 Mfps, an order of magnitude greater than the current iteration of the imaging system. At approximately 3 ns between frames, this will allow the capture of shock experiments at the mesoscale, since an interface moving as fast as 10 km/s will move 30 μm in this time. The increased magnification required to image at this scale will be made possible by the increased X-ray source brightness.

In the experimental study of cavity collapse in a solid, there is the need to explore different materials, and higher X-ray flux increases the possibility of using higher-density media. For this purpose, a dedicated gas gun at beamline ID19 is planned, like that existing at the APS synchrotron. Other important aspects of cavity collapse that are not in the scope of this Thesis are cavities of varied geometry and multiple neighbouring cavities interacting under shock load. Such experimental work can then be used to further verify our confidence in simulation codes like SCIMITAR3D for capturing physical processes such as cavity collapse in explosives like HMX. These models can then be used to design and optimise energetic materials configurations, to tune factors such as the initiation thresh-

old to obtain outcomes for a specific application.

In the realm of simulation work on cavity collapse in solids, there are still many unexplored avenues of research. There has already been extensive work in the field of energetics, on explosives like HMX, and, even though this work has revealed the process in new detail, there are still numerous unanswered questions. Most notably, the role that strength plays in the collapse process of cavities in different materials is not clear. Continued investigation through simulations, using both strength and strengthless models is required, to establish how the effects of strength persist into the hydrodynamic regime, and whether the material under shock is solid, liquid or mixed phase. Furthermore, for PMMA and other polymer materials, a more sophisticated model, including damage and a temperature-dependent heat capacity, is needed to completely capture some of the finer details in the transition to hydrodynamic behaviour.